Synthesis and Characterisation of Novel Superconductors

Thesis submitted in accordance with the requirements of the University of Liverpool for the degree of Doctor in Philosophy

by

A. G. M^{c}Lennan

September 2013

Acknowledgements

I would like to thank my supervisor Professor Matthew Rosseinsky for the opportunity to work within his research group, the use of state-of-the art equipment and his supervision during my doctoral work. I would also like to thank him for the many opportunities to go to conferences, courses and synchrotron facilities which enriched my time in his group. In addition I would like to express my thanks to my secondary supervisor Dr. Claridge for all of his advice throughout my work.

I give my appreciation to my mentor Dr. Ganin for his advice and technical knowledge on my synthetic, analytical and written aspects of my work.

I would like to express my thanks to Professor Kosmas Prassides research group in the University of Durham for their collaboration, my introduction to the ESRF facility and aid with high pressure magnetic measurements.

The University of Liverpool core services staff also receives my gratitude for the provision of accurate analytical services for my air-sensitive materials, creation of specialised glassware and maintenance of equipment vital to my work.

Lastly I would like to thank my family, in particular my wife and children for their support while writing this work.

Synthesis and Characterisation of Novel Superconductors

by A. G. M^{c}Lennan

Abstract

This work presents and discusses the recent advances in high temperature superconductors. It focuses on how both the superconducting fullerides and iron selenides have contributed to the state-of-the-art of high temperature superconductors.

The discovery of the relationship between the critical temperature and the proximity of the Cs_3C_{60} material to the Mott metal-insulator transition has clearly demonstrated unconventional superconductivity in fullerides. However, the best samples of Cs_3C_{60} were synthesised in purities of ~80 % which complicates the analysis of the physical properties of this important material. Furthermore, the use of hazardous and dangerous solvents such as methylamine and ammonia limits the availability of these materials for a broader scientific community and therefore, a facile and efficient synthetic procedure would strongly benefit the field. Within this work a novel synthetic method for Cs_3C_{60} in a common THF solvent has been developed producing nearly single phase samples with a critical temperature (T_c) of 33 K.

Intercalation of alkali metals into a FeSe host can produce the materials with T_c up to 46 K. However, the structure and composition $A_xFe_ySe_2$ (A=K, Rb and Cs) is under debate. In this work this problem was explored by the creation of a subsolidus $K_xFe_ySe_2$ powder phase diagram at 750^{o}C. This allowed me to identify the existing range for superconducting samples and assess their qualities. It was found that the minority phase with a refined composition of close to $K_{0.5}Fe_2Se_2$ and specific cell volume of 209.73 Å^3 which is probably responsible for superconductivity. As the high temperature route does not allow the isolation of the superconducting phase in pure form a novel low temperature route has been developed. It involved the reaction of FeSe with potassium acenide reducing agents in THF where the use of the organo-metallic agent was to moderate the reductive capability of potassium. This proof-of-concept method produced superconducting materials with up to with 11 % of superconducting fraction and T_c = 33 K.

Table of Contents

1. Introduction

1.1. Superconductivity and magnetism

1.1.1. Superconductivity

1.1.1.1. Discovery and defining properties

In 1911 the first example of a superconductor, mercury, was discovered when the metal was cooled below 4.2 K where it exhibited zero electrical resistance.[1] The temperature at which this phenomenon occurred was termed the critical temperature (T_c). Below this temperature a material experiencing this phenomenon will conduct electricity indefinitely without external influence. The second defining property of superconducting materials was discovered by Meissner and Ochsenfeld 22 years later.[2] This new property manifested itself as the total exclusion of magnetic flux from a superconductor at temperatures below the T_c and was named the Meissner-Ochsenfeld effect.[2]

Initially the link between structure and superconductivity was not made as X-ray diffraction experiments did not find any structural transition between the normal and superconducting states.[3] In 1950 the isotope effect was discovered while investigating the T_cs of different mercury isotopes. This revealed that the T_c increases with decreasing isotopic mass.[4, 5] This relationship suggests that the T_c is related to the isotopic mass (M) using equation 1-1.[6]

$$T_c \propto \frac{1}{\sqrt{M}} \qquad \textbf{(1-1)}$$

The relationship between isotopic mass and T_c led to the idea that superconductivity, in the early materials, was dependent on lattice vibrations. This link was made due to the inverse relationship between the vibrational frequency and the reduced mass in a diatomic molecule. It therefore stands to reason that a similar relationship would exist between the lattice vibrations and the isotopic mass of a constituent atom. Considering that lattice vibrations are the primary cause of the resistance at room temperature it stands to reason that the lattice vibrations would be used in the theory of early superconductors.

1.1.1.1. Bardeen-Cooper-Schrieffer (BCS) theory and conventional superconductors

The theory relating lattice vibrations (where the quanta are called phonons) to T_c was postulated in 1957 by Bardeen, Cooper and Schrieffer.[7] The BCS theory predicts that below the T_c of a superconducting material there is a slight attractive force experienced by two electrons. This force is mediated by phonons which interact with the conduction electrons resulting in the coulomb repulsion between electrons being overcome. The result of this slight attractive force is that two electrons become weakly bound together forming a Cooper pair (Figure 1.1).[8] The formation of Cooper pairs is the root cause of the superconducting materials displaying the properties of zero electrical resistance and the Meissner effect. The small pairing energy is easily overcome by thermal energy which is why superconductors require cooling in order to transition into the superconducting state.

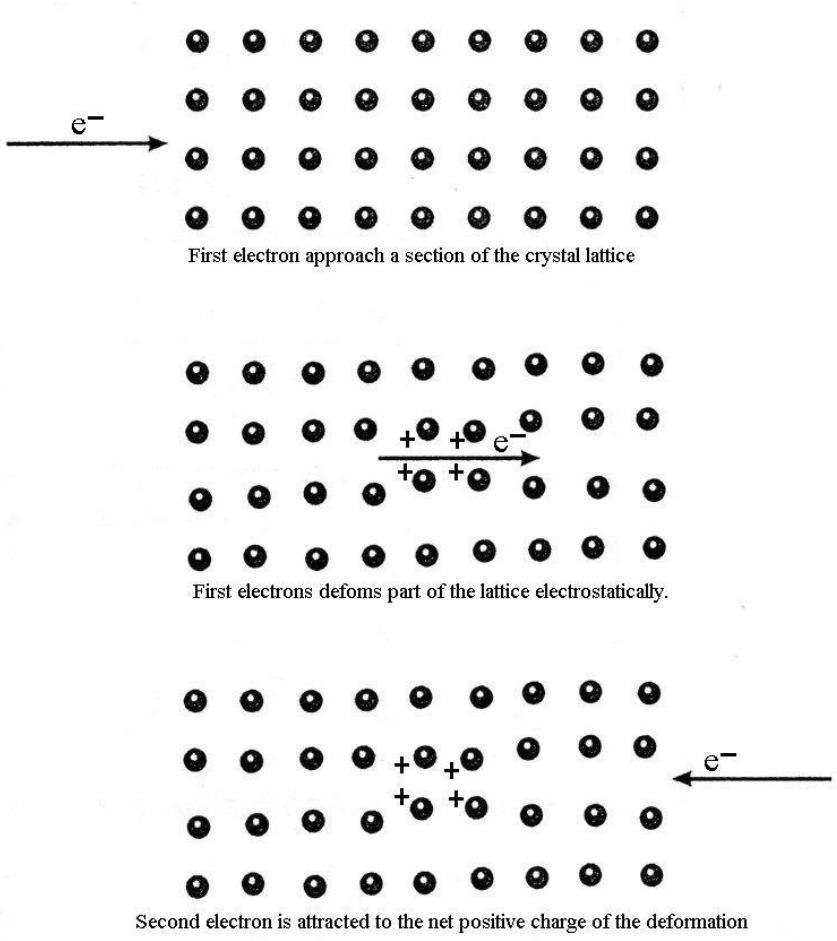

Figure 1.1 Graphical depiction of the formation of Cooper pairs due to lattice vibrations as described by the BCS theory.[9]

In conventional superconductors the Cooper pairs are formed such that their spin and orbital angular momentum cancel. This allows the paired electrons to observe the Pauli exclusion principle, where two electrons in the same shell cannot have the same spin and angular momentum, and can be described by a wave function. This wave function is known as an order parameter which, in the case of a conventional superconductor, has symmetry similar to that of the wave function of s electrons which is referred to as a singlet state or having s wave symmetry.

Once formed the Cooper pairs are not restricted to the original electrons involved in their formation. The pairing is dynamic and occurs constantly with pairs breaking and reforming by exchanging electrons between Cooper pairs. This means that as the pairs move through the lattice they do so in an ordered fashion. The result is that the motion of each pair is fixed with respect to the motion of another pair and this is consistent across the whole ground state. The effect this has is to prevent the lattice from scattering the pairs which results in the absence of resistance while a material is in a superconducting state.

The BCS theory holds for conventional superconductors which all follow BCS predictions for T_c, isotope effect and s wave symmetry. The BCS theory due to realistic limitations of phonon frequency predicts a range of T_cs up to ~30 K. This range is not a hard limit and there is flexibility for example MgB_2 is a conventional superconductor with a T_c of 39 K.[3, 10] This exceptionally high T_c for a binary system was rationalised by the materials phonons being enhanced by the light atomic mass of boron and strong coupling to the conduction electrons. The BCS theory fails to describe materials with T_cs above that of MgB_2 and order parameters of different symmetry than s wave. These unconventional superconductors are responsible for the highest observed T_cs to date and are classified as high temperature superconductors.

1.1.1.1. High temperature superconductors

Up until 1986 the highest T_c was for Nb_3Ge at 23.3 K at this point a new class of superconductors was discovered with a composition of $La_{1.8}Ba_{0.2}CuO_4$ and a T_c of 35 K[11] (Figure 1.2). This significant discovery demonstrated that superconductivity was not limited to T_cs of less than 30 K and could potentially lead to materials with even higher T_cs. The discovery of superconductors based on metal oxides lead to a huge effort in the investigation of the chemistry of these materials. The products of this research were an entire array of superconducting cuprate based materials such as $YBa_2Cu_3O_{7-x}$ (T_c = 93 K)[12],

$Bi_2Sr_2Ca_3Cu_4O_{12}$ (T_c = 104 K)[13] and the current highest T_c superconductor $HgBa_2Ca_2Cu_3O_8$ (T_c = 134 K)[14].

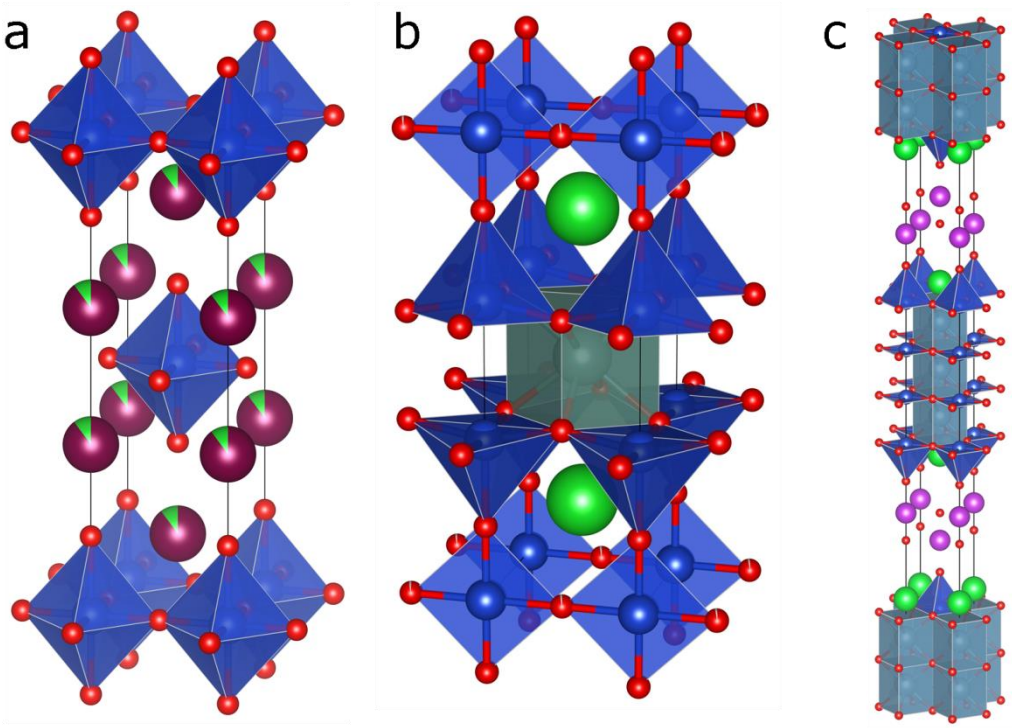

Figure 1.2 Crystal structures of (a) $La_{1.8}Ba_{0.2}CuO_4$; (b) $YBa_2Cu_3O_{7-x}$ and (c) $Bi_2Sr_2Ca_3Cu_4O_{12}$

The cuprate superconductors all have complex structures of tetragonal (an example space group (SG) SG = *I*4/*mmm*) or orthorhombic (SG = *Pmmm*) symmetry. These structures are based on the perovskite structure and contain plains and/or chains of copper oxide. Initially the parent materials are antiferromagnetic insulators which then need to be doped to become metallic. Doping the parent material alters the oxidation state of the Cu directly affecting the electronic properties of the material resulting in the suppression of the antiferromagnetic state and allowing the superconducting properties to be expressed (Figure 1.3). The superconductivity in these compounds is thought to be related to the CuO sheets where the superconductivity is found to propagate in a parallel direction with the sheets. The interplay between the magnetic states of the cuprate parent materials and the superconducting compositions demonstrates an important link between magnetism and superconductivity.

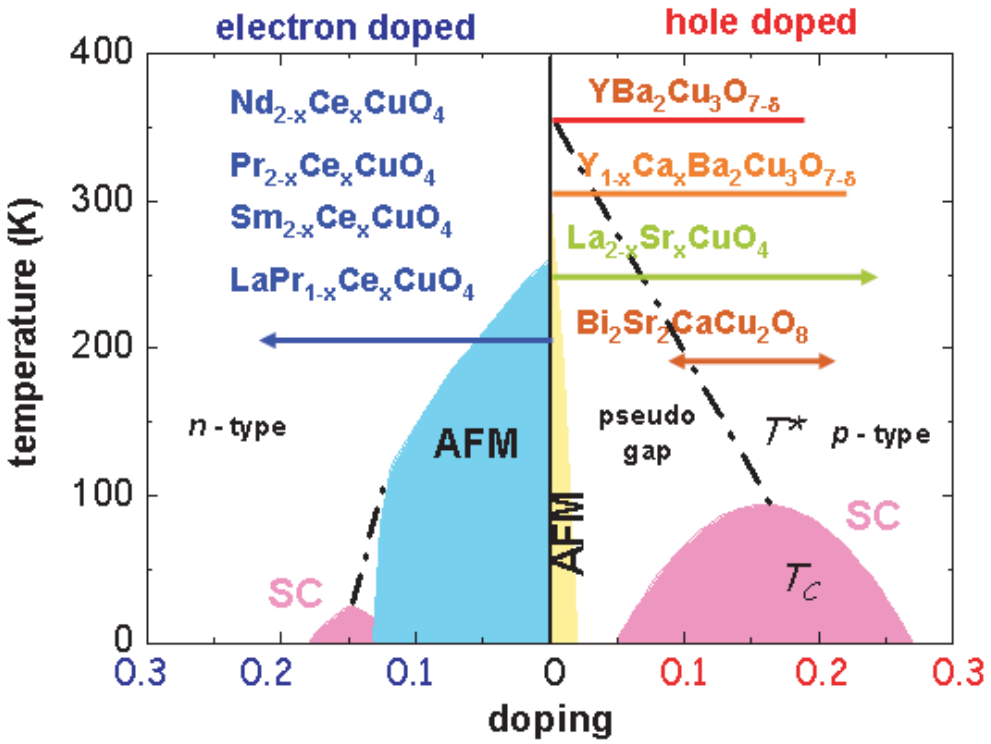

Figure 1.3 Regions of the phase diagram for several different high temperature superconductors.[15]

The cuprates are unconventional superconductors due to their anisotropic paring state and the superconductivity is unlikely to be brought about solely by electron-phonon coupling.[16] The BCS theory works for superconductivity in materials where the Cooper pairs create a state with a total angular momentum of 0. The cuprates form a superconducting state with different order parameter symmetry than s wave, for example d wave symmetry is common.[3] This results in a state where the Cooper pairs have angular momentum counter to the stipulations of the BCS theory. In addition the BCS theory predicts that the parent state of superconductors should be metallic.[3] The proximity of these superconductors to an antiferromagnetic insulating state is then a strong indicator of unconventional superconductivity. Therefore the high temperature superconductors' properties are not accounted for by the BCS theory.

1.1.1.1.1. Iron based superconductors

The cuprates are not the only high T_c materials available, in 2008 a new class of iron based superconductors were discovered. These new superconductors began with the composition $LaFeAsO_{1-x}F_x$ which gave a T_c of 26 K.[17] This material consists of tetragonal [FeAs] layers separated by [LaO] square

based pyramid units where some of the oxygen is replaced by fluorine (Figure 1.4). Other examples of iron pnictide superconductors are $Ba_{0.6}K_{0.4}Fe_2As_2$ (T_c = 38 K), $NdFeAsO_{1-y}$ (T_c = 54 K) and KFe_2As_2 (T_c = 3.8 K) all of which share the [FeAs] layers of the $LaFeAsO_{1-x}F_x$ material (Figure 1.4).[18]

The iron based superconductors typically crystallise into a tetragonal form of either *I*4/*mmm* or *P*4/n*mm* symmetry.[18, 19] Where they all share the layers of edge sharing [FeX] (X = pnictide or chalcogenide) tetrahedral units. These structures undergo a similar phase transition into the superconducting state that the cuprates do. The tetragonal structure of the iron superconductors becomes orthorhombic on cooling (Figure 1.5). These layers are held together by weak Van der Waals forces or electrostatic interactions which means that guest species can be intercalated easily between the layers.[18] The T_cs of these materials are heavily dependent on the type and amount and type of guest species that is intercalated into the parent materials. An excellent example of this behaviour is between $Ba_{0.6}K_{0.4}Fe_2As_2$ and its parent material $BaFe_2As_2$ where the replacement of a fraction of the parent materials Ba with K results in an 90 % increase in the T_c.[18] The large range of intercalation chemistry has seen a wide range of these materials made with an equally wide range of superconducting properties.[18]

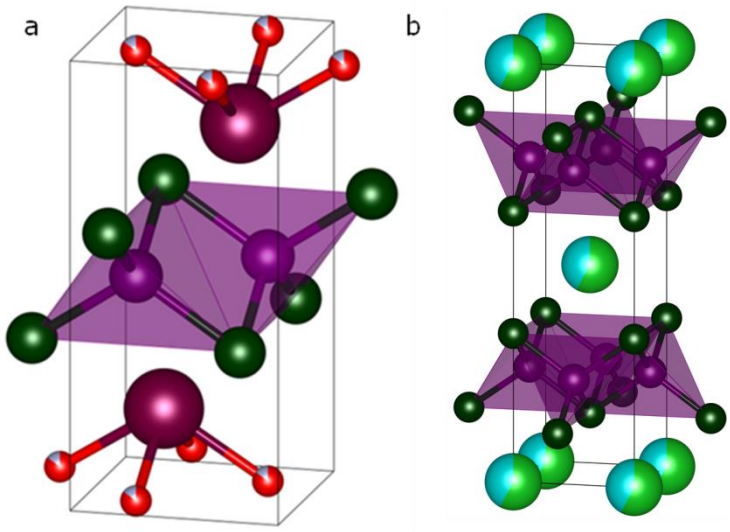

Figure 1.4 The common feature of iron based superconductors is the [FeX] (X = pnictide or chalcogenide) layers and is shown by the purple polyhedral. (a) Crystal structure of $LaFeAsO_{1-x}F_x$. (b) Crystal structure of $Ba_{0.6}K_{0.4}Fe_2As_2$.

Like the cuprate superconductors the iron pnictide materials can be hole or electron doped in order to achieve a superconducting state.[18, 19] An example

of a material requiring electron doping is $BaFe_2As_2$ where its phase diagram is represented in figure 1.5. In this material there is a significant overlap between the magnetic and the superconducting states. This indicates that superconductivity and the magnetic state could either co-exist or be phase separated within these materials.[19] Similarly to the cuprate superconductors this proximity to an antiferromagetic insulating state combined with the T_cs that the BCS theory cannot predict means that the iron based superconductors are also unconventional.

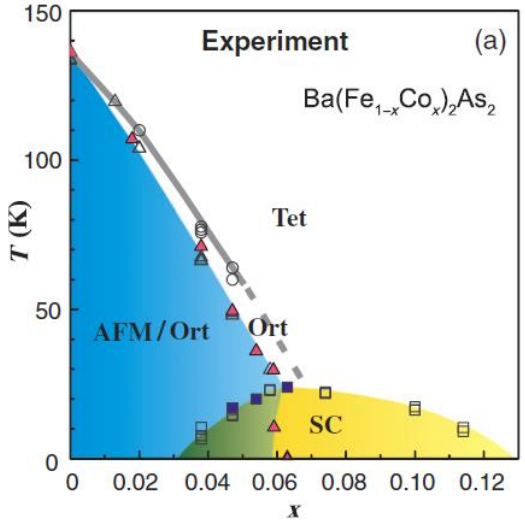

Figure 1.5 Phase diagram for $Ba(Fe_{1-x}Co_x)_2As_2$.[18]

High temperature superconductors like the cuprates and iron pnictides are produced by the suppression of the antiferromagnetic properties of their parent material.[3, 18] The current understanding of how their superconducting state is brought about is through electron coulomb repulsion producing a weak attraction between electrons. The electron-phonon interactions described by BCS theory are then replaced by magnons which then couple to the electrons. Since magnons occur in magnetic materials the subject of magnetism is important for high temperature superconductivity.[3]

1.1.2. Magnetism

Superconductivity was predicted by the BCS theory to be a case of perfect diamagnetism. It is an incredibly strong effect capable of eclipsing the response from the other forms of magnetism. The effect is so strong that it will completely expel the magnetic flux lines from the interior of the sample while in

its superconducting state (Figure 1.6). The field is expelled as an electric current is established in the surface of the superconductor and creates an opposing magnetic field. The magnetic field can only penetrate the surface of a superconductor to a certain distance which is termed the London penetration depth. The total exclusion of a magnetic field from the core of the material while it is in the superconducting state is known as the Meissner effect.[2]

In order to properly understand the relationship between superconducting materials and diamagnetism it is necessary to define the basic forms of magnetism. Parallels can be drawn between the configuration of electrons in the superconducting state and diamagnetic materials. Therefore the distinction between diamagnetism and paramagnetism is important. Since some theories for high temperature superconductors are based upon magnetic interactions it seems appropriate to define ferro and antiferromagnetism as well.[3]

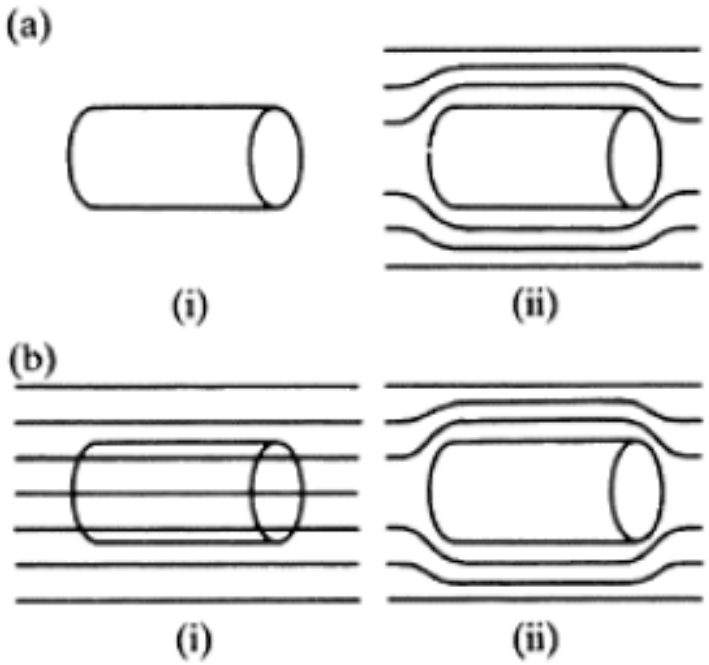

Figure 1.6 The Meissner effect for a superconducting material; (a) at temperatures below T_c in the absence of a magnetic field (i) and in an applied magnetic field (ii); (b) in a constant applied magnetic field at temperatures above the T_c (i) and below (ii).[3]

The superconducting state of a material is not only influenced by temperature but also the strength of the magnetic field applied to it. The minimum field strength that is required to push a superconductor into the normal state is called the critical field (H_c). The critical field is dependent on the temperature where H_c is 0 when the temperature is at the superconductors T_c.

The H_c is also dependent on the superconducting material itself and can show distinct differences between some superconductors. This distinction results in two different types of superconductors named type 1 and type 2. For type 1 superconductors, like mercury and other simple metals, there is only one H_c value. However, the type 2 case is more complex and shows two different H_c values (H_{c1} and H_{c2}) which have different temperature dependencies but converge at the materials T_c. For the type two case magnetic fields above H_{c1} result in a mixed state where both the superconductivity and the normal state behaviour is observed. The superconducting behaviour is only suppressed entirely when the magnetic field strength exceeds the H_{c2} value. The type 2 superconducting materials are in general much more structurally complex than the type 1 variants, consisting of alloys and ceramic layered materials.

1.1.2.1. Diamagnetism and paramagentism

Magnetism is a bulk property of a material and is generally classified into one of four groups as paramagnetic, ferromagnetic, antiferromagnetic or diamagnetic.[3] These four types of magnetism can be distinguished by their response to an applied magnetic field. The magnetic field strength (H) in the units of Oersted (Oe) can be described by the magnetic flux density (B) in gauss in equation 1-2. Where μ_0 is the permeability of free space.

$$\boldsymbol{B = \mu_0 H} \qquad \textbf{(1-2)}$$

The way that material's respond to an applied magnetic field is by increasing (paramagnetic) or decreasing (diamagnetic) B locally around the material. As a result of the applied magnetic field the material experiences its own field which is referred to as the magnetisation (M) in A M^{-1}.[3] This modifies the magnetic flux density equation shown above to reflect the presence of the samples magnetisation to give equation 1-3.

$$\boldsymbol{B = \mu_0 (H + M)} \qquad \textbf{(1-3)}$$

The measurements of magnetic materials use the magnetic susceptibility (χ) to describe the magnetic properties of that particular material. χ (dimensionless) is related to M (A M^{-1}) and H (A M^{-1}) in equation 1-4.[3] Although in SI units χ is dimensionless another common system used is the centimetres

grams seconds (cgs) which gives the units as follows χ in electromagnetic unit (emu) cm^{-3} Oe^{-1} and M in emu cm^{-3}.

$$\chi = \frac{M}{H} \tag{1-4}$$

In order to define a material's magnetic properties χ is related to B in equation 1-5. If a materials response to H is to increase B due to the relationships shown in equation 1-3 and 1-4 χ must be greater than 0. If the response decreases B then the magnitude of M is negative and therefore opposes H which means that χ must be less than 0. The paramagnetic (when χ >0) and diamagnetic (when χ<0) properties can then be assigned based on χ (Figure 1.7).

$$\begin{aligned} \boldsymbol{B} &= \boldsymbol{\mu_0}(\boldsymbol{H} + \boldsymbol{\chi H}) \\ &= \boldsymbol{\mu_0 H}(\boldsymbol{\chi} + \mathbf{1}) \end{aligned} \tag{1-5}$$

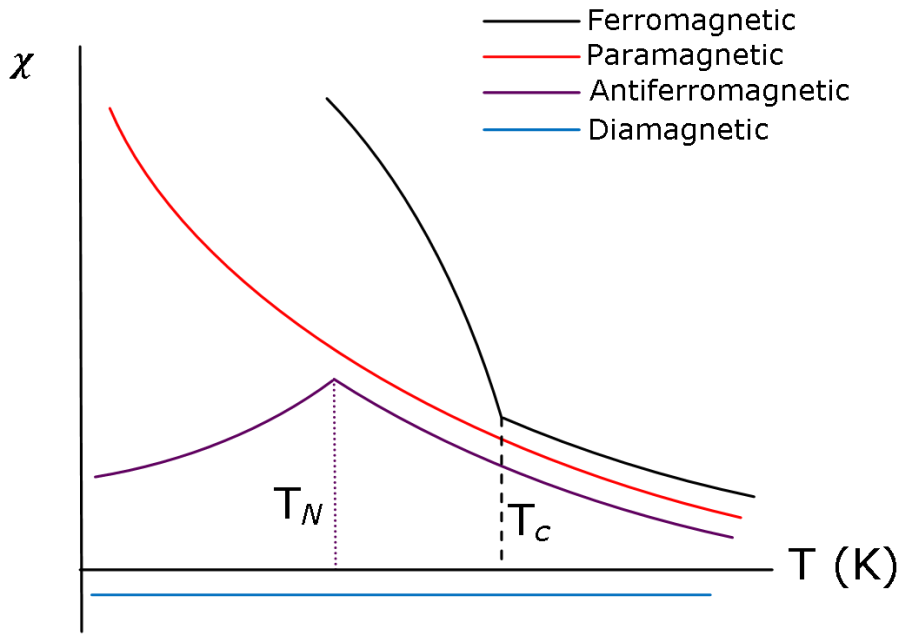

Figure 1.7 Temperature dependence of magnetic susceptibility for ferromagnetic, paramagnetic, antiferromagnetic and diamagnetic behaviour.

Diamagnetism is a very weak response to an applied magnetic field that is present in all materials. It is generated by the movement of electrons within an atom or molecule. The effect of diamagnetism is negligible when other types

of magnetism are present as they are all far stronger magnetic responses. An interesting property of diamagnets is that they (weakly) repelled by magnetic fields.[3]

Paramagnetism is a very simple form of magnetism and is generated by the presence of unpaired electrons in a material. When the paramagnetic material is subjected to a magnetic field the magnetic moments of the unpaired electrons tend to align with the magnetic field and therefore with each other. When the magnetic field is removed the thermal energy is then capable of randomising the unpaired electrons magnetic moments. This ordering and randomizing of the magnetic moments due to the presence or absence of a magnetic field can be described by the Curie law (equation 1-6). Where *C* is the Curie constant and *T* is the temperature in K.

$$\chi = \frac{C}{T} \qquad \textbf{(1-6)}$$

A plot of $1/X$ vs. T is used to characterise Curie paramagnets as the gradient is $1/C$. This then allows information to be obtained on the effective magnetic moment. The Curie constant is given by equation 1-7 where b is a universal constant ρ_{eff} is the effective magnetic moment and N is the concentration of magnetic atoms. For equation 1-8 N_A is Avogadro's number, μ_B is the Bohr magneton and K_B is Boltzmann's constant.

$$C = bp_{eff}^2 N \qquad \textbf{(1-7)}$$

$$b = \frac{N_A \mu_B^2}{3K_B T} \qquad \textbf{(1-8)}$$

When the magnetic moments of the electrons in a material experience co-operative behaviour the Curie law breaks down (Figure 1.8). A modification of the Curie law called the Curie-Weiss law is used equation 1-9 where θ is the Weiss constant. The co-operative behaviour that results in the need for this modification can be the precursor to either ferromagnetism or antiferromagnetism. Which behaviour the material will express can be predicted using the sign of the Weiss constant. For $\theta>0$ the material will become ferromagnetic below the Curie temperature (T_c) and for $\theta<0$ the antiferromagnetic behaviour will be expressed below the Nèel transition (T_N).

$$X = \frac{C}{T-\theta} \qquad \textbf{(1-9)}$$

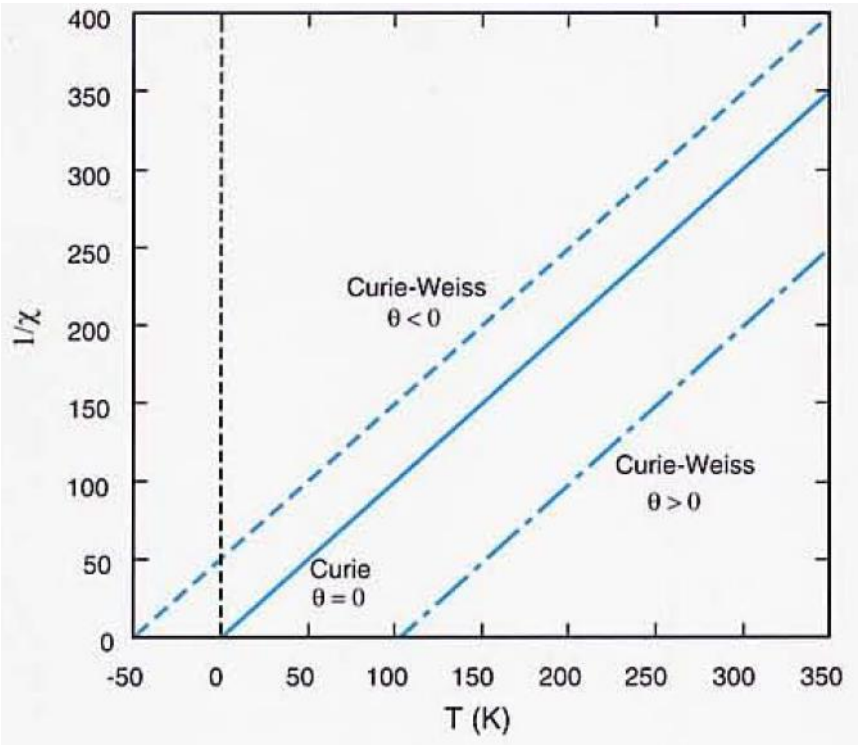

Figure 1.8 The temperature dependence of inverse magnetic susceptibility for paramagnets showing Curie (θ = 0) and Curie Weiss ($\theta \neq 0$) behaviour.[20]

1.1.2.2. Ferromagnetism and antiferromagnetism

Ferromagnetic materials consist of domains which are small regions (volumes between 10^{-24} to 10^{-17} m^3) contained within a crystal. Within these domains all of the electron spins are aligned parallel to each other due to exchange interactions created by electron-electron repulsion. At temperatures above the T_c these domains are randomly orientated due to a long range magnetic dipole interaction. It is these domains that create the Curie-Weiss paramagnetic behaviour shown in figure 1.9. Below the T_c the randomly orientated domains become ordered (Figure 1.9) and co-operate with each other which makes the ferromagnetic response to an applied magnetic field much stronger than the paramagnetic. This co-operative behaviour where the domains are aligned parallel to the magnetic field causes a larger increase to the flux

density than that of a paramagnet where the electron spins on each atom act independently to one another.

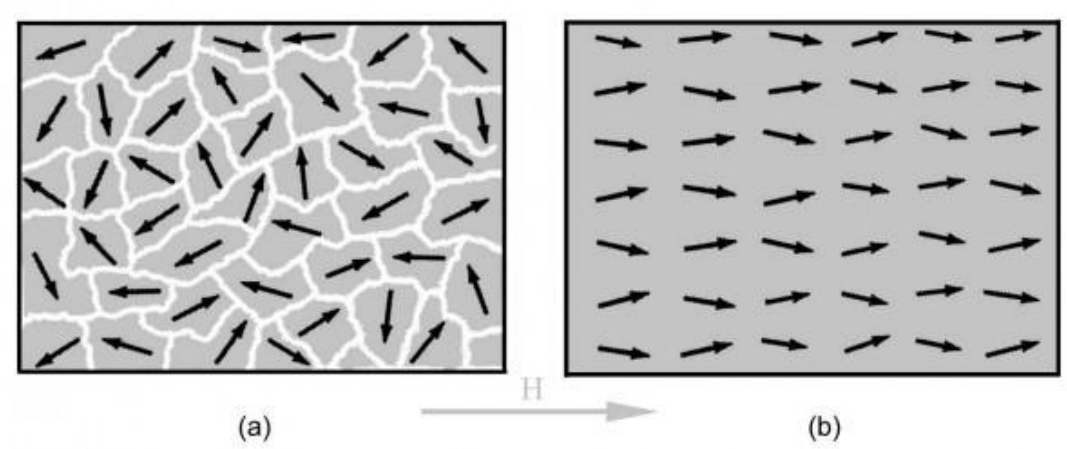

Figure 1.9 (a) Randomly orientated magnetic domains for a ferromagnet in the absence of an applies field. Where the domain boundaries are shown as white lines. (b) On application of a magnetic field to the ferromagnet the domains align parallel to the magnetic field.[21]

The antiferromagnetic form of magnetism involves the co-operative alignment of electron spins on different atoms. This co-operation between spins results in distinct regions of parallel aligned spins within a material for example in NiO the parallel aligned spins form discrete layers (Figure 1.10). When the temperature of an antiferromagnet is decreased below the T_N the magnetic regions magnetic moments align anti-parallel to the neighbouring regions. This means that the magnetic moments will cancel another out resulting in very small values of magnetisation. As the temperature is increased the increasing thermal energy allows some of the magnetic moments to align with the applied field which begins to increase the magnetisation. This occurs up to the T_N at which point the long-range order is overcome and the magnetic moments randomly orientate.

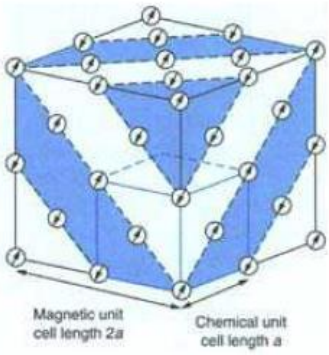

Figure 1.10 The alignment of magnetic moments for antiferromagnetically ordered NiO which cooled below its T_N. Where each layer (blue and white) contains Ni ions with magnetic moments aligned parallel to each other but arranged anti-parallel to the subsequent layer.[3]

1.1.3. Investigation of high temperature superconductors

The BCS theory fails to account for the high T_c superconductors due to a combination of complex structures and superconducting properties. Therefore a logical step in understanding the origins of superconductivity in the high T_c materials is to investigate the phenomenon in structurally simple materials. Two such materials are the tri-alkali metal fullerenes (A_3C_{60} A = alkali metal) and the iron selenide superconducting materials. Both the A_3C_{60} and FeSe based superconductors have similarities to both conventional and unconventional superconductors.

The A_3C_{60} materials offer a clear view of the relationship between structure and unconventional superconductivity.[22] Whereas the FeSe based superconductors offer strong links in structure and superconductivity between the cuprate, pnictide and conventional superconductors.[19] This means the investigation of these materials can provide significant information on high temperature superconductors in general. However, both systems still require answers to synthetic problems hampering the investigation of the superconductivity in these materials.[19, 23]

1.2. Tri-alkali metal fullerides

The superconducting A_3C_{60} (A = K, Rb and Cs) systems are all based on cubic structures. Additionally these materials have low structural disorder, precise obtainable alkali metal compositions and no phase transition to lower symmetry

on cooling below the T_c. This means that the investigation of superconductivity in these systems can focus on the electronic properties of the material. The wide range of A_3C_{60} compositions including binary and ternary materials means that the effects of the material structure and composition on superconductivity have been investigated in detail.

The superconductivity found in A_3C_{60} systems is not the only fascinating aspect about the alkali metal fullerides. They also have a rich and diverse intercalation chemistry involving a range of structures and polymorphs, compositions and properties. This makes these materials fascinating but also adds an additional layer of complexity when synthesising the superconducting A_3C_{60} compositions. An example of this complexity is seen in the Cs_3C_{60} system where on synthesis materials are often contaminated with other compositions making the investigation of the properties difficult.[24, 25]

1.2.1. Fullerenes as intercalation hosts

Spherical fullerene molecules consist of sixty covalently bonded carbon atoms arranged into a truncated icosahedron (symmetry I_h).[26] This arrangement results in the formation of twelve non-adjacent pentagons and twenty hexagons with carbon atoms at the vertices. Within this structure are two C-C bond lengths of 1.444 Å (6:5) 1.382 Å (6:6) with the former corresponding to the edges of a hexagon-pentagon pair and the latter which is between two hexagons (Figure 1.11). [27, 28]

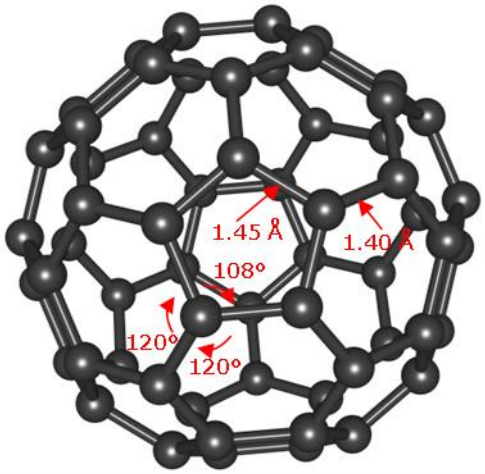

Figure 1.11 Graphical representation of a C_{60} molecule. The configuration of the atoms in the fullerene avoids the strain associated with two adjacent pentagons. The fullerene has a diameter of 7 Å in which the carbon atoms are in equivalent sp_2 hybridised environments with two types of bonds one between two hexagons (6:6, 1.382 Å) and one between a hexagon and a pentagon (6:5, 1.444 Å).[26-28]

The 60 π electrons in C_{60} molecule fill the orbitals up to the highest occupied molecular orbital (HOMO, with h_u symmetry). This makes the triply degenerate t_{1u} the lowest unoccupied molecular orbital (LUMO) and the t_{1g} the LUMO + 1. The electronic structure and small band gap energy of 1.8 eV [29] identifies both the LUMO and LUMO +1 as important to the chemistry of C_{60}.[27, 30] This molecule has two accessible unoccupied molecular orbitals making it electrophilic in nature and can accept electrons up to the formation of a C_{60}^{-12} anion (Figure 1.12). The stability conferred by a fully occupied HOMO causes the fullerene molecule to be far more easily reduced than oxidised. This property is clearly shown by the possibility of six one-electron reductions compared to the single one-electron oxidation.[31]

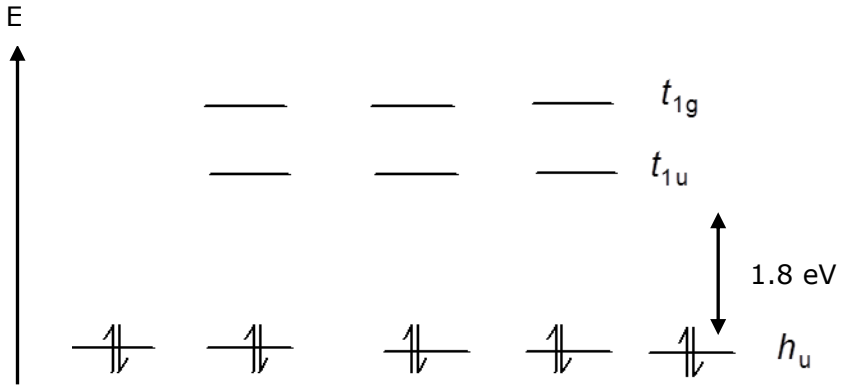

Figure 1.12 Electronic structure of the C_{60} molecule showing the HOMO (h_u), LUMO (t_{1u}) and LUMO +1 (t_{1g}) orbitals.[27, 29-31]

The current method for producing fullerenes in high yields wasn't uncovered until five years after the initial discovery of C_{60}. This method consisted of arc-processing graphite under a low helium pressure at a temperature of 3500 °C. This raw material was found to contain large concentrations of the two most common spherical fullerenes C_{60} and C_{70}.[32] The isolation of each allotrope was then made possible by chromatographic separation on the raw product from arc-processing.[33]

In their solid state form, under ambient conditions, C_{60} molecules crystallise in a face centred cubic (FCC) close packed array with a lattice parameter of 14.17 Å (Figure 1.13).[34] The fullerene structure is then held together by Van der Waals forces at an intermolecular distance of 10.02 Å (Figure 1.13).[27, 30, 34-36] Rietveld refinement of the C_{60} structural model against synchrotron x-ray experiments along with NMR studies indicate that the molecules are rotationally disordered[37-39] with C_{60}-C_{60} interactions controlling their orientation.[30] As with every spherical packing motif the C_{60} FCC array has interstitial holes. Within the FCC unit cell these sites are split into 8 smaller tetrahedral (with a radius of 1.12 Å and co-ordinated to four C_{60} molecules) and 4 larger octahedral (with a radius of 2.06 Å and co-ordinated by six C_{60} molecules) sites. The unit cell also contains four C_{60} molecules which produce a ratio of three interstitial sites to one C_{60} which allow the possibility of intercalating three species per C_{60} molecule. The fullerenes electron accepting nature coupled with its ability to accommodate large intercalates into its structure gives this material a wide range of intercalation chemistry.

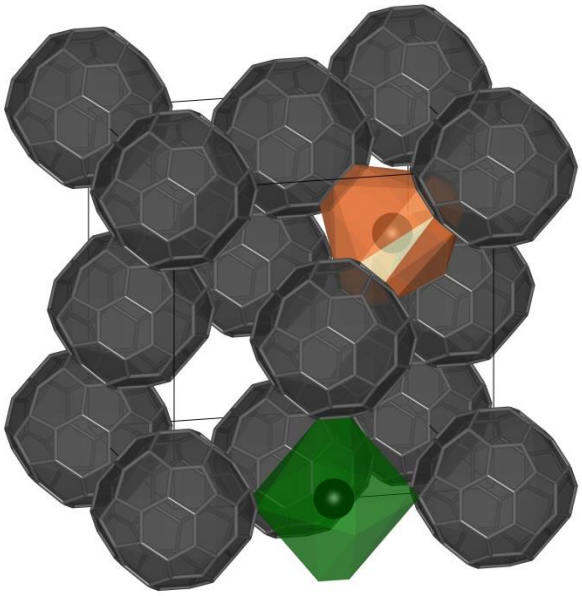

Figure 1.13 Face-centred cubic structure of C_{60} (space group (SG) = $Fm\bar{3}\,m$, a= 14.17 Å). The molecules are represented as spherical shells to reflect the orientational disorder at room temperature. One tetrahedral (orange) and one edge sharing octahedral (green) site in this array are indicated where the centres of each are displayed with a sphere. The polyhedral are truncated at the surface of the fullerene sphere.

1.2.2. Alkali metal fullerides

The electronic structure of a fullerene molecule shows that it can accept up to 12 electrons, so could potentially react with up to 12 alkali metals. It is possible to get as high as x = 11 and 12 in A_xC_{60} for sodium[40] and lithium[41] respectively. The lithium fullerenes have a compositional range of Li_4C_{60}[42] to $Li_{12}C_{60}$[41] and the sodium intercalates from Na_1C_{60}[43] to $Na_{11}C_{60}$[40]. For A_xC_{60} (A = Li and Na) compounds where x>6 the cations are small enough to cluster in the octahedral interstitial holes of the FCC C_{60} structure (Figure 1.14). For alkali metals with larger ionic radii than sodium the stoichiometry does not proceed past A_6C_{60}.[27] For the alkali metals Na, K, Rb and Cs the compositions of x = 3, 4 and 6 have been observed and can be synthesised in reasonable quantities.[27, 39, 44-46]

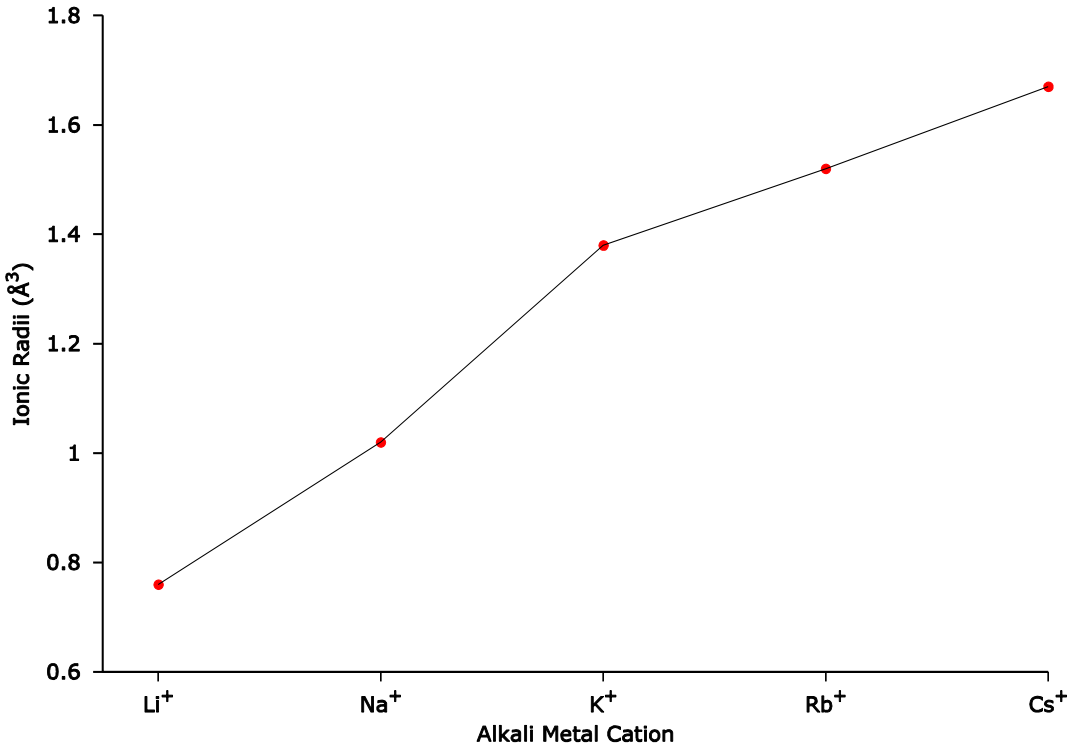

Figure 1.14 Increase in (C_n=6) ionic radii within the alkali metal group.[47] The tetrahedral and octahedral site of FCC C_{60} are 1.12 Å^3 and 2.06 Å^3 respectively. This means that the octahedral site can accommodate any alkali metal but the tetrahedral site must expand to allow any cation larger than Na^+. Substantial structural changes are therefore expected on intercalation of ions larger than sodium.

1.2.2.1. A_1C_{60}

A prime example of the structural diversity of the alkali metal fullerides is the A_1C_{60} compositions. In these compositions the size of the alkali metal cation determines what structure the intercalation compound will take upon synthesis. In Na_1C_{60} the material crystallises in a structure based on the FCC arrangement of C_{60} molecules with the cations occupying the tetrahedral sites producing giving simple cubic symmetry (SG = $Pa\bar{3}$). The reason for this is that the similar size of the T_d site to the ionic radii of the Na^+ cation means that all of the sodium is intercalated into this site (Figure 1.15).[43] In contrast to this are the A_1C_{60} (A = K, Rb and Cs) compounds where the cations are larger than the T_d of the FCC C_{60} array. These produce an orthorhombic structure (SG = *Pnnm*) based on a body centred cubic (BCC) packing of C_{60} molecules where the alkali metals occupy T_d sites. The interesting point about this particular structure is that it is polymeric where cycloaddition of the 6:6 bond of one C_{60} to another creating a chain of C_{60}s along the *a*-axis (Figure 1.15). The polymeric structure is obtained using slow cooling of the A_1C_{60} indicating that this is a thermodynamically stable

structure. A metastable structure can be obtained by altering the cooling protocol for synthesising Rb_1C_{60} from slowly cooling from 465 K to quenching through the temperature range 360 – 270 K. This produces an FCC structure where the Rb^+ cations occupy the O_h sites in the C_{60} FCC array.[48]

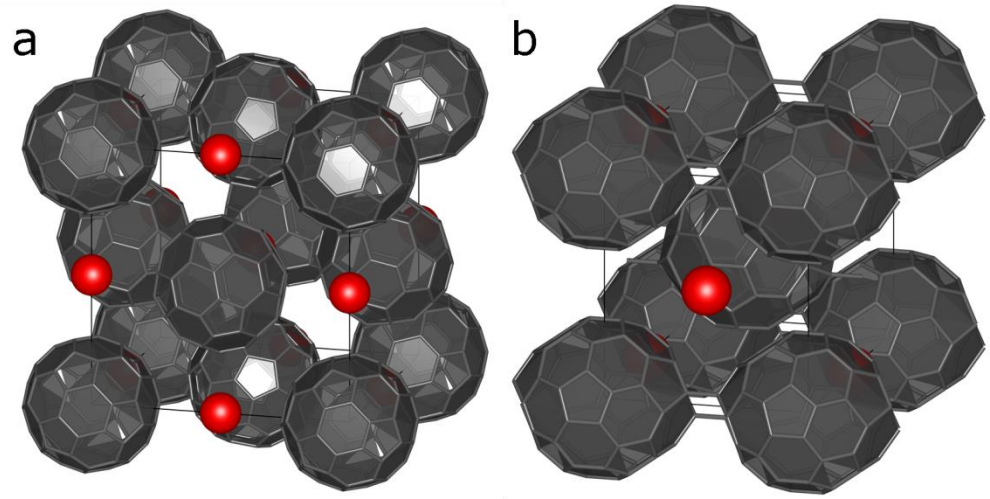

Figure 1.15 (a) the structure of Na_1C_{60} (SG = *Pa*$\bar{3}$) where the sodium cations occupy the tetrahedral sites of the C_{60} FCC lattice. (b) A_1C_{60} (SG = *Pnnm*, A = K, Rb and Cs) structure where the alkali metals occupy the tetrahedral sites of a BCC C_{60} array.

1.2.2.2. A_2C_{60}

Interestingly only sodium has been isolated in the A_2C_{60} composition as the larger cations are too large to form a stable structure where they occupy the tetrahedral sites (Figures 1.16). The structure of these materials is heavily dependent upon the ionic radii of the intercalating cation. This is due to the octahedral site being capable of accommodating any alkali metal but the tetrahedral site having a much more limited range.[47, 49] Intercalation into the octahedral site therefore produces minimal structural change in comparison to the tetrahedral site which forces a structural change when the intercalate is of sufficient size. This explains why Na_2C_{60} has been isolated as lithium is far too small to support this structure. Alkali metals with sizes larger than sodium are too big to occupy the tetrahedral site of the fluorite type structure of the A_2C_{60} composition and therefore are unstable.[27]

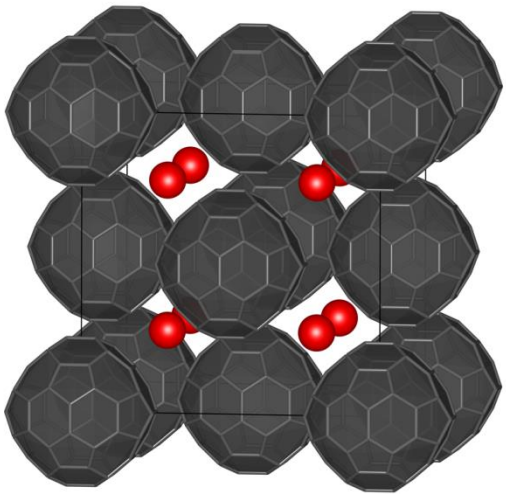

Figure 1.16 Na_2C_{60} (SG = $Fm\bar{3}\,m$) the sodium cations occupy the tetrahedral sites of a FCC C_{60} array.

1.2.2.3. A_3C_{60}

One exciting group of these intercalation compounds are the A_3C_{60} (A= Na, K, Rb and Cs) fulleride salts in which the cations completely occupy the interstitial sites of the C_{60} FCC structure (Figure 1.17).[27] When cations with a greater ionic radius than sodium are intercalated the molecules become merohedrally disordered.[46, 50] For example in K_3C_{60}, the fulleride anions direct a six membered ring towards the site increasing its size from 1.1 Å to 1.5 Å whilst the size of the octahedral site remains unchanged at 2.06 Å.[27, 46, 50] In A_3C_{60} compositions the orientation of the C_{60} anions are dictated by repulsive interactions and not by C_{60}-C_{60} interactions like in the structure of pure fullerene.[27, 51] When mixtures of alkali metals are intercalated the alkali metal with the largest radii occupies octahedral site selectively and the tetrahedral site accommodates the smaller cation.[51] This effect becomes more pronounced when larger alkali metals, especially Rb or Cs, occupy the octahedral site for example in $Rb_2(T_d)Cs(O_h)C_{60}$.[51, 52]

Interestingly the Cs_3C_{60} analogue shows polymorphism. One polymorph is the described FCC phase and the other has a structure based on β-W dubbed the "A15" phase with a space group of $Pm\bar{3}\,n$. Intermetallic compounds of this structure follow the general composition of A_3B and is the structure of industrially important superconductors such as Nb_3Sn.[53] The arrangement of fullerenes in the "A15" structure gives two non-equivalent cation positions depending on whether the closest Cs^+ contact is a hexagon (6d site) or a pentagon (6c site) fullerene face. Rietveld refinement of powder data against the

two models shows that the preferred contact is the hexagonal face.[24] The reason behind this selectivity in this structure is due to 6d sites larger size (Cs-C distance of 3.66 Å) which supports the cations larger size. This means that the "A15" structures anions point their hexagonal faces towards each other (interanion distance of 3.80 Å) which is a different interaction to that observed in the FCC structure (hexagon face to pentagon face).[23, 24]

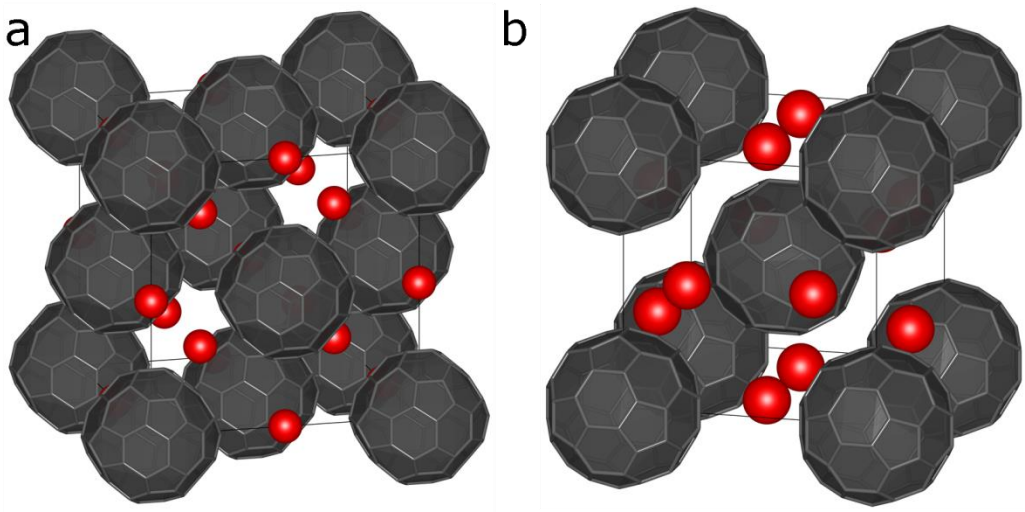

Figure 1.17 The structures of A_3C_{60} (a) FCC structure (SG= *Fm*$\bar{3}$ *m*) for A_3C_{60} where A = Na, K, Rb and Cs. Where the 2 T_d and single O_h interstitial sites are occupied by the cations. (b) "A15" polymorph of Cs_3C_{60} (SG= *Pm*$\bar{3}$ *n*) which is based upon a BCC C_{60} lattice where the Cs cations occupy the tetrahedral sites.

1.2.2.4. A_xC_{60} (3<x≥4)

The structural variation continues in A_4C_{60} (A = Li, Na, K, Rb and Cs) where again the structure is very dependent on the ionic radii of the alkali metal. The Li and Na A_4C_{60} have refined compositions of $Li_{3.49}C_{60}$[42] and $Na_{3.82}C_{60}$[54] which crystallise in a monoclinic space group of *I*2/*m*. These two compositions do have different structures despite the similar space group, the lithium compound is polymeric extending along the *b*-axis (Figure 1.18) and the sodium compound is not. For the A_4C_{60} compositions where K and Rb are used the materials produced are not deficient in the alkali metal. The use of larger alkali metals than Na produces a material with higher symmetry (body centred tetragonal (BCT) SG = *I*4/*mmm*) than the Na or Li compounds (monoclinic) (Figure 1.18). In the A_4C_{60} (A = K and Rb) structures the fullerene molecules are rotationally disordered about the 4-fold axis along the (001) direction. When the composition Cs_4C_{60} is targeted it produces a material which has a structure based upon the body centred packing of fulleride anions much like the K and Rb analogues but has a

significant difference. This difference is that the intercalation of the larger Cs cation (compared to K and Rb) forces the anions to become rotationally ordered. The loss of the anion disorder along the (001) direction causes the loss of the 4-fold axis which lowers the symmetry from BCT to orthorhombic (*Immm*). As a result of the drop in symmetry the alkali metal site in A_4C_{60} (A = K and Rb) is split into two sites in the Cs_4C_{60} structure (Figure 1.18).

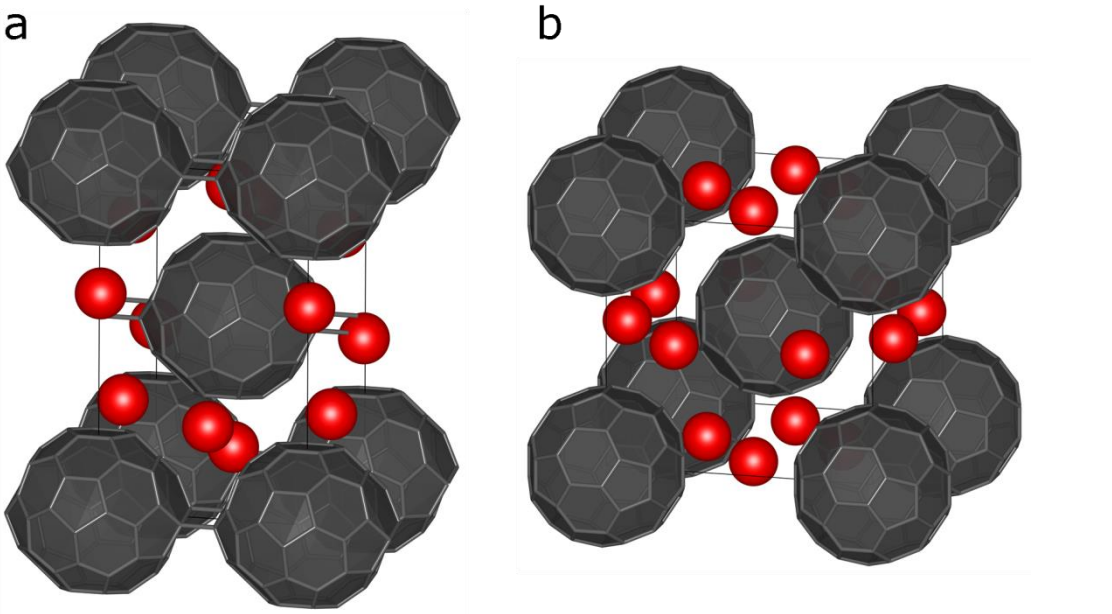

Figure 1.18 (a) the structure of $Li_{3.49}C_{60}$(SG = *I*2/*m*)[42] viewed along the *a*-axis the C_{60}s are polymerised along the *b*-axis (width of the page), the $Na_{3.82}C_{60}$ has the same space group, BCC arrangement of C_{60}s and cation positions but without the polymerisation along the *b*-axis. (b) A_4C_{60} structure (SG = *I*4/*mmm*) for K and Rb, the orientational disorder of the C_{60}s has been removed by eliminating the four fold axis for clarity. The cations occupy the tetrahedral sites of the BCC C_{60} array and have the point symmetry of m2m. This is also a representation of the Cs_4C_{60} analogue except that the cation positions are split into 2 Cs positions of point symmetry 2*mm* and *m*2*m*.

1.2.2.5. A_xC_{60} (x≥6)

The A_6C_{60} is an important composition as the A_3C_{60} (A = K, Rb and Cs) can be prepared using this composition as a starting material. The A_6C_{60} composition is also another example of the diverse crystal chemistry within the A_xC_{60} systems. For example the structure of the Na_6C_{60} compound is based upon the FCC arrangement of C_{60}.[55] This FCC arrangement has a total 3 interstitial sites consisting of 2 T_d and 1 O_h per C_{60} molecule. This means that the Na^+ cations cluster in the octahedral site in the form of two tetrahedra where each Na position is half filled (Figure 1.19). The formation of Na clusters in O_h site of

Na_xC_{60} (x>6) continues up to $Na_{11}C_{60}$.[40] The larger alkali metals (K, Rb and Cs) are all too large to cluster on the O_h site only being able to occupy the 2 T_d and single O_h sites of C_{60} FCC array. Therefore the intercalation of six alkali metals with ionic radii larger than that of Na forces a change of C_{60} packing from a FCC arrangement to a body centred cubic arrangement.[56] This produces six alkali metal sites of distorted tetrahedral co-ordination to 4 C_{60} molecules.

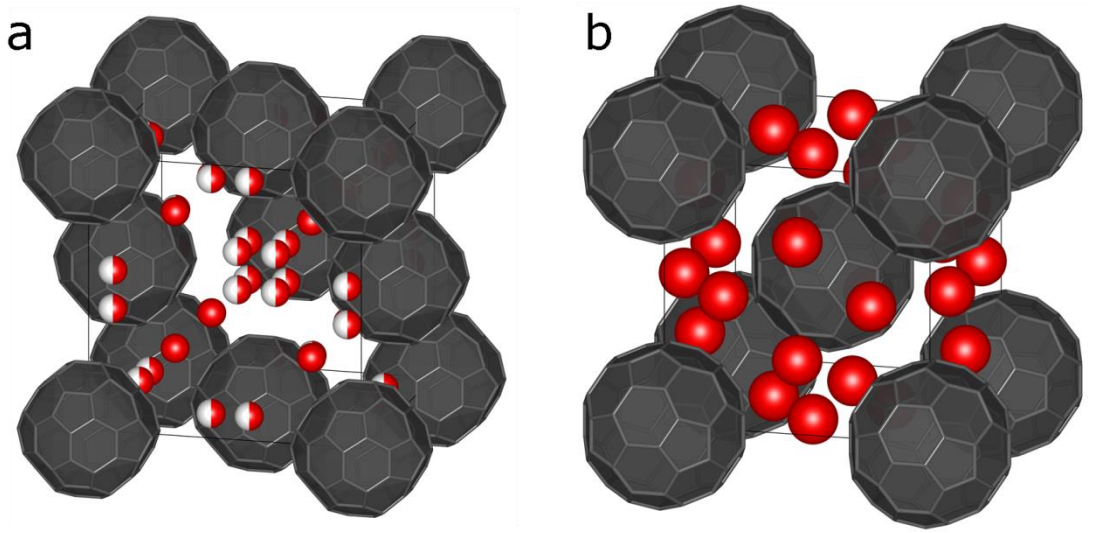

Figure 1.19 (a) the structure of Na_6C_{60} (SG = $Fm\bar{3}\,m$) where the sodium cations occupy the 2 T_d and single O_h site. Where 4 Na cations cluster in the O_h site in the form of two tetrahedra. The C_{60} molecule on the forward face has been removed to show the Na^+ ions occupying the O_h site (b) A_6C_{60} (A = K, Rb and Cs) where the cations occupy the tetrahedral sites of a BCC arrangement of C_{60}s.

1.2.3. Superconducting properties of A_3C_{60} Fullerides

A_3C_{60} fullerides are famous for their exciting property which is superconductivity and their potential to give new clearer data on superconducting mechanisms.[27, 35, 51] Remarkably, the superconducting transition temperature (T_c) shows a general trend by increasing monotonically upon the expansion of the unit cell volume (Figure 1.20).[27, 35] For example, the successive intercalation of larger alkali metal cations applies chemical pressure to the crystal lattice through the interstitial sites and increases the inter-fulleride separation. From this series we could conclude that just by forcing the inter-fulleride separation further apart we can achieve any T_c. This series, at first, appears simple until fullerene material doped with the larger alkali metals like Rb and Cs are taken into account.

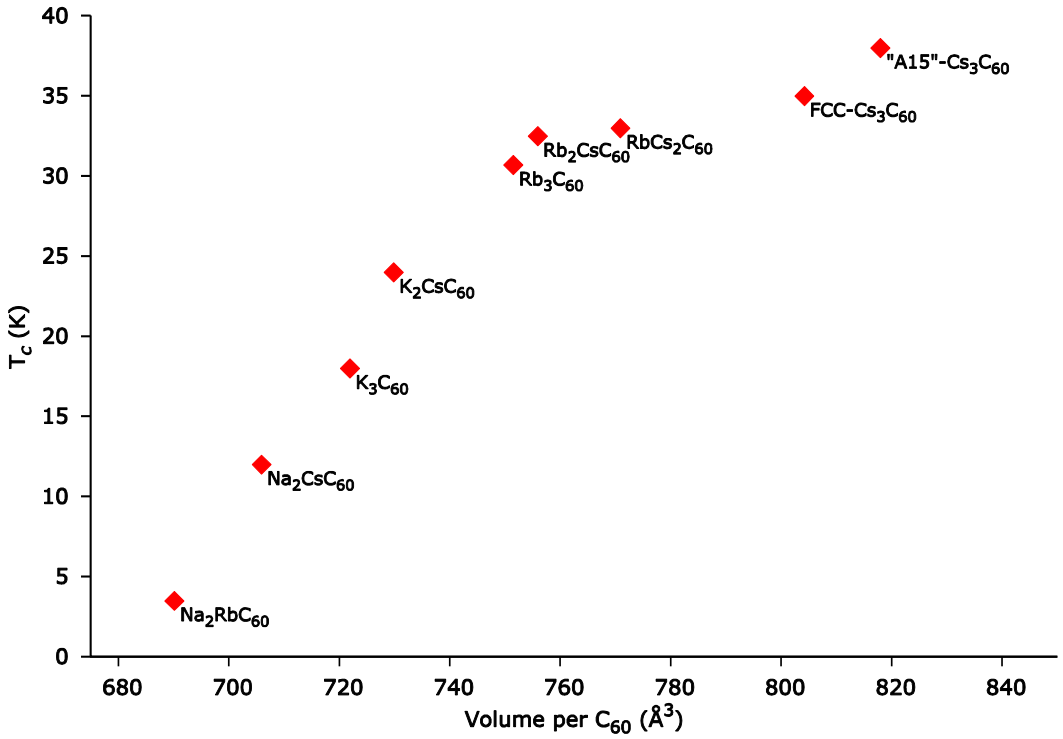

Figure 1.20 Superconducting transition temperature (T_c), as a function of unit cell volume per C_{60}^{3-} anion in A_3C_{60} (A= Na, K, Rb, Cs) where the compounds shown are FCC.[23, 24, 44, 57-64]

The origin of superconductivity in these materials has been strongly debated since their conception.[65] Early experiments and theories suggested that an electron-phonon pairing mechanism was responsible for the superconductivity in these materials. One such model is the Bardeen-Cooper-Schrieffer (BCS) theory which puts emphasis on the density of states at the Fermi level and electron-phonon interactions. The superconducting A_3C_{60} fullerenes appear to be heavily influenced by these two factors on first appearance. With a half-filled triply degenerate t_{1u} band and a strong intramolecular vibrational mode of H_g symmetry available to couple with those electrons. [66-68] One could naively conclude that these superconductors are conventional until the experimental evidence is analysed in more detail.

The confusion with regards to the coupling mechanism in these systems is highlighted by the two compounds K_3C_{60} and Rb_3C_{60}. These two materials are conducting, as expected from the half-filled t_{1u} band, and superconducting under ambient pressures. Both of these materials show behaviour that has aspects of conventional and unconventional superconductors. The first indication of conventional behaviour is high pressure experiments performed on the subject materials. The application of hydrostatic pressure demonstrated that Rb_3C_{60} on compression to the volume of K_3C_{60} the T_c dropped to roughly the equivalent of

the K_3C_{60} material.[69, 70] Significantly further compression of both compounds suppressed the T_c along the same trend line. This is very strong evidence for the linking of the density of states at the Fermi level, a significant BCS parameter, to the T_c. These high pressure experiments are not conclusive and cannot distinguish between pairing models which involve intramolecular C_{60} vibrations and purely electronic models. The second indication of the conventional nature of A_3C_{60} (A= K and Rb) systems is the presence of the isotope effect. This effect is a powerful demonstration of the coupling between phonon vibrations and paring electrons strongly favouring a conventional approach. The materials K_3C_{60} and Rb_3C_{60} when made with $^{13}C_{60}$ enriched fullerene display this effect.[66, 71] However, the presence of a drop in T_c is not definitive; analysis of the isotope coefficients gave α_cs of 0.3 and <0.2 for K_3C_{60} and Rb_3C_{60}.[72, 73] Values lower than the BCS theory prediction (α_c = 0.5) indicate the presence of electron-electron interactions. Superficially these two important compounds appear to be conventional but on delving deeper into their properties a more complex nature that is difficult to explain develops.

The most conclusive evidence for a non-conventional paring mechanism comes from Cs_3C_{60}. This critical material can crystallise in one of two polymorphs; both of which have starkly different properties than K_3C_{60} and Rb_3C_{60}. Both the FCC and "A15" are Mott-insulators and non-superconducting under ambient conditions. For Cs_3C_{60} it is only under the application of hydrostatic pressure that the superconductivity emerges. The polymorphs FCC and "A15" have maximum T_cs of 35 K[23] and 38 K[24] respectively under pressure. These values are much lower than the extrapolated value from the monotonic trend previously established and the BCS predictions.[23, 24, 74, 75] The production of a T_c dome by varying pressure is completely unexplainable under conventional methods. By the scaling of T_c for both the FCC and "A15" polymorphs with the bare bandwidth (W_c) the T_cs dependency was linked to the proximity of the material to the metal-insulator transition point (Figure 1.21). In addition to this was the observation that for the "A15" polymorph the superconducting state co-exists with the AFM state and is generated during the AFMs suppression. Both of these factors are seen in other highly electron correlated superconducting systems and confirms that the A_3C_{60} system does in fact belong with these correlated systems.

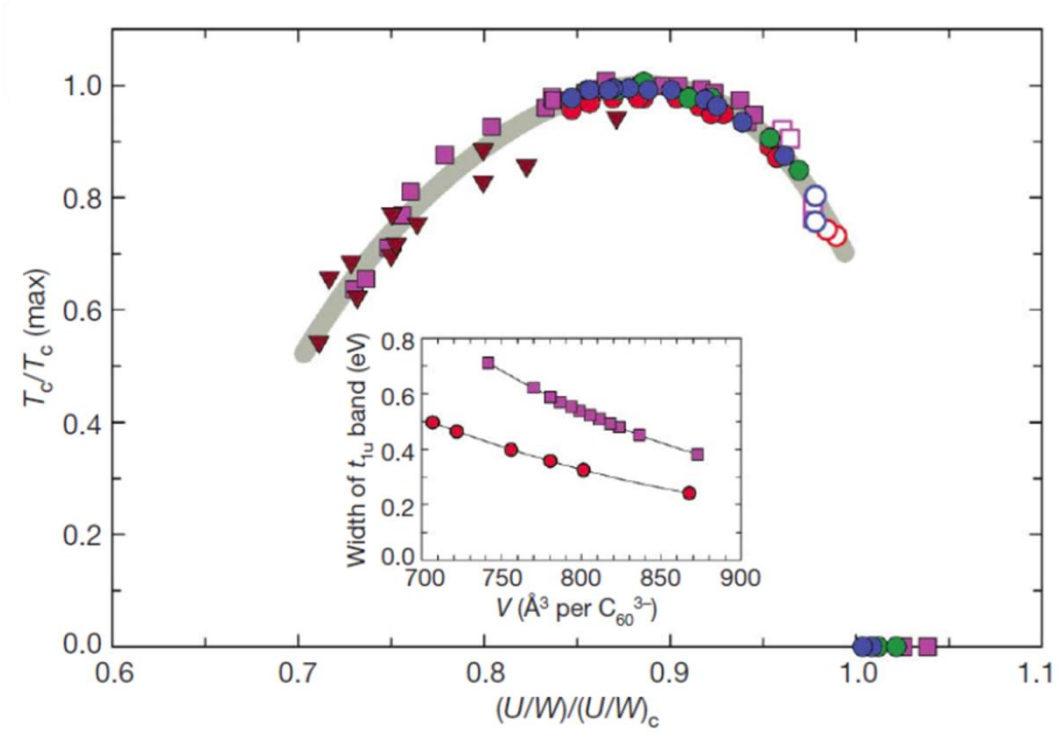

Figure 1.21 T_c/T_c(max) vs. (U/W)/(U/W)$_c$ allows the plotting of both Cs_3C_{60} polymorphs on a single packing independent curve. The inset shows the dependence of the t_{1u} bandwidth on volume (per C_{60}).[23]

In the expanded Cs_3C_{60} system the transition to a superconducting state is achieved using hydrostatic pressure, in other significant high T_c systems this can also be done using chemical pressure. This chemical pressure is incurred through doping the parent system with another element. A good example of this is the electron doped material $La_{2-x}Sr_xCuO_{4+y}$ in which Sr doping changes an antiferromagnetic material into a superconducting one. For the $La_{2-x}Sr_xCuO_{4+y}$ system the antiferromagnetic region is $x \leq 0.06$ and becomes superconducting above this value of x ($T_{c\,max}$ = 40 K at x = 0.15).[76]

In the case of the $La_{2-x}Sr_xCuO_{4+y}$ there is a structural transition between a tetragonal (SG = *F*4/*mmm*) phase at room temperature and an orthorhombic (SG = *Cmca*) phase at 10 K. This means that drawing conclusions on the mechanisms and origin of superconductivity for high T_c superconductors difficult. This is where the superconducting A_3C_{60} materials, specifically Cs_3C_{60} could shed some light. Due to the fullerides being cubic, highly crystalline with low disorder and precise compositions they should at least offer a less convoluted view of superconductivity. Unfortunately the clarity provided by the Cs_3C_{60} system is clouded by synthetic impurities which must be taken into account for when making conclusions on the origin of superconductivity in these materials.

1.3. Iron selenide based superconductors

The iron selenides are a relatively new system which has produced a new classification of unconventional superconductor. The parent FeSe material is metallic and superconducting at the composition of $Fe_{1.01}Se$. The fact that the parent FeSe is metallic means that is has some similarities to conventional superconductors like mercury. However, the unconventional nature of this superconductor becomes clear due to the observation of a dome in the T_c dependence pressure from ambient to 14 GPa with a maximum T_c of 37 K.[77]

These FeSe based materials are distinct from their close relatives the iron pnictides as the FeSe parent compound has a non-magnetic ground state[78], is metallic and shows superconducting (T_c = 8 K[79]) behaviour.[80-82] The iron pnictides, on the other hand, are non-superconducting insulators until doped.[82] The iron pnictides, selenides and oxyarsenides are structurally related both having layers of tetrahedral [FeX] (X = pnictide or chalcogenide). Where the iron layers are thought to be crucial to the presence and properties of superconductivity in these materials.[18] This provides a strong structural relationship between the iron based superconductors opening up the possibility of obtaining a global view of the important structural factors in determining the superconducting behaviour of these materials.

The non-magnetic ground state also makes the superconducting iron selenide stand apart from the cuprates which have parent materials that are AFM insulators.[83] In addition to this the iron selenides have a more simplistic composition than the cuprates. Despite the differences between the cuprates and the iron selenide superconductors there are distinct similarities between the two. They are both layered structures and the superconducting materials are compositionally sensitive.[19, 84, 85] Generating an understanding of how structure relates to superconductivity in these materials could aid in the identification of common structural parameters for high T_c superconducting materials in general.

Since the iron selenide superconductors are relatively new, compared to the fullerenes, there is considerable debate on the links between structure and superconductivity in these materials. For example in the superconducting ($T_c \approx$ 33 K) $K_xFe_ySe_2$ systems phase separation was observed using TEM[86] and X-ray diffraction.[80] The phase separation in these systems means that there is significant doubt over what the exact nature of the superconducting phase is. The identification this phase and its important structural parameters would

provide significant information on the origins of superconductivity in the $A_xFe_ySe_2$ system.

1.3.1. Structures in the iron selenide system

1.3.1.1. Fe_xSe

The parent material for the superconducting iron selenides has a large and complex phase diagram. The structures of this material consist of monoclinic (*γ*-FeSe), orthorhombic (*ε*-FeSe), hexagonal (*δ*-FeSe) and tetragonal (*β*-FeSe) structures.[87] The superconducting structure of iron selenide is the *β*-FeSe variant which is located in a narrow range between 49.0 and 49.4 at.% Se (Figure 1.22). This variant takes on the anti-PbO structure (SG = *P*4/*nmm*) and consists of layers of edge sharing distorted [FeSe] tetrahedral units (Figure 1.23).[77, 79] A common phase shown in FeSe materials at room temperature and ambient temperature is the *δ*-FeSe phase (SG = *P*63/*mmc*). This hexagonal phase is based upon the NiAs structure and has a much wider composition and temperature range than the *β*-FeSe.

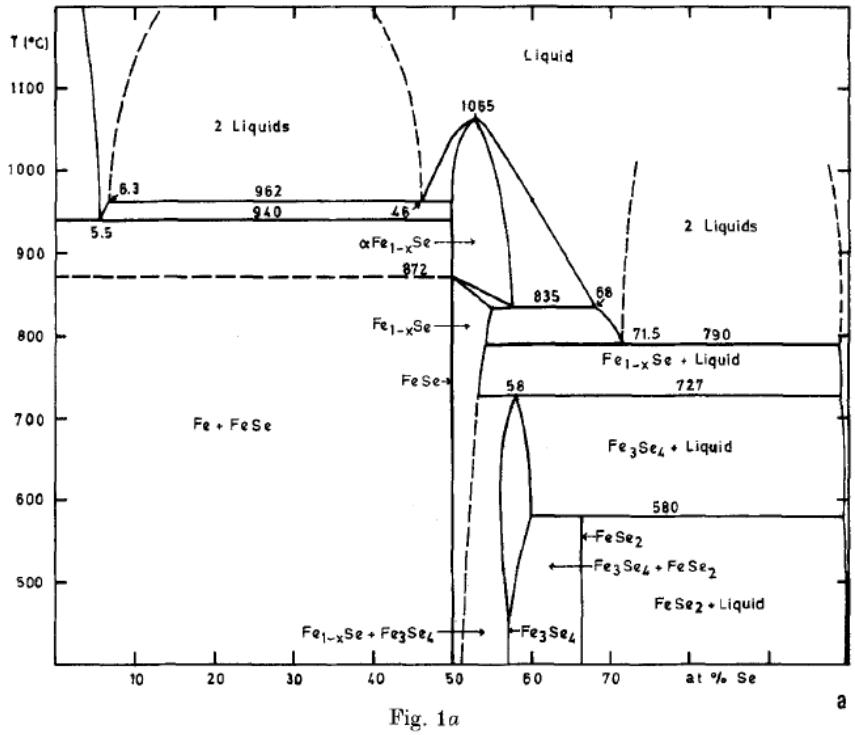

Fig. 1*a*

Figure 1.22 Temperature and at.% Se dependent FeSe phase diagram

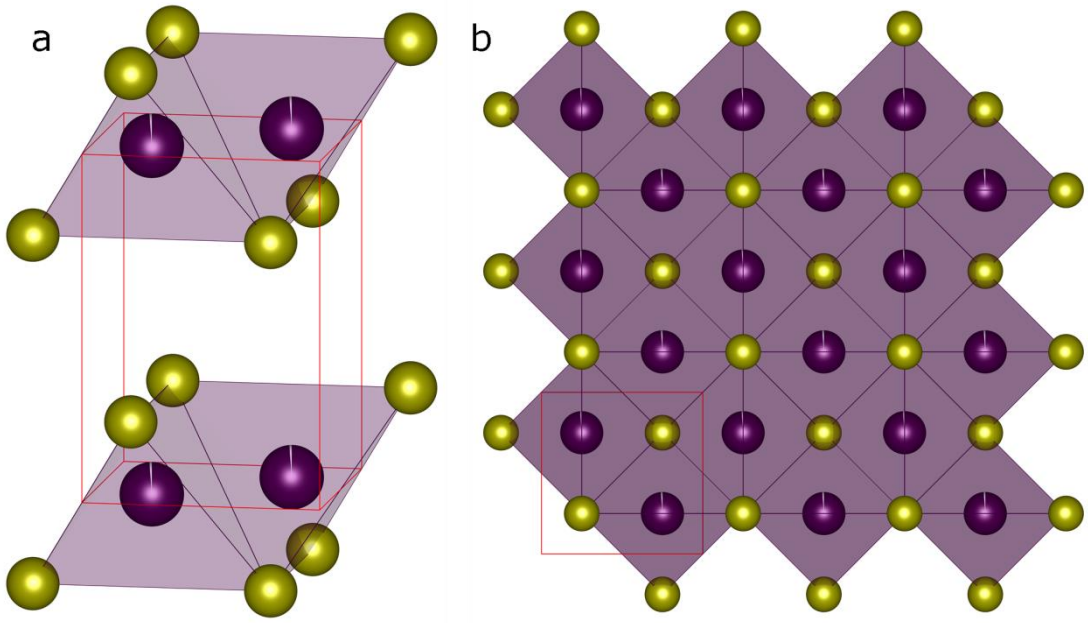

Figure 1.23 Structure of *β*-FeSe (tetragonal, SG = *P*4/*nmm*) where the selenium anions are yellow, the iron cations are purple and the unit cell is outlined in black. The two diagrams are (a) viewed along the *ab* plane and (b) the view along the *c*-axis.

1.3.1.2. $A_xFe_ySe_2$ (A = alkali metal)

The intercalation of alkali metals in between the layers of the *β*-FeSe phase produces material with the $ThCr_2Si_2$ (SG = *I*4/*mmm*) structure. This structure produces the general structure $A_xFe_2Se_2$ (A = alkali metal) can be described as the stacking of alternating A sheets and $[Fe_2Se_2]$ layers. Where the K, Fe and Se ions occupy sites of tetragonal symmetry of 4/*mmm*, 4*mm* and $\bar{4}$ *m*2 point groups respectively (Figure 1.24). The iron oxidation state in the parent FeSe material is +2. On intercalation with an alkali metal the parent material is reduced. Therefore the iron oxidation state of the materials produced as a direct intercalation of the *β*-FeSe is <2+. The more alkali metal that is intercalated the closer the oxidation state gets to 1+ which is an unstable state for iron.[88] This is the likely reason that the only *I*4/*mmm* phases that have been isolated are for the Li and Na analogues synthesised at room temperature.[81, 89] The $NaFe_2Se_2$ phase gave an analysed composition of $NaFe_2Se_2(NH_3)_y$[90] (T_c = 46 K, SF = 50 %) giving an iron oxidation state of +1.6.[89] The only high purity Li analogues synthesised had the refined composition of $Li_{0.6(1)}(NH_2)_{0.2(1)}(NH_3)_{0.8(1)}Fe_2Se_2$[81] ($T_c$ = 43 K, SF = 50 %) synthesised at -78 °C in liquid ammonia.[81]

The ammonia based methods when applied to $K_xFe_2Se_2$ have produced single phase material and a tentative structure for the superconducting phase.[90]

It was also demonstrated that ammonia also intercalates with ammonia in between the FeSe layers as with the Li based analogues.[89, 90] Interestingly the $K_xFe_2Se_2$ materials produced using ammonia in the fashion described by Ying *et.al*. 2013 gives a range of T_cs between 30 and 44 K and shielding fractions of upto 63 %.[90] As successful as this method is in producing quality $K_xFe_2Se_2$ superconducting material the presence of ammonia in the structure means that linking the material back to solvent free materials is difficult.

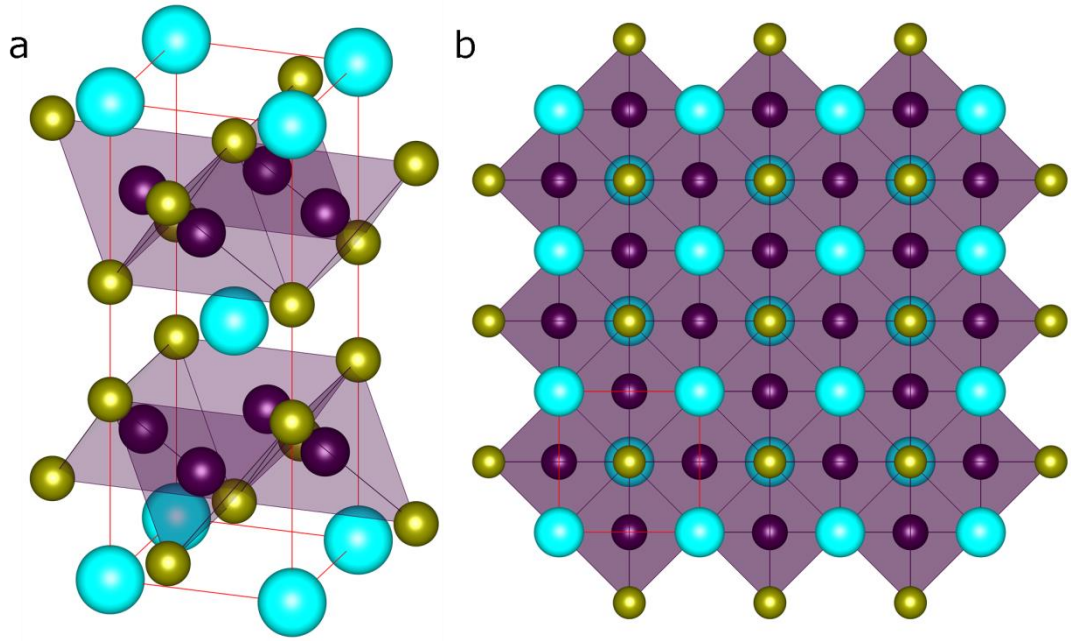

Figure 1.24 Structure of $A_xFe_2Se_2$ (tetragonal, SG = *I*4/*mmm*) where the selenium anions are yellow, the iron cations are purple, the A cation is in turquoise and the unit cell is outlined in black. The two diagrams are (a) viewed along the *ab* plane and (b) the view along the *c*-axis.

The most common structure observed when synthesising $A_xFe_ySe_2$ (A = K, Rb and Cs) materials using high temperatures is based on a √5 x √5 x 1 cell expansion of the $ThCr_2Si_2$ structure type (Figure 1.25).[80, 91, 92] This structure has up to 20 % iron vacancies which are ordered leading to the formation of the supercell in the basal *ab* plane. The alkali metal cations occupy 8 co-ordinate sites situated between the iron selenide layers. The change to the superstructure form from the $ThCr_2Si_2$ structure leads to the splitting of each atomic site into 2. This leads to the iron selenide layers becoming non-uniform with two layer thicknesses.[92] The *I*4/*m* phase has a *c*-axis that is 1.25 times per interlayer separation larger than the *β*-FeSe material and this expansion is thought to integral for the increased T_c (compared to FeSe) in the $K_xFe_ySe_2$ materials.[19, 93]

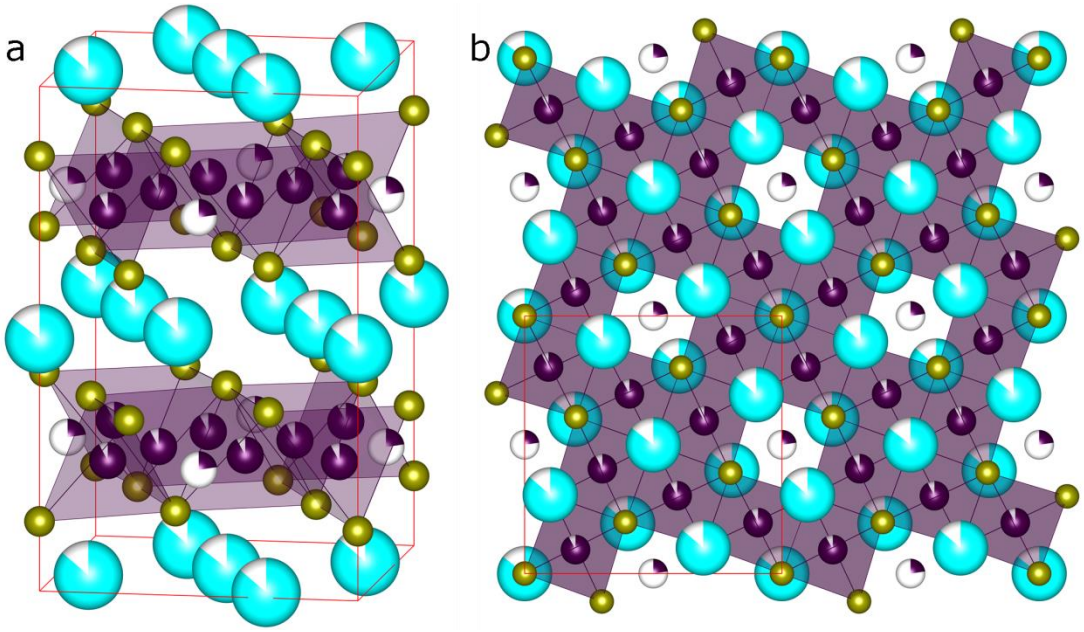

Figure 1.25 Structure of $K_xFe_ySe_2$ (tetragonal, SG = *I*4/*m*) where the selenium anions are yellow, the iron cations are purple, the A cation is in turquoise and the unit cell is outlined in black. The two diagrams are (a) viewed along the *ab* plane and (b) the view along the *c*-axis. The colour of the atoms is a representation of site occupancy where full colour is 100 % and grey is 0 %.

The confusion in assigning the superconductivity and magnetic properties in the $A_xFe_ySe_2$ materials becomes clear when phase separation is taken into account. The phase separation manifests itself as two distinct $K_xFe_ySe_2$ phases which correspond to the *I*4/*mmm* and *I*4/*m* structures described above.[80] Phase separation is clearly shown by using TEM images on $K_{0.8}Fe_xSe_2$ where nanoscale separation of the *I*4/*m* and *I*4/*mmm* phases was observed (Figure 1.26).[86] It was suggested using the TEM images that it was the iron vacancy disordered state (*I*4/*mmm* structure) rather than the vacancy ordered state (*I*4/*m* structure) that was responsible for the superconducting properties of the material studies.[86] This has also been observed using powder X-ray diffraction where both the *I*4/*mmm* and *I*4/*m* structures are observed in the powdered single crystals showing superconductivity.[80] Again this superconductivity was not assigned to the vacancy ordered phase (SG = *I*4/*m*) but was attributed to the *I*4/*mmm* variant.[80] This structural ambiguity has resulted in the absence of a structural and compositional link between the $A_xFe_ySe_2$ systems and superconductivity.

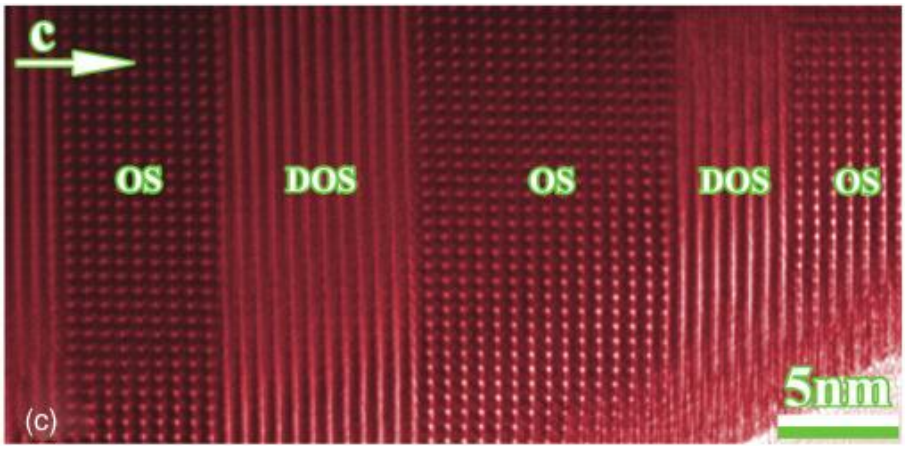

Figure 1.26 High resolution TEM image of $KFe_{1.8}Se_2$ along the [1-30] zone-axis. This highlights discrete layers of the vacancy ordered state (OS) and disordered state (DOS).[86]

1.3.2. Superconductivity in the iron selenide system

The superconductivity in the iron selenides systems is clearly unconventional. The presence of a T_c dome with varying pressure excludes the conventional BCS theories for determining superconductivity in these systems. Low temperature experiments demonstrated a structural transition from the tetragonal *β*-FeSe into the orthorhombic *ε*-FeSe (SG = *Cmma*) phase on cooling below 70 K.[94] This transition into the orthorhombic space group has no effect on the cell volume which decreases smoothly with decreasing temperature.[94] The application of pressure at low temperature converts the superconducting orthorhombic FeSe phase into the non-superconducting *δ*-FeSe hexagonal phase (Figure 1.27). The pressure experiments were able to demonstrate a link between the Se-Fe-Se inter layer separation (defined as 2c/(a+b)) and superconductivity. The unconventional superconductivity in FeSe is therefore heavily dependent upon the structure.

The unusual nature of the superconducting properties of FeSe is further reinforced by the demonstration of T_cs of up to 65 K in FeSe single layer thin films.[95] Where an optimal annealing procedure can increase the T_c from 55[96] to 65[95] K. This annealing protocol gives rise to three possibilities which could induce superconductivity and change the structure of the FeSe. The first is that Se is evaporated from the structure effectively electron doping the material. The second is the loss of oxygen from the $SrTiO_3$ substrate leading to doping of the FeSe indirectly. The third possibility is the re-arrangement of the FeSe atoms within the layer leading to the creation of the superconducting state. Further experimentation is required to determine which reason is responsible for the superconductivity (T_c = 65 K). The observation of such a high T_c in the FeSe

material hints at the possibility of obtaining other FeSe based superconductors with comparable T_cs.

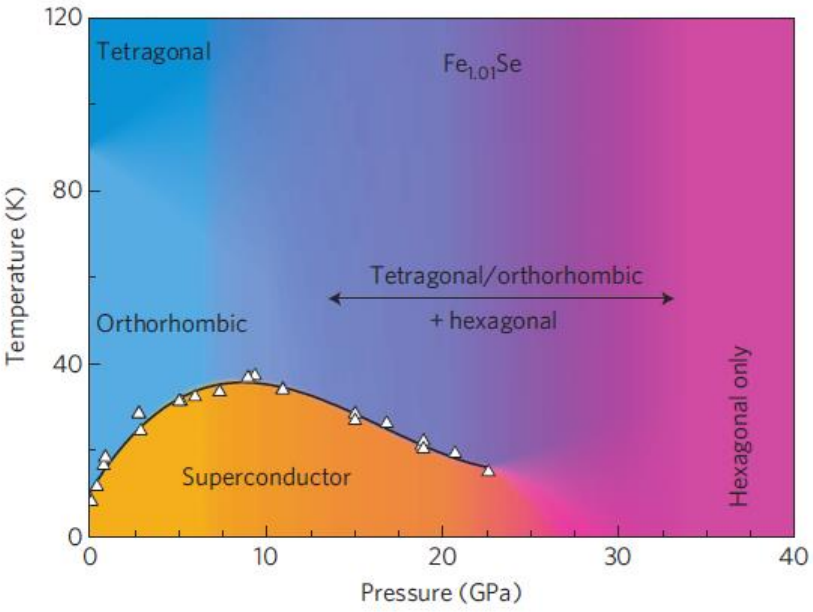

Figure 1.27 Electronic phase diagram as a function of pressure for the $Fe_{1.01}Se$ system.[78]

1.3.2.1. Superconductivity in $A_xFe_ySe_2$ system

Unlike the superconductivity in the A_3C_{60} (A = alkali metal) systems in the $A_xFe_ySe_2$ materials there is no clear dependence of the T_c on the alkali metal ionic radii. With the alkali metal fullerenes the largest cations give the larges T_cs but for the K, Rb and Cs containing materials in the $A_xFe_ySe_2$ system the T_c is ~32 K.[97, 98 99] This is unusual as in similar systems that contain larger layer separations the T_c is very dependent on the intercalate.[80, 81, 89, 100] The observation that the T_cs for the $A_xFe_ySe_2$ materials are identical could indicate that the phase responsible may have different doping levels for each of the alkali metals. This makes the identification of the exact composition of the superconducting phase in the $A_xFe_ySe_2$ systems important. This problem could be solved by the production of superconducting powder materials made using identical subsolidus methods over a wide compositional range. This would allow the evaluation of the compositions of the *I*4/*m* and *I*4/*mmm* present within the materials by bulk probes like powder X-ray diffraction and Rietveld analysis.[80]

Like the FeSe parent material the $A_xFe_ySe_2$ systems are unconventional systems showing transitions from an antiferromagnetically ordered state into the superconducting (Figure 1.28).[101] As the superconducting region is enveloped by

insulating states both in terms of iron composition and temperature it was concluded that the parent $K_xFe_2Se_2$ compound of the superconductor must be insulating also.[19] This assumes that it is the *I*4/*m* phase which is responsible for the superconducting behaviour in these materials. Serious doubt has recently been cast over the assumption that the *I*4/*m* phase is superconducting. Using powder X-ray diffraction on powdered superconducting single crystals Shoemaker *et.al*. demonstrated that the *I*4/*mmm* phase with compositions in the region of $K_{0.5}Fe_2Se_2$ were present in all superconducting samples.[80] They also synthesised pure powders of $K_{0.8}Fe_{1.6}Se_2$ (SG = *I*4/*m*) material and were unable to find any indication that this phase could be doped into a superconducting state.[80] Which lead to their conclusion that the *I*4/*m* phase was not responsible for superconductivity in the $K_xFe_ySe_2$ materials.

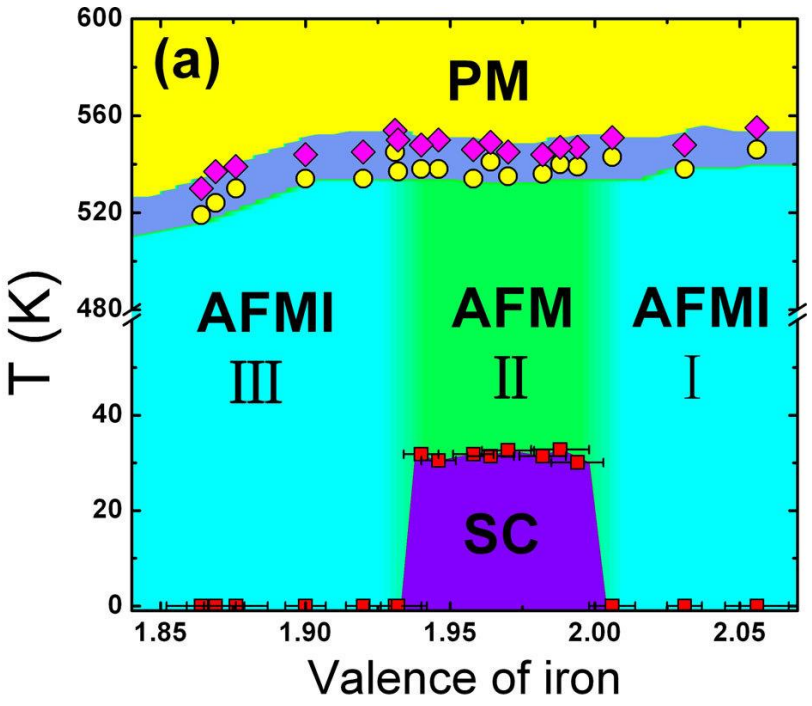

Figure 1.28 Phase diagram of $K_xFe_{2-y}Se_2$ as a function of iron valence.[101]

Additional conformation of the unusual superconducting properties of the $A_xFe_ySe_2$ series is the observation of two superconducting regions in the pressure related phase diagram (Figure 1.29).The first superconducting region (Figure 1.29) has a maximum T_c of ~32 K decreasing to 0 K at around 10 GPa and the second region exists in a small pressure range (11-13 GPa) with a maximum of T_c of 49 K. The first superconducting region appears to have a plateau in T_c between 0 and 3 GPa and a slight curve in the decrease in T_c between 3 and 10 GPa. This shows a similar dependence on pressure that the

superconducting FeSe material experiences in that excessive pressure is detrimental to superconductivity. Qualitatively the T_c dependence of the first superconducting region looks like right hand side of the T_c(P) dome observed for the FeSe materials which hints at a similar origin of superconductivity between the $A_xFe_ySe_2$ and FeSe superconducting systems.

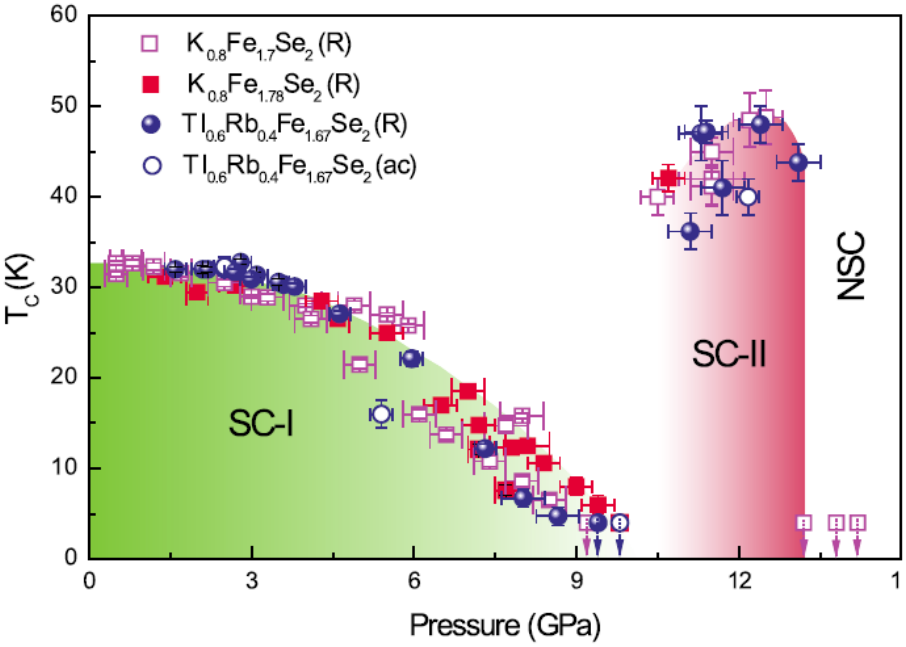

Figure 1.29 T_c(P) for several $A_xFe_ySe_2$ compounds which are indicated in the diagram.[102]

The second superconducting region (Figure 1.29) shows a much higher T_c than region 1 and exists at higher pressures. This region hints at the possibility of obtaining intercalated FeSe based materials with T_cs up to 49 K. In 2012 several materials exhibiting these increased T_cs where synthesised from ammonia[81, 89, 100] or pyridine[103]. They exhibited T_cs of 40[89], 43[81, 89, 100] and 46 K[103] for the KFe_2Se_2 (nominal composition), $Li_{0.6}(NH_2)_{0.2}(NH_3)_{0.8}Fe_2Se_2$ (refined composition) and $Li_x(C_5H_5N)_yFe_{2-z}Se_2$ systems respectively. Considering observation of materials that show T_cs up to 46 K and the reports of T_cs of up to 65 K in single layer FeSe films it is a distinct possibility that materials which display higher T_cs can be made via intercalation of the FeSe parent.

1.4. Thesis aims

The work carried out in this thesis focuses on the synthesis and characterisation of two unconventional superconductors. Both the Cs_3C_{60} and the $K_xFe_ySe_2$ systems are high temperature superconductors with T_cs in the range of 33 – 38 K. Although both systems are very different there are synthetic and analytical challenges that still need to be overcome for them.

The objective of chapter 3 is to improve upon the existing reactions for Cs_3C_{60}. The primary goal is to identify key parts of the synthesis which play the biggest role over the phase assembly in the final Cs_3C_{60} product. The Cs_3C_{60} material produced is then assessed using PXRD to obtain phase assemblies and SQUID magnetometry for its superconducting properties.

The objective of chapter 4 is to produce a phase diagram of the $K_xFe_ySe_2$ system. One of the major goals of this chapter is to produce superconducting powders of $K_xFe_ySe_2$ materials. An additional goal is to determine the superconducting phase within this system and link its structure to the superconducting properties of the material. This structural link to superconductivity is investigated using PXRD, ICP and SQUID magnetometry.

The objective of chapter 5 capitalises on the success of chapter 4 in determining the correct phase involved with superconductivity. The work attempts to synthesise the critical composition $K_{0.5}Fe_2Se_2$ of this phase using room temperature solution based methods. The produced method seeks to take advantage of the range of redox potentials available to alkali metal acene reducing agents dissolved in THF. The quality of the materials is then investigated primarily using PXRD and SQUID magnetometry.

The final chapter 6 summarises the contribution of each of the chapters to the 'state of the art' for the Cs_3C_{60} and $K_xFe_ySe_2$ systems in terms of both the synthetic methods and the materials properties.

1.5. References

1. H. K. Onnes, *Proceedings of the Koninklijke Akademie Van Wetenschappen Te Amsterdam*, 1911, **14**, 113-115.
2. W. Meissner and R. Ochsenfeld, *Naturwissenschaften*, 1933, **21**, 787-788.
3. L. Smart and E. Moore, *Solid state chemistry : an introduction*, 3rd ed. edn., CRC Press, Boca Raton, Fla. ; London, 2005.
4. E. Maxwell, *Physical Review*, 1950, **78**, 477-477.
5. C. A. Reynolds, B. Serin, W. H. Wright and L. B. Nesbitt, *Physical Review*, 1950, **78**, 487-487.
6. H. Frohlich, *Proceedings of the Physical Society of London Section A*, 1950, **63**, 778-778.
7. J. Bardeen, L. N. Cooper and J. R. Schrieffer, *Physical Review*, 1957, **108**, 1175-1204.
8. L. N. Cooper, *Physical Review*, 1956, **104**, 1189-1190.
9. J. Khachan and S. Bosi, *Superconductivity*, University of Sydney School of Physics, 2013.
10. C. Buzea and T. Yamashita, *Superconductor Science & Technology*, 2001, **14**, R115-R146.
11. A. N. Christensen and B. Lebech, *Acta Chemica Scandinavica*, 1990, **44**, 902-906.
12. J. J. Capponi, C. Chaillout, A. W. Hewat, P. Lejay, M. Marezio, N. Nguyen, B. Raveau, J. L. Soubeyroux, J. L. Tholence and R. Tournier, *Europhysics Letters*, 1987, **3**, 1301-1307.
13. S. Losch, H. Budin, O. Eibl, M. Hartmann, T. Rentschler, M. Rygula, S. Kemmlersack and R. P. Huebener, *Physica C*, 1991, **177**, 271-280.
14. E. V. Antipov, S. M. Loureiro, C. Chaillout, J. J. Capponi, P. Bordet, J. L. Tholence, S. N. Putilin and M. Marezio, *Physica C*, 1993, **215**, 1-10.
15. A. Erb, M. Lambacher, A. Habel and R. Gross, *Accessible regions of the phase diagram for the different compounds of the high temperature superconductors*, http://for538.wmi.badw-muenchen.de/projects/P4_crystal_growth/, Accessed 25/09, 2013.
16. M. Norman, *arXiv.org*, 2013.
17. Y. Kamihara, T. Watanabe, M. Hirano and H. Hosono, *Journal of the American Chemical Society*, 2008, **130**, 3296.
18. D. C. Johnston, *Advances in Physics*, 2010, **59**, 803-1061.
19. E. Dagotto, *Reviews of Modern Physics*, 2013, **85**, 849-867.
20. M. McElfresh, Quantum Design, Editon edn., 1994, p. 34.
21. itaca, *The response of a ferromagnetic material to an applied magnetic field.*, http://www.itacanet.org/basic-electrical-engineering/part-5-magnetic-materials/, Accessed 18/09, 2013.
22. Y. Takabayashi, A. Y. Ganin, P. Jeglic, D. Arcon, T. Takano, Y. Iwasa, Y. Ohishi, M. Takata, N. Takeshita, K. Prassides and M. J. Rosseinsky, *Science*, 2009, **323**, 1585-1590.
23. A. Y. Ganin, Y. Takabayashi, P. Jeglic, D. Arcon, A. Potocnik, P. J. Baker, Y. Ohishi, M. T. McDonald, M. D. Tzirakis, A. McLennan, G. R. Darling, M. Takata, M. J. Rosseinsky and K. Prassides, *Nature*, 2010, **466**, 221-U293.
24. A. Y. Ganin, Y. Takabayashi, Y. Z. Khimyak, S. Margadonna, A. Tamai, M. J. Rosseinsky and K. Prassides, *Nature Materials*, 2008, **7**, 367-371.
25. T. T. M. Palstra, O. Zhou, Y. Iwasa, P. E. Sulewski, R. M. Fleming and B. R. Zegarski, *Solid State Communications*, 1995, **93**, 327-330.
26. H. W. Kroto, J. R. Heath, S. C. Obrien, R. F. Curl and R. E. Smalley, *Nature*, 1985, **318**, 162-163.
27. M. J. Rosseinsky, *Journal of Materials Chemistry*, 1995, **5**, 1497-1513.

28. J. H. Weaver, J. L. Martins, T. Komeda, Y. Chen, T. R. Ohno, G. H. Kroll, N. Troullier, R. E. Haufler and R. E. Smalley, *Physical Review Letters*, 1991, **66**, 1741-1744.
29. S. H. Yang, C. L. Pettiette, J. Conceicao, O. Cheshnovsky and R. E. Smalley, *Chemical Physics Letters*, 1987, **139**, 233-238.
30. S. Margadonna and K. Prassides, *Journal of Solid State Chemistry*, 2002, **168**, 639-652.
31. Q. S. Xie, E. Perezcordero and L. Echegoyen, *Journal of the American Chemical Society*, 1992, **114**, 3978-3980.
32. W. Kratschmer, L. D. Lamb, K. Fostiropoulos and D. R. Huffman, *Nature*, 1990, **347**, 354-358.
33. R. Taylor, J. P. Hare, A. K. Abdulsada and H. W. Kroto, *Journal of the Chemical Society-Chemical Communications*, 1990, 1423-1424.
34. P. A. Heiney, J. E. Fischer, A. R. McGhie, W. J. Romanow, A. M. Denenstein, J. P. McCauley, A. B. Smith and D. E. Cox, *Physical Review Letters*, 1991, **66**, 2911-2914.
35. M. J. Rosseinsky, *Chem. Mat.*, 1998, **10**, 2665-2685.
36. R. M. Fleming, A. P. Ramirez, M. J. Rosseinsky, D. W. Murphy, R. C. Haddon, S. M. Zahurak and A. V. Makhija, *Nature*, 1991, **352**, 787-788.
37. P. C. Chow, X. Jiang, G. Reiter, P. Wochner, S. C. Moss, J. D. Axe, J. C. Hanson, R. K. McMullan, R. L. Meng and C. W. Chu, *Physical Review Letters*, 1992, **69**, 2943-2946.
38. R. Tycko, G. Dabbagh, M. J. Rosseinsky, D. W. Murphy, R. M. Fleming, A. P. Ramirez and J. C. Tully, *Science*, 1991, **253**, 884-886.
39. R. Tycko, *J. Phys. Chem. Solids*, 1993, **54**, 1713-1723.
40. T. Yildirim, O. Zhou, J. E. Fischer, N. Bykovetz, R. A. Strongin, M. A. Cichy, A. B. Smith, C. L. Lin and R. Jelinek, *Nature*, 1992, **360**, 568-571.
41. L. Cristofolini, M. Ricco and R. De Renzi, *Physical Review B*, 1999, **59**, 8343-8346.
42. S. Margadonna, D. Pontiroli, M. Belli, T. Shiroka, M. Ricco and M. Brunelli, *Journal of the American Chemical Society*, 2004, **126**, 15032-15033.
43. T. Yildirim, J. E. Fischer, A. B. Harris, P. W. Stephens, D. Liu, L. Brard, R. M. Strongin and A. B. Smith, *Physical Review Letters*, 1993, **71**, 1383-1386.
44. D. R. Buffinger, R. P. Ziebarth, V. A. Stenger, C. Recchia and C. H. Pennington, *Journal of the American Chemical Society*, 1993, **115**, 9267-9270.
45. M. J. Rosseinsky, A. P. Ramirez, S. H. Glarum, D. W. Murphy, R. C. Haddon, A. F. Hebard, T. T. M. Palstra, A. R. Kortan, S. M. Zahurak and A. V. Makhija, *Physical Review Letters*, 1991, **66**, 2830-2832.
46. A. F. Hebard, M. J. Rosseinsky, R. C. Haddon, D. W. Murphy, S. H. Glarum, T. T. M. Palstra, A. P. Ramirez and A. R. Kortan, *Nature*, 1991, **350**, 600-601.
47. R. D. Shannon, *Acta Crystallographica Section A*, 1976, **32**, 751-767.
48. O. Chauvet, G. Oszlanyi, L. Forro, P. W. Stephens, M. Tegze, G. Faigel and A. Janossy, *Physical Review Letters*, 1994, **72**, 2721-2724.
49. K. Prassides, *Current Opinion in Solid State & Materials Science*, 1997, **2**, 433-439.
50. R. C. Haddon, A. F. Hebard, M. J. Rosseinsky, D. W. Murphy, S. J. Duclos, K. B. Lyons, B. Miller, J. M. Rosamilia, R. M. Fleming, A. R. Kortan, S. H. Glarum, A. V. Makhija, A. J. Muller, R. H. Eick, S. M. Zahurak, R. Tycko, G. Dabbagh and F. A. Thiel, *Nature*, 1991, **350**, 320-322.
51. K. Tanigaki and K. Prassides, *Journal of Materials Chemistry*, 1995, **5**, 1515-1527.
52. S. Saito, S. G. Louie and M. L. Cohen, *Solid State Communications*, 2007, **142**, 186-189.
53. B. T. Matthias, T. H. Geballe, S. Geller and E. Corenzwit, *Physical Review*, 1954, **95**, 1435-1435.

54. Y. Takabayashi, Y. Kubozono, S. Fujiki, S. Kashino, K. Ishii, H. Suematsu and H. Ogata, International Symposium on Nanonetwork Materials, Fullerenes, Nanotubes, and Related Systems, Kamakura, Japan, 2001.
55. M. J. Rosseinsky, D. W. Murphy, R. M. Fleming, R. Tycko, A. P. Ramirez, T. Siegrist, G. Dabbagh and S. E. Barrett, *Nature*, 1992, **356**, 416-418.
56. O. Zhou, J. E. Fischer, N. Coustel, S. Kycia, Q. Zhu, A. R. McGhie, W. J. Romanow, J. P. McCauley, A. B. Smith and D. E. Cox, *Nature*, 1991, **351**, 462-464.
57. K. Tanigaki, I. Hirosawa, T. W. Ebbesen, J.-I. Mizuki and J. S. Tsai, *Journal of Physics and Chemistry of Solids*, 1993, **54**, 1645-1653.
58. Y. Maniwa, T. Saito, A. Ohi, K. Mizoguchi, K. Kume, K. Kikuchi, I. Ikemoto, S. Suzuki, Y. Achiba, M. Kosaka, K. Tanigaki and T. W. Ebbesen, *Journal of the Physical Society of Japan*, 1994, **63**, 1139-1148.
59. K. Tanigaki, I. Hirosawa, T. W. Ebbesen, J. Mizuki and S. Kuroshima, *Chemical Physics Letters*, 1993, **203**, 33-36.
60. S. Q. Feng, X. Zhu, E. Wu, J. Fu, J. C. Mao, Z. N. Gu, J. X. Qian, X. H. Zhou, Z. X. Jin and B. Yin, *Solid State Communications*, 1991, **80**, 639-642.
61. P. W. Stephens, L. Mihaly, P. L. Lee, R. L. Whetten, S. M. Huang, R. Kaner, F. Deiderich and K. Holczer, *Nature*, 1991, **351**, 632-634.
62. M. Baenitz, M. Heinze, K. Luders, H. Werner and R. Schlogl, Symposium on Novel Forms of Carbon II, at the 1994 MRS Spring Meeting, San Francisco, Ca, 1994.
63. M. Baenitz, M. Heinze, K. Luders, H. Werner and R. Schlogl, *Physica C-Superconductivity and Its Applications*, 1994, **235**, 2503-2504.
64. J. P. McCauley, Q. Zhu, N. Coustel, O. Zhou, G. Vaughan, S. H. J. Idziak, J. E. Fischer, S. W. Tozer, D. M. Groski, N. Bykovetz, C. L. Lin, A. R. McGhie, B. H. Allen, W. J. Romanow, A. M. Denenstein and A. B. Smith, *Journal of the American Chemical Society*, 1991, **113**, 8537-8538.
65. A. P. Ramirez, *Physica B*, 1994, **199**, 596-599.
66. O. Gunnarsson, *Reviews of Modern Physics*, 1997, **69**, 575-606.
67. C. M. Varma, J. Zaanen and K. Raghavachari, *Science*, 1991, **254**, 989-992.
68. M. Lannoo, G. A. Baraff, M. Schluter and D. Tomanek, *Physical Review B*, 1991, **44**, 12106-12108.
69. D. Varshney, *High Pressure Research*, 2006, **26**, 203-222.
70. O. Zhou, G. B. M. Vaughan, Q. Zhu, J. E. Fischer, P. A. Heiney, N. Coustel, J. P. McCauley and A. B. Smith, *Science*, 1992, **255**, 833-835.
71. M. Ricco, F. Gianferrari, D. Pontiroli, M. Belli, C. Bucci and T. Shiroka, *Epl*, 2008, **81**.
72. M. S. Fuhrer, K. Cherrey, A. Zettl, M. L. Cohen and V. H. Crespi, *Physical Review Letters*, 1999, **83**, 404-407.
73. C. C. Chen and C. M. Lieber, *Journal of the American Chemical Society*, 1992, **114**, 3141-3142.
74. M. T. McDonald, *Structural and electronic properties of fulleride superconductors [electronic resource]*, http://etheses.dur.ac.uk/301/.
75. C. C. Chen, S. P. Kelty and C. M. Lieber, *Science*, 1991, **253**, 886-888.
76. C. Rial, E. Moran, M. A. Alariofranco, U. Amador and N. H. Andersen, *Physica C*, 1995, **254**, 233-248.
77. S. Margadonna, Y. Takabayashi, Y. Ohishi, Y. Mizuguchi, Y. Takano, T. Kagayama, T. Nakagawa, M. Takata and K. Prassides, *Physical Review B*, 2009, **80**, 6.
78. S. Medvedev, T. M. McQueen, I. A. Troyan, T. Palasyuk, M. I. Eremets, R. J. Cava, S. Naghavi, F. Casper, V. Ksenofontov, G. Wortmann and C. Felser, *Nature Materials*, 2009, **8**, 630-633.
79. T. M. McQueen, Q. Huang, V. Ksenofontov, C. Felser, Q. Xu, H. Zandbergen, Y. S. Hor, J. Allred, A. J. Williams, D. Qu, J. Checkelsky, N. P. Ong and R. J. Cava, *Physical Review B*, 2009, **79**.

80. D. P. Shoemaker, D. Y. Chung, H. Claus, M. C. Francisco, S. Avci, A. Llobet and M. G. Kanatzidis, *Physical Review B*, 2012, **86**.
81. M. Burrard-Lucas, D. G. Free, S. J. Sedlmaier, J. D. Wright, S. J. Cassidy, Y. Hara, A. J. Corkett, T. Lancaster, P. J. Baker, S. J. Blundell and S. J. Clarke, *Nature Materials*, 2013, **12**, 15-19.
82. J. Wen, G. Xu, G. Gu, J. M. Tranquada and R. J. Birgeneau, *Reports on Progress in Physics*, 2011, **74**.
83. G. R. Stewart, *Reviews of Modern Physics*, 2011, **83**, 1589-1652.
84. A. J. Williams, T. M. McQueen, V. Ksenofontov, C. Felser and R. J. Cava, *Journal of Physics-Condensed Matter*, 2009, **21**, 6.
85. X. W. Yan, M. Gao, Z. Y. Lu and T. Xiang, *Physical Review B*, 2011, **83**, 4.
86. Z. Wang, Y. J. Song, H. L. Shi, Z. W. Wang, Z. Chen, H. F. Tian, G. F. Chen, J. G. Guo, H. X. Yang and J. Q. Li, *Physical Review B*, 2011, **83**.
87. W. Schuster, H. Mikler and K. Komarek, *Monatshefte für Chemie / Chemical Monthly*, 1979, **110**, 1153-1170.
88. P. W. Atkins and D. F. Shriver, *inorganic chemistry*, 4th ed. / Peter Atkins ... [et al.]. edn., Oxford University Press, Oxford, 2006.
89. T. P. Ying, X. L. Chen, G. Wang, S. F. Jin, T. T. Zhou, X. F. Lai, H. Zhang and W. Y. Wang, *Sci. Rep.*, 2012, **2**.
90. T.-P. Ying, G. Wang, S.-F. Jin, S.-J. Shen, H. Zhang, T.-T. Zhou, X.-F. Lai, W.-Y. Wang and X.-L. Chen, *Chinese Physics B*, 2013, **22**.
91. P. Zavalij, W. Bao, X. F. Wang, J. J. Ying, X. H. Chen, D. M. Wang, J. B. He, X. Q. Wang, G. F. Chen, P. Y. Hsieh, Q. Huang and M. A. Green, *Physical Review B*, 2011, **83**, 4.
92. J. Bacsa, A. Y. Ganin, Y. Takabayashi, K. E. Christensen, K. Prassides, M. J. Rosseinsky and J. B. Claridge, *Chemical Science*, 2011, **2**, 1054-1058.
93. J. Guo, S. Jin, G. Wang, S. Wang, K. Zhu, T. Zhou, M. He and X. Chen, *Physical Review B*, 2010, **82**, 180520.
94. S. Margadonna, Y. Takabayashi, M. T. McDonald, K. Kasperkiewicz, Y. Mizuguchi, Y. Takano, A. N. Fitch, E. Suard and K. Prassides, *Chemical Communications*, 2008, 5607-5609.
95. S. He, J. He, W. Zhang, L. Zhao, D. Liu, X. Liu, D. Mou, Y.-B. Ou, Q.-Y. Wang, Z. Li, L. Wang, Y. Peng, Y. Liu, C. Chen, L. Yu, G. Liu, X. Dong, J. Zhang, C. Chen, Z. Xu, X. Chen, X. Ma, Q. Xue and X. J. Zhou, *Nature Materials*, 2013, **12**, 605-610.
96. Q.-Y. Wang, Z. Li, W.-H. Zhang, Z.-C. Zhang, J.-S. Zhang, W. Li, H. Ding, Y.-B. Ou, P. Deng, K. Chang, J. Wen, C.-L. Song, K. He, J.-F. Jia, S.-H. Ji, Y.-Y. Wang, L.-L. Wang, X. Chen, X.-C. Ma and Q.-K. Xue, *Chinese Physics Letters*, 2012, **29**.
97. X. G. Luo, X. F. Wang, J. J. Ying, Y. J. Yan, Z. Y. Li, M. Zhang, A. F. Wang, P. Cheng, Z. J. Xiang, G. J. Ye, R. H. Liu and X. H. Chen, *New Journal of Physics*, 2011, **13**, 12.
98. W. Bao, Q.-Z. Huang, G.-F. Chen, M. A. Green, D.-M. Wang, J.-B. He and Y.-M. Qiu, *Chinese Physics Letters*, 2011, **28**, 086104.
99. G. Seyfarth, D. Jaccard, P. Pedrazzini, A. Krzton-Maziopa, E. Pomjakushina, K. Conder and Z. Shermadini, *Solid State Communications*, 2011, **151**, 747-750.
100. E. W. Scheidt, V. R. Hathwar, D. Schmitz, A. Dunbar, W. Scherer, F. Mayr, V. Tsurkan, J. Deisenhofer and A. Loidl, *European Physical Journal B*, 2012, **85**.
101. Y. J. Yan, M. Zhang, A. F. Wang, J. J. Ying, Z. Y. Li, W. Qin, X. G. Luo, J. Q. Li, J. Hu and X. H. Chen, *Sci. Rep.*, 2012, **2**.
102. L. L. Sun, X. J. Chen, J. Guo, P. W. Gao, Q. Z. Huang, H. D. Wang, M. H. Fang, X. L. Chen, G. F. Chen, Q. Wu, C. Zhang, D. C. Gu, X. L. Dong, L. Wang, K. Yang, A. G. Li, X. Dai, H. K. Mao and Z. X. Zhao, *Nature*, 2012, **483**, 67-69.
103. A. Krzton-Maziopa, E. V. Pomjakushina, V. Y. Pomjakushin, F. von Rohr, A. Schilling and K. Conder, *Journal of Physics-Condensed Matter*, 2012, **24**, 6.

2. Methods

2.1. Introduction

The success of any experiment depends not only upon the conditions of the reaction itself but also on the preparation supporting it. This is especially true for air-sensitive materials where sensitive measurements are required. This chapter will detail the preparation and set up required to perform the reactions explored in the later chapters. Also it will describe the methods that make the analysis of the products of the reactions possible. Additionally descriptions of the relevant theoretical background for the two main characterisation techniques, powder X-ray diffraction (PXRD) and superconducting quantum interference device (SQUID) magnetometry, will be presented.

2.2. Air sensitive chemistry

The compounds chosen for synthesis and characterisation in this thesis are Cs_3C_{60} and $K_xFe_ySe_2$. The synthetic methods used to produce these materials require the use of alkali metals (excluding francium) and/or intermediate alkali metal reducing agents. Alkali metals are highly reactive soft metals with an electronic configuration of ns^1 (n = period number of the alkali metal in the periodic table).[1] The reactivity of the alkali metals is based on this single s electron which is readily donated resulting in a full $(n-1)p^6$ shell for the alkali metal cation. The ease at which this s electron is donated makes the alkali metals very reactive in their elemental state.[1] All alkali metals react in the presence of oxygen and moisture to form oxides and hydroxides (Figures 2.1 and 2.2). This means that rigorous methods are required not only for safety but they are crucial to obtaining materials with the correct composition.

a $4Li_{(s)} + O_{2(g)} \longrightarrow 2Li_2O_{(s)}$

b $2Na_{(s)} + O_{2(g)} \longrightarrow Na_2O_{2(s)}$

c $A_{(s)} + O_{2(g)} \longrightarrow AO_{2(s)}$

A = K, Rb and Cs

Figure 2.1 Balanced equations for the reaction of alkali metals and oxygen.

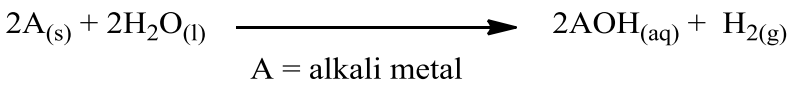

Figure 2.2 General balanced equation for the reaction of alkali metals and water

2.2.1. Glove boxes

Handling air-sensitive and pyrophoric solids is best done in an inert gas glove box (Figure 2.3). A glove box consists of a work space enclosed by a gas tight box which is equipped with transfer ports.[2] The box is filled with a suitable inert gas such as helium or argon (Li metal reacts with nitrogen) so that the sensitive solids can be manipulated easily.[1, 2] The transfer ports are connected to the same gas supply as the box and also to a vacuum pump which through a valve allows the ports to be purged. The ports' ability to purge means that items can be brought into the glove box without contaminating the work space with air.[2] The glove box enables the air-sensitive solids to be manipulated so that analytical data can be collected without exposure to air. Bench top techniques such as grinding a sensitive material into a powder fine enough to be loaded into a capillary for PXRD become possible.

The quality of atmosphere in the work space of a glove box is of paramount importance for the materials contained within. This quality is determined using sensors which detect the oxygen and moisture contents accurately in the ppm range. The operational purity of the inert gas inside the work space is <0.1 ppm of oxygen and water. This purity is maintained by the purification systems supplied with the glove box which can be regenerated, to maintain performance, using 5 % H_2/N_2 gas at regular intervals. Even with all of these measures in place the air-sensitive materials within the work space were contained in an appropriately tightly sealed vial and placed within a jar sealed with a rubber ring and clamp. The additional storage protocols enable the preservation of materials for years allowing maximum flexibility with time frames in which to obtain any analytical results.

Figure 2.3 MBraun LABmaster glove box workstation.[3]

2.2.2. Schlenk lines

The ability to perform common 'wet' synthetic techniques on air sensitive materials is an powerful capability providing access to techniques such as that enable high levels of control over composition.[4] These 'wet' chemical techniques can be performed in specially designed glove boxes but contamination of other products with volatile solvents is a concern. Therefore when operating a dry box, i.e. a glove box that is not used with solvents, it is necessary to perform 'wet' chemical synthesis on a Schlenk line (Figure 2.4).

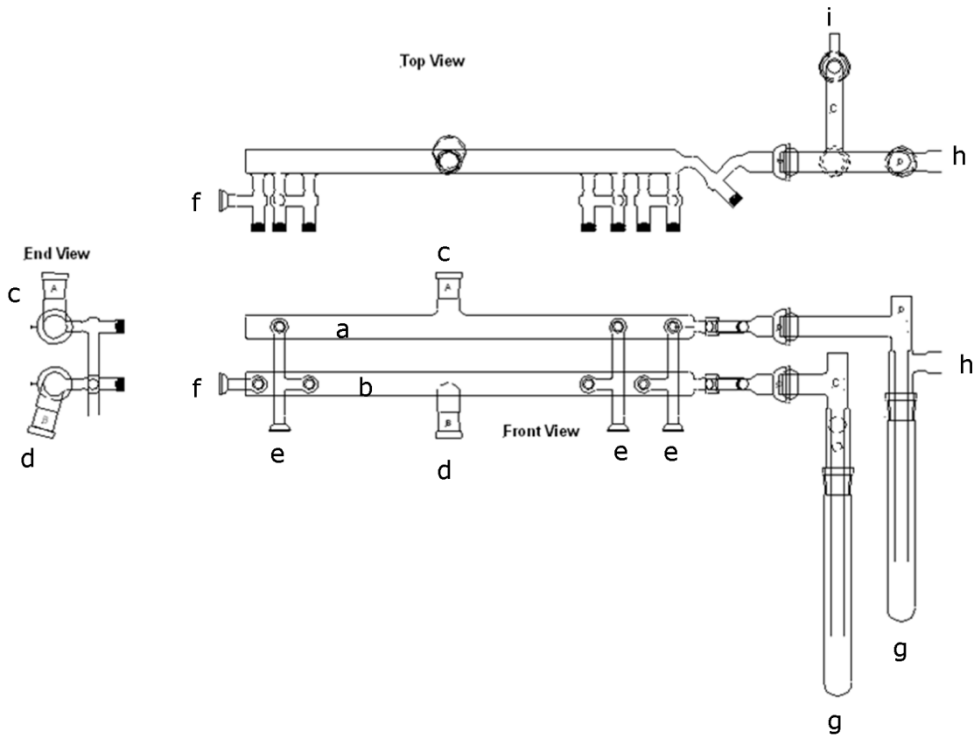

Figure 2.4 Schematic of the dual manifold Schlenk line used in this work. (a) Can be changed based on experiment to be a high vacuum or low vacuum line line; (b) Is the low vacuum or inert gas line based on the experiment; (c) and (d) are ports for pressure gauges; (e) are the greaseless ball joints for attaching reaction vessel to; (f) Is the outlet for the inert gas, if used, to which a bubbler is attached; (g) Vacuum traps which are cooled by placing a liquid nitrogen Dewar around them; (h) Is the connection to the turbo molecular pump and (i) is the connection to the rotary pump or inert gas. This Schlenk line can be converted from vacuum/inert gas to a dual vacuum set up depending on the experimental needs.

The Schlenk line consists of two sections, one containing pure inert gas and the other connected to a vacuum pump. These two sections are connected via valves which enable a vessel to be exposed to the vacuum or inert gas. The corrosive nature of some solvents and compounds means that the vacuum pump has to be protected by a glass trap situated in between the pump and the Schlenk line. A Dewar is then fitted around this trap and filled with a suitable cryogen which condenses any solvent vapour before it can reach the pump. The inert gas as is flows through the Schlenk line is always vented through a gas bubbler filled with either mercury or more typically mineral oil. The bubbler serves multiple purposes; firstly it prevents the back flow of air into the Schlenk line; secondly it provides a method of determining the flow of inert gas; thirdly it prevents pressure build up within the glass line and fourthly it will direct the inert gas flow through any opening with less resistance to the flow of gas.[2]

With the Schlenk line set up in this manner it is then possible to use PVC vacuum tubing to connect glassware to the Schlenk line. This glassware can then be purged of air, put under positive pressure of inert gas or otherwise prepared for use. These vessels can then be used to perform a variety of tasks from solvent transfers using a cannula or syringe to purification methods like filtration. The ability to use 'wet' in addition to 'dry' methods with air-sensitive materials allows great scope for problem solving particularly when room temperature methods are required.

Another configuration of Schlenk line that is also used in this thesis is one equipped with two vacuum pumps and called a dual vacuum line (Figure 2.4). The first pump is a rotary pump capable of achieving pressures of $1x10^{-3}$ mbar (low vacuum) and the second is a rotary/turbo molecular pump system capable of achieving pressures of $1x10^{-7}$ mbar. The dual vacuum setup of a Schlenk line is particularly useful for removing solvent from freshly prepared materials. The rotary pump, being capable of removing large volumes of gas without damage, is used to get the container filled with an air-sensitive material into a pressure range where the turbo molecular pump can operate. When the turbo molecular pump reduces the pressure of the container into the $1x10^{-5}$ mbar range the container can be placed into a suitable furnace for annealing (whilst still being attached to the vacuum line). The turbo molecular pump coupled with a liquid nitrogen trap can maintain a suitably oxygen/moisture free environment such that the material can be heated for up to 24 hours without any detectable decomposition. This procedure is called annealing under dynamic vacuum and is capable of removing all solvent from a sample but is heavily dependent on how volatile the guest solvent is.[5]

2.2.2.1. Gas scrubbing columns

In order to achieve a situation in which all major sources of air and moisture are controlled, gas purification methods are required for Schlenk lines using inert gasses. This was achieved by making two glass columns 0.5 m in length of 5 cm outer diameter and connecting them via flexible metal tubing to an argon cylinder (99.99 % purity) and to the Schlenk line via flexible PVC vacuum tubing. The first column, for moisture extraction, was half filled with 4 Å molecular sieves which were activated under low vacuum at 350 °C before being sealed using greaseless PTFE high vacuum taps.[2, 6, 7] The second column was prepared following the description in Ashby *et. al.* 1974 for the preparation of an oxygen scrubbing column using $MnCO_3$ and vermiculite.[6] The $MnCO_3$ coating was

then converted to MnO by the use of 5 % H_2/N_2 gas passed through the column which was heated in a clamp furnace to 350 °C for 8 hours.[6] This produced a column filled with green MnO coated vermiculite which would turn brown on exposure to air. With these two columns placed between the gas source and the Schlenk line the purity of the argon gas used to perform the 'wet' chemical techniques in this thesis was assured.

2.2.3. Glassware preparation

All glassware had to be rigorously cleaned and dried before use either in a glove box or on a Schlenk line. Considering the effort required in preparing to handle air-sensitive compounds the use of rigorously clean glassware is a necessity. All glassware was subject to the following cleaning protocol before use.

Firstly the standard protocols were applied such as using soap and water to remove grease and any other dirt built up during storage. This was then followed by rinsing with tap water, and then a small amount of acetone followed by water again. The glassware was then submerged in a base bath for 12 hours. If the glassware contained a glass frit the time spent in the base bath was reduced to 1 hour to avoid damage to the frit. The equipment was then removed from the base bath and thoroughly washed with tap water and then rinsed out with 3 lots of distilled water. The glassware was then placed into a glass oven at 150 °C for 12 hours before use. This ensured clean and dry apparatus before each reaction eliminating the possibility of contamination of any products by the glassware.

After each reaction the glassware was promptly cleaned using a method specific to the reaction that had been performed. If a reaction using alkali metal fullerides had been done then the first wash was with ~100 ml of acetone. This had the effect of dissolving most of the alkali metal fullerene (decomposition of the product was observed as a dark green precipitate). This washing was followed by the general protocol above. If this failed to remove all waste then the glassware was heated to 550 °C using a glass blower's furnace in air which would remove all carbon residues. If iron selenide was used then the glassware would be washed in aqua regia (3:1 HCL to HNO_3) followed by water which removes all contamination from the iron selenide reactions. This cleaning solution could then be stored in a suitable glass container and re-used to minimise waste.

The cleanliness of the glassware was not the only concern addressed during glassware preparation. When using glassware under vacuum or high

pressure the structural integrity of the apparatus must be taken into account. A common problem with specialist glassware is the presence of pin holes in the walls of the glass as a result of joining two pieces together. This could potentially provide a point of weakness where the glass could fail if put under very low or high pressures (as well as a source of contamination). The glassware in this work was regularly checked for these problems using a spark test. This test using a high voltage gun shows any pin holes clearly allowing them to be repaired. The second test the glassware was put through was to check for defects from incomplete annealing which was done using polarised lenses. If any defects were found, detected by a change in colour of the glass when viewed using the polarised lenses, the glassware was then re-annealed. Checking key pieces of glassware in this fashion minimises the risk of failure during reaction, creating safe conditions and minimising the chance of exposing the reaction to ambient atmosphere.

2.2.4. Solvent purification

The intercalation of alkali metals into a material using a solvent medium requires a rigorously dried and deoxygenated solvent. The three solvents used in this work are THF, hexane and methylamine. Their drying protocols are described in this section, THF and hexane will be described together as they are both distilled over sodium/benzophenone. The methylamine solvent is dealt with separately as it a vacuum distillation of the solvent from a small amount of lithium metal.

2.2.4.1. Tetrahydrofuran and Hexane

A round bottomed flask (3 L) was purged of air on a Schlenk line using vacuum and back filling with nitrogen gas (repeated 3 times). The solvent (HPLC grade, 2 L) was then poured into the round bottomed flask under a flow of nitrogen (Table 2.1). Sodium metal (5 g), stored in mineral oil, was then cut up into small pieces (~1 cm), washed in a small amount of hexane to remove the mineral oil and then added to the flask. This flask was then closed to ambient atmosphere, covered and left under nitrogen for 12 hours. This produced pre-dried THF which could then be decanted into a distillation kit for drying.

The distillation kit was assembled and connected to the Schlenk line including a two necked round bottomed flask (1 L), still head (250 ml) and reflux condenser. The whole apparatus was then flushed with nitrogen for 10 minutes

prior to adding the solvent. To the round bottomed flask benzophenone (10 g, $5.5x10^{-2}$ mol, 0.11 mol dm^{-3}) was added along with glass anti-bumping granules (1 g, dried in a glass oven for 12 hours). The pre-dried solvent (500 ml) was then added to the still through a funnel along with any additives (Table 2.1). At this point the pre-dried solvent in the 3 L flask was securely closed, removed from the Schlenk line and placed in a dark solvent storage cupboard. Sodium metal (5 g) was then cut into small pieces, washed in hexane to remove the mineral oil and then added to the still.

Once all sodium was added the still was isolated from ambient atmosphere by an appropriate stopper. The water was turned on so that a trickle could be seen flowing through the condenser and into the sink. The isomantle (380 W) was then set to setting 6 and after 25 minutes the solvent was refluxing steadily. The still was then refluxed over 8 hours initially in order to achieve the correct colour indicating that the solvent was properly dry (Table 2.1). The still was then shut down by turning off the isomantle and turning up the nitrogen flow until the still was cool.

Solvent collection was done by first purging an appropriate storage vessel of air by evacuating the vessel and backfilling it with nitrogen 3 times. The vessel was then attached to the collection arm of the still head under an inert gas flow, while the still was cool. The still head's 3 way valve was then returned into a position where the solvent could reflux into the still. Once all equipment was secured the still was restarted and refluxed for at least 2 hours (or more to obtain the correct indicator colour). The solvent was then collected in the still head and then dispensed into the collection flask for immediate use.

Table 2.1 Summary of distilled solvents, any additives used to solubilise the benzophenone and the colour produced when the solvent is sufficiently dry.[7]

Solvent	Additives	Colour
THF	N/A	Purple
Hexane	5 ml Diglyme	Blue

The benzophenone reacts with sodium to form the monoradical anion which gives a deep blue solution and then will react again to form the diradical anion generating the purple colour observed in dry THF stills. In the presence of wet solvent the radical anions react with the water to form diphenylmethanol which if in the presence of adequate amounts of sodium will react releasing hydrogen gas and regenerating the ketyl radicals.

2.2.4.2. Methylamine

First lithium metal (76.1 mg, 10.8 mmol, 72 mmol dm^{-3}) was loaded into a reaction vessel inside an argon filled glove box along with a glass stir bar (Figure 2.5 a). This vessel was then sealed and connected to the dual vacuum line via a two connection manifold. The methylamine (MA) (150 ml), which is kept inside a sealed Schlenk vessel, was also connected to this manifold and the whole system was evacuated to high vacuum. It was necessary to ensure that the system was at low vacuum first before going to high vacuum in order to protect the turbo molecular pump. The manifold was then closed to the high vacuum, opened to low vacuum and the argon atmosphere was removed from the reaction vessel.

A low temperature bath of dry ice and ethanol (-72 °C) was placed around the reaction and a bath of ethanol (22 °C) around the MA vessel providing a significant temperature gradient to drive the condensation of MA into the reaction vessel (Figure 2.5 b). The manifold was then closed to the vacuum line; the MA vessel was opened so that the solvent could condense into the reaction vessel and stirring switched on. Once the MA had condensed into the reaction vessel the vessels were closed and the manifold evacuated to high vacuum. Upon dissolution of the lithium metal in the solvent a blue colour was observed due to solvated electrons (Figure 2.5 c). During this time the manifold was closed to vacuum and the MA vessel disconnected, cleaned and dried in an oven. The vessel was then reconnected and high vacuum restored before continuing.

The pure, dry MA was then re-condensed into the storage vessel by closing the manifold to high vacuum, putting the low temperature bath around the storage vessel and an ethanol bath around the reaction vessel. The reaction vessel was then opened slowly and the MA re-condensed back into the storage vessel (Figure 2.5 d). The process takes heat from the surroundings of the reaction vessel and so it was necessary to exchange the ethanol bath around the reaction vessel at regular intervals in order to keep up the temperature gradient. Once the process was complete the storage vessel was closed and the manifold and reaction vessel were evacuated to low vacuum. At low vacuum the manifold was closed to the vacuum and the vessels disconnected. A solution of toluene and iso-propanol (80:20) was added to the reaction vessel which contained lithium hydroxide and un-reacted lithium metal. This was then left open in a fume hood to fully react before water was added. The resulting liquid was then neutralised and disposed of according to regulation.

Figure 2.5 Purification of methylamine (MA) using lithium metal. (a) Schlenk vessel containing the glass stir prior to loading with lithium metal. (b) Both the lithium loaded Schlenk vessel and the MA storage vessel were attached to the manifold. The Schlenk vessel and the manifold were under high vacuum whilst the Schlenk vessel was cooled using an ethanol/dry ice bath. (c) Once the MA is condensed into the Schlenk vessel the lithium dissolved creating a blue solution. (d) The MA is condensed back into the cooled storage vessel by evaporation. The white precipitate in the Schlenk vessel is the lithium hydroxide product created when the metal reacts with moisture in the MA.

Alkali metals are soluble in liquid MA producing highly reductive solutions. These solutions at the concentrations indicated in this method give an opaque blue

solution due to a strong absorption band that has its maxima in the near infrared.[8] This highly reductive solution is easily capable of reducing water and oxygen producing the appropriate products indicated in figure 2.1 and 2.2. The presence of water and oxygen in the ammonia therefore is indicated by the colour of the solution where a clear or translucent solution shows the presence of the impurities. Although the solutions of alkali metals and liquid MA are stable over short periods of time, the amine will decompose into the alkalimetal amide releasing hydrogen gas over long time periods.[8] To minimise the chance of decomposition the exposure of MA to alkalimetals should be limited to a few hours.

2.2.5. Synthesis of solid state precursors Fe_ySe_2

The synthesis of $K_xFe_ySe_2$ materials involved two stages, first the iron and selenium were reacted together to form a Fe_ySe_2 precursor and a second stage in which the relevant precursor was reacted with potassium targeting specific points on the phase diagram. This reaction sequence allowed the precise targeting of a particular point on the phase diagram and preventing the potassium vapour produced at high temperatures from reacting with the glass.

The method for producing the precursors was adapted with modifications from that of Cava *et.al.* (2009) and performed by Dr A Ganin.[9] The synthetic method for the production of the Fe_ySe_2 precursors is detailed below for the purpose of clarity. Stoichiometric amounts of iron pieces (Aldrich 99.99 %) and selenium shot (Aldrich 99.999 %) were loaded into a silica glass ampoule (8 mm outer diameter (OD)) in an argon filled glove box. This ampoule was then taken to a dual manifold vacuum line where it was evacuated to high vacuum ($1x10^{-5}$ mbar) and sealed using an oxygen-propane torch. This ampoule was then loaded into a second silica glass ampoule (12 mm OD) and sealed again under high vacuum on the dual manifold vacuum line. The ampoule was then placed in a calibrated furnace at a starting temperature of 750 °C. This temperature was sustained for 15 hours followed by heating to 1075 °C at a rate of 1 °C min^{-1}. Once this temperature had stabilised it was held for 12 hours before being cooled at a rate of 2 °C min^{-1} to room temperature. This annealing protocol served the purpose of achieving a homogeneous precursor.

The ampoule was then taken back into the argon filled glove box where it was cut open and the produced Fe_ySe_2 material removed. The products mass was recorded before being ground with a pestle and mortar and a small sample

was loaded into a 0.5 mm capillary tube. The material's X-ray powder pattern was recorded on a Bruker Advance D8 lab diffractometer using Mo $K_{\alpha 1}$ radiation.

2.2.6. Microanalysis

Microanalysis was used to determine the carbon, hydrogen and nitrogen contents of some of the products made during this thesis. To comply with the air-sensitive nature of the samples the microanalysis preparation was carried out in a glove box. In order to obtain results on the product without exposure to air *c.a.* 1 mg of material was loaded into a tin capsule. The loaded capsule was then placed into a 'crimping' device which when operated hermetically sealed the capsule with a cold weld (Figure 2.6). The sealed capsules were then loaded into a microanalysis machine and analysed by the core services staff at the University of Liverpool.

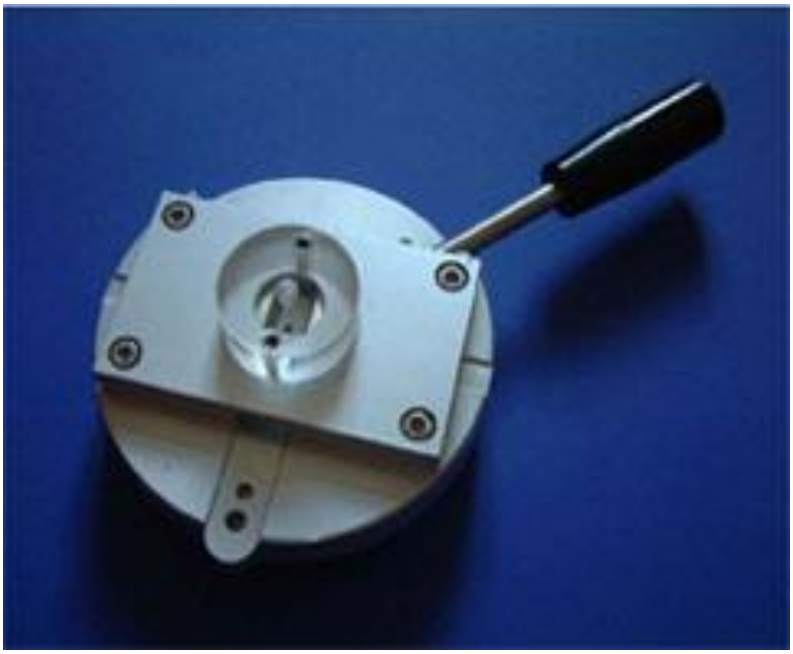

Figure 2.6 Crimping device used to hermetically seal the tin capsules after loading with material for microanalysis.[10]

Utilising the Pregl-Dumas[11] method of "flash" combustion accurately weighed samples encapsulated in tin are introduced into a constantly Helium purged silica combustion tube, typically at 950 °C, and injected with 10 seconds of pure oxygen. Under these conditions, tin rapidly combusts and produces temperatures of up to 1800 °C.

The completely oxidised sample is then passed through a copper-filled reduction tube to remove excess oxygen and reduce nitrogen oxides to elemental nitrogen. The eluted gas of nitrogen, carbon dioxide and water are then separated in a chromatographic column before passing over a thermal conductivity detector (TCD) that determines the changes in intensity, of each element and therefore their concentrations measured against a previous set of calibrating certified standards under the same conditions.

2.2.7. Inductively coupled plasma (ICP) analysis

The compositions of the potassium iron selenide materials were determined by the use of ICP-OES. The air-sensitive nature of the $K_xFe_ySe_2$ materials is not a concern here as the compositions can be calculated from the relative intensities (in ppm) of each of the elements. The potassium iron selenide (9 mg) samples were loaded into glass vials (40 ml) and tightly closed inside an argon filled glove box. The loaded vials were then removed from the glove box and taken to a fume hood.

The vials containing the $K_xFe_ySe_2$ material for analysis were then opened one by one and a 25 ml aliquot of a digestion solution of H_2O_2:HNO_3 (peroxide to acid ratio of 1:1.09) diluted to 9.7 vol.% was added. The vials were re-sealed and agitated by hand 3 times over 30 minutes. The resulting solutions were then analysed by a Spectro Ciros ccd ICP-OES radial view instrument by George Miller in the University of Liverpool chemistry departments core services. Each sample was analysed six times in order to accurately calculate the spread of data. The machine set-up and parameters are contained within appendix A.

2.2.8. Raman spectroscopy

The Raman spectra were recorded using 514.5 nm radiation illuminating a 500 μm diameter using collection times of 20 x 10 s. This was performed by Dr. A. Ganin on a JY LabRam-HR spectrometer which was operated in a backscattered geometry. The calibration of this equipment was done by referencing the 520.07 cm^{-1} line of silicon.

Two phase-pure standard samples were used (C_{60} and Cs_6C_{60}) and were used to ensure the instrument was correctly calibrated. The observed peaks for C_{60} and Cs_6C_{60} were a singlet peak at 1464 cm^{-1} and a peak at 1430 cm^{-1}

respectively. This meant that for each electron transferred to the C_{60} the wavenumber decreased by 5.67 cm^{-1}.

2.3. Powder X-ray Diffraction

Crystalline solids are characterised by the presence of long-range order in the arrangement of atoms in a fixed shape and volume. Solids which do not have long-range ordering of their atoms, for example glasses, are classified as amorphous. In addition to these amorphous materials are semi-crystalline materials, such as plastics, that are defined by a lesser degree of long-range ordering when compared to crystalline solids. Regardless of how crystalline a solid is they all consist of atoms in close proximity to each other (typically between a few tenths of Angstroms up to 2.5 Å).[12]

The interatomic distances in solids are on the same order of magnitude as the wavelengths encompassed by X-ray radiation (0.1 to 100 Å).[12] This makes the solid material capable of diffracting X-rays where the maximum diffraction takes place when the distance between two atoms is that of the radiation wavelength. Due to the presence of many planes created by the huge number of atoms in a solid sample constructive and destructive interference of the diffracted beam occurs. This creates an observable pattern of maxima from which detailed information about the solid material can be obtained.

Bulk techniques such as powder X-ray diffraction can take advantage of the long-range structural ordering in crystalline solids. The crystal lattice of a crystalline material consists of a simple unit cell which can be translated throughout the lattice. The unit cell is the simplest repeating unit in a crystal lattice and consists of the lattice parameters which are defined as the lengths *a*, *b*, *c* and the angles *α*, *β*, *γ*. The unit cell contains specific information on the location, type and number of atoms in a material all of which is contained within a powder X-ray pattern. A typical powder X-ray pattern contains information about a material's structure in four ways (Figure 2.7); firstly the peak positions can be used to gain knowledge about the sample crystal system and cell metrics using Bragg's law. Secondly the peak intensities coupled with a structural model give information on the types of atoms present and their positions. Thirdly the peak widths can yield information on the microstructure of a material and finally the oscillations in the background can produce data on short range order.

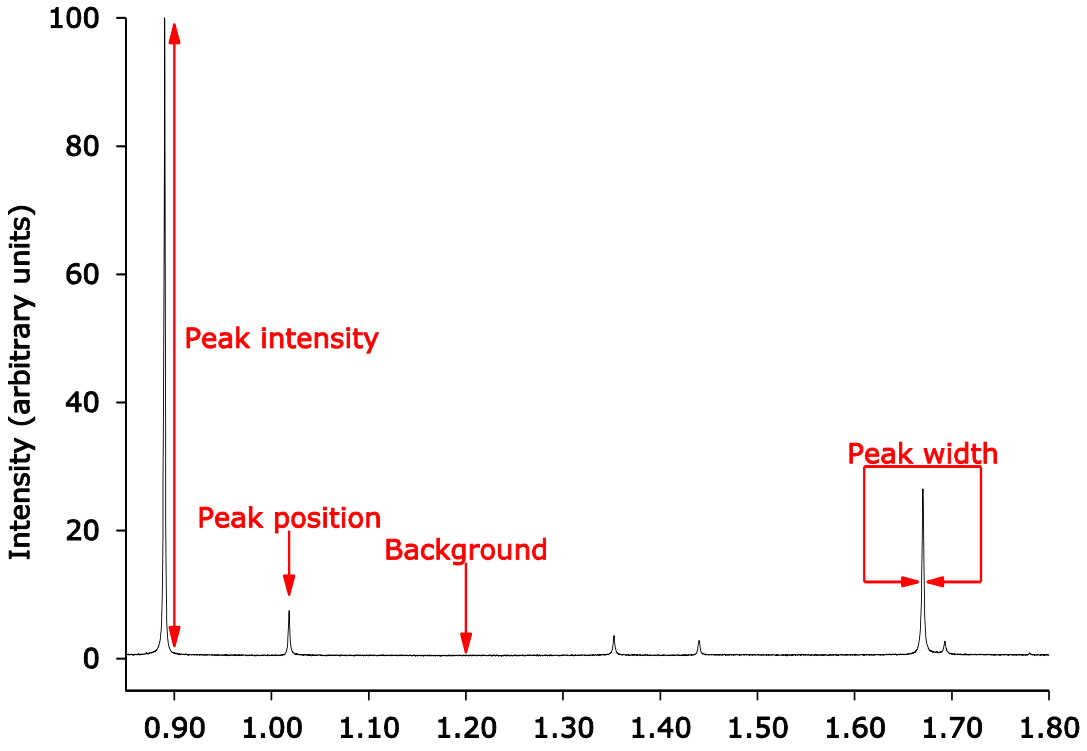

Figure 2.7 Powder X-ray diffraction pattern indicating the areas in a pattern where information is contained.

2.3.1. Bragg's law and the structure factor

The Bragg equation in equation 2-1 states the condition that has to be met in order for diffracted beams to constructively interfere (Figure 2.8). Where *n* is the order of reflection; λ is the wavelength; d_{hkl} is the interplanar distance and θ_{hkl} is the Bragg angle. This condition is that only when the *n* is an integer multiple of the λ can two diffracted beams from adjacent planes constructively interfere.

$$n\lambda = 2d_{hkl}\, sin\theta_{hkl} \qquad \textbf{(2-1)}$$

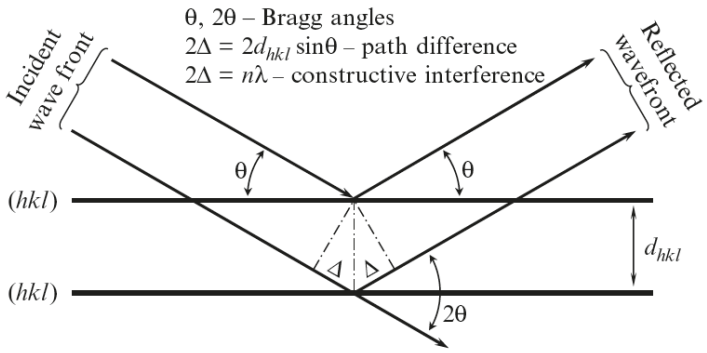

Figure 2.8 Graphical representation of Braggs' law.[12]

The maxima created by diffracted beams that observe the Braggs law for constructive interference are called Bragg peaks. The Bragg peaks positions can then be calculated, in terms of the Bragg angle, and $\underline{d}_{hkl}$ determined. If the crystal system is then determined using the *d*-values it is possible to obtain the unit cell metrics.

Each different Bragg peak observed by X-ray diffraction for a material will have different intensities. These intensities are related to the structure of a material especially with regards to atom type and their positions. The intensity of a diffracted peak is related to the structure factor in equation 2-2. Where K is a scale factor; p_{hkl} is the multiplicity factor; L_θ is a Lorentz multiplier (dependent upon the diffraction geometry); P_θ is a polarisation factor; A_θ is the absorption multiplier; T_{hkl} is the preferred orientation factor; E_{hkl} is the extinction multiplier and $|F_{hkl}|^2$ is the structure factor.[12] This equation contains all of the contributions to the integrated intensity from sample preparation, preferred orientation effects, to experimental setup such as the Lorentz multiplier. The major contribution to the integrated intensity of a diffraction peak comes from the structure factor itself.[12]

$$\boldsymbol{I_{hkl} = K \times p_{hkl} \times L_\theta \times P_\theta \times A_\theta \times T_{hkl} \times E_{hkl} \times |F_{hkl}|^2} \qquad \textbf{(2-2)}$$

The structure amplitude, which is directly related to the structure factor, is summed over all atoms in equation 2-3. Where each *j* represents the *j*th atom; $i = \sqrt{-1}$; $s = \sin\theta_{hkl}/\lambda$. Each atom has direct contributions through its occupation (g^j); atomic displacement (t^j); atomic scattering (f^j) factors and its fractional co-ordinates through hx^j, ky^j and lz^j. Both the atomic displacement and scattering factors are dependent on θ and λ.

$$\boldsymbol{F_{hkl} = \sum_{j=1}^{n} g^j t^j(s) f^j(s) e^{[2\pi i(hx^j + ky^j + lz^j)]}} \qquad \textbf{(2-3)}$$

The total amount of X-rays scattered by atoms (more specifically their electrons) in a material is described by the atomic scattering factor. This factor consists of two parts the first is the normal atomic scattering factor which is dependent upon the number of electrons in the scattering atom. The second is the combination of the real and imaginary parts of the anomalous scattering factors which depend on the wavelength used and atom type. This means that it is possible to differentiate between two different atoms using X-ray diffraction so long as the atoms have different numbers of electrons. The parameters are s =

$\sin\theta/\lambda$; f_0^j is the normal atomic scattering factor; $\Delta f^{j'}$ and $\Delta f^{j''}$ are the real and imaginary components of the anomalous scattering factor.

$$f^j(s) = f_0^j(s) + \Delta f^{j\prime} + i\Delta f^{j\prime\prime} \quad \textbf{(2-4)}$$

2.3.2. Sample preparation

The ideal powder sample for PXRD consists of an infinite number of randomly orientated crystallites with a size range of between 1 and 10 μm in size. The sample must also be representative of the bulk. Real materials are very rarely produced satisfying the ideal conditions and as such proper protocols for ensuring that samples for PXRD obey the ideal as much as possible are necessary. Common problems experienced in PXRD analysis directly related to sample preparation include preferred orientation; surface roughness; texture and sample height. Taking steps, like grinding in a pestle and mortar, to ensure a homogenised and fine powder is used counteracts all of the common problems associated in sample preparation.

Additional problems often observed come from diffractometer geometry specific assumptions. In the case of a diffractometer in reflection geometry with a flat plate holder the sample must be infinitely thick. If the diffractometer is in transmission mode then the sample must be thin enough to allow the transmission of X-rays through the sample. Both of these issues can seriously affect the intensities of the diffracted peaks.

The PXRD patterns in this work were all run using a diffractometer in transmission mode. The samples are all finely ground in a pestle and mortar before loading into a capillary. The size of the glass capillary is selected so that the absorption coefficient multiplied by the capillary radius (μR) is kept at less than 4 which allowed the implementation of absorption corrections.[13]

2.3.3. X-ray radiation sources

2.3.3.1. Lab diffractometers

The most common method of generating X-rays are the X-Ray tubes supplied with lab diffractometers. The X-rays for lab diffractometers are generated by accelerating an electron from a cathode and onto a target anode (Figure 2.9). The X-rays are generated by the anode when the incoming high

energy electrons are absorbed. The high energy electrons collide with the core electrons of the metal atoms in the anode. The core electrons of the metal atoms are then displaced allowing electrons in higher energy orbitals to occupy the hole left by the displaced core electron. As the electron from a higher energy orbital moves to the lower energy state it emits the excess energy in the form of photons with energies in the X-ray spectrum. There are multiple possibilities for what energy level the initial core electron is removed from. This creates the effect called Bremsstrahlung radiation as the anode metal can produce photons with a range of wavelengths.

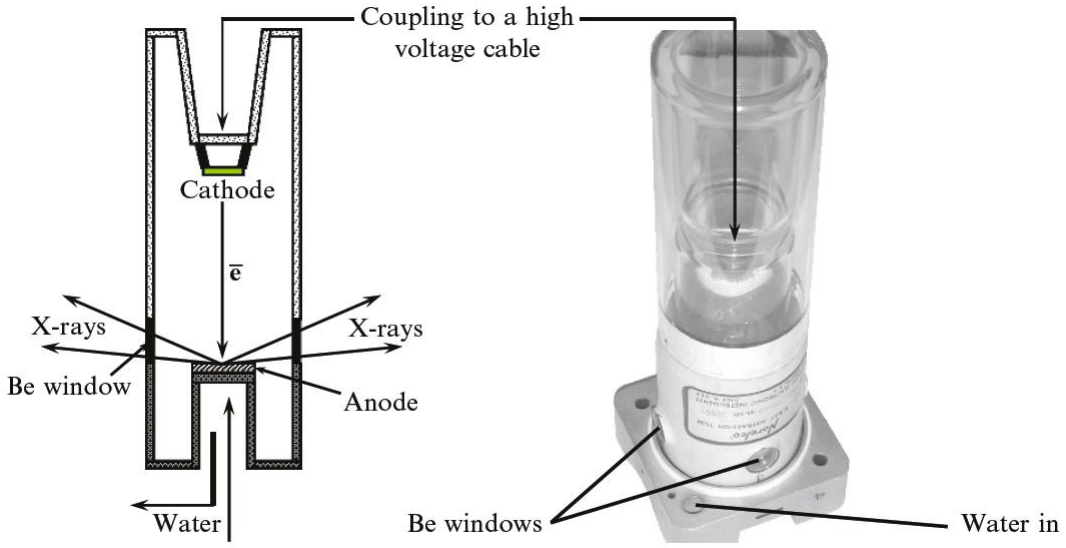

Figure 2.9 Schematic diagram of a sealed tube fixed anode X-ray source for a lab diffractometer.[12]

Bremsstrahlung radiation is undesirable for X-ray analysis as it will produce many overlapping peaks complicating any diffraction pattern recorded. Monochromatic radiation is obtained by the use of a single crystal monochromator, for example they can be made up of Ge single crystals. The monochromatic radiation is produced as the monochromator only reflects radiation with wavelengths that obey Bragg's law for the d-spacings of the single crystals in the monochromator. The consequence of this is that a significant fraction of radiation is discarded, since it is the wrong wavelength, reducing the intensity of X-rays available.

2.3.3.1.1. Bruker D8 Advance lab diffractometer

Laboratory powder X-ray diffraction (PXRD) patterns were collected on a Bruker D8 Advance diffractometer in capillary geometry mode. It was equipped with a Ge crystal monochromator and a molybdenum X-ray source supplying $K\alpha_1$ at a wavelength of 0.70932(1) Å. It was equipped with fixed Soller (2.5 °) and divergence slits (1 mm). The detector equipped on the diffractometer was a LynxEye with a 3 ° window.

2.3.3.2. Synchrotron sources

The X-ray radiation produced by synchrotron sources in comparison to lab sources has a higher collimation, intensity and resolution. These advantages are reinforced by a lower beam divergence when compared to a lab source as well as variable monochromatic wavelengths. As such the synchrotron sources are very useful when PXRD patterns of a sample prove to be multiphasic and the high resolution of the synchrotron radiation allows detailed information to be obtained from each phase.

In general synchrotrons used in this work generate their radiation by the following method (Figure 2.9). Under vacuum an electron gun generates electrons which are then accelerated up to high energies, which are specific to each synchrotron, in a series of particle accelerators. The first accelerator is the linear accelerator (linac) and feeds electrons into the second accelerator called a booster ring. The second accelerator brings the electrons up to their final energy before being fed into the third accelerator known as the storage ring. The storage ring consists of a number of alternating straight and curved sections, depending on the size of the ring. The curved sections direct the electrons around the storage ring and as a result of the changing direction of the electrons produce synchrotron light. The straight sections house the insertion devices. These insertion devices also create synchrotron light but unlike the bending magnets of the curved sections they produce more intense tuneable light. The insertion devices cause the electrons to follow either an undulating or wiggling path which due to the large number of directional changes in the electrons path results in the high intensity radiation.

Since the produced radiation is emitted in a tangential direction to the electron path and so the beam lines are situated to take advantage of this (Figure 2.10). This enables the guiding of the light into the experimental stations where it can be focused and filtered for use by the beam lines optics. The monochromatic light is then directed through collimators to reduce air scatter, in the case of a PXRD line, at the sample stage of the diffractometer.

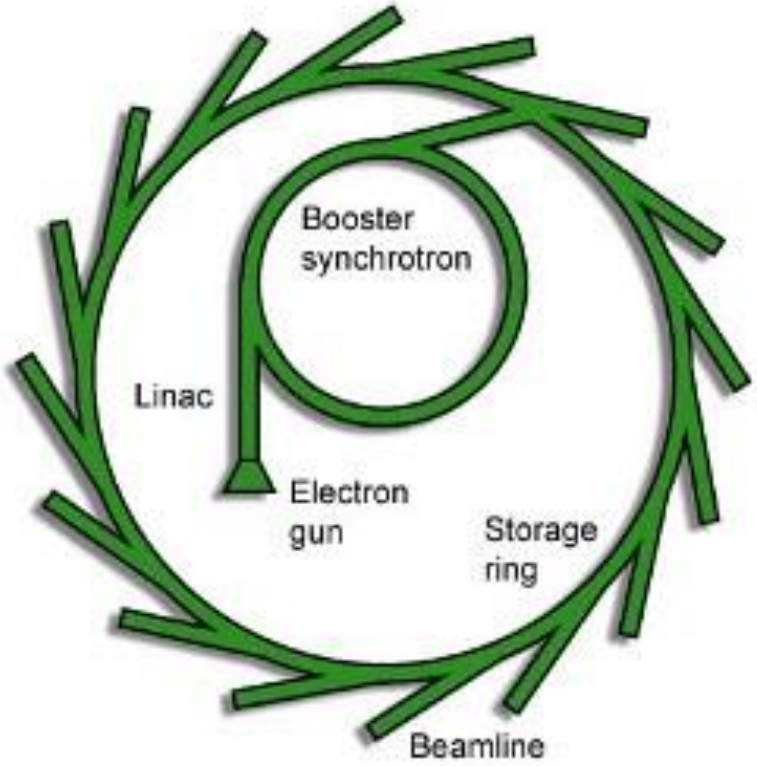

Figure 2.10 Schematic of the areas of Diamond light source responsible for electron generation, acceleration, storage and use.[14]

2.3.3.2.1. Diamond light source powder diffraction line I11

The Diamond light source, a third generation synchrotron, initially accelerates electrons in its linac to 100 MeV. These electrons are then fed into the booster synchrotron which consists of two straight sections joined by two curved sections and further accelerates the electrons to 3 GeV before injecting them into the storage ring.

The I11 beam line uses radiation produced from an undulator insertion device generating radiation with energies in the range of 5-30 KeV.[15] This white light is made monochromatic by two Si(111) monochromators which are cooled using liquid nitrogen.[15, 16] The diffractometer has two different detectors one consists of 5 arms of 9 single crystal and solid state detectors referred to as multiple analysing crystals (MACs) and the other is a position sensitive detector (PSD) (Figure 2.11).[16] The difference between the two detectors is that the MAC detector is of a higher resolution but takes longer to achieve the same number of counts as the PSD.

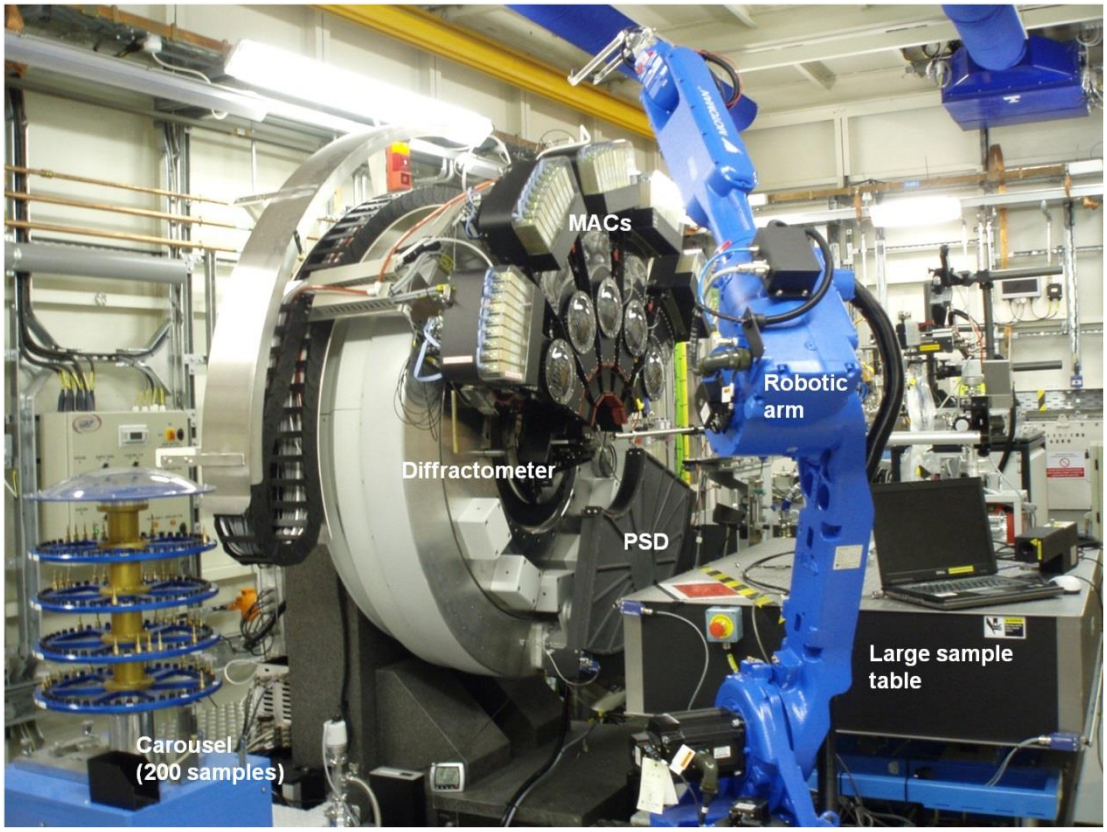

Figure 2.11 I11 heavy duty diffractometer, arrangement of MAC detectors, PSD and robotic arm.[17]

2.3.3.2.2. European Synchrotron Radiation Facility (ESRF) powder diffraction line ID31

The ESRF is a third generation synchrotron and its linac supplies electrons to its booster synchrotron at energies of 200 MeV. The electrons are then accelerated to energies of 6 GeV in the booster ring before being inserted into the storage ring.

The ID31 beam line takes radiation from a straight part of the ring and as such is supplied by an insertion device called an undulator. Specifically the ID31 beam lines X-rays are generated by three undulators which cover an energy range of 5 to 60 KeV. The beam is monochromated using a double-crystal monochromator which is cryogenically cooled. This monochromator is highly adaptable with a choice of either a Si (111) or Si (311) crystals making it up. The Si (111) is used for standard operation and is cooled using liquid nitrogen. The Si (311) is for higher energy resolution and is maintained at a constant temperature of -60.00(5) °C. The size of the monochromated beam is controlled by water cooled slits and incidents with the samples at a typical size of 2.5 mm width and 1.5 mm high. The detector arm of the diffractometer in ID31 consists of 9 detectors and Si (111) crystals which are mounted on a single rotation stage. This combined with a calibration of the offset and channel efficiencies using a silicon standard allows the combination of the data collected from all 9 detectors. The ability to combine the data from all detectors increases efficiency as the arm only has to move by 2.3 ° in order to measure 18 in 2θ.

2.3.3.2.3. Super photon ring-8 GeV (SPring-8) powder diffraction line BL44B2

The SPring-8 third generation synchrotron facility accelerates electrons initially in the linac to 1 GeV before insertion into the booster ring. The electrons then are accelerated to the operating energy of 8 GeV using an acceleration voltage of 18.2 MV and a RF frequency of 508.58 MHz before insertion into the storage ring.

The beam line BL44B2 has radiation supplied using a bending magnet on a curved part of the storage ring. The white light is monochromatized by a double crystal monochromator made up of Si (111) single crystals with the ability to provide X-rays in the energy range of 12.4-33.5 KeV with a beam size of 3 mm width and 0.2 mm high (Figure 2.11). The diffractometer in the experimental hutch is equipped with a Debye-Scherrer camera (radius 286.48

mm) containing a 2D imaging plate detector. This camera is capable of taking data every 0.01 ° up to 75 ° 2θ.

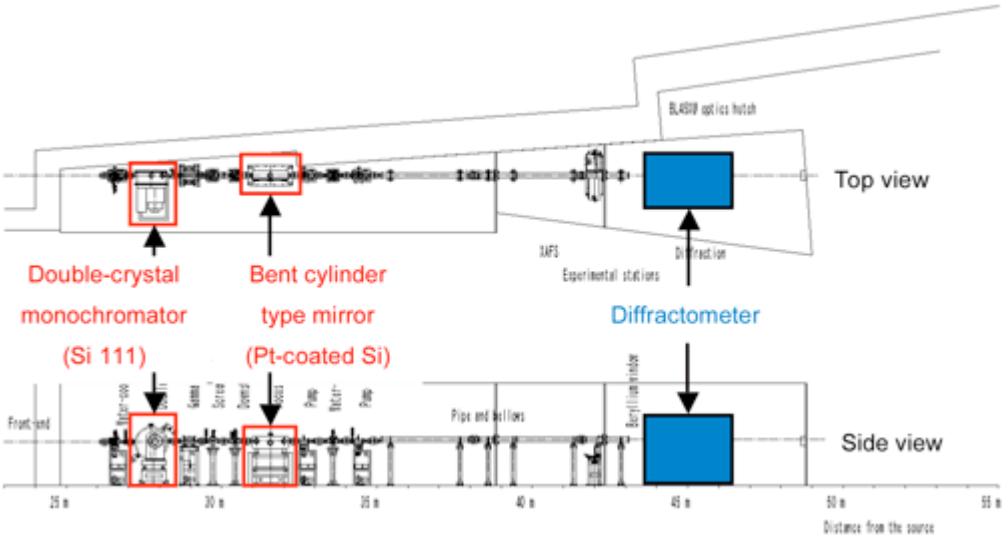

Figure 2.12 Schematic layout of the optics and experimental station of the RIKEN materials science beam line.[18]

2.3.4. Powder X-ray diffraction analysis

The software used to analyse the collected PXRD patterns in this project is TOPAS Academic V5 where the input files are written in J-Edit.[19] TOPAS is classified as profile and structure analysis software. It has capabilities including indexing, whole powder pattern decomposition, Rietveld refinement and combining data from multiple sources such as single crystal, powder and neutron diffraction data. The combination of J-Edit and TOPAS Academic allows the writing of input files with customised outputs, calculations and functions. This flexibility combined with the speed and stability of the programs kernel allows for setting up complex and automated refinements of many data sets simultaneously.

2.3.4.1. Pawley method

A Pawley refinement is a very useful technique for PXRD analysis when there is no, or an inadequate, structural model available for a material.[12, 20] The only requirement for a Pawley refinement to be applicable is an approximate unit cell and space group.[12] The intensities of each reflection in the PXRD pattern are treated as a free parameter in the least squares refinement routine. This type of whole powder pattern decomposition then calculates more exact lattice

parameters than the starting model and generates the *d*-spacing of each reflection and their intensities. This information can then be used in structure solution techniques to help produce a structural model capable of being used in a Rietveld refinement. An additional benefit of the Pawley refinement is that in cases where the structural model is in question the peak shape can be investigated in the absence of any structural inaccuracies. Once the peak shape is confirmed as correct or not, any issues with the structural model can be examined in detail.

2.3.4.2. Rietveld method

The Rietveld method differs from other whole powder pattern methods, like Pawley refinements, in that the integrated peak intensities are calculated from a structural model.[12, 21, 22] The model consists of sample specific effects such as preferred orientation and absorption in addition to the parameters that make up the structure amplitude. The Rietveld method also takes into account geometrical factors from the methods used to record the data.[12] During each iteration of the Rietveld refinement the calculated pattern produced by the structure model is compared against the observed pattern of the material. The parameters of the model are then adjusted in an iterative process that minimises the difference between the calculated and observed patterns using least squares minimisation protocols. This means that the Rietveld method is capable of generating detailed knowledge about the structure of a specific material so long as an approximate starting model is given.

2.3.4.3. Accuracy determination of refinement models

A structural model refined by the Rietveld method is assessed for quality by two methods. The first is observational comparison of the difference between the calculated and observed X-ray patterns providing a 'sanity' check that the structure model is applied correctly. The second is the used of mathematical figures of merit produced by the least squares minimisation routines during the refinement.

The relevant figures of merit used in this thesis are shown in equations 2-5 to 2-7. Where n is the number of atoms; p is the number of parameters; w_i is the weighting given to a data point i; Y_i^{obs} and Y_i^{calc} are the observed and calculated intensities a data point i and $\sigma(Y_i^{obs})$ is the error of the intensity at

data point Y_i^{obs}. These consist of the weighted profile residual (R_{wp}), the expected profile residual (R_{exp}) and the goodness of fit (X^2). The R_{wp} is not biased to a particular structural model and is meaningful (Equation 2-5). The smaller the R_{wp} becomes the better the calculated pattern fits the observed.

$$\boldsymbol{R_{wp} = \sqrt{\left[\frac{\sum_{i=1}^{n} w_i\left(Y_i^{obs} - Y_i^{calc}\right)^2}{\sum_{i=1}^{n} w_i\left(Y_i^{obs}\right)^2}\right]} \times 100} \qquad \textbf{(2-5)}$$

$$\boldsymbol{w_i = 1/\sigma(Y_i^{obs})^2} \qquad \textbf{(2-6)}$$

The expected profile residual (R_{exp}) in equation 2-7 is a measure of the best possible value of R_{wp} that can be expected for the statistics of the observed pattern. Comparing the R_{wp} to the R_{exp} is used as an indication of the progression of a refinement.

$$\boldsymbol{R_{exp} = \sqrt{\left[\frac{n-p}{\sum_{i=1}^{n} w_i\left(Y_i^{obs}\right)^2}\right]} \times 100} \qquad \textbf{(2-7)}$$

A more formal comparison of R_{wp} and R_{exp} is the use of the goodness of fit (GOF) parameter in equation 2-8 which is the square of the ratio between R_{wp} and R_{exp}. The best possible outcome for a refinement in terms of GOF is to achieve unity. However, this is not usually achievable for high quality data obtained from a synchrotron source as R_{exp} is very low. A secondary use for the GOF is to determine if a refinement is over parameterised or the structural model has become unreal. If the GOF is less than 1 this means that the current fit is better than the best possible fit as calculated from the observed patterns statistics. The square of GOF (X^2) is also frequently used to show the quality of fit and the same general rule in GOF for determining the quality of fit is used.

$$\boldsymbol{GOF = X = \sqrt{\frac{\sum_{i=1}^{n} w_i\left(Y_i^{obs} - Y_i^{calc}\right)^2}{n-p}} = \left[\frac{R_{wp}}{R_{exp}}\right]} \qquad \textbf{(2-8)}$$

2.3.4.4. Parameter correlation and estimated standard deviations

A common 'road block' to physically sensible Rietveld refinements is extensive parameter correlation. For example the atom site occupancies, displacement parameters and absorption correction parameters are all heavily correlated. Another example is the background function and peak shape parameters where the former can begin to fit the latter and vice versa. These correlations can be positive where two values increase with each other, like with occupancies and displacement values, negative or inversely correlated. The relationships of these correlations can be viewed using correlation matrices and the interactions anticipated.

A good method of minimising the effect of parameter correlation on the accuracy of the refinement is to perform the refinements in consecutive steps as described in McCusker *et.al*. 1999.[23] Where correlated parameters are not refined together. Instead one parameter is fixed to a sensible value while the other is allowed to refine. For example the site occupancies are allowed to refine first while the displacement parameters are fixed to sensible values, which can be defined using literature values for similar materials. In the case of displacement parameters the values obtained from neutron experiments are particularly useful as unlike X-rays, neutrons do not have a $\sin(\theta)/\lambda$ dependence of the scattering cross sections. Another particularly useful method is if there is good chemical analysis for the material which can be used to restrain the overall composition thereby decoupling the occupancies and displacement parameters. A third useful technique is the use of combined refinements where a second data set is recorded and used which is obtained under different conditions or from a different source.[23]

Another important issue of Rietveld refinements to be aware of is the meaning of the calculated errors presented by the refinements software. The errors correspond to estimated standard deviations (e.s.d.) which are related to the mathematical model used to fit the data with. As such they only reflect the precision of the refined values and are not measures of the accuracy of the values. The assumption that is made for the e.s.d. is that the counting statistics are the sole source of the errors, this does not account for systematic errors given by ill-fitting background functions, peaks shapes or a poor structural model.[23] Therefore when assessing for example compositions calculated from refinements, particularly important to this work, the error will be higher than the e.s.d. given for that particular value. A generally accepted way of converting the

e.s.d. into a more reasonable error is to multiply the value to between 3 and 5 σ.

2.3.4.5. Minimisation routines

Rietveld and Pawley refinement methods utilise a non-linear least squares minimisation in order to obtain realistic values for the models supplied to them.[12] TOPAS V5 uses a modified version of this method where the modifications enhance the likelihood of convergence and stability of the minimisation routine.[13] The refinements use this form of non-linear least squares refinement to minimise on the objective function (SX^2) in equation 2-9. Where the parameter descriptions are carried on from section 2.3.4.3. The TOPAS software applies any contributions from restraints (X_R^2) and penalties (X_P^2) along with the residual (X_O^2) minimised during the refinement combining them to give SX^2.[13]

$$\boldsymbol{SX^2 = X_O^2 + X_P^2 + X_R^2} \quad \textbf{(2-9)}$$

$$\boldsymbol{X_O^2 = K \sum_{i=1}^{n} w_i (Y_i^{obs} - Y_i^{calc})^2} \quad \textbf{(2-10)}$$

$$\boldsymbol{K = 1 / \sum_{i=1}^{n} w_i (Y_i^{obs})^2} \quad \textbf{(2-11)}$$

$$\boldsymbol{w_i = 1 / \sigma(Y_i^{obs})^2} \quad \textbf{(2-12)}$$

Where Y_i^{obs} and Y_i^{calc} are the observed and calculated intensities a data point i; n is the amount of data points; w_i is the weighting given to a data point i and $\sigma(Y_i^{obs})$ is the error of the intensity at data point Y_i^{obs} .

2.3.4.6. Peak shape determination

The peak shapes of the PXRD patterns of the materials presented in this thesis are done using standard or combinations of standard analytical peak shapes. In order to accurately account for the line shape of a peak the background must be dealt with properly or it may begin to fit some of the intensity which should be dealt with by a peak shape. In this work the background is fitted using a Chebychev polynomial function of no more than 13 terms for data obtained using synchrotron radiation. This function coupled with a

visual inspection of the functions contribution to the pattern ensures the background is accounted for sensibly.

The peak shapes applied to the materials in this work are phase dependent, for example a highly crystalline isotropic phase can be dealt with using a pseudo-Voigt (PV) or a Thompson-Cox-Hastings (TCHZ) function.[21] The more complex phases like the Rb_3C_{60} materials which have complex anisotropic profile broadening are dealt with using a anisotropic peak shape which was developed on this type of material.[24] The implementation of the anisotropic peak shape described by Stephens *et.al.*[24] in TOPAS is slightly different to that described in the paper. This results in a slight variation in the refined values between Rietveld programs but still produces identical fits for the fit of the refined model.[24] This variation between refinement software packages means that comparison of the values obtained from different programs is meaningless. Although direct comparison between software for Stephens anisotropic peak shape is not possible, is it pertinent to give the refined values which are contributions (in radians) to the full width half maximum (FWHM) and the equation used to implement them (Equations 2-13 to 2-16). The use of more complex peak shapes than these will be explained in the relevant chapter.

$$\boldsymbol{\sigma(M_{hkl}) = \sum_{HKL} S_{HKL} h^H k^K l^L} \quad \textbf{(2-13)}$$

$$\boldsymbol{\Gamma = d^2 \times \sqrt{\sigma(M_{hkl})} \times tan\theta \times \left(\frac{0.0018}{\pi}\right)} \quad \textbf{(2-14)}$$

$$\boldsymbol{G_{FWHM} = \Gamma \times (1 - \eta)} \quad \textbf{(2-15)}$$

$$\boldsymbol{L_{FWHM} = \Gamma \times \eta} \quad \textbf{(2-16)}$$

Where $\sigma(M_{hkl})$ is the variance in M_{hkl}; S_{HKL} has crystal system specific terms defined for H+K+L=4 for example there are 15 independent parameters based on crystallographic directions for the triclinic system which represent the θ independent contributions to the FWHM in radians from each direction; Γ is the θ dependent anisotropic contribution to the FWHM in radians; d is the d-spacing; G_{FWHM} and L_{FWHM} are the contributions of the anisotropic line shape to the Gaussian and Lorentzian parts of the peaks; η is the Gaussian-Lorentzian mixing parameter.

2.4. Magnetic measurements

2.4.1. SQUID magnetometer

The magnetic and superconducting properties of the samples produced during this thesis were investigated using a Magnetic property measurement system (MPMS) (Figure 2.13). This device is capable of precisely controlling the temperature of a sample in the range of 2-400 K and applying magnetic fields up to seven teslas.[25] The device itself is configured to detect the magnetic moment of a material allowing analysis of the magnetisation and magnetic susceptibility.[25]

Several components make up the MPMS system which allows it to record data in a very flexible way. The first and second are the temperature and magnet control systems. The third is the superconducting SQUID amplifier system which contains an rf SQUID detector. The fourth is the sample handling system which allows the sample to step and rotate through the detection coils without producing excessive mechanical vibrations. The fifth is the computer and the software provided which both automates the data collection procedures and aids in data processing.[25]

Figure 2.13 MPMS Squid magnetometer. [26]

The data collection is achieved by moving the sample through the superconducting detector coil. This is done using a series of steps where each change of the samples' position causes a change in the magnetic flux within the

coil leading to a change in the current. The SQUID is a sensitive current to voltage converter and where the variations in the voltage are recorded. Since this is done several times the voltage is recorded and averaged. The signal to noise ratio can be improved by repeating this process several times and averaging those results. The data collected is initially in the form of voltage vs the sample position. The integration of the area of this plot gives a very accurate measurement of the magnetic moment of the sample.[25]

2.4.1.1. Ambient and high pressure sample preparation

The magnetic measurements for the materials synthesised in this thesis were recorded at various pressures depending on the material involved. The samples were prepared for ambient pressure experiments by loading ~30 mg of material into a glass ampoule (6 mm outer diameter (OD)) with a single open end in a helium-filled glove box. This ampoule was then sealed using a greaseless high vacuum tap coupled with an o-ring face seal fitting. The equipment was taken to a Schlenk line and put under a partial pressure of He before sealing with an oxygen/propane torch. The sealed ampoule was then attached to the SQUID magnetometers sample rod using Kapton tape (due to its non-magnetic and temperature resistant properties). The measurements were performed by Dr. A. Ganin.

The high pressure magnetic measurements required to detect superconductivity in the Cs_3C_{60} materials were carried out in an EasyLAb Mcell 10 (Figure 2.14). The high pressure cell measurements were carried out by Professor Kosmas Prassides' research group in the University of Durham. The measurements on superconductivity using this cell used the tin superconducting transition shift method to give a very precise measurement of the pressure.

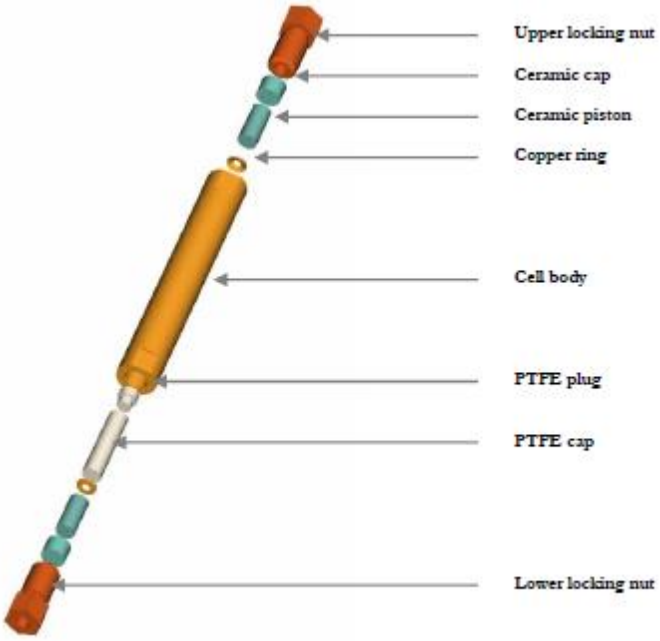

Figure 2.14 3D Schematic representation of the EasyLab Mcell 10 high pressure device. [27]

To perform this method a tin manometer sample is placed inside the PTFE cap along with the sample requiring measuring. The T_c of the tin (3.1-3.87 K) vs pressure is known and therefore the pressure the sample is under can be determined.[28] Once complete a pressure transmitting oil is added into the PTFE cap which acts as a pressure transmitting medium. The whole cell can then be closed using the PTFE plug and pressurised using a hydraulic press ram. The requirements of the hydraulic press are that it must be capable of supplying pressures in excess of 1.5 ton of force.[28]

Also further to determining the exact pressure of the sample in the cell is the need to successfully account for the background produced by the cell. This is done by recording a blank recording of the empty cell using the automated background subtraction feature of the MPMS software.[28] This then allows the subtraction of this background during 'live' sample measurements.

2.4.2. Superconductivity measurements

The measurements using the SQUID on the superconducting samples in this thesis are geared towards investigating the Meissner effect of the sample in question. Investigating this effect yields the critical temperature (T_c). The T_c (for an ideal superconductor) is defined as the temperature at which the applied magnetic field is expelled from inside the material. The experiment which

determines the T_c is called a field-cooled (FC) measurement where a small magnetic field is applied to the sample as it is cooled through its critical temperature (Figure 2.16).[25] The T_c is best defined using the derivative of the magnetization vs temperature plot and is clearly shown where *d*M/*d*T begins to increase.

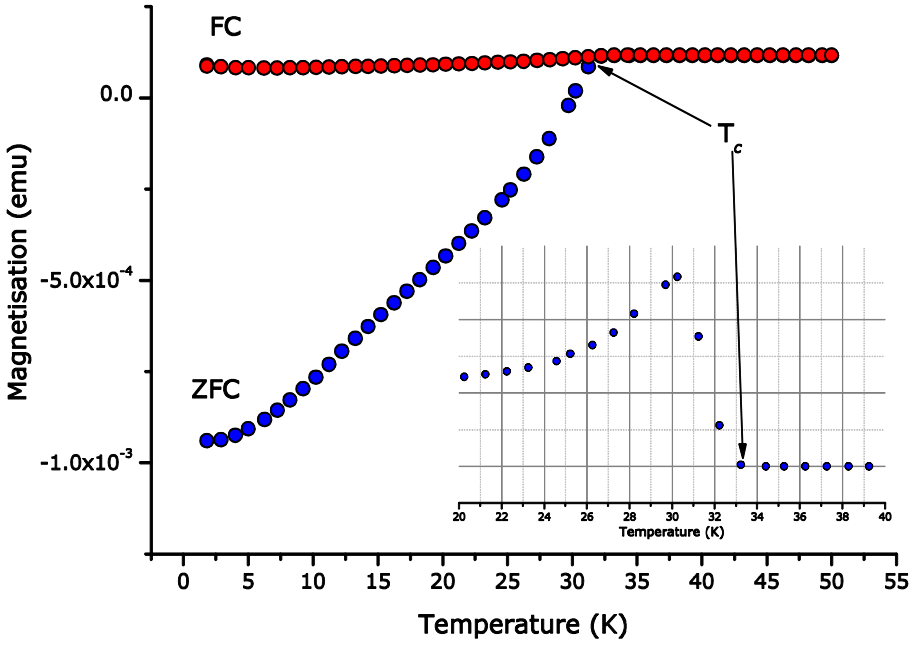

Figure 2.15 Magnetisation vs temperature data for the $K_{0.75}Fe_{1.702}Se_2$ superconductor. FC and ZFC represent the field cooled and zero field cooled experiments respectively. T_c is the critical temperature and the inset is *d*M/*d*T.

The second piece of information which can be gained, after the investigation of the Meissner effect, on warming up the sample is the shielding fraction (SF). The SF is a measure of the percentage of sample that the magnetic field is screened from by the superconductor below its T_c.[25] The SF measurement is calculated using equation 2-17. Where ρ is the density of the material in g cm^{-3} obtained from PXRD Rietveld analysis; Δ_{mom} in emu is the modulus of the difference in the long moment between the paramagnetic and superconducting states; H is the strength of the magnetic field in Oe and m is the mass in grams of the material. This experiment can also be used to evaluate the T_c of a material in addition to the FC experiment.

$$SF = \left(\frac{4\pi p \Delta_{mom}}{Hm}\right) \times 100 \qquad \textbf{(2-17)}$$

The observed splitting at the superconducting transition between the FC and ZFC experiments is due to the method that they were performed with. At the superconducting transition the Cooper pairs form and persistent currents exist on the surface. This persistent current is responsible for the expulsion of all magnetic flux making the superconductor a "perfect" diamagnet. When the FC experiment is performed the material transitions into its superconducting state whilst magnetic flux has already penetrated it. This results in some of the magnetic flux becoming trapped within the core of the superconductor by shielding effect of the persistent surface currents. This results in the susceptibility of the material during an FC experiment being reduced considerably. When the magnetic field is applied during the ZFC experiment the sample is already in its superconducting state and therefore no magnetic flux penetrates beyond the London penetration depth. This means that the material during the ZFC experiment experiences no reduction in susceptibility resulting in the observed splitting between ZFC and FC data.

2.5. References

1. P. W. Atkins and D. F. Shriver, *inorganic chemistry*, 4th ed. / Peter Atkins ... [et al.]. edn., Oxford University Press, Oxford, 2006.
2. D. F. Shriver and M. A. Drezdzon, *The manipulation of air-sensitive compounds*, 2nd ed. edn., Wiley, New York, 1986.
3. MBraun, *LABmaster Glove box Workstation*, http://www.mbraun.co.uk/products/glovebox-workstations/labmaster-glovebox/#features, Accessed 11/09, 2013.
4. X. H. Liu, W. C. Wan, S. M. Owens and W. E. Broderick, *Journal of the American Chemical Society*, 1994, **116**, 5489-5490.
5. A. Y. Ganin, Y. Takabayashi, Y. Z. Khimyak, S. Margadonna, A. Tamai, M. J. Rosseinsky and K. Prassides, *Nature Materials*, 2008, **7**, 367-371.
6. E. C. Ashby and R. D. Schwartz, *Journal of Chemical Education*, 1974, **51**, 65.
7. W. L. F. Armarego and C. L. L. Chai, *Purification of laboratory chemicals*, 5th ed. edn., Butterworth-Heinemann, Amsterdam ; London, 2003.
8. Atkins, Overton, Rourke, Weller and Armstrong, *Shriver and Atkins Inorganic Chemistry*, 4th edn., 2006.
9. T. M. McQueen, Q. Huang, V. Ksenofontov, C. Felser, Q. Xu, H. Zandbergen, Y. S. Hor, J. Allred, A. J. Williams, D. Qu, J. Checkelsky, N. P. Ong and R. J. Cava, *Physical Review B*, 2009, **79**.
10. Microanalysis, *F5109 Sealing device*, http://www.microanalysis.co.uk/product_details.php?top=Micro%20CHNOS&sub=Microanalytical%20tools%20and%20sundries&category=213&prod_code=F5109&product=F5109&description=Sealing%20Device%20for%20Liquids%2020503002, Accessed 11/09, 2013.
11. R. K. Patterson, *Analytical Chemistry*, 1973, **45**, 605-609.

12. V. K. Pecharsky and P. Y. Zavalij, *Fundamentals of powder diffraction and structural characterization of materials*, 2nd ed. edn., Springer, New York, 2009.
13. A. Coelho, Coelho Software, Editon edn., 2013, vol. 5.
14. Diamond-Light-Source, *How do synchrotrons work*, http://www.diamond.ac.uk/Home/About/Synchrotrons/Machine.html, Accessed 11/09, 2013.
15. C. C. Tang, S. P. Thompson, T. P. Hill, G. R. Wilkin and U. H. Wagner, *Zeitschrift Fur Kristallographie*, 2007, 153-158.
16. S. P. Thompson, J. E. Parker, J. Potter, T. P. Hill, A. Birt, T. M. Cobb, F. Yuan and C. C. Tang, *Review of Scientific Instruments*, 2009, **80**.
17. I11, *I11 experimental hutch showing the heavy duty diffractometer*, http://www.diamond.ac.uk/Home/Beamlines/I11.html, Accessed 11/09, 2013.
18. Bl44B2, *Optical layout of RIKEN Materials Science Beamline*, http://www.spring8.or.jp/wkg/BL44B2/instrument/lang/INS-0000000546/instrument_summary_view, Accessed 11/09, 2013.
19. *Bruker AXS, Karlsruhe*, 2003.
20. G. S. Pawley, *Journal of Applied Crystallography*, 1981, **14**, 357-361.
21. R. A. Young, *The Rietveld method*, Oxford University Press, Oxford, 1993.
22. H. M. Rietveld, *Acta Crystallographica*, 1966, **S 21**, A228.
23. L. B. McCusker, R. B. Von Dreele, D. E. Cox, D. Louer and P. Scardi, *Journal of Applied Crystallography*, 1999, **32**, 36-50.
24. P. W. Stephens, *Journal of Applied Crystallography*, 1999, **32**, 281-289.
25. M. McElfresh, Quantum Design, Editon edn., 1994, p. 34.
26. SQUID, *Magnetic Property Measurement System (MPMS)*, http://www.qdusa.com/products/mpms.html, Accessed 11/09, 2013.
27. EasyLab, *EasyLab Mcell 10 high pressure cell for the MPMS system*, www.almax-easylab.com/admin/Uploadnew/ML04_03d%2520-%2520Mcell%252010%2520Technical%2520Note%25202013.pdf+&cd=2&hl=en&ct=clnk&gl=uk, Accessed 11/09, 2013.
28. Amax-easyLab, Amax-EasyLab, Editon edn., 2013.

3. Synthesis of Cs_3C_{60}

3.1. Introduction

The synthetic challenges of A_3C_{60} compounds, particularly those containing high caesium contents, are highlighted consistently in the literature.[1-6] The solid state synthetic protocols for these materials consist of reactions between stoichiometric amounts of alkali metal and fullerene via vapour phase or by diffusion.[4, 7, 8] These methods are very effective in synthesising $A_{(3-y)}A'_yC_{60}$ (A and A' = K, Rb, Cs) materials but require high reaction temperatures.[9] However, due to the limited chemical stability of some compositions at elevated temperatures, such as Cs_3C_{60}, wet chemical methods were utilised. These methods take advantage of an array of solvents such as liquid amines[1, 5, 6, 10-12], toluene[13, 14] and THF[3].

These solution methods can be as effective as the solid state reactions producing materials with high shielding fractions (SF).[1, 5, 6, 10-12] For example the use of ammonia to synthesize face centred cubic (FCC) Cs_3C_{60} gives SFs of up to 80 %.[6] In contrast to this is the synthesis of A_3C_{60} materials utilising toluene or THF which had varying amounts of success with SFs ranging from 1-40 %[3, 13, 14]. The SFs in these cases were heavily dependent on the subsequent thermal treatment where total removal of the solvent from the material was required to match the SFs obtained for materials made via solid state routes.[15]

Wet chemical methods have the potential to become the most effective protocols for making materials containing high caesium contents, for example Cs_3C_{60}.[16] These techniques offer the potential for greater control over the initial reaction.[3, 4, 17] This control becomes important for methods producing materials with caesium rich compositions which must contend with the more stable competing phases of Cs_1C_{60} and Cs_4C_{60} (Figure 3.1).[2, 5, 6, 18-23] These two phases are more stable than Cs_3C_{60} due to the large size mismatch between the Cs radii and the tetrahedral site in the face centred cubic (FCC) C_{60} array. Due to the difficulty in making high purity Cs_3C_{60} many attempts to synthesise the material were tried before its structure was eventually identified.[2, 5, 6, 17, 23, 24]

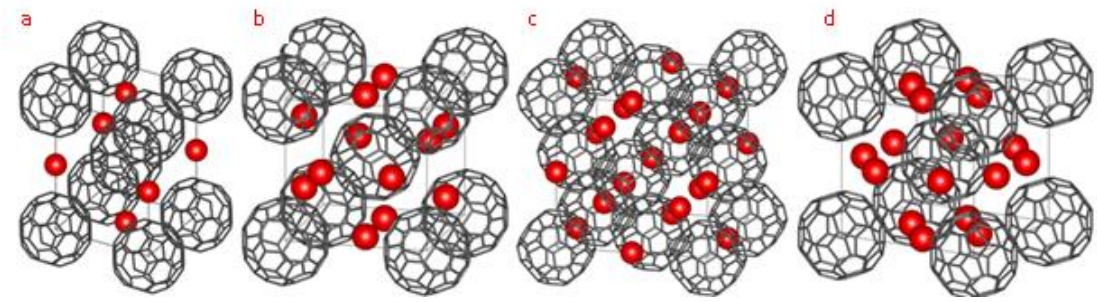

Figure 3.1 (a) Structure of CsC_{60} red atoms are caesium cations (SG= *Pmnn*); (b) "A15" polymorph of Cs_3C_{60} (SG= *Pm*$\bar{3}$ *n*); (c) FCC structure (SG= *Fm*$\bar{3}$ *m*) of Cs_3C_{60} and (d) structural representation of BCO (Cs_4C_{60}) (SG= *Immm*).[5]

The first successful synthesis of high SF (67 %) Cs_3C_{60} material came in 2008 and allowed the identification of the crystalline phases responsible for superconductivity.[5] This material was synthesised by reacting stoichiometric amounts of Cs metal and C_{60} powder in liquid methylamine (MA). This was followed by drying under dynamic vacuum and crystallisation of the final phase assembly by annealing in a furnace. The material produced contained the phases "A15" (Figure 3.1 b), FCC (Figure 3.1 c) and body centred orthorhombic (BCO) (Figure 3.1 d) in the amounts 77.7 %, 8.9 % and 13.4 % respectively.[5] This material contained a large enough fraction of the "A15" polymorph to allow the determination of its physical properties showing this phase to have a critical temperature (T_c) of 38 K. It also allowed the investigation of the "A15" T_cs dependence on pressure which was able to show a direct link between the T_c and the cell volume of the "A15" phase.[5]

The MA protocol used to make large fractions of the "A15" Cs_3C_{60} polymorph was unable to produce the FCC material in purities large enough for in depth analysis of its physical properties.[5] This problem was solved by the synthesis of Cs_3C_{60} in ammonia with subsequent exposure of the sample to MA vapour where the latter step aided the re-combination of Cs_1C_{60} (Figure 3.1 a) and the BCO phase. This synthesis yielded a material that contained 86 % of the FCC polymorph which allowed the determination of its superconducting properties.[5, 6] The analysis of the FCC polymorphs superconducting properties gave a T_c of 35 K with an SF of 80 %. This material was then used to link the T_cs of both the FCC and "A15" phases to the proximity to the Mott metal-insulator transition. These solution based methods were integral in the production of analysable quantities of superconducting material that allowed definitive conclusions to be drawn on these systems.[6]

The solution-based syntheses for the production of the two Cs_3C_{60} polymorphs are not perfect. There is an inherent difficulty in handling and controlling the heterogeneous reactions in liquid amines where the BCO impurity formed during the reaction is insoluble in NH_3 and MA.[25] The precipitation of the BCO phase during the synthesis of Cs_3C_{60} would cause a shift in the equilibrium position favouring the production of Cs_1C_{60} and BCO. The short-comings of the current synthetic methods can be thought of purely as a lack of control over the initial formative step resulting in impurities.

The polymorphism displayed by Cs_3C_{60} provides explanation for some of the physical properties that they display. The "A15" phase crystallises with a cubic crystal structure (a= 11.78282(8) Å, SG = $Pm\bar{3}n$) based upon a body centred packing of C_{60} molecules.[5, 6, 16] Pressurisation experiments show no structural change other than a decrease in cell volume indicating that this is the superconducting phase. Under ambient pressures the "A15" Cs_3C_{60} polymorph shows antiferromagnetic ordering with a T_N of 46 K; this high temperature ordering is unique to this polymorph.[5, 26]

The FCC polymorphs' structure is merohedrally disordered about the [100] direction by a 90 ° rotation of the C_{60}s. This structure has a smaller interanion distance of 3.59 Å through pentagon-hexagon faces than that of the "A15" type.[6] Unlike the "A15" structure the FCC polymorph contains both tetrahedral and octahedral sites. In the FCC structure there is a large size difference between the octahedral site (mean Cs-C distance 3.90 Å) and the tetrahedral (mean Cs-C distance 3.45 Å). This size difference results is the Cs^+ ion having a very large isotropic temperature parameter (B_{iso} = 11.65(7) $Å^2$) which is not observed for the smaller sites within the FCC structure or that of the "A15" polymorph.[5, 6] The FCC polymorphs' role in superconductivity is confirmed on high pressure x-ray diffraction which like the "A15" variant shows only a decrease in cell volume. Interestingly, long range antiferromagnetic ordering in this material is only observed in zero-field muon-spin relaxation experiments below a temperature of 2.2 K.[26] The extremely low T_N displayed by the FCC material is due to the geometrically frustrated structure inherent to the FCC lattice inhibiting magnetic order.

The importance of these materials is clear not only because of their interesting properties but also for the part they play in the bigger picture of high temperature superconductors. The presence of impurities in Cs_3C_{60} materials

impacts negatively on the quality of the information that can be obtained on its physical properties.

The main impurities in the Cs_3C_{60} materials are BCO and Cs_1C_{60} which, if the nominal composition of the synthesised material is Cs_3C_{60}, are linked. The issue with these impurities comes from the magnetic Cs_1C_{60} which may make analysis of the superconducting properties of the Cs_3C_{60} phases difficult. In addition to the magnetic contribution the Cs_1C_{60} material can be amorphous, semi-crystalline or crystalline which can impact on the analysis of the x-ray data.[5] The highest purity material obtained for the "A15" polymorph contained the phase fractions 77.7(6) %, 7.7(10) % and 13.4 % for the "A15", FCC and BCO phases respectively.[5] The best literature material for the FCC polymorph contains 86.71(1) %, 1.18(3) % and 12.11(4) % for the FCC, "A15" and BCO phases respectively.[6] This indicates that there is value in experiments which find out how these impurities form, are removed and more importantly prevented in order to keep the materials as simple as possible.

3.1. The effect of temperature on the production of "A15" Cs_3C_{60} in liquid methylamine

This section explores an alternative method of synthesis for "A15" Cs_3C_{60} from a Cs_3C_{60} precursor. The synthesis performed by Ganin *et.al*. 2008 utilised stoichiometric amounts of Cs and C_{60} which have markedly different levels of solubility. For example sodium metal saturates at 17.5 mole % metal in ammonia whereas C_{60} is insoluble.[10, 27] This gives rise to heterogeneous reaction conditions in which a powerful reducing agent can easily over-reduce the fullerene past the C_{60}^{3-} charge state as it dissolves on reaction.

Due to the large increase in solubility for C_{60}^{n-} (n= 1 to 3) in liquid amines, shown by the generation of a red solution, it was thought that a Cs_3C_{60} precursor could take advantage of this. Rather than the reaction taking place between the alkali metal and fullerene it would then be between BCO and any under reacted fullerene. In addition to this is the fact that making a large amount of Cs_3C_{60} precursor allows for minimisation of weighing errors and changes between batches. This aspect should allow for a better comparability between different reactions as all samples begin from an identical source.

The utilisation of primary amine solvents and their success is rooted in the high solubility of alkali metals in the solvent producing a homogenous reductive medium.[28] This applies particularly to ammonia but all reactions involving this as a liquid are limited to the temperature range between -78 and -33 °C.[29] Alternatively vessels that can withstand ammonias pressure (8.5 Atm) at room temperature can be used.[29] Therefore the logical use of alkyl amine solvents, such as MA, which maintains the desirable aspects of ammonia coupled with a wider temperature range (-93 to -6 °C) and lower pressure (in a sealed vessel at room temperature) of 2.9 Atm. These types of solvents give comparable and in some cases better results than the vapour phase methods particularly when the larger alkali metals are involved.[5, 6, 12, 16]

3.1.1. Method: Synthesis of Cs_3C_{60} precursor

Cs_3C_{60} is not only sensitive to air and moisture but also to any magnetic impurities that may be present in the reactants when purchased. High quality

caesium ingot (>99.95 %) was purchased to ensure only Cs was intercalated. This is important as if there is an impurity from another alkali metal this could affect the T_c of the product.[16] In particular impurities in fullerene solids can give magnetic contributions when measuring samples which could obscure the magnetic properties of the product and are removed by sublimation under dynamic vacuum in a furnace.

Fullerene (2.0 g, 2.78 mmols) was ground into a fine powder with a pestle and mortar then put into a silica ampoule (18 mm) in an argon glove box. The ampoule was connected to a tap and attached onto a dual vacuum line. The ampoule was then placed inside a clamp furnace with the sample in the centre. The connections were then evacuated to low vacuum (10^{-1} mbar) and foil placed around the exposed glass to prevent the polymerisation of the fullerene in light. The argon atmosphere in the ampoule was then released under low vacuum (10^{-1} mbar) and the furnace program started (RT---> 5°C/min, 550 °C, 24hrs--->5 °C/min, RT). Once complete the sublimed fullerenes were taken, under vacuum, into an argon filled glove box where the end of the ampoule was cut off, the fullerene material removed, ground and stored in a brown glass bottle.

For the solid state synthesis of Cs_3C_{60}, fullerene powder was loaded into the bottom of a silica ampoule (12 mm) with a neck using a glass funnel (Table 3.1). Caesium metal was then loaded into a silica glass insert (8 mm) and slid into place on top of the fullerene supported by the neck in the glass ampoule. The ampoule was then sealed under vacuum and put into a furnace for annealing at 350 °C. Once complete the ampoule was opened inside an argon glove box and ground using a pestle and mortar. The product was then resealed in a silica ampoule (8 mm) and annealed at 300 °C (Table 3.2). The material was then ground in an argon glove box before being analysed using microanalysis and powder x-ray diffraction to determine its composition (Figure 3.2, Tables 3.3 and 3.4).

Table 3.1 Reactant masses, annealing program and recovered mass for the innitial Cs_3C_{60} solid state precursor.

Sample	Mass of Cs /mg	Mass of C_{60} /mg	Annealing program	Mass recovered / mg
AM6_1	297.1	538.9	RT--> 2 °C/min, 350 °C, 18 hrs-->5 °C/min, RT	788.0
AM32_1	296.3	536.6	RT--> 2 °C/min, 350 °C, 18 hrs-->5 °C/min, RT	809.5

Table 3.2 Mass of material loaded, final annealing protocol and end masses for the Cs_3C_{60} solid state precursor.

Sample	Mass of Cs_3C_{60} /mg	Annealing program	Mass recovered /mg
AM6_2	780.9	RT--->2 °C/min, 300 °C, 48 hours--->5 °C/min, RT	770.4
AM32_2	803.1	RT--->2 °C/min, 300 °C, 48 hours--->5 °C/min, RT	801.4

Table 3.3 Microanalysis results for the precursors used for the Cs_3C_{60} precursor.

Sample ID	% C	% H	% N	Composition
Theoretical	64.35	x	x	Cs_3C_{60}
AM6_2	65.35	x	x	$Cs_{2.9}C_{60}$
AM32_2	63.94	x	x	$Cs_{3.05}C_{60}$

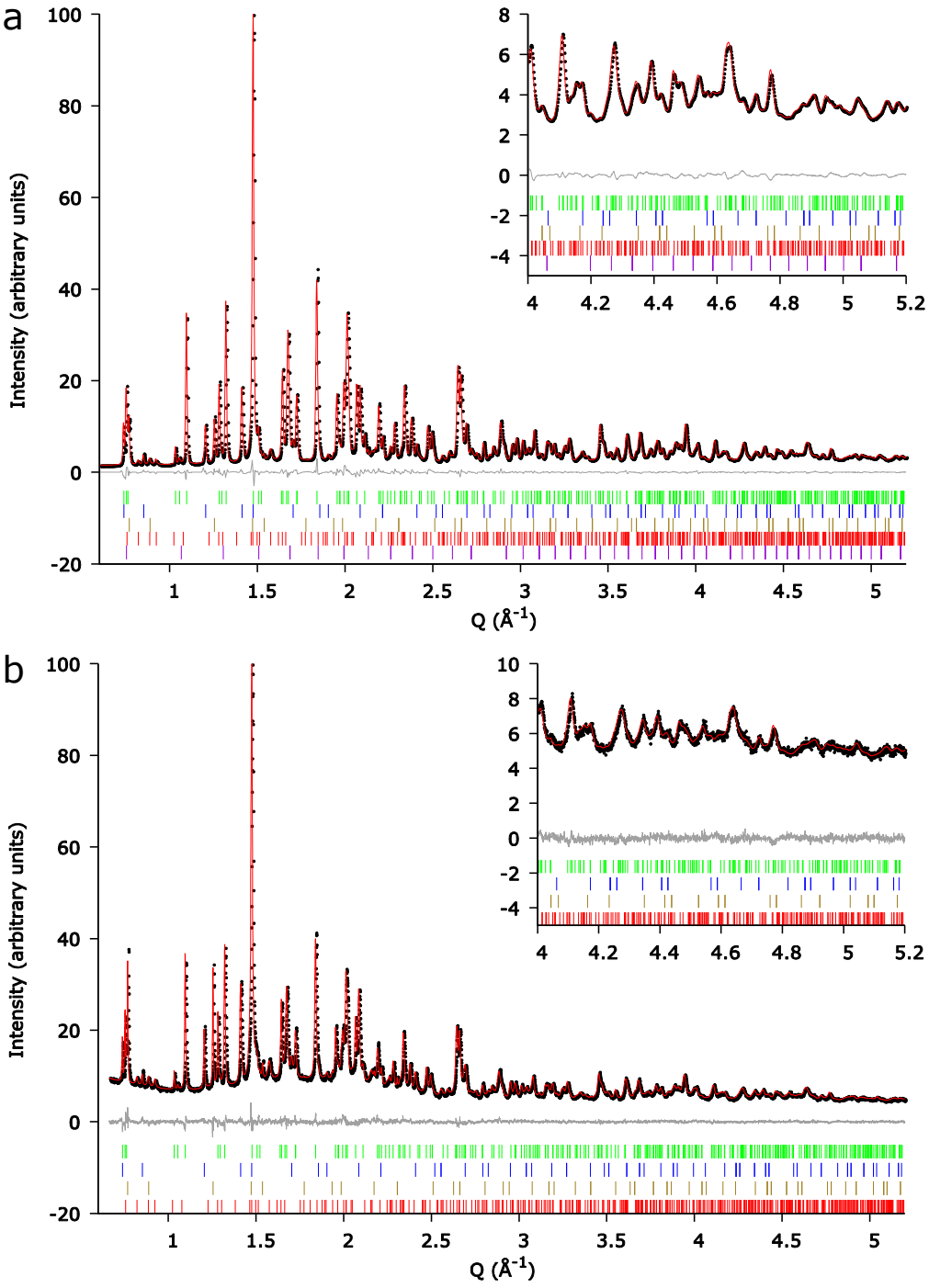

Figure 3.2 Rietveld plots for the two precursors where the structural models were refined against synchrotron powder x-ray data. Observed (black dots) and calculated (red line) data of the room temperature synchrotron powder X-ray diffraction pattern. The tics represent Bragg reflection positions of the BCO (green), FCC (blue), C_{60} (olive), Cs_1C_{60} (red) and Cs_6C_{60} (dark violet) phases. (a) The material was synthesized with the nominal composition $Cs_{3.0}C_{60}$ and given the designation AM6_2. The wavelength was λ = 0.826403 Å. (b) The material was synthesized with the nominal composition $Cs_{3.0}C_{60}$ and given the designation AM32_2. The wavelength was λ = 0.819315 Å.

Table 3.4 Details from the Rietveld refinement of the data displayed in Figure 3.8.

Parameter \ ID	*AM6_2*	*AM32_2*
R_{wp} (%)	2.90	3.44
R_{exp} (%)	1.97	1.09
λ (Å)	0.826403	0.819315
BCO (%)	42.2(3)	58.6(4)
FCC (%)	11.8(1)	11.1(1)
Cs_1C_{60} (%)	20.5(3)	13.2(5)
C_{60} (%)	25.5(3)	15.9(3)
Cs_6C_{60}	0	1.2(1)
FCC V per C_{60} ($Å^3$)	802.73(5)	802.27(6)
FCC xrd composition	$Cs_{2.99(1)}C_{60}$	$Cs_{2.93(1)}C_{60}$

3.1.2. Method: Synthesis of Cs_3C_{60} using MA

Due to the hazardous nature of pressurised vessels containing liquid methylamine the described five reactions were performed one at a time. The following reaction protocol was repeated for each of the five samples and the exact masses used given in table 3.5. The independent variable investigated was the liquid phase reaction temperature. This was varied between -40 and 40 °C at 20 °C intervals giving five different temperatures (the -40 °C sample was repeated for variable temperature diffraction experiments) at which the solution reaction was performed.

Precursor Cs_3C_{60} (90 mg, 0.080 mmol) and a glass stir bar were loaded into a medium wall reaction vessel (calibrated with respect to volume) using a glass funnel in an argon filled glove box (Table 3.6). The reaction vessel was then sealed, taken out of the argon glove box and put onto a dual vacuum line via a manifold with two greaseless ball joints using Calrez o-rings. A storage vessel containing anhydrous MA (drying procedure described in chapter 2) was then connected in parallel to the reaction vessel and the vacuum manifold was evacuated to high vacuum (10^{-5} mbar) using a Leybold turbo-molecular pump system. The manifold was then closed to the high vacuum, opened to low vacuum and the argon atmosphere released from the reaction vessel.

After low vacuum was established the manifold and reaction vessel were evacuated to high vacuum. Once high vacuum was attained a low temperature bath, prepared by using iso-propanol and dry ice (-78 °C) or a Huber cold finger (set to -78 °C), was placed around the reaction vessel. To facilitate the re-condensation procedure an iso-propanol bath at room temperature (22 °C) was placed around the MA storage vessel. The manifold was then closed to the vacuum lines and the MA vessel slowly opened to start the condensation of MA into the reaction vessel. At this point the stir function (300 rpm) of the hotplate was activated. Once the MA (37 ml) had condensed, the vessels were closed to the manifold which was then evacuated to high vacuum and the baths removed.

The first reaction vessel was warmed from -78 °C to -40 °C; the second reaction to -20 °C; the third reaction to 0 °C; the fourth to 20 °C and the fifth was heated to 40 °C. These experiments used an appropriate bath with either a hotplate and thermocouple pair or the Huber cold finger as a temperature control. The reaction solution was allowed to continue stirring for 1 hour at which point the low temperature bath was placed around the MA vessel. The manifold was then evacuated to high vacuum and closed before the reaction vessel was slowly opened (but not fully) and the MA vessel which was opened completely. This allowed the re-condensation of the MA to begin and the rate of evaporation controlled by the reaction vessels' tap and the set temperature. Once all liquid MA was removed the manifold and reaction vessel were evacuated to low vacuum (10^{-1} mbar) and the reaction vessel then taken to an argon filled glove box where the material was removed and reground.

Table 3.5 Summary of reaction masses and temperatures used.

Sample ID	Mass of precursor / mg	Precursor ID	Reaction temperature/ °C
AM19_1(-40°C)	90.0	AM6_2	-40
AM40_1(-40°C)	90.4	AM32_2	
AM16_1(-20°C)	90.4	AM6_2	-20
AM18_1(0 °C)	90.5	AM6_2	0
AM17_1(20°C)	90.8	AM6_2	20
AM36_1(40°C)	91.4	AM32_2	40

The recovered Cs_3C_{60} (exact masses for each sample are in Table 3.6) were loaded into separate silica ampoules (8 mm) which were then closed using

a Young's tap and attached to a dual vacuum line. The ampoule was then placed inside a tube furnace with the sample in the centre and secured by a clamp. The line and attachments were all evacuated to high vacuum after which the line was switched to a rotary pump and the argon atmosphere was removed from the ampoule. Once low vacuum was re-established the tube furnace was run with the program RT---> 5°C/min, 120 °C---> 5°C/min, 120 °C, 1hrs--->5 °C/min, RT (Table 3.6). As the MA was removed from the sample the pressure initially increased but after 40 minutes low vacuum was restored and at this point the sample was taken to high vacuum. Once the program was completed the sample was taken to an argon glove box, removed and reground.

This material was analysed using powder synchrotron x-ray diffraction by sealing 5-9 mg of material in glass capillaries under argon for the experiments. The wavelengths for the experiments are given in the tables containing appropriate Rietveld refinement data. Due to time constraints AM40_2 was not measured.

Table 3.6 Summary of masses and annealing protocols for removing MA from the as made product using MA as the solvent. Annealing program was done using dynamic high vacuum ($1x10^{-5}$ mbar).

Sample ID	Mass used/ mg	Annealing program
AM19_2(-40°C)	42.5	RT→5 °C min^{-1}, 120 °C, 2 hrs→5 °C min^{-1}, RT
AM40_2(-40°C)	35.8	
AM16_2(-20°C)	36.1	
AM18_2(0 °C)	44.2	
AM17_2(20°C)	55.6	
AM36_2(40°C)	40.4	

The recovered material (exact masses for each sample are in Table 3.7) was put into a silica ampoule (4 mm) and sealed under helium gas (300 mbar) on a dual vacuum line. The ampoule was then put into an oven on the following program: RT--->5 °C/min, 180 °C, 48 hrs--->5°C/min, RT (Table 3.7). Once the program was finished it was taken to an argon glove box where the material was removed and reground.

This material was analysed using powder synchrotron x-ray diffraction by sealing 5-9 mg of material in glass capillaries under argon for the experiments. The wavelengths for the experiments are given in the tables containing appropriate Rietveld refinement data.

Table 3.7 Summary of reaction masses, annealing protocols and recovered masses for the final annealing step in the synthesis of Cs_3C_{60} using MA as the solvent.

Sample ID	Mass used /mg	Annealing program	Mass recovered/ mg
AM19_3(-40°C)	35.6	RT→5 °C min^{-1}, 180 °C, 48 hrs→5 °C min^{-1}, RT	31.5
AM40_3(-40°C)	29.4		25.1
AM16_3(-20°C)	29.6		25.4
AM18_3(0 °C)	37.7		36.1
AM17_3(20°C)	48.5		46.7
AM36_3(40°C)	30.4		25.3

3.1.3. Solution phase reaction temperature dependence of the "A15" polymorph in methylamine.

The reaction in MA is a very crucial step in the synthesis of the target material and can be investigated by controlling the reaction temperature. By varying the temperature between -40 and 40 °C the amount of Cs_3C_{60} formed during the reaction can be controlled. Qualitatively from the patterns obtained after the initial annealing protocol the increase in the "A15" polymorph becomes clear after heating the solution past 0 °C (Figure 3.3). The quantity of the "A15", BCO and Cs_1C_{60} phases are in each of the materials is then dependent on the solution reaction temperature (Figure 3.3 and Table 3.8). What is less clear and requires Rietveld analysis is the FCC phase which exhibits large changes in its full width at half maximum (FWHM) as the reaction temperature is increased (Table 3.8). This indicates that it is the crystallinity of the FCC phase that is affected by reaction temperature rather than its fraction.

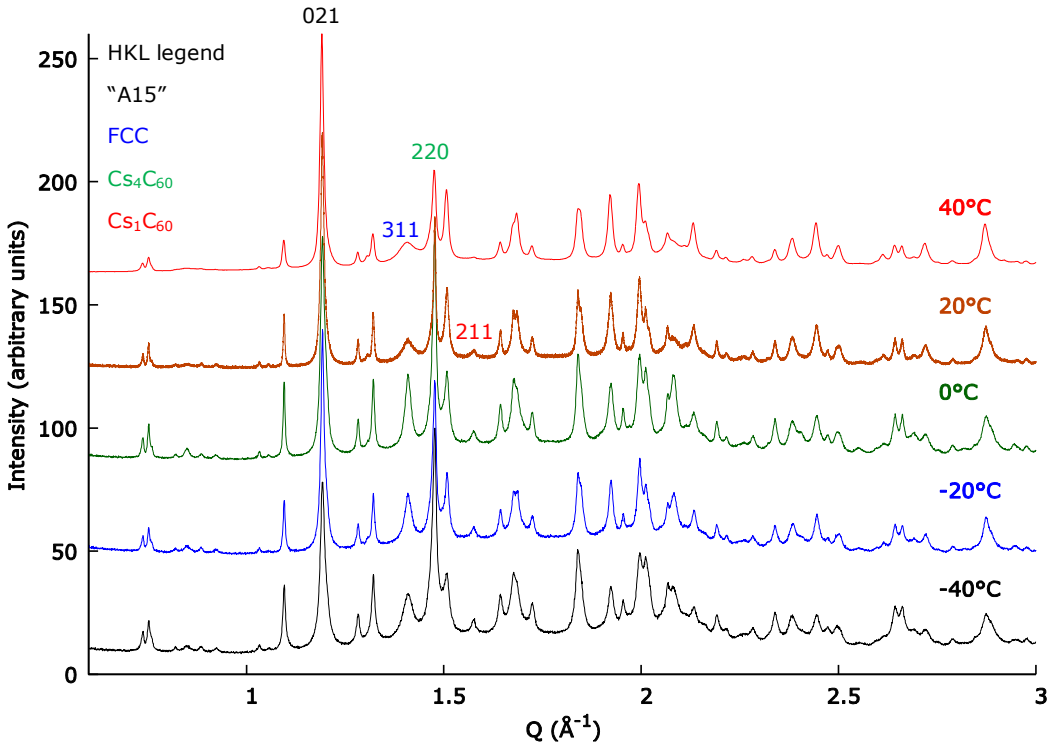

Figure 3.3 Synchrotron x-ray patterns after the first annealing step under dynamic vacuum. The materials are designated the names AM19_2(-40 °C), AM16_2(-20 °C), AM18_2(0 °C), AM17_2(20 °C) and AM36_2(40 °C). The Rietveld analysis of the data is tabulated in Table 3.8. A typical refinement is shown in appendix B figure 8.1.

Table 3.8 Refinement details produced from the analysis of the diffraction experiments done on samples AM16_2-AM19_2 and AM36_2.

ID / Parameter	AM19_2	AM16_2	AM18_2	AM17_2	AM36_2
Reaction temperature T (°C)	-40	-20	0	20	40
Solvent removal protocol	RT→5 °C min^{-1}, 120 °C, 2 hrs→5 °C min^{-1}, RT				
R_{wp} (%)	2.34	2.27	2.17	3.42	1.75
R_{exp} (%)	1.44	1.66	1.43	2.83	1.09
λ (Å)	0.8264	0.8264	0.8264	0.8264	0.81932
"A15" (%)	26.1(2)	36.9(2)	32.7(2)	45.7(1)	44.9(2)
BCO (%)	35.3(2)	30.1(1)	33.2(2)	26.5(1)	25.5(2)
FCC (%)	23.2(2)	19.8(1)	22.8(2)	17.9(1)	25.6(2)
Cs_1C_{60} (%)	15.4(2)	13.2(1)	11.3(1)	9.9(1)	4.0(1)
"A15" *V per C_{60}* ($Å^3$)	816.72(7)	816.08(6)	816.28(5)	816.84(2)	818.08(4)
BCO *V per C_{60}* ($Å^3$)	829.35(5)	828.74(5)	828.62(4)	829.08(2)	830.22(4)
FCC *V per C_{60}* ($Å^3$)	807.6(1)	806.08(8)	806.69(7)	806.62(9)	809.4(2)
Cs_1C_{60} V per C_{60} ($Å^3$)	660.0(2)	659.9(2)	659.5(1)	661.8(2)	660.2(4)
"A15" xrd composition	$Cs_{2.77(2)}C_{60}$	$Cs_{2.91(1)}C_{60}$	$Cs_{2.91(1)}C_{60}$	$Cs_{2.921(5)}C_{60}$	$Cs_{2.928(8)}C_{60}$
FCC xrd composition	$Cs_{2.95(1)}C_{60}$	$Cs_{3.00(2)}C_{60}$	$Cs_{3.00(1)}C_{60}$	$Cs_{3.00(1)}C_{60}$	$Cs_{3.00(2)}C_{60}$

Although quantitative analysis of the material after annealing at 120 °C generally agrees with the qualitative assessment it gives a convoluted picture (Table 3.8). The relationships between the phases are masked by the overlap between the FCC and BCO phases coupled with the large range of broadening observed for the FCC peaks. With only one unique reflection for the FCC material (HKL:311 at a Q spacing of 1.411 $Å^{-1}$) and at most 25 % of this phase present means that the low crystallinity of this phase in some of these samples can be quite a problem. This problem is overcome by improving the crystallinity of the material through a second stronger annealing protocol at higher temperatures for longer periods of time. This further annealing then enables more accurate conclusions to be drawn from the data.

The data obtained from the second annealing protocol (Figure 3.4) proves to be more decisive and retains the qualitative trend observed in figure 3.8. By increasing the initial reaction temperature from -40 to 40 °C the amount of the "A15" polymorph increases by 25 %. This increase is coupled with a decrease in both the BCO and Cs_1C_{60} by 15 % and 11 % respectively (Figure 3.5 a. and Table 3.9). Interestingly the variation in phase fractions of the FCC polymorph only differs slightly throughout the experimental series. Therefore reaction in MA at higher solution phase reaction temperatures increases the reaction between Cs_1C_{60} and BCO producing higher "A15" fractions (Figure 3.5 a. and Table 3.9). The recombination of Cs_1C_{60} and BCO on exposure to MA was hypothesised in connection to our previous work in producing high quality FCC samples.[6] The same effect is demonstrated here for the production of the "A15" majority materials.

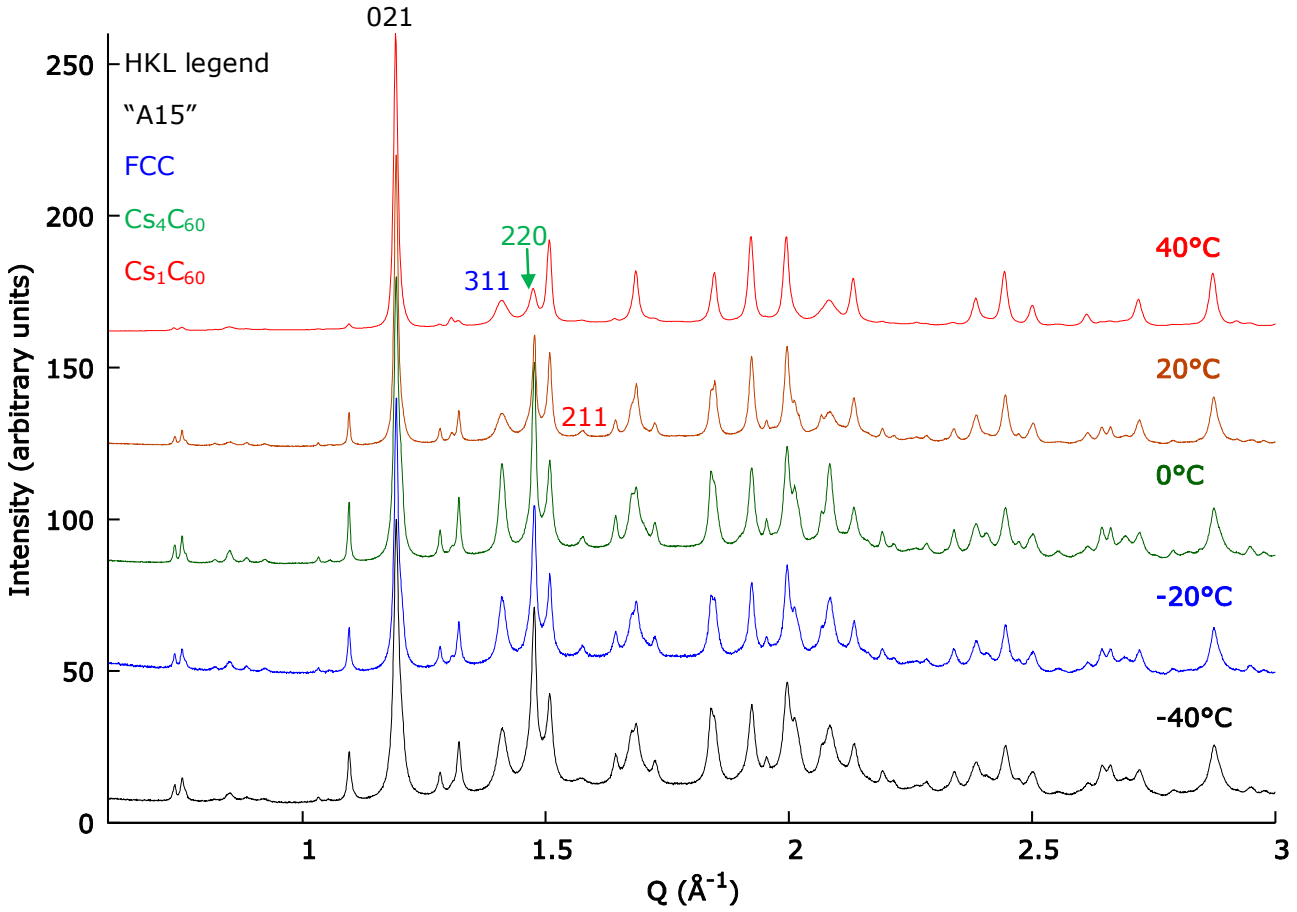

Figure 3.4 Synchrotron x-ray patterns after the final annealing step under 300 mbar pressure of He. The materials are designated the names AM19_3(-40 °C), AM16_3(-20 °C), AM18_3(0 °C), AM17_3(20 °C) and AM36_3(40 °C). The temperature in brackets indicates the temperature at which the solution phase reaction was carried out at. The Rietveld analysis of the data is tabulated in Table 3.9 and shown graphically in Figure 3.5. A typical refinement is shown in appendix B figure 8.2.

The experimental conditions have been analysed with respect to phase assembly but the volumes and compositions of the Cs_3C_{60} phases are also of interest. To interpret the effect of the conditions on the phases themselves the refined compositions and volumes must be taken into account. The superconducting properties of these materials have been strongly linked to inter-fulleride separation; a parameter which is dependent on the composition. The caesium ion composition does not vary by a significant amount across the whole experimental range for all phases. The "A15" material has an average composition of $Cs_{2.86(2)}C_{60}$ which is identical to the published value of $Cs_{2.85(1)}C_{60}$ (Figure 3.5 (b)).[5] The FCC composition has an average of $Cs_{2.97(1)}C_{60}$ which is slightly larger than published value of $Cs_{2.901(6)}C_{60}$ but still comparable.[6] This demonstrates that the experimental methods used here are effective and the results comparable to published material.

The inter-fulleride separation of these materials could also have a dependency on the methods utilised to synthesis them. This is best investigated by analysis of the cell volumes produced from refinement of a structural model against synchrotron x-ray data. Unlike with the compositions, the cell volumes, normalised per C_{60}, show an interesting variation throughout the experimental series. A significant jump in cell volume is observed for all phases in samples which have been reacted above 0 °C in the solution phase. At -40 °C the "A15" volume is 816.31(5) $Å^3$ per C_{60} this increases to a final volume of 817.36(7) $Å^3$ per C_{60} at 40 °C. This jump in cell volume brings the 20 and 40 °C material up to a more comparable volume to what has been published using the $3Cs+C_{60}$ method.[5] The increase in cell volume is not linked to a change in composition for those phases in the samples exhibiting it (those prepared at 20 and 40 °C) (Figure 3.5 (c), (d) and Table 3.9). Since the annealing protocols are identical for all samples the only conclusion is that the variation in solution phase reaction temperature is responsible.

The experiments have also allowed the assessment of the solid state precursor as a starting material for the production of "A15" rich material. Compared to the "A15" rich material produced by Ganin et. al. using stoichiometric amounts of caesium metal and fullerene powder the use of a solid state precursor results in inferior material. This inferiority is based upon the 27 and 13 % (Figure 3.5 and Table 3.9) lower phase fraction of "A15" material generated by the 20 and 40 °C samples compared to the best published figures.[5] Future reactions aiming to produce high quality material should, therefore, sacrifice the added precision afforded by a large precursor in favour of higher fractions of the target phase.

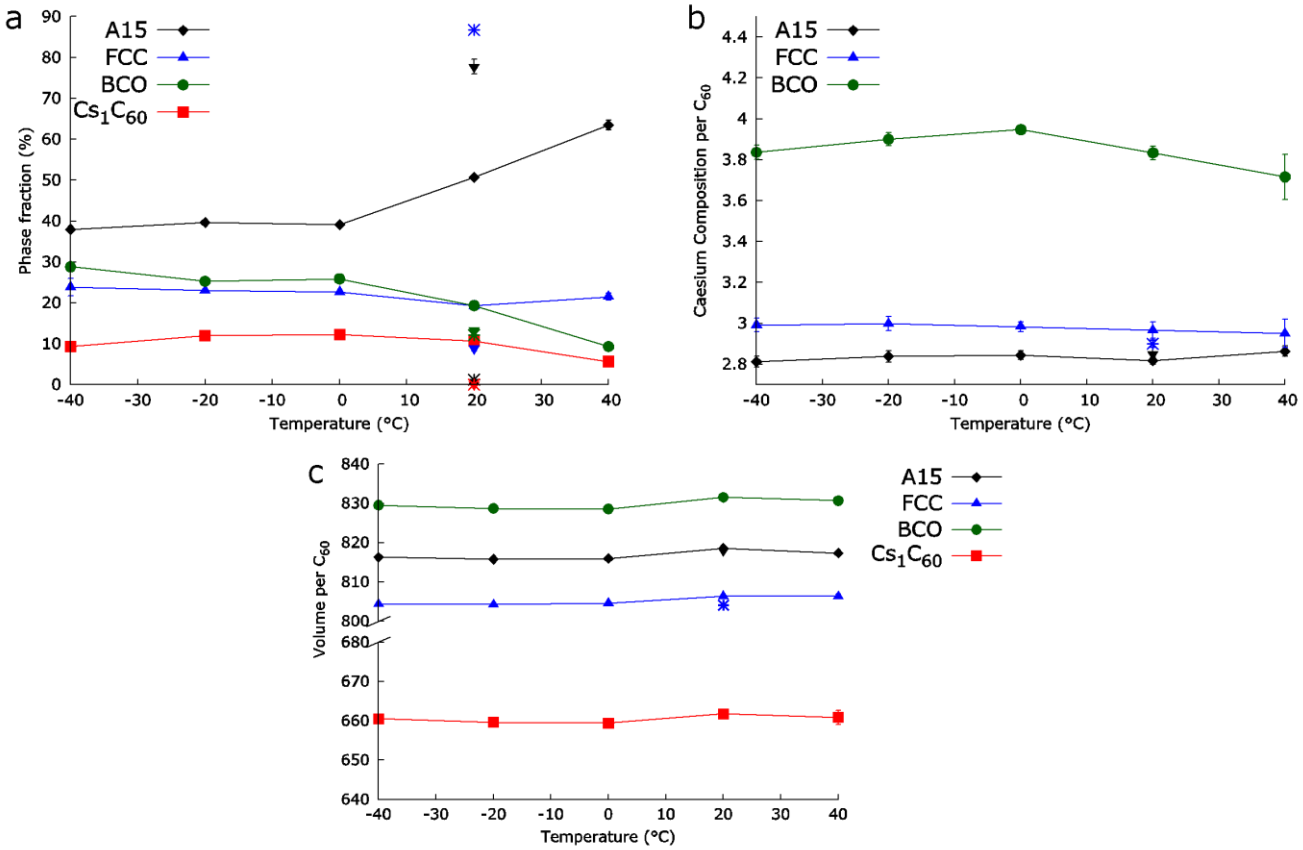

Figure 3.5 The dependency of selected refined parameters against solution phase reaction temperature in the range of -40 to 40 °C is shown. The Rietveld refinements were done on samples produced after the second annealing step under 300 mbar of He. The star[6] and inverse triangle[5] points represent data taken from the literature the colours of the points match the legend. The error bars correspond to 3σ. (a) The development of the phase fractions for "A15", BCO, FCC and Cs_1C_{60}. (b) The refined caesium composition per C_{60}. The composition of Cs_1C_{60} was fixed at nominal due to its low fraction and poorly crystalline state. (c) The refined volumes per C_{60} for the "A15", BCO, FCC and Cs_1C_{60} phases.

Table 3.9 Refinement details produced from the analysis of the diffraction experiments done on samples AM16_3-AM19_3, AM36_3 and AM40_3. AM40_3 is a repeat of AM19_3 using the AM32_2 precursor for the purpose of performing VT experiments on material that was prepared at -40 °C.

ID / Parameter	AM19_3	AM40_3	AM16_3	AM18_3	AM17_3	AM36_3
Reaction temperature T (°C)	-40	-40	-20	0	20	40
Solvent removal protocol	RT→5 °C min^{-1}, 120 °C, 2 hrs→5 °C min^{-1}, RT					
Annealing protocol	RT→5 °C min^{-1}, 180 °C, 48 hrs→5 °C min^{-1}, RT					
R_{wp} (%)	2.14	3.63	1.8517	1.90778	2.35228	2.70028
R_{exp} (%)	0.50	2.85	0.62638	0.48047	0.53144	1.01633
λ (Å)	0.826400	0.399881	0.826400	0.826400	0.826400	0.819320
"A15" (%)	38.3(2)	38.3(4)	40.4(2)	40.91(15)	50.74(16)	63.48(40)
BCO (%)	24.4(2)	39.9(4)	24.7(2)	24.85(12)	19.39(12)	9.30(20)
FCC (%)	20.7(2)	10.1(4)	22.8(2)	22.11(11)	19.26(16)	21.51(30)
Cs_1C_{60} (%)	16.6(2)	11.8(2)	12.1(1)	12.13(10)	10.61(09)	5.71(30)
"A15" *V per C_{60}* ($Å^3$)	816.31(5)	816.2(1)	815.78(6)	815.95(5)	818.64(3)	817.36(7)
BCO *V per C_{60}* ($Å^3$)	829.56(5)	828.54(9)	828.77(5)	828.56(4)	831.58(4)	830.7(3)
FCC *V per C_{60}* ($Å^3$)	804.34(8)	804.7(5)	804.24(7)	804.59(5)	806.40(9)	806.4(2)
Cs_1C_{60} V per C_{60} ($Å^3$)	660.5(2)	658.8(3)	659.6(1)	659.4(1)	661.8(2)	660.9(6)
"A15" xrd composition	$Cs_{2.812(9)}C_{60}$	$Cs_{2.83(2)}C_{60}$	$Cs_{2.838(1)}C_{60}$	$Cs_{2.844(8)}C_{60}$	$Cs_{2.817(6)}C_{60}$	$Cs_{2.864(8)}C_{60}$
FCC xrd composition	$Cs_{2.99(1)}C_{60}$	$Cs_{2.89(7)}C_{60}$	$Cs_{3.00(1)}C_{60}$	$Cs_{2.984(8)}C_{60}$	$Cs_{2.97(1)}C_{60}$	$Cs_{2.95(2)}C_{60}$

3.1.3.1. Investigation of the annealing steps influence over the "A15" polymorph by variable temperature x-ray diffraction

The role of the MA solvent in this system was further investigated by the use of variable temperature (VT) synchrotron x-ray experiments that followed the ramping used in the annealing protocol. The experiments were done on the as made material from the two temperature extremes at -40 °C and 40 °C. The VT experiments were performed *in-situ* at a synchrotron powder x-ray diffraction beam line. The samples in question were loaded into glass capillaries (0.5 mm diameter) and heated whilst in the beam using a heat gun. The heat gun temperature was controlled by a digital controller which was set with the following protocol; RT→5 °C min^{-1}, 180 °C. Patterns were recorded at 5 °C intervals.

Qualitative and Rietveld analysis of the patterns collected for the -40 °C material show that the "A15" phase is missing (Figure 3.6 (a) and (b)). The variable temperature analysis shows that the system is static up until 60 °C at which point the "A15" fraction increases and the fractions of the non-Cs_3C_{60} phases decrease. This process is very rapid in-between the temperatures of 60-100 °C with a gradient of 0.55(4) % $°C^{-1}$ after which the rate of change of the "A15" phase fraction diminishes to 0.133(6) % $°C^{-1}$ (Figure 3.6 (b)). This may possibly indicate that a "sweet spot" for optimal annealing of "A15" rich materials lies between 60 and 100 °C. Observation of the "A15" cell volume as a function of temperature shows a general increase in line with a thermal expansion with no phase transitions (Figure 3.6 c). This coupled with the increase in phase fraction indicates that once formed the "A15" phase is stable with respect to the temperature range used and does not begin to decompose.

An important observation is that the phase fraction of the BCO phase also begins to decrease from 60 °C. The amount of BCO and Cs_1C_{60} phases decrease by 27.5 and 10 wt.% respectively on heating from room temperature to 180 °C. This is coupled with an increase in the phase fractions of the "A15" and FCC phases amounting to 33 and 5 wt.% respectively. This would seem to indicate that the BCO and Cs_1C_{60} were recombining to form Cs_3C_{60} material the majority of which is the "A15" polymorph. Due to the capillary being a closed system and the sample is the as made product there is solvent present.[5, 6] This solvent is then available to facilitate the reaction between BCO and Cs_1C_{60} generating

Cs_3C_{60} material. This effect of MA vapour on materials containing BCO is known for FCC rich systems and is demonstrated here for an "A15" system.[6]

The interplay between solution phase reaction temperature and annealing is more complex than was indicated by experiments in section 3.2.3. In both cases there is a possible link between BCO and the "A15" polymorph in which MA facilitates the conversion to "A15" on increasing temperature. The VT experiment can account for all of the produced "A15" Cs_3C_{60} produced in the reaction performed at -40 °C. Considering that there is no sign of "A15" material at the start of the experiment it is logical to conclude that the early stages of the annealing protocol are responsible for this quantity of "A15". As in this experiment the "A15" phase fraction was still increasing at the end of the heating protocol, it is possible that even greater fractions are possible. This then leaves the question: what is the role of the solution phase reaction temperature?

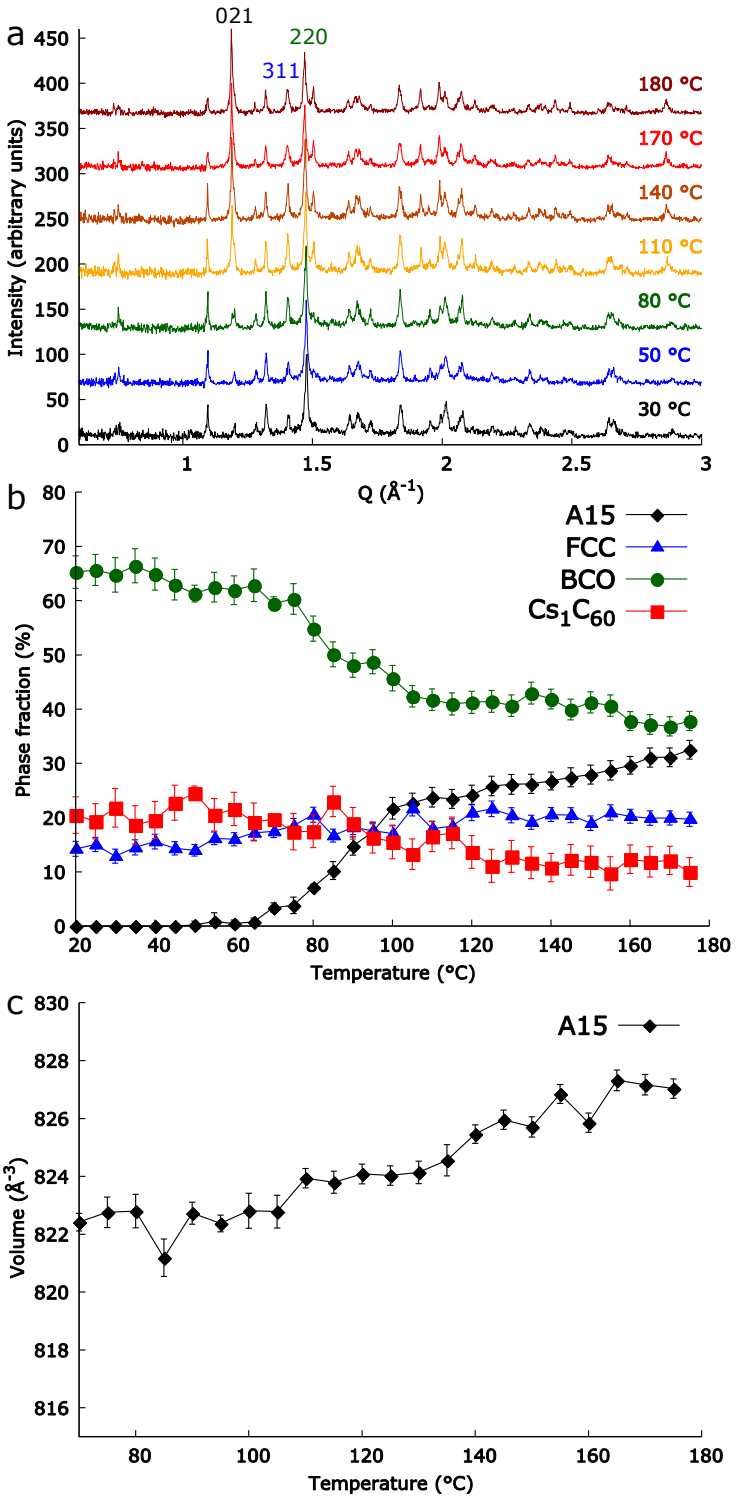

Figure 3.6 The powder x-ray patterns shown were recorded for the as made material AM40_1(-40 °C) which is a repeat of AM19_1(-40 °C). Parameters from Rietveld refinement of the structural models on the VT synchrotron data are graphically displayed in (b) and (c). (a) Gives examples of the variable temperature synchrotron patterns. The temperature at which the patterns were recorded is shown in the colour of the pattern on the right. (b) Shows the development of the phases on heating the as made material to 180 °C in a capillary. (c) Displays the increase in cell volume per C_{60} obtained from the "A15" phase as a function of temperature. A typical refinement is shown in appendix B figure 8.3.

The sample prepared at 40 °C is considerably different to that of the as made material prepared at -40 °C. At first there is no FCC material, however, on Rietveld refinement a broad hump corresponding to the 311 (Q 1.411 $Å^{-1}$) reflection is present at 25 °C and above (Figure 3.7 a). Unlike the material prepared at -40 °C the as made material prepared at 40 °C has an appreciable amount of "A15" present initially (26(2) %). In this case the system is static up to 80 °C and then increases at a steady rate up until 175 °C at which point it appears to level out at 53(2) % (Figure 3.7 b). As observed for the -40 °C material the cell volume of the "A15" material also shows no phase transitions within the annealing protocols temperature range (Figure 3.7 c). The analysis of the VT X-ray data reveals that the BCO and Cs_1C_{60} decreased by 30 % and 16 % respectively over the course of the experiment. Within the experiment the "A15" and FCC polymorphs increase by 26 % and 20 % respectively. As with the VT experiments on the material prepared at -40 °C there is a link between BCO and Cs_3C_{60} where upon the former is converted into the latter. There is however, one significant difference between the -40 and 40 °C prepared materials which is the initial presence of the "A15" polymorph in the 40 °C sample.

This VT experiment clarifies the role of both the temperature of the solution phase reaction and the subsequent annealing steps. The high reaction temperatures whist the material is in solution serves to crystallise "A15" material straight away. The annealing protocol then allows MA to facilitate the reaction of BCO and Cs_1C_{60} to form Cs_3C_{60} specifically the "A15" polymorph. This effect of MA is unusual and in the case of Cs_3C_{60} formed from ammonia favours the FCC polymorph.[6] There are two possible theories for this unusual behaviour; firstly it is possible that the effect of MA vapour on which Cs_3C_{60} polymorph is favoured is dependent on the amount of MA present. Secondly there could be some inherent difference between the materials produced using different solvents which could favour FCC and "A15".[6]

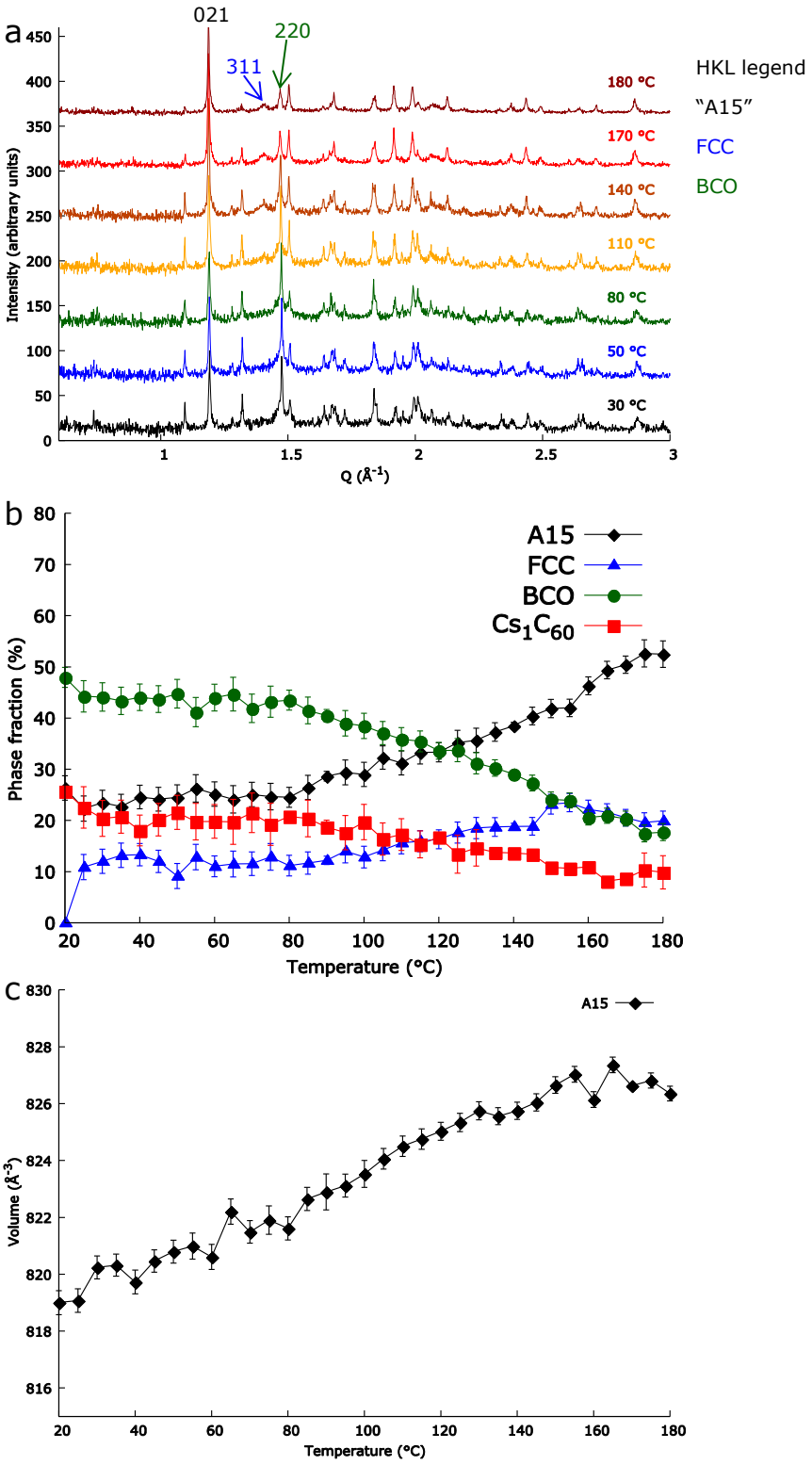

Figure 3.7 The powder x-ray patterns shown were recorded for the as made material AM36_1(40 °C). Parameters from Rietveld refinement of the structural models on the VT synchrotron data are graphically displayed in (b) and (c). (a) Gives examples of the VT synchrotron patterns. The temperature at which the patterns were recorded is shown in the colour of the pattern on the right. (b) Shows the development of the phases on heating the as made material to 180 °C in a capillary. (c) Displays the increase in cell volume per C_{60} obtained from the "A15" phase as a function of temperature. A typical refinement is shown in appendix B figure 8.4.

3.2. Synthesis of Cs_3C_{60} using Tetrahydrofuran

Due to the trend of increasing "A15" content with reaction temperature in MA not plateauing at 40 °C the possibility exists that if the solution could be heated further phase pure material could be achievable. We cannot heat our reaction in MA above 40 °C because the pressure of the solvent in a closed vessel becomes too great (6 Atm). Therefore other solvents with lower vapour pressures must be turned to. The use of THF opens up a new temperature range (-108 (melting point) to 66 °C (boiling point)) for synthesising A_3C_{60} compounds.[3]

The benefits of using an ether solvent with such a high boiling point are that it allows a wider variety of Schlenk procedures to be used. For example techniques such as anti-solvent precipitation, recrystallization and filtration become less hazardous and easier to accomplish. THF also adds much needed flexibility to the critical reaction step, in which C_{60} is first reduced, which allows for greater levels of control to be applied. Perhaps the most important aspect of using THF is that it is a good solvent for other one electron reducing agents that could moderate the reductive capability of Cs.[30] Before this additional flexibility can be capitalised on the new solvent needs to be investigated in its simplest form to gauge its applicability.

3.2.1. Method: Synthesis of Cs_3C_{60} in THF

Due to the use of multiple bulky glass vessels and the physical space needed to transfer anhydrous THF (drying method described in chapter 2) these experiments were performed one at a time.

The following reaction protocol was repeated for each of the samples and the exact masses used and conditions given in table 3.10 and 3.11. Caesium metal (32.0 mg, 0.241 mmol), sublimed C_{60} (59.6 mg, 0.0827 mmol) and a glass stir bar were loaded into a medium wall reaction vessel using a glass funnel in an argon filled glove box (Table 3.11). The reaction vessel was then sealed, taken out of the argon glove box and put onto a Schlenk line via PVC rubber tubing and using Viton o-rings. A storage vessel containing freshly distilled tetrahydrofuran (THF) was then connected in parallel to the reaction vessel. The equipment was then evacuated to high vacuum (10^{-5} mbar) and purged three times with purified argon gas. The solvent and reaction vessels were then opened to the rest of the line under a slight flow of inert gas.

PTFE greaseless keys were then replaced with rubber septa and a cannula (18 gauge) was then removed from an oven and purged through the septa with the inert gas for 3 minutes. Once the cannula was purged both ends were fully inserted into the vessels and THF (37 ml) was transferred into the reaction vessel by establishing a pressure difference. After the transfer the vessels were closed to the manifold which was then isolated and a water bath was then put into position to control the reaction vessels temperature. The reaction vessel temperature was held at one of three temperatures X °C (X= 20, 40, 60 °C) using a silicone oil bath with a hotplate and thermocouple (Table 3.10). The reaction solution was allowed to continue stirring for 1 hour. The manifold was then opened to low vacuum and the reaction vessel evacuated at Y °C (Y = 20 or 60 °C) with the solvent being isolated in an intermediate trap cooled by liquid nitrogen (Table 3.10). Once dry the manifold and reaction vessel were evacuated to low vacuum (x10^{-1} mbar), both vessels disconnected and the reaction vessel then taken to an argon filled glove box where the material was removed and reground (Figure 3.8).

The recovered Cs_3C_{60}·xTHF is loaded into an Pyrex ampoule (8 mm) which is then sealed using a greaseless tap and attached to a dual vacuum line (Table 3.11). The ampoule was then placed inside a tube furnace with the sample in the centre and secured by clamp. The line and attachments were all evacuated to high vacuum via low vacuum, after which the argon atmosphere was released from the ampoule under low vacuum. Once low vacuum was re-established the tube furnace was run with the program RT---> 5°C/min, Z °C, 15hrs--->5 °C/min, RT (Z = 180 or 350 °C) (Table 3.11). Once the program was completed the sample was taken to an argon glove box, removed and reground (Figure 3.8, Table 3.11).

a $$3Cs_{(s)} + C_{60(s)} \xrightarrow[X\ °C]{THF/Stirring} Cs_3C_{60}\cdot THF$$

b $$Cs_3C_{60}\cdot THF \xrightarrow[180\ °C,\ 15\ hours]{-THF} Cs_3C_{60}$$

Figure 3.8 (a) depicts the first part of the reaction of stoichiometric Cs and C_{60} in THF where X = 20, 40 and 60 °C. (b) depicts how the THF solvent is removed from the as made product under dynamic high vaccuum (5 x 10^{-5} mbar)

Table 3.10 Summary of reaction temperatures, masses used and recovered for the synthesis of Cs_3C_{60} in THF.

Sample ID	Mass of Cs/ mg	Mass of C_{60}/ mg	Recovered/ mg	Reaction temperature/ °C	Evaporation temperature/ °C
AM45_1(20°C)	33.0	59.6	72.4	20	20
AM159_1(40°C)	33.0	59.6	60.1	40	20
AM160_1(60°C)	33.0	59.7	57.8	60	20
AM158_1(60°C)	33.1	59.8	60.2	60	60
AM162_1(60°C)	32.9	59.6	58.3	60	60

Table 3.11 Summary of amounts used, recovered and the annealing protocol for Cs_3C_{60} samples made in THF.

Sample ID	Mass used /mg	Annealing program	Mass recovered/ mg
AM45_2(20°C)	55.3	RT→5 °C min^{-1}, 180 °C, 15 hrs→5 °C min^{-1}, RT	52.2
AM159_2(40°C)	60.1	RT→5 °C min^{-1}, 180 °C, 15 hrs→5 °C min^{-1}, RT	55.0
AM160_2(60°C)	57.8	RT→5 °C min^{-1}, 180 °C, 15 hrs→5 °C min^{-1}, RT	54.3
AM158_2(60°C)	60.2	RT→5 °C min^{-1}, 350 °C, 15 hrs→5 °C min^{-1}, RT	57.1
AM162_2(60°C)	58.3	RT→5 °C min^{-1}, 180 °C, 15 hrs→5 °C min^{-1}, RT	54.6

3.2.2. Solution phase reaction temperature dependence on the phase assembly of Cs_3C_{60} made in THF.

The use of THF produces an altogether different situation compared to that observed by liquid MA methods at 20 °C where not only the phase assembly is different but also the FCC Cs_3C_{60} material produced. As with the material synthesised using MA, altering the temperature at which the reaction occurs at produces interesting results. Once the reaction temperature exceeds 40 °C the "A15" polymorph is favoured (Figures 3.9 (a) and (b)). This has important implications for the scope of the experiments because not only does the phase assembly change but the total amount of Cs_3C_{60} phases drops overall. This system shows the same "A15" fraction dependency on temperature as the MA experiments where heating the reaction solution also promoted the formation of the "A15" phase. Interestingly the system shows no significant change between 40 and 60 °C indicating that any further improvements to the phase assembly is unlikely to occur without exceeding the boiling point of THF. The synthesis of Cs_3C_{60} in MA demonstrated that during the solution phase step heating could increase "A15" at the expense of the BCO and Cs_1C_{60}. In the synthesis of Cs_3C_{60} using THF "A15" and additional BCO is produced at the expense of the FCC polymorph.

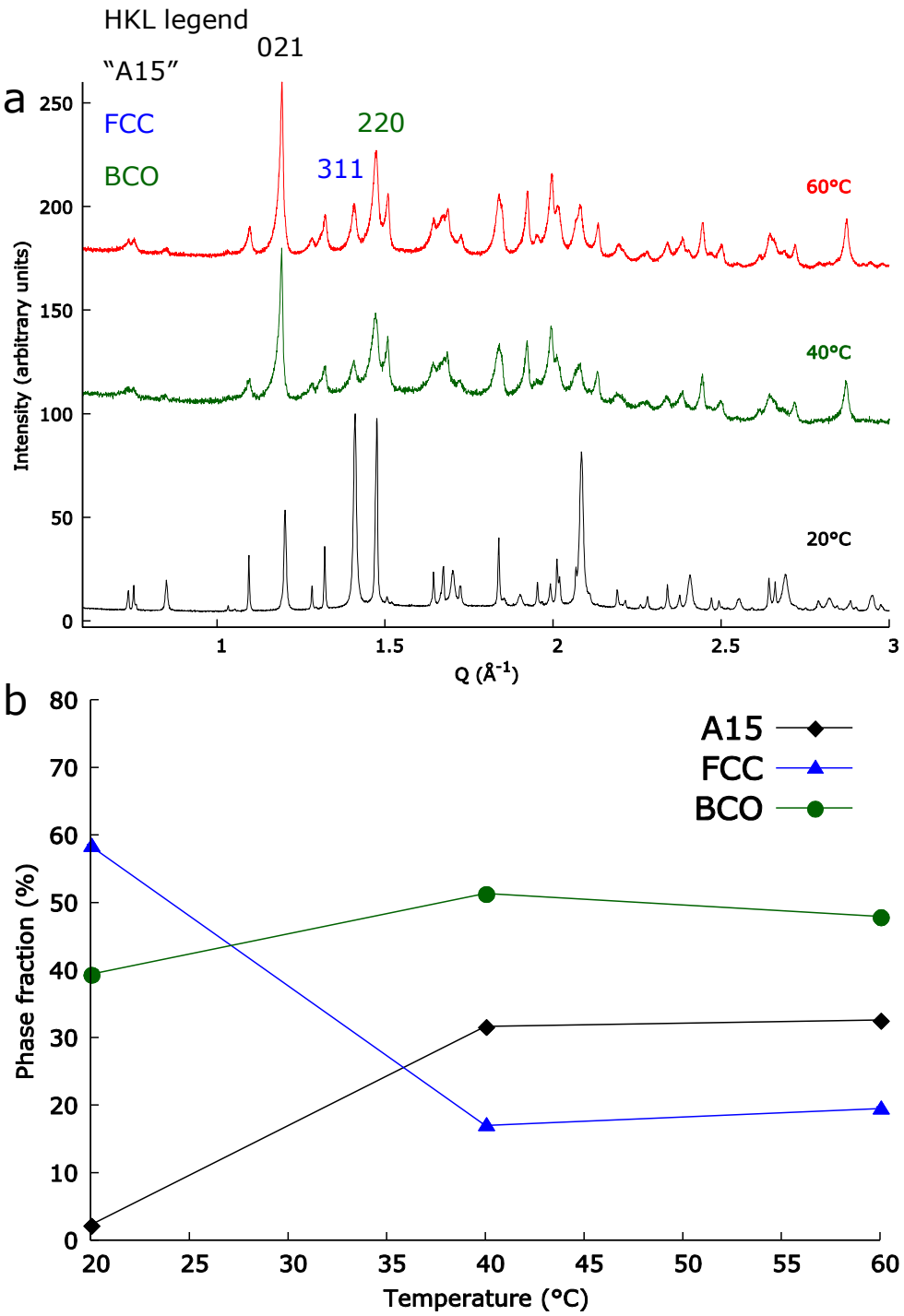

Figure 3.9 Shows the raw data and analysis for the samples AM45_2(20 °C), AM159_2(40 °C) and AM160_2(60 °C). (a) Reacting caesium and C_{60} in THF at temperatures of 20, 40 and 60 °C yields the above patterns. After completion of the subsequent annealing protocol they indicate that above 20 °C (reaction temperature) crystallisation of the "A15" polymorph is favoured over the FCC material. (b) Phase fractions as calculated from Rietveld refinement of the structural models against the collected data at the specified reaction temperatures. The error bars are contained within the data points. A typical refinement is shown in figure 3.12.

The main effect of evaporating the THF off at 60 °C is the much faster precipitation of the as made material when compared to removal at 20 °C. If the solvent removal occurs at 20 °C we obtain pattern (a) after annealing at 180 °C (Figure 3.10). Removal of the solvent at 60 °C results in a very different material shown in pattern (b) (Figure 3.10). The phase composition within this pattern conforms to a small amount of "A15", FCC, BCO plus a previously unidentified phase. This unknown phase cannot be indexed due to the small number of unique peaks available to calculate against. Due to the unknown phases contribution to the peak at 1.5 $Å^{-1}$ and the large background this pattern cannot be refined against. Quantitatively there is information in the large broadening of the 311 and 220 peaks of the FCC and BCO phases (Figure 3.10). It is therefore logical to assume that the rapid removal of the solvent caused the material to crystallise very quickly. The fast crystallisation therefore leads to the formation of small particles of product resulting in a huge amount of broadening. Annealing this material to 350 °C instead of the 180 °C used previously produces pattern (c) in figure 3.10 which is clearly recognisable as containing "A15", FCC and BCO without the unknown phase (Table 3.12). These samples indicate the importance of a controlled crystallisation step where the crystallites formed on evaporation have time to fully develop before annealing.

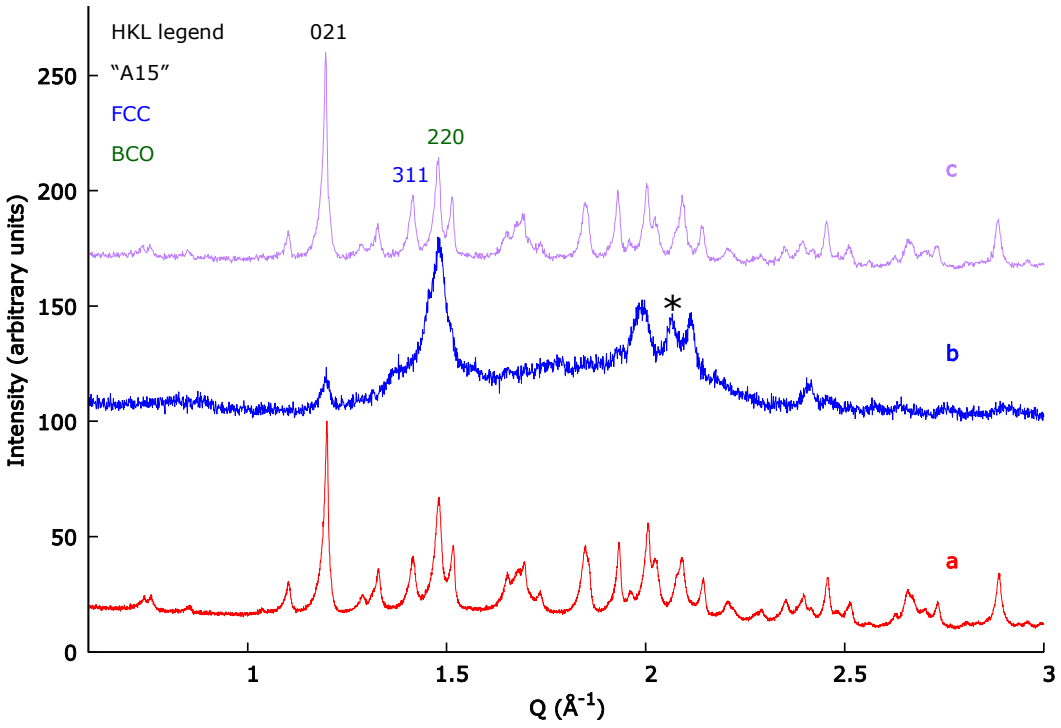

Figure 3.10 Comparison of patterns collected after annealing where the reaction temperature step was done at 60 °C. The material in pattern (a) (AM160_2) was cooled to 20 °C before the solvent was evaporated and the sample annealed at 180 °C. Pattern (b) (AM162_2) was produced from material that had its solvent removed at 60 °C and was annealed at 180 °C. The * represents the only non-overlapped peak of an unknown phase which is removed after annealing at 350 °C. The material that gave pattern (c) (AM158_2) had its solvent removed in the same manner as pattern b but was then annealed at 350 °C. A typical refinement is shown in figure 3.12.

Table 3.12 Refinement details produced from the analysis of the diffraction experiments done on samples AM45_2, AM158_2, AM159_2 and AM160_2.

Parameter \ ID	AM45_2	AM159_2	AM160_2	AM158_2
Reaction T (° C)	20	40	60	60
Evaporation T (° C)	20	20	20	60
Annealing T (° C)	180	180	180	350
R_{wp} (%)	3.44	3.22	3.41	6.26
R_{exp} (%)	2.45	2.76	2.72	5.84
λ (Å)	0.825000	0.709319	0.709319	0.709319
"A15" (%)	2.25(3)	31.7(3)	32.6(2)	40.0(5)
BCO (%)	39.40(21)	51.3(4)	47.9(2)	38.0(7)
FCC (%)	58.35(20)	17.0(3)	19.5(2)	22.0(6)
"A15" *V per C_{60}* (Å^3)	816.33(7)	816.06(9)	816.19(5)	815.4(1)
BCO *V per C_{60}* (Å^3)	829.31(3)	831.1(2)	830.79(7)	828.9(2)
FCC *V per C_{60}* (Å^3)	805.16(8)	808.0(2)	807.20(9)	802.8(2)
"A15" xrd composition	$Cs_{3.0}C_{60}$	$Cs_{2.82(3)}C_{60}$	$Cs_{2.84(1)}C_{60}$	$Cs_{3.00(4)}C_{60}$
FCC xrd composition	$Cs_{2.941(6)}C_{60}$	Cs_3C_{60}	Cs_3C_{60}	Cs_3C_{60}

3.2.2.1. Investigation of the annealing protocols effect on the phase assembly of BCO made in THF by variable temperature x-ray diffraction experiments

VT synchrotron experiments were used to probe the effects of annealing on the as made material. The VT experiments were performed *in-situ* at a synchrotron powder x-ray diffraction beam line. The samples in question were loaded into glass capillaries (0.5 mm diameter) and heated whilst in the beam using a heat gun. The heat gun temperature was controlled by a digital controller which was setup to record patterns at 25 °C intervals from 50 to 450 °C.

The as-made material produced from the reaction of stoichiometric amounts of caesium and fullerene powder is completely different to that observed for synthesis using liquid amines.[5, 6] Qualitatively no Cs_3C_{60}, BCO or Cs_1C_{60} phases were observed in material until the temperature reached 175 °C

(Figure 3.11 (a)). Beyond this temperature the material reached its end phase composition within the following 100 °C (Figure 3.11 (b)). During this 100 °C range the amorphous background between Q 1.25 and 1.75 $Å^{-1}$ is gradually removed. At the same temperature that the phase fractions settle out the amorphous background is completely gone supporting the idea that the phases are already formed and are crystallized by the annealing. This indicates that in the case of this reaction the role of the annealing step is to crystallize the material and remove solvent from its structure.

An interesting observation is that for the synthesis of Cs_3C_{60} using pure THF the stabilised phase fractions of the VT experiment are very different to that observed for the product after annealing under dynamic vacuum (Figures 3.11 (a) and (b), Table 3.13). Rietveld refinement of the material after the variable temperature experiment shows that for this material it is possible to obtain 70 % of the FCC Cs_3C_{60} phase. However, the material was annealed at 180 °C under dynamic vacuum and only 60 % of the product was the FCC polymorph (Figures 3.12 a, b and Table 3.13). Observing the change in phase fractions as a function of temperature shows that at 175 °C there is 63 % of the FCC phase present at this temperature. This indicates that in order to obtain the largest amount of FCC phase annealing temperatures should exceed 250 °C.

In terms of what is produced from this reaction the VT experiments suggest that it should be able to produce material with 70 % of the target charge state (C_{60}^{3-}). What is seen is that without the correct annealing protocol this cannot be reached. The use of THF as a solvent for the synthesis of Cs_3C_{60} materials is interesting as it strongly favours the FCC polymorph when reacted at room temperature. The VT experiment shows that the "A15" polymorph does not form at any of the investigated annealing temperatures. This reinforces the idea that the FCC polymorph is completely favoured for reactions done at room temperature. Unlike the reaction of the solid state Cs_3C_{60} precursor in MA there appears to be no link between annealing protocol and additional conversion of BCO into Cs_3C_{60}. The ability of some protocols to facilitate the conversion of BCO into Cs_3C_{60} has been observed in two different systems involving MA but not for a system utilising THF it is likely that this rejuvenating effect is closely linked to MA.[6]

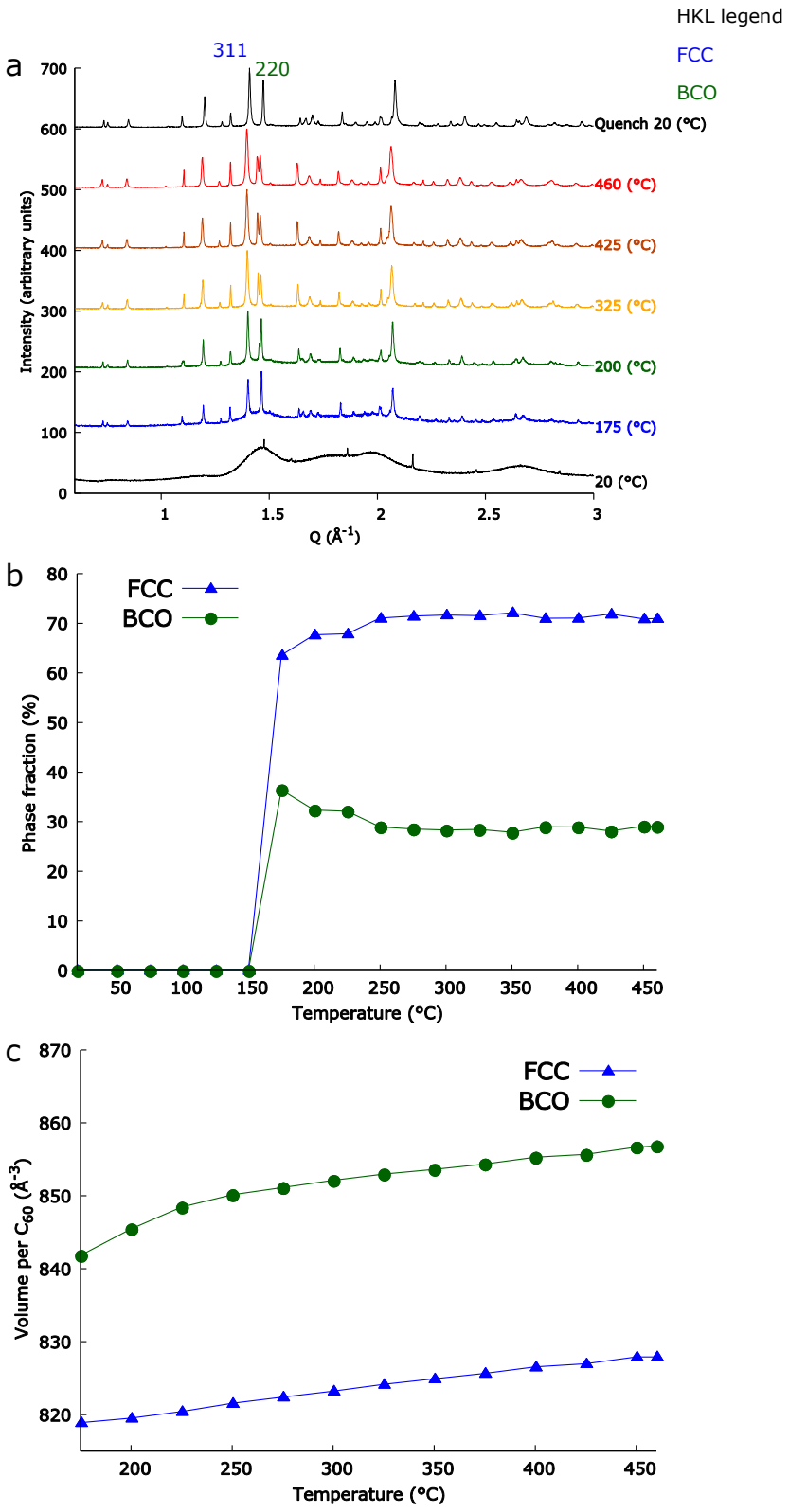

Figure 3.11 This shows the data and analysis of the VT experiment performed on AM45_1 as made material with a nominal composition of Cs_3C_{60}. (a) The evolution of crystalline phases from an amorphous pattern on heating as made material. Patterns between 20 °C and 175 °C are omitted as the material continues to be amorphous until 175 °C. (b) Gives the phase fraction results as a function of temperature to compliment the qualitative assessment. (c) Increase in cell volume as the VT experiment progressed.

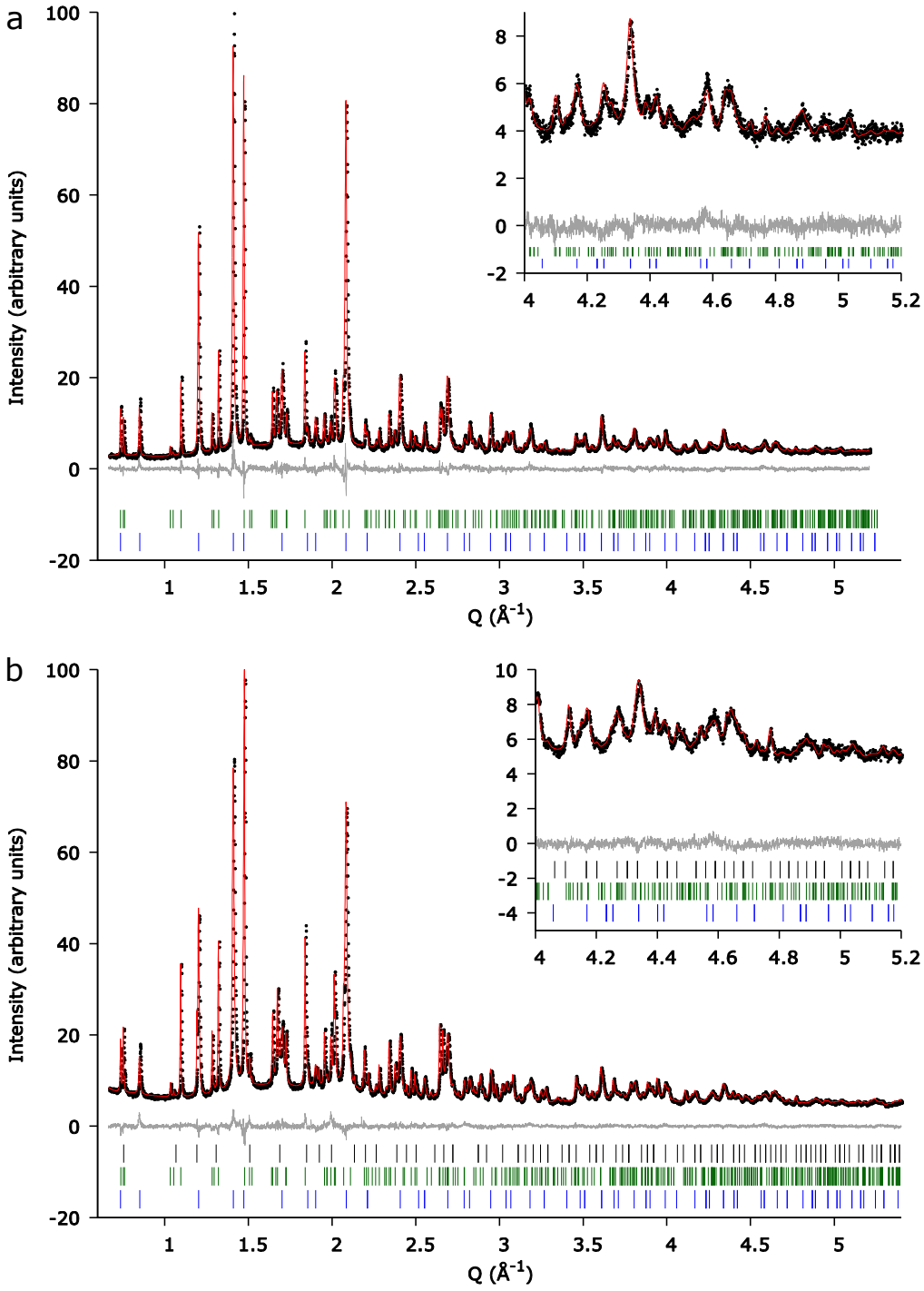

Figure 3.12 The Rietveld plots for the samples AM45_1(quenched after the VT experiment) and AM45_2(after annealing as per the method) which were synthesized with the nominal composition $Cs_{3.0}C_{60}$ using THF as the solvent. Where the observed (black dots), calculated (red line) and difference (grey line) and the ticks represent Bragg reflection positions of the BCO (green) and FCC (blue). The patterns were recorded at a wavelength of λ = 0.825000 Å and the refinement results shown in table 3.13. a. AM45_1 after quenching from 460 ° C to room temperature at the end of the VT diffraction experiment. b. AM45_2 which was produced after annealing AM45_1 as made material at 180 °C under dynamic vacuum.

Table 3.13 Refinement details produced from the analysis of the diffraction experiments done on samples produced from the THF synthesis as made material quenched after VT experiments and after annealing under dynamic vacuum.

ID / Parameter	*AM45_1*	*AM45_2*
Conditions	(VT)Quenched from 460 °C	Annealed as per method
R_{wp} **(%)**	5.63	3.44
R_{exp} **(%)**	3.91	2.45
λ (Å)	0.825000	0.825000
"A15" (%)	0	2.25(3)
BCO (%)	29.6(3)	39.40(21)
FCC (%)	70.4(3)	58.35(20)
"A15" *V per* C_{60} (Å^3)	0	816.33(7)
BCO *V per* C_{60} (Å^3)	831.35(6)	829.31(3)
FCC *V per* C_{60} (Å^3)	806.10(7)	805.16(8)
FCC xrd composition	$Cs_{2.897(7)}C_{60}$	$Cs_{2.941(6)}C_{60}$

Overall using THF in these reactions has three important points; firstly reactions at room temperature give very little "A15" but the potential (from VT experiments) for large amounts of FCC Cs_3C_{60}. Secondly THF does not promote the formation of Cs_3C_{60} to the same degree as MA or the combination of MA and ammonia (see section 3.2.).[5, 6] Thirdly the FCC material produced at room temperature has a considerably smaller volume per C_{60} than that produced by amine solvents both in this work and others.[5, 6]

Due the lower purity of materials made at temperatures which give larger cell volumes for the FCC material; there could be consequences for the superconducting properties that this material might display. These consequences could be lower shielding fractions or T_c which would impact negatively on the use of THF as a solvent for making Cs_3C_{60}. What can be taken advantage of is the ability of THF to selectively make FCC and not "A15", which has the potential to give high quality FCC materials. Before this property can be taken advantage of

two problems must be overcome; firstly low sample sizes and secondly over-reduction of C_{60}.

3.2.3. Investigation into the effect of scaling on the phase assembly of Cs_3C_{60} made in THF

For the application of THF for use as a solvent in favour of amine systems one very important obstacle must be dealt with. The amount of Cs_3C_{60} material previously produced (theoretical mass of 90 mg) by the THF method is not enough to ensure total characterisation. At the end of the experiments roughly 60 % of the Cs_3C_{60} material is recovered this leaves far too little material for all of the analytical steps. Considering that analysis of the magnetic and superconducting properties in a SQUID ideally takes up 30 mg of material that leaves just enough to ensure synchrotron x-ray patterns can be recorded. Ideally microanalysis, SQUID, x-ray diffraction (ambient, high pressure, low temperature and VT), Raman spectroscopy, solid state NMR and multiple annealing experiments would all be performed. Due to the exploratory nature and sub optimal phase assemble of the THF method thus far material has only been required for assessing the phase fractions using x-ray diffraction. The possibility of using THF to selectively make FCC material means that significant amounts of material will be required.

3.2.3.1. Method: Synthesis of Cs_3C_{60} in THF scaled by a factor of three.

Using the method outlined in section 3.3.1. a sample was scaled up by a factor of three (Table 3.14). The volume of THF (111 ml) and the reaction time (3 hours) were also increased by this factor to ensure that the concentration used was identical and the material was given enough time to react fully. Once the reaction had completed the reaction vessel was evacuated to low vacuum ($x10^{-1}$ mbar), the same level that was achieved in section 3.3.1. The material was then taken to an argon filled glove box, ground in a pestle and mortar before being loaded into a capillary for x-ray diffraction.

The three samples of as made Cs_3C_{60} (60 mg) were loaded into a Pyrex ampoule (8 mm) which is then sealed using a greaseless tap and attached to a dual vacuum line (Table 3.15). The line and attachments were all evacuated to high vacuum via low vacuum, after which the argon atmosphere was released from the ampoule under low vacuum. Once low vacuum was re-established the tube furnace was run with the programs described in table 3.15. Once the programs were completed the samples were taken to an argon glove box, removed and reground (Table 3.15).

Table 3.14 Summary of reaction temperatures, masses used and recovered for the synthesis of Cs_3C_{60} in THF.

Sample ID	Mass of Cs/ mg	Mass of C_{60}/ mg	Recovered/ mg	Reaction temperature/ °C	Evaporation temperature/ °C
AM44_1(20°C)	95.1	171.0	252.4	20	20

Table 3.15 Summary of amounts used, recovered and annealing protocols for Cs_3C_{60} samples made in THF at a 3x scale.

Sample ID	Mass used /mg	Annealing program	Mass recovered/ mg
AM44_3(20°C)	60.0	RT→5 °C min^{-1}, 180 °C, 15 hrs→5 °C min^{-1}, RT	56.2
AM44_2(20°C)	60.4	RT-->5 C/min, 180 C, 45 hrs-->5 C/min RT	52.3
AM44_4(20°C)	60.1	RT-->5 C/min, 250 C, 15 hrs-->5 C/min RT	57.6

3.2.3.2. Analysis of the effect of scaling up on Cs_3C_{60} material synthesised in THF

The scale was increased to three times that of the original reactions and the produced material was subjected to different annealing protocols to investigate its affects. The as made material shows an unusual reaction pathway which includes the formation of Cs_6C_{60} as well as BCO and FCC material (Figure 3.13). Unlike the synthesis of 90 mg of Cs_3C_{60} which forms amorphous material initially the scaled synthesis forms four crystalline phases. The presence of

Cs_6C_{60} directly points towards caesium initially over-reducing the fullerene before reacting further to form the C_{60}^{3-} charge state. The fact that this system has the potential to form C_{60}^{4-} and C_{60}^{6-} material demonstrates its complexity. Under the present conditions the scaled up synthesis fails to reproduce the results of the small scale reaction. The phase assembly after extensive annealing contains "A15", FCC and BCO and also sacrifices the apparent selectivity for FCC over "A15" at room temperature.

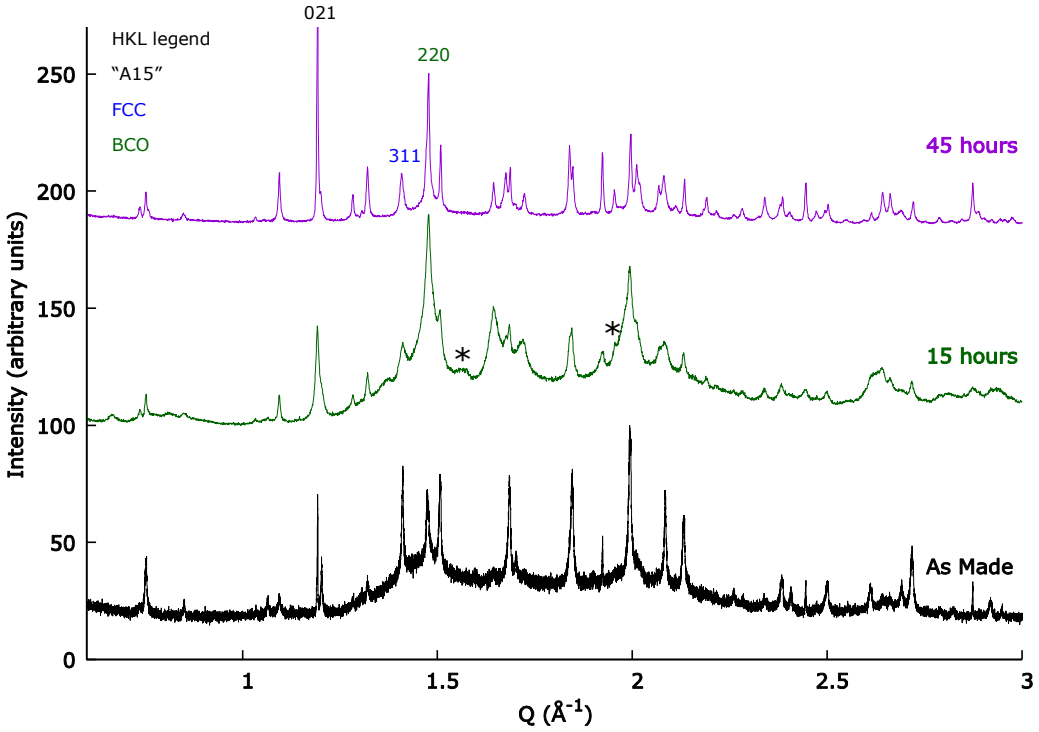

Figure 3.13 Observed patterns show the presence of crystalline phases at every annealing step. The labels correspond to the samples as follows where the text in the bracket is the total annealing time: AM44_1 (As Made), AM44_3 (15 hours) and AM44_2 (45 hours). The * represent the same unidentified phase as found in figure 3.10.

The increase in scale leads to the material requiring much longer annealing times than the smaller scale reaction in order to fully crystallise the final phase assembly. If the material is only annealed for fifteen hours at either 180 or 250 °C the large amorphous background remains but the Cs_6C_{60} phase is no longer present (Table 3.16, Figures 3.14, 3.15, 3.16 and 3.17). This indicates that the annealing protocol causes the Cs in Cs_6C_{60} to diffuse first forming additional BCO, FCC and "A15". This stage is missing in the small scale reaction and considering that the lower scale synthesis produces better material it can be stated that the formation of Cs_6C_{60} is undesirable.

In the case of the scaled up material, time is the most important factor to consider when obtaining the final material. Increasing the annealing time to 45 hours gives material which displays an x-ray pattern with comparable crystallinity to that of AM45_2. As observed in previous experiments the amorphous phase is transient and is removed after the full annealing protocol is applied. This means that rather than just removing the solvent from the material the annealing protocol must also facilitate the diffusion reaction of the Cs_6C_{60}. The requirement of additional annealing time to fully crystallise the material is therefore due to the additional step in which Cs diffuses out of the Cs_6C_{60} and into the more Cs deficient phases. Therefore the phase assembly found in material synthesised targeting 90 mg of material does not translate on scaling the reaction. This leads to the conclusion that the issue with over reducing C_{60} must be controlled beforehand.

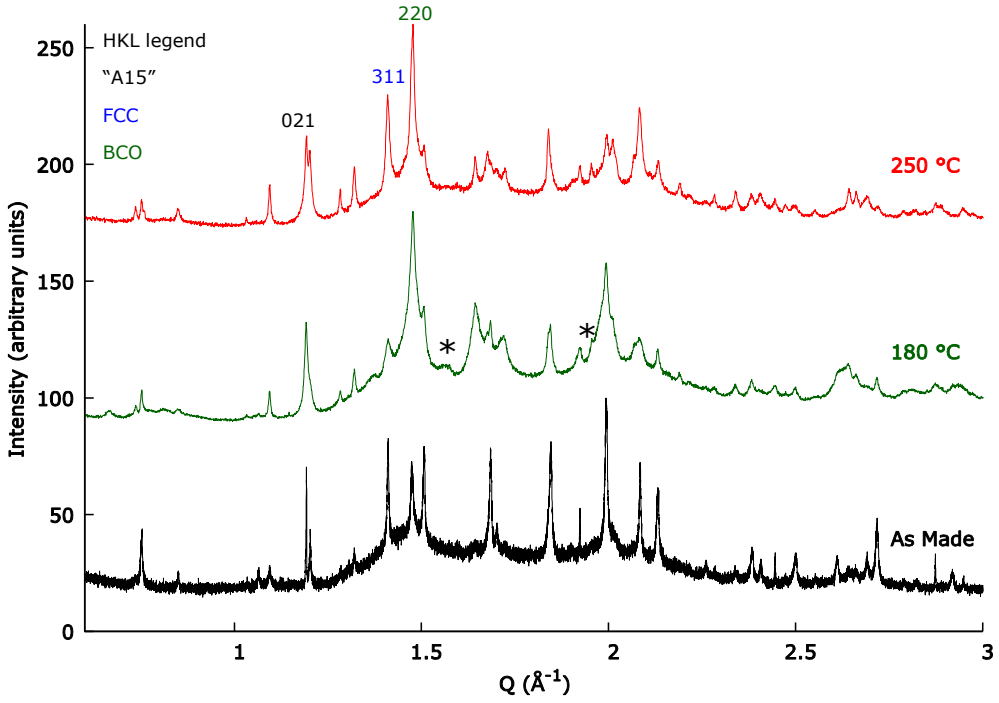

Figure 3.14 Observed patterns show the evolution of the crystalline phases as the annealing temperature is increased but the annealing time kept constant at 15 hours. The labels correspond to the samples as follows where the text in the bracket is the annealing temperature: AM44_1 (As Made), AM44_3 (180 °C) and AM44_4(250 °C). The * represent the same unidentified phase as found in figure 3.10.

The synthesis of Cs_3C_{60} in THF suffers from two major problems; firstly significant amounts of over-reduced products are formed in the critical step of the reactions. Secondly there is only a narrow temperature range in which FCC Cs_3C_{60} is favoured meaning that using temperature to recombine the by-products, like with the MA synthesis, cannot be used to make phase pure material. This makes the initial reaction step in solution important and effort needs to be applied in making sure that the by products are not formed. Addressing these issues would allow the selectivity of THF at 20 °C to be capitalised on. To conclude, the use of THF has potential in these reactions, especially with respect to FCC material, but preventative measures must be applied so that over-reduction can be ruled out.

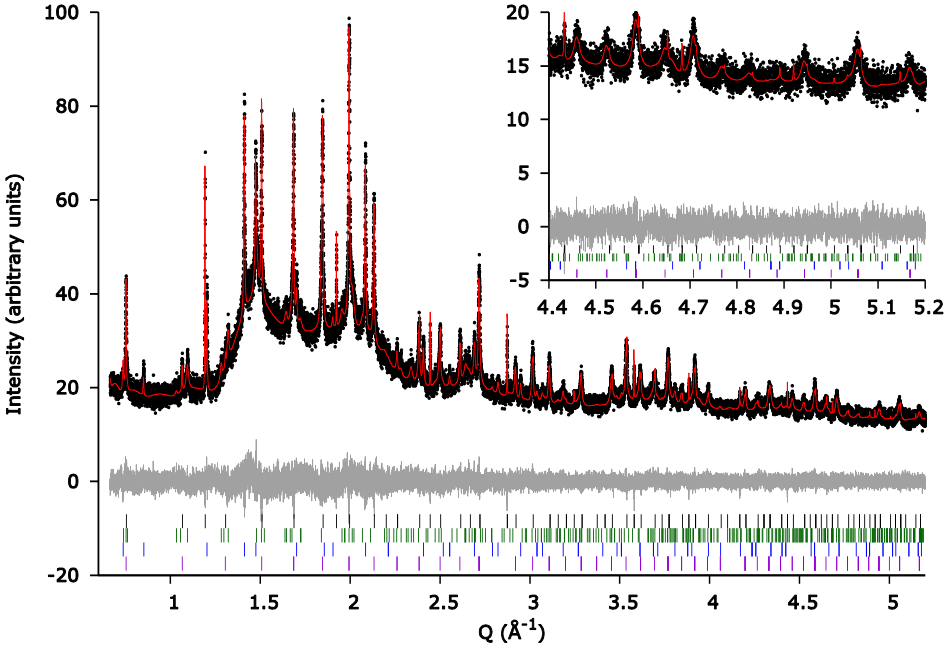

Figure 3.15 Observed (black dots) and calculated (red line) data of the room temperature synchrotron powder X-ray diffraction pattern. The material was synthesized with the nominal composition $Cs_{3.0}C_{60}$ and corresponds to the sample AM44_1. The tics represent Bragg reflection positions of the "A15" (black), BCO (green), FCC (blue) and Cs_6C_{60} (dark violet) phases. The wavelength was λ = 0.825000 Å.

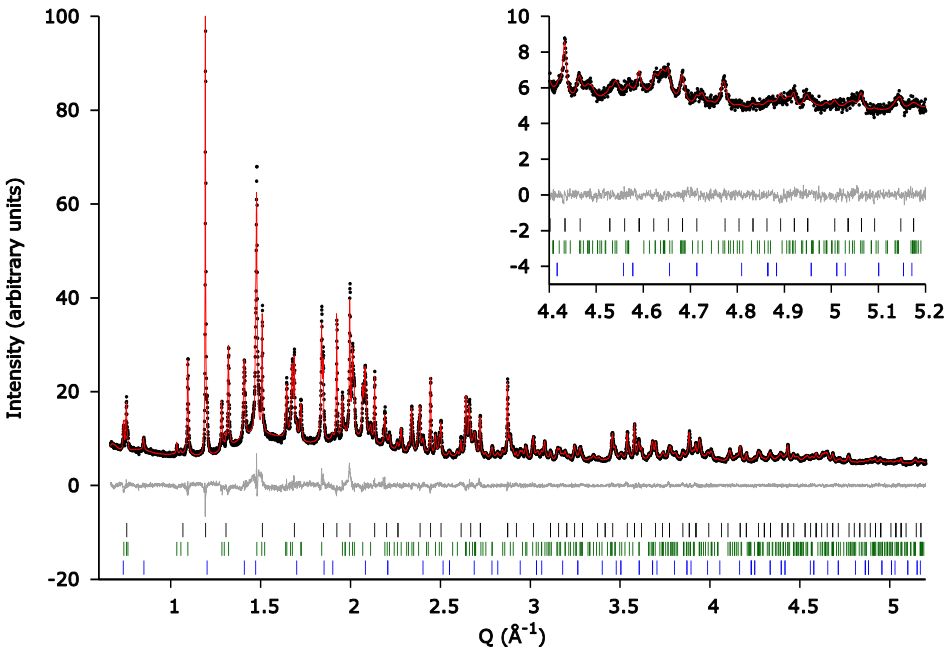

Figure 3.16 Observed (black dots) and calculated (red line) data of the room temperature synchrotron powder X-ray diffraction pattern. The material was synthesized with the nominal composition $Cs_{3.0}C_{60}$ corresponds to the sample (AM44_2). The tics represent Bragg reflection positions of the "A15" (black), BCO (green) and FCC (blue) phases. The wavelength was λ = 0.825000 Å.

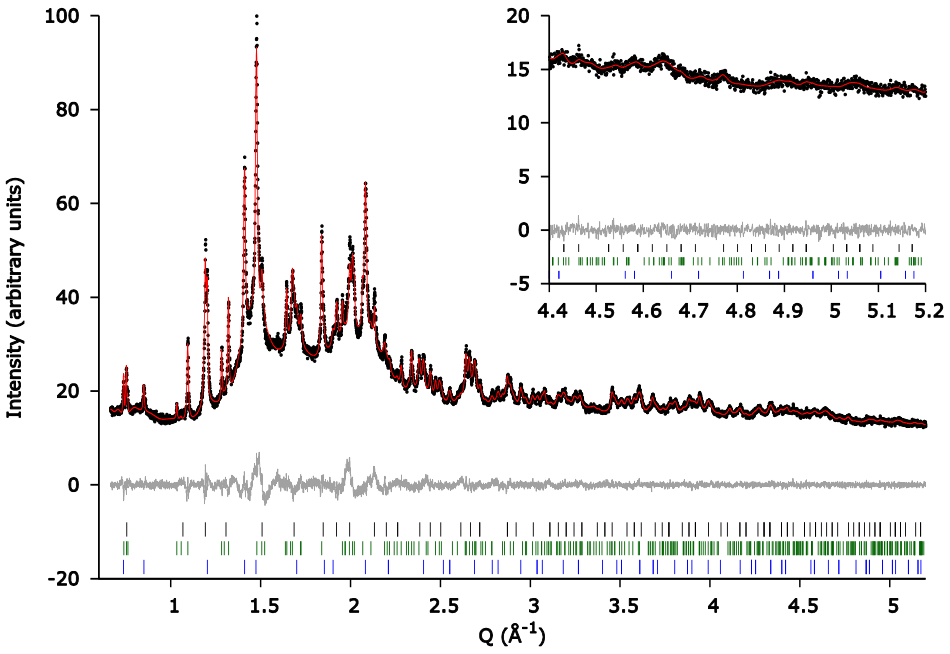

Figure 3.17 Observed (black dots) and calculated (red line) data of the room temperature synchrotron powder X-ray diffraction pattern. The material was synthesized with the nominal composition $Cs_{3.0}C_{60}$ corresponds to the sample AM44_4. The tics represent Bragg reflection positions of the "A15" (black), BCO (green) and FCC (blue) phases. The wavelength was λ = 0.825000 Å.

Table 3.16 Refinement details produced from the analysis of the diffraction experiments done on samples AM44_1, AM44_2 and AM44_4.

ID / Parameter	AM44_1	AM44_2	AM44_4
Annealing T (° C)	As made	180	250
Annealing Time (Hr)	N/A	40	15
R_{wp} (%)	4.86	3.93	3.17
R_{exp} (%)	4.21	2.40	1.99
λ (Å)	0.825000	0.825000	0.825000
"A15" (%)	6.61(3)	27.9(3)	21.7(5)
BCO (%)	32.03(29)	53.5(3)	48.3(6)
FCC (%)	22.09(10)	18.6(3)	29.9(5)
Cs_6C_{60} (%)	39.27(17)	0	0
"A15" *V per C_{60}* (Å^3)	815.62(2)	815.68(4)	817.2(1)
BCO *V per C_{60}* (Å^3)	829.0(2)	828.81(4)	829.3(1)
FCC *V per C_{60}* (Å^3)	803.82(4)	807.67(7)	805.6(1)
Cs_6C_{60} V per C_{60} (Å^3)	818.86(3)	0	0
"A15" xrd composition	Cs_3C_{60}	$Cs_{2.989(5)}C_{60}$	Cs_3C_{60}
FCC xrd composition	$Cs_{2.92(2)}C_{60}$	$Cs_{2.82(1)}C_{60}$	$Cs_{2.90(2)}C_{60}$

3.3. Targeting the C_{60}^{3-} charge state of alkali metal fullerides with $Cs[Mn(Cp^*)_2]$

Based on the previous sections the largest problem faced by these systems is that once over-reduction has occurred getting, back to a C_{60}^{3-} charge state is very difficult. Since Cs metal has a redox potential of $E_{1/2}^{+/0}$ =-2.785 vs SCE it is no surprise that a compositional range over stable Cs_xC_{60} compositions is observed for the synthesis of Cs_3C_{60} materials using the metal.[31-33] What is needed for this system is a preventative method rather than a cure for the formation of BCO material. One such method aiming to synthesise K_3C_{60} utilised the intermediate one electron reducing agent $K[Mn(Cp^*)_2]$ to prevent the formation of K_4C_{60}.[3]

It is therefore anticipated that a similar approach could reduce or eliminate the BCO phase if applied to Cs-C_{60} system. With a reduction potential of $E_{1/2}^{0/1}$ =-2.17 vs SCE the Cs analogue of $Na[Mn(Cp^*)_2]$ could offer better control over the reaction than Cs metal alone.[31, 34] With the added control of a fully dissolved and considerably milder (than Cs) reducing agent like $Cs[Mn(Cp^*)_2]$ we may be able to selectively synthesize Cs_3C_{60}.

3.3.1. Method: Synthesis of Cs_3C_{60} Using $Cs[Mn(Cp^*)_2]$ in THF

The $Cs[Mn(Cp^*)_2]$ was synthesised using the method outlined for $Na[Mn(Cp^*)_2]$, by reacting freshly prepared Cs napthalide with $Mn(Cp^*)_2$ with extensive modification (Figure 3.18).[34] Caesium metal (548.0 mg, 4.12 mmol) and Napthalene (530.0 mg, 4.14 mmol) were reacted together for 1 hour in THF (120 ml) at 30 °C. This solution was then transferred by cannula to a vessel containing $Mn(Cp^*)_2$ (1.34 g, 4.12 mmol) under constant stirring and then reacted for 15 minutes (Figure 3.18).

$$Cs + C_{10}H_8 \xrightarrow[THF]{} CsC_{10}H_8 \xrightarrow[Mn(Cp^*)_2]{} Cs[Mn(Cp^*)_2] + C_{10}H_8 \xrightarrow[-THF + Hexane]{} Cs[Mn(Cp^*)_2]$$

Figure 3.18 Reaction schematic for the production of the $Cs[Mn(Cp^*)]_2$ reducing agent.

The THF was then evaporated off into a liquid nitrogen trap and the resulting orange solid suspended with hexane (40 ml). The suspension was then

separated using a frit and the precipitate washed with three lots of hexane (20 ml) before being dried under dynamic vacuum until a pressure of at least 1 $x10^{-1}$ mbar was achieved. The dried material was ground in a glove box giving a yield of 92.8 %. Powder x-ray diffraction and microanalysis showed absence of starting material and gave a composition of $Cs_{1.0(1)}[Mn(Cp^*)_2]$.

The FCC rich Cs_3C_{60} was prepared by first making a solution of $Cs[Mn(Cp^*)_2]$ and a suspension of C_{60} in THF (Table 3.17). The $Cs[Mn(Cp^*)_2]$ suspension was then added drop-wise to the C_{60} through a cannula over 1.5 hours (Figure 3.19). The reaction mixture quickly turned from orange to the dark red colour indicative of the C_{60}^{3-} anion. The mixture was then stirred for 30 minutes and the volume subsequently reduced to 22 % of the volume of THF added.

The Cs_3C_{60}·xTHF material was precipitated from the solution by the slow addition of dry hexane (20 ml) at which point the black crystalline product became visible leaving a pale yellow solution remaining (Figure 3.19). The anti-solvent precipitation of the Cs_3C_{60}·xTHF by hexane was a sensitive step in which the yield and crystallinity of the product could be affected. The slow addition of hexane produces large particles of Cs_3C_{60}·xTHF leaving a clear yellow solution. Once precipitated, the product was then filtered through a frit, washed three times with hexane (10 ml) and dried by passing argon over the material. The final brown material was then reground in a glove box. When evacuated to pressures of $5x10^{-5}$ mbar the solvated product loses its brown colour and becomes a black material which is amorphous according to powder X-ray diffraction.

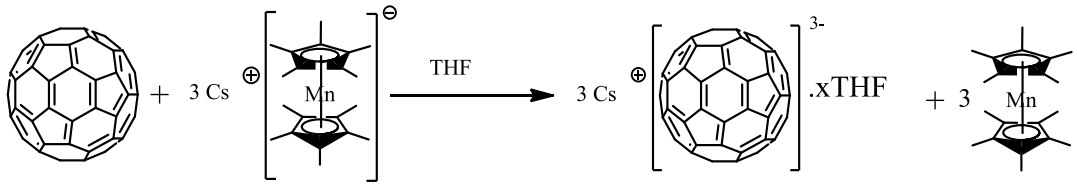

Figure 3.19 Reaction schematic depicting the reaction between stoichiometric $Cs[Mn(Cp^*)]_2$ and C_{60} producing Cs_3C_{60}.

For AM65_X (X = 2, 3, 4 and 5) samples Cs_3C_{60}·3.6THF (48.0 mg) was split into four parts and annealed under dynamic vacuum ($1x10^{-5}$ mbar) for 15 hours at the following individual temperatures; 180, 250, 350, 400 °C (Tables 3.18). For AM108 and AM111 the optimal annealing temperature of 350 °C was

used. The resulting materials were then ground in a glove box analysed by CHN (Table 3.19), by X-ray diffraction and Raman spectroscopy.

Table 3.17 Summary of reactants and recovered masses for the as made product from the synthesis of Cs_3C_{60} using $Cs[Mn(Cp^*)_2]$ and C_{60} in THF.

Sample ID	Mass of $Cs[Mn(Cp^*)_2]$ / mg	Mass of C_{60}/ mg	Volume of THF used/ml	Recovered/ mg
AM65_1	137.5	72.0	90	63.5
AM108_1	137.5	72.0	180	109.2
AM111_1	274.9	144.1	360	171.5

Table 3.18 Summary table of annealing protocols applied to as made material from the synthesis of Cs_3C_{60} using $Cs[Mn(Cp^*)_2]$ and C_{60} in THF.

Sample ID	Mass used /mg	Annealing program	Mass recovered/ mg
AM65_2	10.5	RT-->5 C/min, 180 C, 15 hrs-->5 C/min RT	8.6
AM65_3	10.5	RT-->5 C/min, 350 C, 15 hrs-->5 C/min RT	9.7
AM65_4	10.5	RT-->5 C/min, 250 C, 15 hrs-->5 C/min RT	7.9
AM65_5	10.2	RT-->5 C/min, 400 C, 15 hrs-->5 C/min RT	8.3
AM108_2	100.0	RT-->5 C/min, 350 C, 15 hrs-->5 C/min RT	79.5
AM111_2	160.0	RT-->5 C/min, 350 C, 15 hrs-->5 C/min RT	153.1

Table 3.19 Microanalysis results for materials synthesised of Cs_3C_{60} by $Cs[Mn(Cp^*)_2]$ and C_{60} in THF.

Sample ID	% C	% H	% N	Composition
AM65_1	63.00	2.03	x	$Cs_{3.3}C_{60}$·3.6THF
AM65_3	64.55	0.17	x	$Cs_{3.0}C_{60}$·0.24THF
AM65_4	64.64	0.13	x	$Cs_{3.1}C_{60}$·0.2THF
AM65_5	65.17	0.21	x	$Cs_{2.9}C_{60}$·0.3THF

3.3.2. Analysis of the phase assembly and superconducting properties of FCC Cs_3C_{60} material synthesised in THF using $Cs[Mn(Cp^*)_2]$

The reaction proceeds as expected for a charge transfer reaction involving C_{60}. A deep red solution is obtained after complete addition of the reducing agent. Once completely precipitated and isolated from the mother liquor the as-made material was carefully dried under inert gas flow to preserve the crystalline material. The material produced and treated in this way had two crystalline phases that fit into the same space group as $K_3C_{60}\cdot(THF)_{14}$ (SG= *C*2/*m*) (Figure 3.20).[35] The as-made material was very sensitive to solvent loss, quickly losing its red colouring and crystalline components becoming black and amorphous.

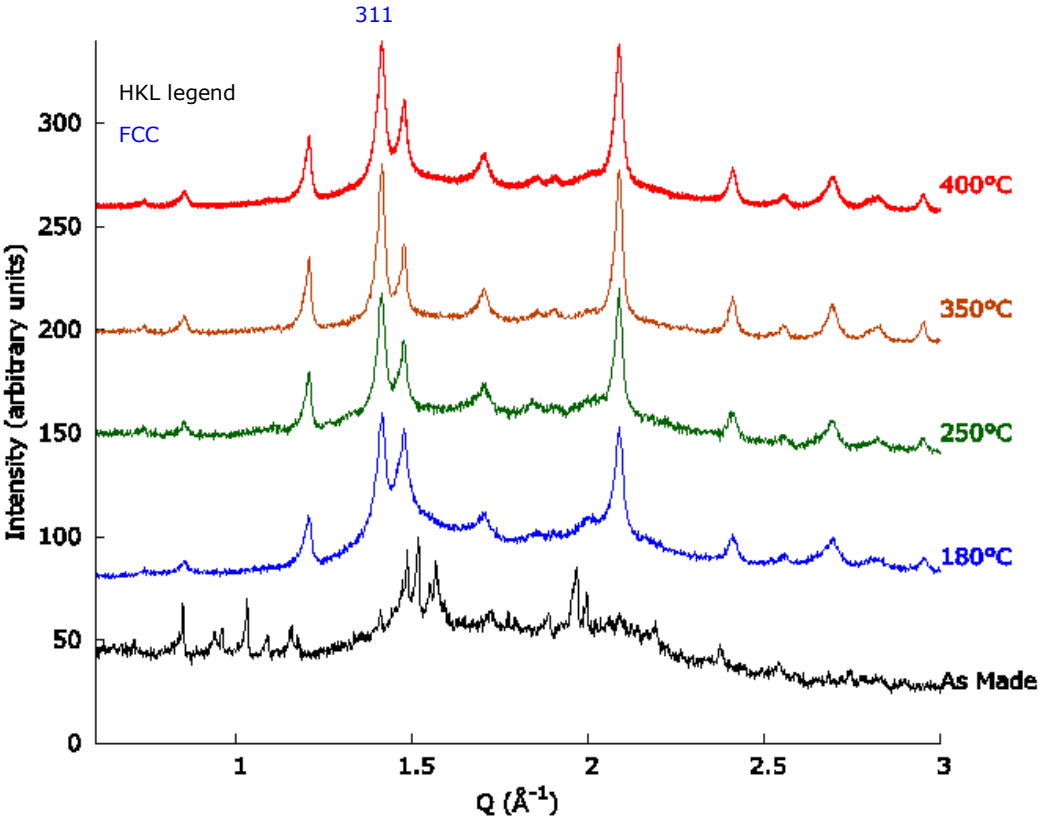

Figure 3.20 Comparing the observed patterns from varying the annealing temperature applied to the as made material in order to remove THF and crystallise the FCC phase. The labels correspond to the samples: AM65_1(As Made), AM65_2(180 °C), AM65_3(350 °C), AM65_4(250 °C), AM65_5(400 °C).

Once heated under dynamic vacuum the solvent begins to leave the structure which was characterised by an increase in pressure from $1x10^{-5}$ to $2x10^{-2}$ mbar. To obtain material that possesses a crystalline FCC phase the annealing temperatures should reach at least 180 °C (Figure 3.20). This is consistent with what was observed for the as-made material produced by the reaction of stoichiometric amounts of Cs and C_{60} in THF in section 3.3.2.1. indicating a similar reaction path to the synthesis of 90 mg of material.

From powder x-ray diffraction it was evident that the material has insignificant amounts of the BCO phase. This confirmed our theory that in the typical MA, ammonia or solid state methods the BCO impurity was due to the caesium metal over-reducing the C_{60}. However, the presence of a broad halo between 1.3 and 2.25 $Å^{-1}$ in the diffraction pattern indicated the presence of an amorphous phase. The existence of solvent in the structure of Cs_3C_{60}, as confirmed by microanalysis analysis, was the likely origin of this halo (Table 3.20, Figure 3.20 and 3.21). The level of crystallinity, however, could be controlled by varying the annealing temperature. The optimal annealing temperature which gave maximum crystallinity was 350 °C (Figures 3.20 and 3.21). The crystallinity was then qualitatively gauged by comparing the amorphous background, peak shape and the ratio of the 311 to 222 peaks. The most crystalline material gave a lower background and sharper peaks (Figures 3.20 and 3.21).

There was an increase in crystallinity between the samples annealed at 180 and 250 °C, which was followed by a smaller final increase between those annealed at 250 and 350 °C (Figure 3.20). Annealing at 400 °C led to an increase in amorphous background and a reduction in crystallinity. It could therefore be concluded that in terms of removing solvent and increasing crystallinity that heating above 350 °C was unnecessary. This qualitative assessment is further backed up by the refined cell volumes of each pattern giving the maximum value for the 350 °C material.

The Rietveld analysis of ESRF ID31 data from the optimal material gave a volume per C_{60}^{3-} of 803.0(2) $Å^3$, 99.8 % that of the value quoted for the highest FCC fraction material to-date (Table 3.20, Figures 3.20 and 3.21). Rietveld refinement of the other post annealed samples also displayed a good agreement except for the 180 °C material. The high background in the 180 °C material increased the uncertainty of the refinement (Table 3.20, Figures 3.20 and 3.21). This unusual background is observed in samples produced in THF that have not

had adequate annealing times (Figure 3.18 pattern representing 15 hours) and further confirmed that the optimal annealing temperature was 350 °C.

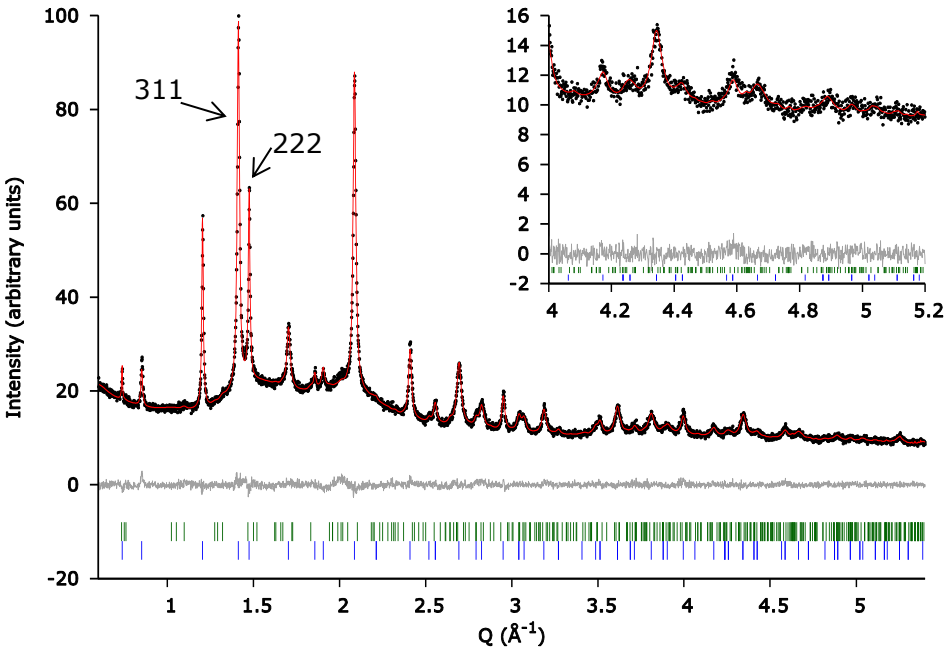

Figure 3.21 Observed (black dots) and calculated (red line) data of the room temperature synchrotron powder X-ray diffraction pattern the Rietveld refinement was done for data collected for AM65_3. The tics represent Bragg reflection positions of the BCO (green) and FCC (blue) phases. The wavelength was λ = 0.399892 Å and the refinement details are tabulated in Table 3.20.

Table 3.20 Refinement details produced from the analysis of the diffraction experiments done on samples AM65_2-5 each annealed at a different temperature as per the method.

Parameter \ ID	*AM65_2*	*AM65_3*	*AM65_4*	*AM65_5*
Annealing T (°C)	***180***	***350***	***250***	***400***
R_{wp} (%)	3.00	3.07	3.87	3.50
R_{exp} (%)	2.68	2.89	3.33	2.25
λ (Å)	0.7093	0.399892	0.7093	0.7093
BCO (%)	0	3.2(2)	11.8(5)	8.5(3)
FCC (%)	100	96.8(2)	88.2(5)	91.5(3)
BCO *V per C_{60}* (Å^3)	0	837.4(3)	820.8(9)	814.1(4)
FCC *V per C_{60}* (Å^3)	800.5(5)	803.0(1)	796.5(1)	797.1(1)
FCC xrd composition	Cs_3C_{60}	$Cs_{2.825(8)}C_{60}$	$Cs_{2.89(2)}C_{60}$	$Cs_{2.891(5)}C_{60}$

Further fine tuning can be performed by adjusting the concentration of the reducing agent, which at the point of addition is a suspension. The focus of this synthesis is the maximum control of the principal reaction step so in an ideal case everything would be in solution. This is not attainable for C_{60} in THF but is attainable for the Cs_3C_{60} product and the reducing agent. A balance must therefore be struck between volume and purity where the trade-off becomes ease and yield vs. quality.

The difference in solubility between $K[Mn(Cp^*)_2]$ and $Cs[Mn(Cp^*)_2]$ means that twice as much THF is required to dissolve the reducing agent at room temperature.[3] As previously noted the addition of hot reagents should be avoided to keep the selectivity of THF towards the FCC polymorph. With the use of a fully dissolved reducing agent and an identical annealing protocol to that of the initial reaction the BCO phase is completely eliminated along with the amorphous halo (Figure 3.22). The change in protocol, however, has some unexpected consequences as the solvated phase shown persists in the final product. The FCC material produced is identical in volume and composition to the materials made in the THF synthesis in the previous section but its volume differs from the literature values by 1 $Å^3$ for the sample annealed at 350 °C.

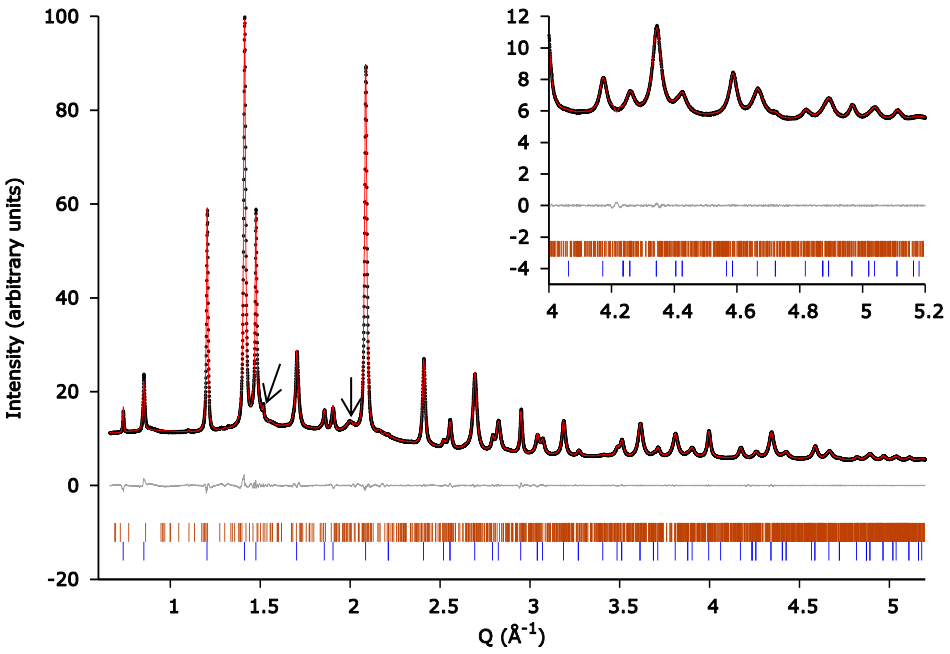

Figure 3.22 Observed (black dots) and calculated (red line) data of the room temperature synchrotron powder X-ray diffraction pattern. The material was synthesized with the nominal composition $Cs_{3.0}C_{60}$ corresponding to the sample AM108_2. The tics represent Bragg reflection positions of the solvated phase (dark orange) and FCC (blue) phases. The wavelength was λ = 0.827157Å and the results are tabulated in table 3.21. The arrows represent the only visible Bragg peaks of the solvated phase.

As concluded in section 3.2.3. additional control over the initial reaction step is required in order to scale up with reproducible results. With $Cs[Mn(Cp^*)_2]$ and the reaction conditions now providing this, the scale can be driven up to twice that of the original method. The reaction itself proceeds in exactly the same fashion as its predecessor, first obtaining a red solution and on precipitation a red-brown powder. The powder pattern and microanalysis show that the material is comparable to that of the smaller scale reaction. However, On investigation by synchrotron x-ray experiments small differences are noticed. The FCC phase from the scaled up reaction is slightly smaller in volume and there is more of the solvated phase than what is observed in the small scale reaction (Table 3.21, Figures 3.22 and 3.23).

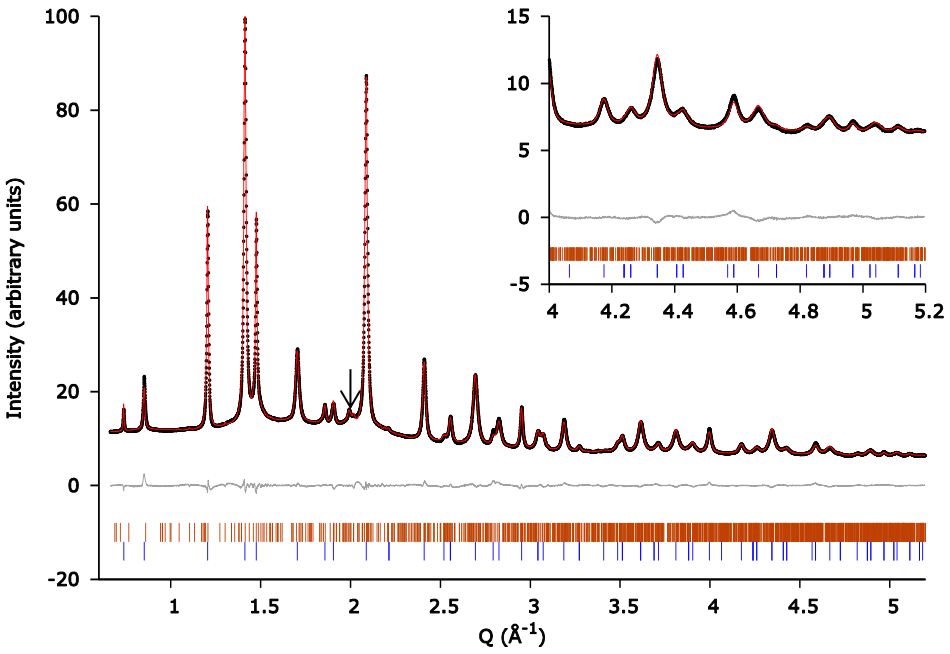

Figure 3.23 Observed (black dots) and calculated (red line) data of the room temperature synchrotron powder X-ray diffraction pattern. The material was synthesized with the nominal composition $Cs_{3.0}C_{60}$ corresponding to AM111_2. The tics represent Bragg reflection positions of the solvated phase (dark orange) and FCC (blue) phases. The wavelength was λ = 0.827157Å. The arrows represent the only visible Bragg peaks of the solvated phase.

Table 3.21 Comparison of the Rietveld values as refined from the synchrotron experiments shown in Figures 3.30, 3.31 and 3.32. Note that AM108_2 and AM111_2 have the solvated phase in which the space group is assumed to be *C*2/*m*, due to the nature of this phase it is represented as a Pawley phase to maximise the information from the FCC Cs_3C_{60} phase.

Parameter \ ID	*AM65_3*	*AM108_2*	*AM111_2*
Scale (mg)	***100***	***100***	***200***
R_{wp} (%)	3.07	1.14	1.78
R_{exp} (%)	2.89	0.28	0.38
λ (Å)	0.399892	0.827157	0.827157
BCO (%)	3.2(2)	0	0
FCC (%)	96.8(2)	100	100
BCO *V per* C_{60} (Å^3)	837.4(3)	0	0
FCC *V per* C_{60} (Å^3)	803.0(1)	803.24(3)	801.92(3)
FCC xrd composition	$Cs_{2.825(8)}C_{60}$	$Cs_{2.942(2)}C_{60}$	$Cs_{2.947(1)}C_{60}$

Further investigation of these materials by Raman spectroscopy reveals that the charge state of the material is C_{60}^{-3} and is in line with our previously published work for FCC rich material.[6] On comparison with literature spectra it becomes clear that the materials from this method are more disordered than those produced from other methods (Figure 3.24 and Table 3.22). The peaks from the materials using the Cs[Mn(Cp*)$_2$] route are much broader that those of the method detailed in Ganin et. al. Nature 2010.[6] One possible cause of this broadening could be due to a lower crystallinity than that observed in materials produced using an amine method. This is likely to be due to the mild and short annealing protocol used to crystallise these materials in this case. One of the general disadvantages to using solution based methods is it produces materials of lower crystallinity but in this case it appears to be much more severe. This aspect then means that although the microanalysis and powder patterns of the samples may look good, they require much more detailed investigation.

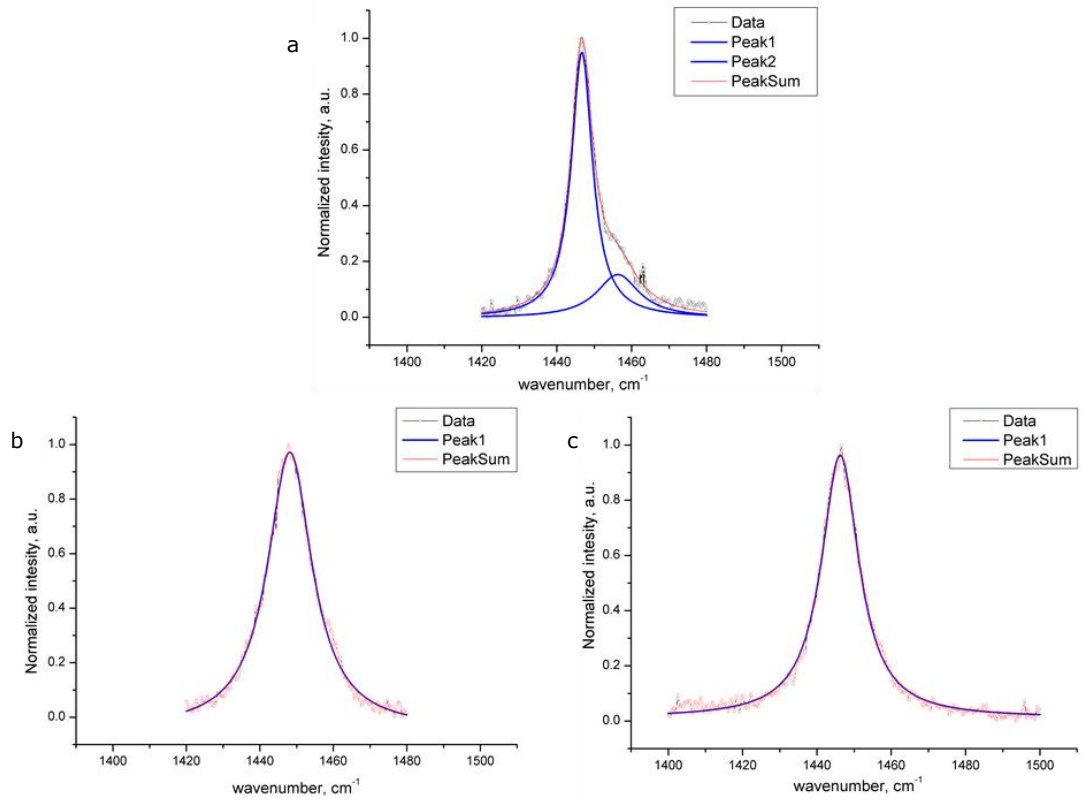

Figure 3.24 Depicts the Raman spectra for Ganin *et.al*. 2010[6] (a), AM108_2 (b) and AM111_2 (c). The blue line represents the peak contribution to the profile, the red line shows the overall fit to the data and the black line represents the data recorded. The

measurements were performed using a wavelength of λ = 514.5 nm on the appropriate range for the Ag(2) vibrational mode of the C_{60}^{-3} anion.

Table 3.22 A summary of the Lorentzian fits for the data shown in figure 3.24. ω_0 represents the peak position, Γ gives the peak width and A is the peak area.

ID / Parameter	Ganin *et.al*. Nature 2010		*AM108_2*	*AM111_2*
Method	$3Cs+C_{60}\backslash NH_3\backslash MA$		$Cs[Mn(Cp^*)]_2\backslash THF$	
Peak	1	2	1	1
ω_0	1446.70(2)	1456.34(4)	1448.15(3)	1446.25(2)
Γ	6.89(8)	13.9(8)	14.8(1)	12.37(8)
A	10.3(1)	3.4(2)	23.6(2)	18.5(1)

The small cell volumes and relatively large disorder observed from powder diffraction and Raman spectroscopy are confirmed by SQUID magnetometry. The materials are superconducting but they do not match up with the literature values. The large and small scale materials have a T_c of 33.5 and 33.0 K and shielding fractions of 6 and 3.5 % respectively (Figures 3.25 a and b). The lower T_c presented by the material is due to the lower unit cell volume presented by these materials when compared to those made by ammonia and MA.[5, 6] The lower shielding fraction can be rationalised by the comparatively lower amount of crystallinity present in materials made using this synthesis.

As with all Cs_3C_{60} superconductors the samples must be put under hydrostatic pressure greater than 0.1 GPa in order for the material to display a superconducting transition (Figure 3.25).[2, 5, 6] The T_c rises to a maximum of 33.5 K and 35 K, for the materials synthesised by $Cs[Mn(Cp^*)_2]$ and amines respectively, at 0.8 GPa. The material synthesised in this work displays the same dome in the critical temperature as the literature FCC polymorph (Figure 3.26).[6] This dome is the result of the tuning of the interfulleride separation by the application of pressure. The BCS theory would predict that the larger the interfulleride separation the higher the T_c, which is clearly not the case for these systems. This result supports the conclusion previously published by this group that the Cs_3C_{60} systems are not BCS superconductors and are in fact highly correlated electron systems.[5, 6, 36]

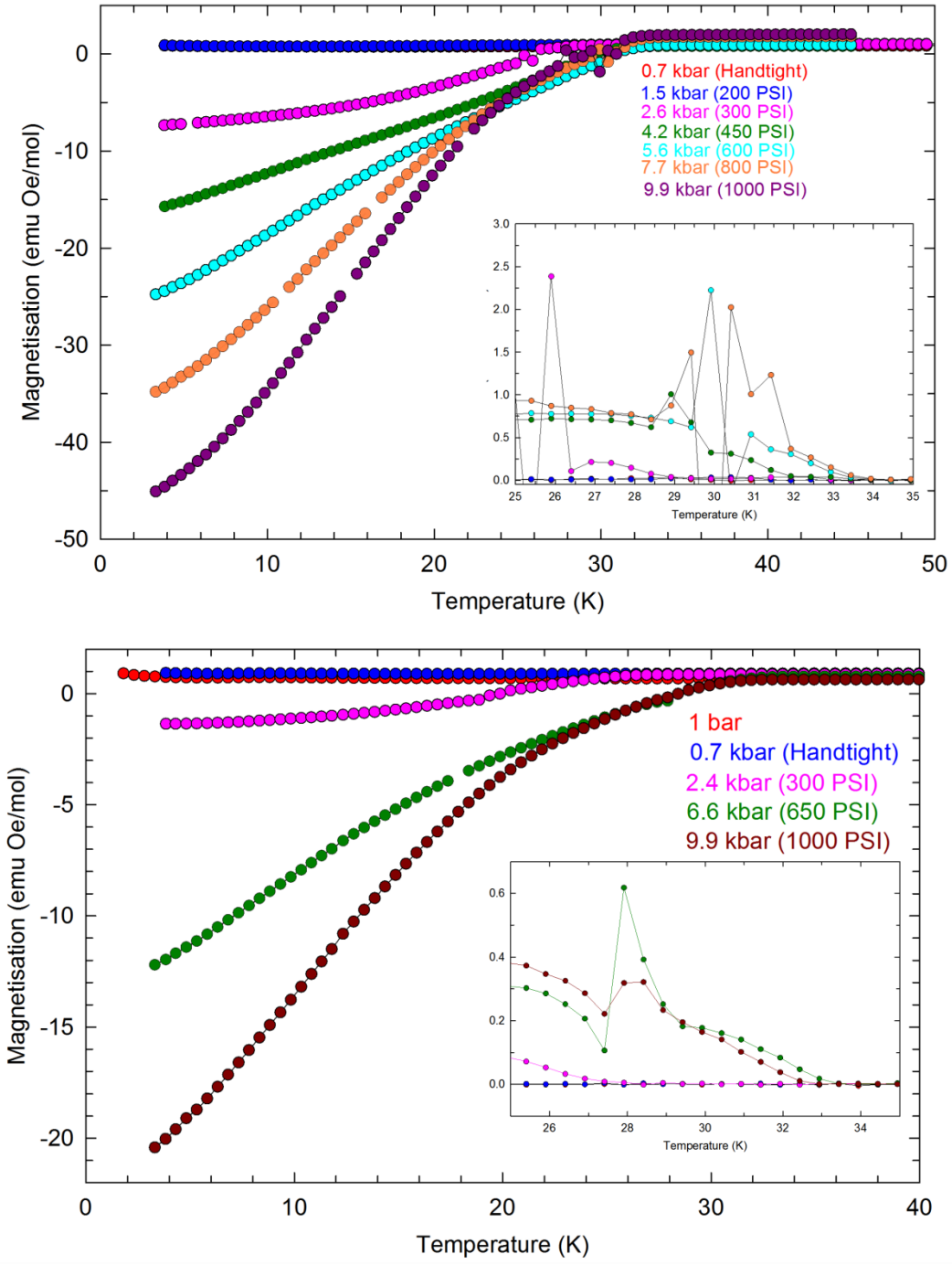

Figure 3.25 High pressure magnetic measurements were done at an applied field of 20 Oe, the inserts are the derivative *d*m/*d*t of the respective data. a. The magnetisation as a function of temperature measurements done on AM108_2 shows the onset of superconduction at 0.7 K bar with a T_c of 29.5 K which rises to a shielding fraction of 6 % with a T_c of 33.5 K at 9.9 kbar. b. The magnetisation as a function of temperature measurements done on AM111_2 shows the onset of superconduction at 2.4 K bar with a T_c of 29.0 K SF of 0.3 % rising to a shielding fraction of 3 % with a T_c of 33.5 K at 9.9 kbar. The Sn superconducting transition is cut off at 3.8 K so the SF can be calculated at this temperature.

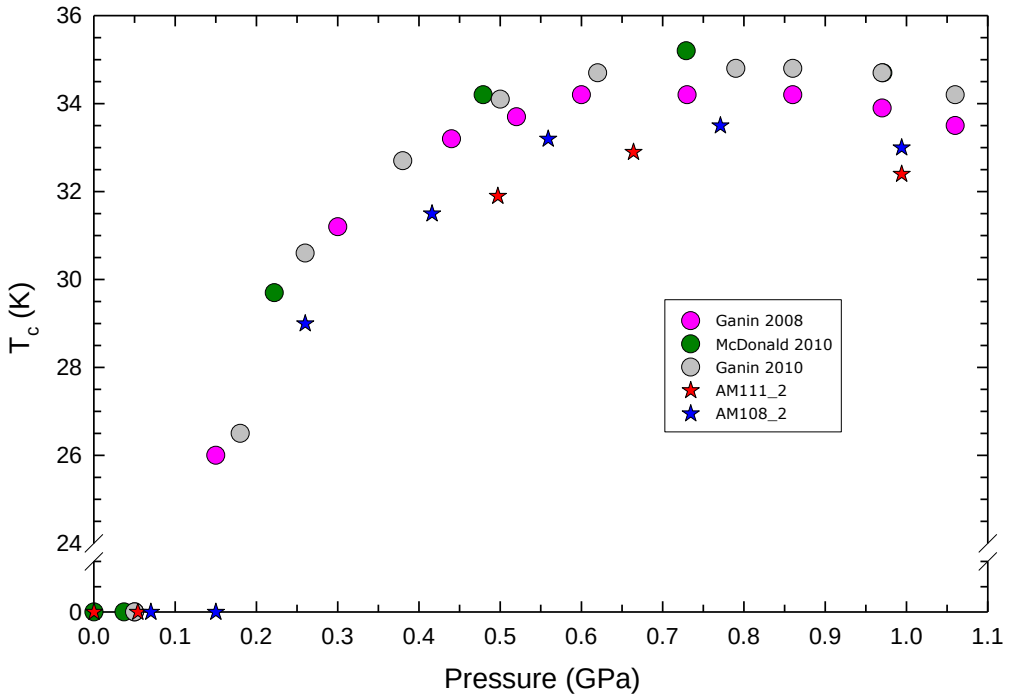

Figure 3.26 Superconducting transition temperature as a function of cell pressure for the FCC phases. The solid symbols were recorded on increasing pressure and the hollow symbols represent measurements taken on decreasing pressure. The labels on the graph give the sample name or source.[5, 6, 16]

3.4. Conclusions

The primary aim of these experiments was to explore the origins of the impurity phases in traditional Cs_3C_{60} methods. Then subsequently use what was found to produce a method that could minimise these impurities in order to maximise the purity of the material. This involved the investigation of the Cs_3C_{60} system in three different synthetic methods; firstly the reaction of a solid state precursor in the solvent MA was studied focusing on the role of reaction temperature and the annealing protocol. The reaction between Cs and C_{60} in MA is well examined by Ganin et al. 2008 and can produce up to 77 % of the "A15" polymorph. One of the points of using MA over ammonia is that there is a wider temperature range that can be explored safely. The use of the solid state precursor allowed the exploration of this system but failed to improve upon the large "A15" phase fractions reported in the literature.

The solid state precursor is an unusual material in itself since it is the first time that the FCC polymorph has been observed in materials produced using a vapour phase method. The solid state precursor had the composition of $Cs_{3.0}C_{60}$ as given by microanalysis and contained ~10 % of the FCC polymorph. The Rietveld analysis of this material from synchrotron x-ray diffraction calculated the BCO as the majority phase with FCC, C_{60} and Cs_1C_{60} phases also present. The FCC composition was calculated to be $Cs_{2.99(1)}C_{60}$ and $Cs_{2.93(2)}C_{60}$ with a cell volume of 802.73(5) and 802.27(6) $Å^3$ per C_{60} respectively. This places the composition of the solid state precursor higher than that of published methods but with a unit cell volume which is significantly lower. The presence of even small amounts of FCC material is unprecedented for this type of vapour phase reaction and makes this precursor well suited to studying the effects of MA on the phases present.

The reaction of solid state precursor in MA in the temperature range -40 to 40 °C results in the demonstration that the "A15" phase is favoured at higher temperatures. The "A15" phase increases up to 64 % on heating of the reaction solution to 40 °C. This increase is coupled with a proportional decrease in the fractions of BCO and Cs_1C_{60}. The relationship between "A15", Cs_1C_{60} and BCO is further confirmed through VT synchrotron experiments on materials produced through the -40 °C and 40 °C reaction methods. Both experiments show an increase in the amount of "A15" coupled with a drop in both BCO and Cs_1C_{60}. The observation that increasing reaction temperature and the annealing protocol

both allow BCO to be converted into "A15" material demonstrates the importance of the solution phase reaction step and the protocol used to anneal the material directly after this step. The "A15" phases shown in the samples have an average composition of $Cs_{2.86(2)}C_{60}$ (within three standard deviations) which is comparable to the published value of $Cs_{2.85(1)}C_{60}$. The volume after the reaction at 20 °C was calculated at 818.64(3) $Å^3$ per C_{60} 0.71 $Å^3$ larger than that published by Ganin et al. in 2008. Increasing the reaction temperature to 40 °C the cell volume decreases by 1.28 $Å^3$ which is 0.57 $Å^3$ smaller than the published value. This indicates that in order to obtain comparable volumes with the method published by Ganin in 2008 precursor based methods require heating. The observation that the optimal cell volumes are obtained after heating above 20 °C supports the conclusion that the best material overall is achieved by using the highest reaction temperatures possible.

The FCC phase remains almost constant at roughly 20 % indicating that its formation is independent of the solution phase reaction temperature. The FCC phase has an average refined composition of $Cs_{2.97(1)}C_{60}$ for all samples in this series. The volume of this FCC phase is 1.3 $Å^3$ smaller than the value from the best literature sample and is 3.6 $Å^3$ larger than the solid state precursor. This shows that the MA does affect the pre-existing FCC phase rather than just producing amorphous material thereby affecting its fraction artificially. There are examples of the incorporation of amines into the FCC structure of A_3C_{60} compounds by a slight orthorhombic distortion of the FCC lattice transforming it into an *Fmmm* space group. It is plausible that the loss of the solvent structure in the Cs_3C_{60} case would give a more variable end volume dependant on how much solvent is in the structure and how it was removed. This would account for the changes in volume between the solid state precursor FCC material and the material after treatment with and removal of MA. An interesting observation is presence of FCC in the solid state precursor, in the as made material prepared at -40 °C and the fact that it levels out at roughly 20 % in all cases once exposed to MA. This indicates that the additional 10 % of FCC produced on reaction in MA is likely to be due to the effect of the existing FCC in the precursor acting as a seed. This means that in order to obtain high quality "A15" material any precursor utilised should be free of the FCC polymorph.

The overall outcome of this set of experiments is that MA is capable of recombining the by-products into small amounts of FCC and larger amounts of "A15". As demonstrated here and in literature MA strongly favours the formation of the "A15" phase. This is more strongly emphasised on increasing the

temperature of the reaction solution where "A15" content is maximised and optimised in terms of the fraction and volume. In addition to this the by-products are consumed to support the increase in Cs_3C_{60} content. On annealing and VT diffraction experiments the same link between "A15" and BCO is established, demonstrating that it is both the reaction temperature and the annealing protocol which determines the final phase assembly.

The second system studied involved utilisation of THF as a solvent which shows another interesting trend in which the majority phase is the "A15" polymorph on heating the reaction media. The system shows no change in phase assembly after the temperature is set at 40 °C and above. This means that in order to get the best out of this system the reaction should not be allowed to exceed 20 °C. The VT synchrotron experiment on as made material yields an interesting observation. When annealed in a capillary the maximum obtainable fraction of FCC material is roughly 70 % but if annealed under dynamic vacuum only 58 % is obtained. This difference can be explained by observing the change in phase fractions as a function of temperature. This shows that at 175 °C there is 63 % of the FCC phase present at this temperature which is very similar to the 58 % observed after the annealing step. Once the temperature exceeds 250 °C the FCC fraction increases to 70 % indicating that annealing temperatures should exceed 250 °C to be optimal.

Scaling the synthesis of stoichiometric amounts of Cs and C_{60} in THF by a factor of three exacerbates the problems of the system. Primarily it sacrifices the selectivity of THF for the FCC polymorph at room temperature for a mixture of "A15", FCC and the products of over reduction. The as-made material highlights the severity of the over reduction problem by containing Cs_6C_{60}. This material then requires significantly longer annealing times for the same amount of material. This additional annealing time is due to the fact that as well as crystallising the phases formed in solution the diffusion reaction of Cs_6C_{60} with the lower Cs containing phases is also occurring. This then results in the production of a significantly worse phase assembly on comparison to the small scale reaction at 20 °C. It is logical to conclude that the production of Cs_6C_{60} within the solution reaction step is highly undesirable.

The third system investigated involved the preventing the over-reduction of C_{60} by the use of the one-electron reducing agent $Cs[Mn(Cp^*)_2]$ which is unlikely to reduce C_{60} to it 4- charge state. Regardless of using a solid state precursor or Cs and C_{60} as the starting points for these reactions it appears that obtaining

high purity materials is no simple task. This is very well highlighted in the literature where the most successful synthetic methods have complex steps. By preventing the formation of the by-products high purity material is obtainable; this idea has been attempted before for the Cs_3C_{60} system by using CsM (M= Hg, Ti or Bi). This concept relies on modifying the reductive capability of Cs by pre-reacting it to form a less active species. For the purposes of this work the use of an alloy is not sufficient because typically they do not lower the redox potential enough. The desired affect can be obtained by the use of a organometallic complex $Cs[Mn(Cp^*)_2]$.

The $Cs[Mn(Cp^*)_2]$ complex is an excellent choice for this type of reaction as it is soluble in THF, recyclable and easy to get out of the end product. By carefully reacting the reducing agent and C_{60} together a material that is 96.8(2) % FCC with a composition and volume of $Cs_{2.804(9)}C_{60}$ and 803.0(1) $Å^3$ per C_{60} can be obtained. This material is lower in caesium content than materials produced by the other routes but has a larger volume than that from materials made using a solid state route. From the previous experiments it can be stated that solvent controls the volume when the compositions are refined to be identical. Here however the composition is greater than three standard deviations lower than all other materials in this chapter. Comparison to the material produced using a Cs, C_{60} and THF method shows that for the higher caesium content there is a significant increase in volume of 2.06 Å. This is a logical observation as it is the intercalated ion which defines the interfulleride separation and hence volume.

An adjustment to the reaction to take advantage of a solution of the reducing agent produces a similar quality of material. Unfortunately here the problem is not the case of over reduction but the removal of solvent. This is a problem seen commonly across the literature for the synthesis of A_3C_{60} compounds in solvents like ammonia, toluene and THF. This adaptation produces an FCC phase identical to that of its predecessor and was produced in sufficient amounts to allow analysis of the superconducting properties using a SQUID. The material displays a T_c of 33.5 K with a maximum SF of 6 % at 9.9 KBar which is significantly smaller than the published values of 35 K and 80 %. This drop in SF and T_c is a result of a lower amount of caesium being intercalated and lower crystallinity owing to the mild annealing protocol.

Using $Cs[Mn(Cp^*)]_2$ to control the charge state during the initial formative stages allows for the successful scaling of the reaction by a factor of 2. This

yields material which has a similar X-ray pattern to its small scale predecessor. Rietveld refinement of the FCC structural model against this data allows the extraction of its volume and composition. The composition is calculated as $Cs_{2.947(1)}C_{60}$ which is very close to that described in literature and by the MA synthesis in this work. The volume (801.92(3) $Å^3$ per C_{60}) is considerably smaller for this material falling below even that of the solid state precursor. Looking back to the experiments testing the annealing temperature for these materials the low volume can be explained by a less than optimal annealing protocol. This means that although the formative step translates on scaling than annealing protocol does not. This insufficiency is reflected in the SQUID magnetometry data which gives a T_c of 33.0 K and a SF of 3.3 %.

The pressure dependency of the T_c follows the same trend as materials synthesised by MA and NH_3/MA methods producing a dome with a maximum at 9.9 Kbar. This tuning of the T_c as a function of pressure can be related to the metal insulator transition point. Where the maximum T_cs can be found when the hydrostatic pressure forces the material closer to this limit. This work then further supports the conclusion that the A_3C_{60} superconductors are not BCS superconductors and are much more akin to $YBa_2Cu_3O_8$ ceramic superconductors in their mechanism.

The synthetic methods utilised here all point towards the unwavering idea where the initial reaction in which the Cs_3C_{60} is to be formed must first be controlled if phase purity is to be achieved. This goal is realised in the use of $Cs[Mn(Cp^*)_2]$ to target the C_{60}^{3-} charge state where the amounts of over-reduced products are minimised. This reducing agent coupled with THF, however, is not the magic bullet hoped for. The remaining issues are therefore: firstly the synthesis requires significant quantities of THF due to the reducing agent's surprisingly low solubility in the solvent. Secondly it produces low cell volumes and crystallinity resulting in low shielding fractions and critical temperatures. The volumes produced by this method being so similar to the solid state precursor could mean that the role of this method in the progression of this research area would be the production of a phase pure precursor. This precursor could then be used with solvents like MA or ammonia to give the large shielding fractions and critical temperatures desired.

3.5. References

1. D. R. Buffinger, R. P. Ziebarth, V. A. Stenger, C. Recchia and C. H. Pennington, *Journal of the American Chemical Society*, 1993, **115**, 9267-9270.
2. T. T. M. Palstra, O. Zhou, Y. Iwasa, P. E. Sulewski, R. M. Fleming and B. R. Zegarski, *Solid State Communications*, 1995, **93**, 327-330.
3. X. H. Liu, W. C. Wan, S. M. Owens and W. E. Broderick, *Journal of the American Chemical Society*, 1994, **116**, 5489-5490.
4. D. W. Murphy, M. J. Rosseinsky, R. M. Fleming, R. Tycko, A. P. Ramirez, R. C. Haddon, T. Siegrist, G. Dabbagh, J. C. Tully and R. E. Walstedt, *Journal of Physics and Chemistry of Solids*, 1992, **53**, 1321-1332.
5. A. Y. Ganin, Y. Takabayashi, Y. Z. Khimyak, S. Margadonna, A. Tamai, M. J. Rosseinsky and K. Prassides, *Nature Materials*, 2008, **7**, 367-371.
6. A. Y. Ganin, Y. Takabayashi, P. Jeglic, D. Arcon, A. Potocnik, P. J. Baker, Y. Ohishi, M. T. McDonald, M. D. Tzirakis, A. McLennan, G. R. Darling, M. Takata, M. J. Rosseinsky and K. Prassides, *Nature*, 2010, **466**, 221-U293.
7. A. F. Hebard, M. J. Rosseinsky, R. C. Haddon, D. W. Murphy, S. H. Glarum, T. T. M. Palstra, A. P. Ramirez and A. R. Kortan, *Nature*, 1991, **350**, 600-601.
8. S. J. Duclos, R. C. Haddon, S. Glarum, A. F. Hebard and K. B. Lyons, *Science*, 1991, **254**, 1625-1627.
9. K. Tanigaki, T. W. Ebbesen, S. Saito, J. Mizuki, J. S. Tsai, Y. Kubo and S. Kuroshima, *Nature*, 1991, **352**, 222-223.
10. X. Chen, Y. Maniwa, C. A. Kuper, S. Glenis, C. L. Lin and M. M. Labes, *Chemistry of Materials*, 1997, **9**, 3049-3051.
11. S. Cooke, S. Glenis, X. Chen, C. L. Lin and M. M. Labes, *Journal of Materials Chemistry*, 1996, **6**, 1-3.
12. S. Glenis, S. Cooke, X. Chen and M. M. Labes, *Molecular Crystals and Liquid Crystals Science and Technology Section a-Molecular Crystals and Liquid Crystals*, 1996, **284**, 139-147.
13. H. H. Wang, A. M. Kini, B. M. Savall, K. D. Carlson, J. M. Williams, M. W. Lathrop, K. R. Lykke, D. H. Parker, P. Wurz, M. J. Pellin, D. M. Gruen, U. Welp, W. K. Kwok, S. Fleshler, G. W. Crabtree, J. E. Schirber and D. L. Overmyer, *Inorganic Chemistry*, 1991, **30**, 2962-2963.
14. J. E. Schirber, D. L. Overmyer, H. H. Wang, J. M. Williams, K. D. Carlson, A. M. Kini, U. Welp and W. K. Kwok, *Physica C*, 1991, **178**, 137-139.
15. R. D. Boss, J. S. Briggs, E. W. Jacobs, T. E. Jones and P. A. Mosierboss, *Physica C-Superconductivity and Its Applications*, 1995, **243**, 29-34.
16. M. T. McDonald, *Structural and electronic properties of fulleride superconductors [electronic resource]*, http://etheses.dur.ac.uk/301/.
17. S. P. Kelty, C. C. Chen and C. M. Lieber, *Nature*, 1991, **352**, 223-225.
18. A. Y. Ganin, Y. Takabayashi, C. A. Bridges, Y. Z. Khimyak, S. Margadonna, K. Prassides and M. J. Rosseinsky, *Journal of the American Chemical Society*, 2006, **128**, 14784-14785.
19. Y. Takabayashi, A. Y. Ganin, M. J. Rosseinsky and K. Prassides, *Chemical Communications*, 2007, 870-872.
20. D. Arcon, M. Pregelj, A. Zorko, A. Y. Ganin, M. J. Rosseinsky, Y. Takabayashi, K. Prassides, H. van Tol and L. C. Brunel, *Physical Review B*, 2008, **77**.
21. M. J. Rosseinsky, *Journal of Materials Chemistry*, 1995, **5**, 1497-1513.
22. S. Margadonna and K. Prassides, *Journal of Solid State Chemistry*, 2002, **168**, 639-652.
23. A. Messaoudi, J. Conard, R. Setton and F. Beguin, *Chemical Physics Letters*, 1993, **202**, 506-508.

24. Y. Ihara, H. Alloul, P. Wzietek, D. Pontiroli, M. Mazzani and M. Ricco, *Physical Review Letters*, 2010, **104**.
25. P. Dahlke, P. F. Henry and M. J. Rosseinsky, *Journal of Materials Chemistry*, 1998, **8**, 1571-1576.
26. Y. Takabayashi, A. Y. Ganin, P. Jeglic, D. Arcon, T. Takano, Y. Iwasa, Y. Ohishi, M. Takata, N. Takeshita, K. Prassides and M. J. Rosseinsky, *Science*, 2009, **323**, 1585-1590.
27. A. Hirsch and M. Brettreich, *Fullerenes : chemistry and reactions. Andreas Hirsch, Michael Brettreich*, Wiley-VCH, Weinheim ; [Great Britain], 2005.
28. R. R. Dewald and J. L. Dye, *Journal of Physical Chemistry*, 1964, **68**, 128.
29. C. S. Cragoe, C. H. Meyers and C. S. Taylor, *Journal of the American Chemical Society*, 1920, **42**, 206-229.
30. N. G. Connelly and W. E. Geiger, *Chemical Reviews*, 1996, **96**, 877-910.
31. L. Echegoyen and L. E. Echegoyen, *Accounts of Chemical Research*, 1998, **31**, 593-601.
32. D. Dubois, G. Moninot, W. Kutner, M. T. Jones and K. M. Kadish, *Journal of Physical Chemistry*, 1992, **96**, 7137-7145.
33. D. L. Reger, S. R. Goode and D. W. Ball, *Chemistry, Principles and Practice*, BROOKS COLE Publishing Company, 2009.
34. J. L. Robbins, N. M. Edelstein, S. R. Cooper and J. C. Smart, *Journal of the American Chemical Society*, 1979, **101**, 3853-3857.
35. C. Janiak, S. Muhle, H. Hemling and K. Kohler, *Polyhedron*, 1996, **15**, 1559-1563.
36. O. Gunnarsson, *Reviews of Modern Physics*, 1997, **69**, 575-606.

4. Phase equilibrium in K-Fe-Se system

4.1. Introduction

Since the discovery of superconductivity in $K_xFe_ySe_2$ materials there has been considerable effort put into determining the origin of its physical properties. These materials have been shown to have critical temperatures (T_c) of 31-33 K[1-3] which is 25 K higher than the T_c of the parent superconductor FeSe (T_c = 8 K).[4] The dramatic increase in the T_c of the iron selenide system on intercalation of alkali metals indicates a dependency of the T_c on the layer separation or perhaps the optimisation of the Se-Fe-Se bond angles. Naturally the structure and phase assembly of this material is of great interest and has been investigated using techniques such as powder X-ray diffraction (PXRD), neutron diffraction and transmission electron microscopy (TEM).[2, 5] As discussed in chapter 1 this has shown the presence of phase separation on the nanoscale[5] and micrometre size regions of magnetic and non-magnetic behaviour[6]. Despite all efforts a clear picture of the superconducting phase and its composition has not been described due to the complications of phase separation.

A big part of the reason why this has not been accomplished is due to the wide range of synthetic methods and nominal compositions used to make the $K_xFe_ySe_2$ materials. The vast majority of synthetic methods for this system consist of single crystals which were heated to temperatures of 1030 °C well above the solidus curve (~800 °C) for the $K_xFe_ySe_2$ system.[2] The single crystals of $K_xFe_ySe_2$ have been grown using multiple methods such as the flux method[2, 3, 7], flame melting[2] and the Bridgeman method[8]. These methods have been used on a range of nominal compositions from $K_{0.8}Fe_{1.6}Se_2$[9] to KFe_2Se_2[3]. With such a large range of nominal compositions and protocols the pathways that form superconducting crystals are not well defined. This means that a systematic study of the effect of the reaction protocols and starting composition on superconductivity is lacking and its production would be beneficial.

Considering the presence of phase separation in the $K_xFe_ySe_2$ system it is logical that powder materials be synthesised to study the bulk material. Using powders to study the system would give a much better idea of the phase assembly and possible candidates for the superconducting phase. The best and currently only example in the literature of powdered samples of $K_xFe_ySe_2$ materials was published by Shoemaker *et.al.* in 2011. Their powders were synthesised with the compositions $K_{0.8}Fe_{1.6}Se_2$ and $KFe_{1.6}Se_2$ at 700 °C then furnace cooled and followed by a homogenisation step at the same temperature.

After the homogenisation step the samples were cooled to ambient in 1 hour. Surprisingly none of the powder samples were superconducting despite having compositions in the range of the superconducting single crystals. However, PXRD and SQUID magnetometry performed on crushed single crystals of the superconducting material concluded that the phase responsible for superconductivity was the minority $K_xFe_ySe_2$ (SG = *I*4/*mmm*) phase.[2] The compositions of the superconducting phases were calculated from Rietveld refinement to be $K_{0.38(2)}Fe_{2.06(28)}Se_2$, $K_{0.55(1)}Fe_{2.00(2)}Se_2$ and $K_{0.58(2)}Fe_{2.00(2)}Se_2$ demonstrating a large spread in the compositions for the *I*4/*mmm* phase.[2] This work highlights the difficulty in defining the superconducting phase and that obtaining superconducting powders may need a cooling protocol that generates the correct lattice strain for the *I*4/*mmm* crystallites.

In addition to the two established potassium iron selenide phases a third was found by Shoemaker *et.al* (Figure 4.1). This phase is based upon a vacancy disordered material with the nominal composition of $KFe_{1.6}Se_2$ which has the space group of *I*4/*mmm*.[2] This phase could potentially cause serious problems with analysing PXRD data. As this vacancy disordered $KFe_{1.6}Se_2$ phase has an identical space group and a composition which is reasonably close to that of the $K_xFe_2Se_2$ phase this means that there may be issues with resolving these two phases.

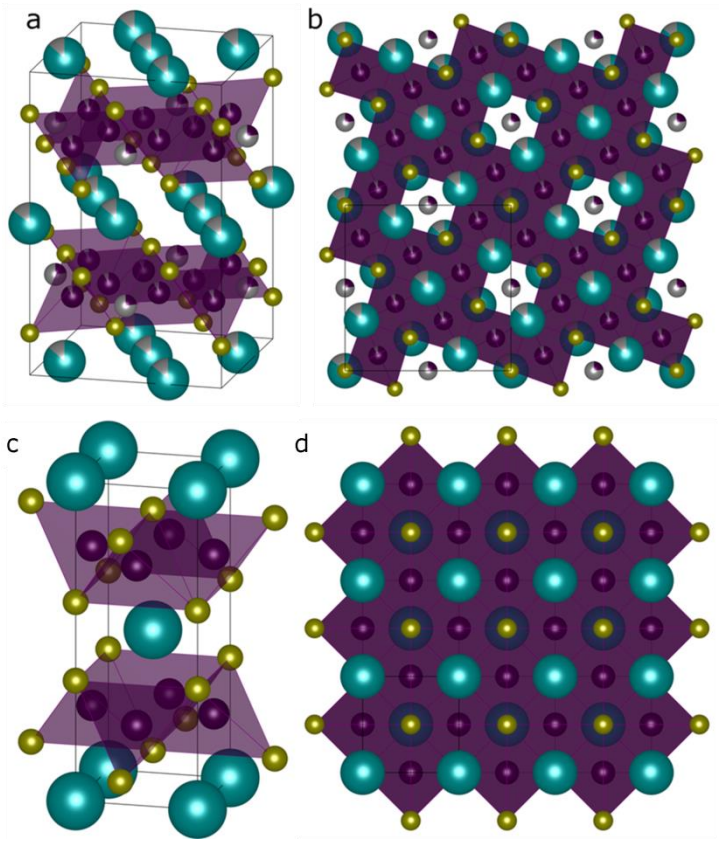

Figure 4.1 (a) Graphical representation of the of the possible crystal structures of $K_xFe_{2-x/2}Se_2$ products with ordered Fe vacancies (tetragonal, SG = *I*4/*m*) and (b) viewed along *c* axis. (c) Graphical representation of the crystal structure of $K_xFe_2Se_2$ products with adopting $ThCr_2Si_2$-structure type (tetragonal, SG = *I*4/*mmm*) and (d) viewed along *c* axis. The unit cell is highlighted as red rectangular. Fe atoms are purple, K atoms are green and Se atoms are yellow.

To overcome the uncertainty about the complex nature of the superconducting phase a systematic assessment of the phase equilibrium in the K-Fe-Se system is required. This can prove to be challenging due to highly air-sensitive nature of the prepared products and would require the assessment of the product without exposing them to ambient. However, the current studies of the K-Fe-Se compounds has been mainly based on single crystals with the most of data on the compositions of $K_xFe_{2-y}Se_2$ reported in the literature relying on local probes, such as energy dispersive X-ray (EDX) analysis which requires, even short, manipulations of the samples in air. This could lead to a significant deviation of stoichiometry, especially, for the experiments carried out on samples of the same nominal compositions but prepared in different labs. In addition to the synthetic and characterization challenges, single crystal growth requires melting of the product which inevitably leads to the reaction with the glass ampoule. This can further obscure the fine correlation between the initial composition and phase equilibrium in the system.

The aims of the experiments here is to firstly establish a phase diagram for the $K_xFe_ySe_2$ system; secondly to identify the critical areas of the phase diagram with respect to superconductivity; thirdly to identify the phase responsible for superconductivity. This strategy utilises solid state methods heavily adapted from Cava *et.al.* to obtain materials that have the best possible homogeneity.[4, 10] The materials produced will be investigated using SQUID magnetometry which will indicate important compositions. This will then be followed by powder X-ray diffraction which will identify the phase responsible for superconductivity.

4.2. Experimental

4.2.1. Synthesis of solid state precursors Fe_ySe_2

The Fe_ySe_2 precursors used in the following experiments were synthesised following the protocol outlined in Chapter 2 section 4.2.1. The exact amounts and target compositions are given in table 4.1.

Table 4.1 Reactant amounts and target compositions for the Fe_ySe_2 precursors.

ID	Target Fe_ySe_2 composition	Fe mass /g	Se mass /g
AG254	$Fe_{2.00}Se_2$	416.3	585.0
AG256	$Fe_{1.84}Se_2$	341.2	524.4
AG269	$Fe_{1.65}Se_2$	219.1	375.5
AG270	$Fe_{1.608}Se_2$	215.0	378.1
AG271	$Fe_{1.7}Se_2$	230.0	382.6
AG272	$Fe_{1.5}Se_2$	207.1	390.4
AG276	$Fe_{1.55}Se_2$	190.3	347.2
AG286	$Fe_{1.6}Se_2$	1104.209	1951.5
AG287	$Fe_{1.625}Se_2$	1167.723	2032
AG288	$Fe_{1.6}Se_2$	1118.0	1975.8
AG290	$Fe_{1.625}Se_2$	1164.8	2026.9
AG291	$Fe_{1.5875}Se_2$	1158.3	2064.2
AG292	$Fe_{1.6375}Se_2$	1190.8	2056.4
AG293	$Fe_{1.563}Se_2$	1146.8	2075.4
AG294	$Fe_{1.675}Se_2$	1257.0	2122.1
AG302	$Fe_{1.728}Se_2$	275.3	450.5
AG303	$Fe_{1.702}Se_2$	274.3	455.7
AG304	$Fe_{1.781}Se_2$	294.3	467.3
AG305	$Fe_{1.649}Se_2$	159.3	273.2
AG313	$Fe_{1.897}Se_2$	667.4	994.8
AG317	$Fe_{1.808}Se_2$	752.4	1175.4
AG318	$Fe_{1.868}Se_2$	488.7	739.7
AG319	$Fe_{1.49}Se_2$	329.3	625.0
AG320	$Fe_{1.524}Se_2$	369.7	689.2
AG328	$Fe_{1.754}Se_2$	425.5	686.0
AG329	$Fe_{1.836}Se_2$	423.3	651.9
AG330	$Fe_{1.925}Se_2$	469.5	686.2
AG331	$Fe_{1.728}Se_2$	425.2	695.8

4.2.2. Synthesis of $K_xFe_ySe_2$ materials

The $K_xFe_ySe_2$ material was made in an alumina crucible to prevent the reaction of potassium metal with the silica ampoule. Potassium metal (Aldrich, 99.95 %) was loaded into an alumina crucible along with stoichiometric amounts of Fe_ySe_2 precursor (Table 4.2). The crucible was pre-weighed and then carefully loaded into a silica ampoule (12 mm OD) before being connected to a dual vacuum manifold and sealed under a reduced pressure of argon gas (0.5 atm).

The ampoule was then placed into a calibrated furnace at room temperature before being heated to 750 °C at 1 °C min^{-1} and held there for three days (Figure 4.2 a). After the holding time had elapsed the ampoule was cooled at a rate of 2 °C min^{-1} to room temperature. It was observed that the glass ampoule was intact and without any evidence for reaction with potassium, which would be indicated by brownish tint of the silica (Figure 4.2 b). The ampoule was then opened an argon filled glove box and the sample mass was recorded by weighing the crucible. Only a marginal change in sample mass was observed indicating that no loss of the product due to reaction with the container took place. The phase composition of the products was identified from X-ray powder diffraction (both lab data and synchrotron radiation for selected products) which was carried out on a small amount (~8 mg) of material pre-loaded into a capillary (0.2 mm or 0.5 mm diameter). These samples were investigated for superconductivity by using a SQUID to record the magnetisation as a function of temperature on *c.a.* 30 mg of product sealed in a silica ampoule (6 mm OD). It was found that none of these materials contained any superconducting materials with a T_c greater than 8 K (β-FeSe) and therefore further annealing protocols are required.

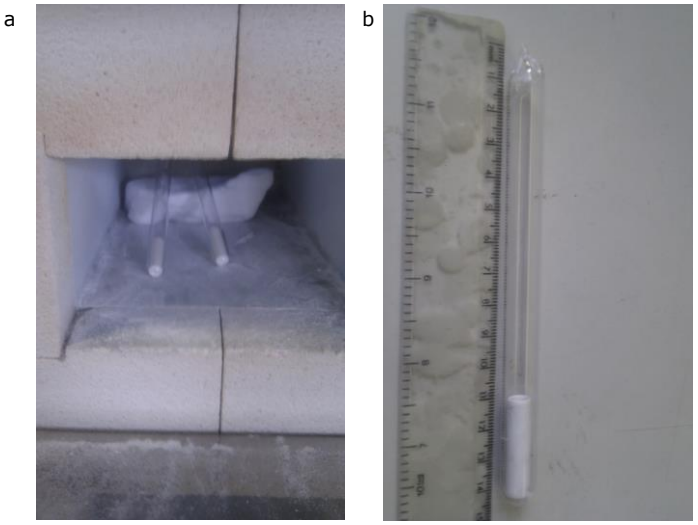

Figure 4.2 (a) Arrangement of sealed silica ampoules in the calibrated furnace before annealing. (b) Sealed silica ampoule containing alumina crucible loaded with material after annealing.

Table 4.2 List of $K_xFe_ySe_2$ materials made from the first annealing step (RT → 750 °C, 1 °C min^{-1}, 72 hours → RT, 2 °C min^{-1}) summarizing the target composition amounts of starting materials used, their target composition and the mass recovered from the first annealing step.

ID	Target Composition	Corresponding Fe_ySe_2 precursor	Potassium /mg	Fe_ySe_2 /mg
AG277_1	$K_{0.7}Fe_{1.65}Se_2$	AG269	30.0	274.1
AG278_1	$K_{0.784}Fe_{1.608}Se_2$	AG270	33.5	270.7
AG279_1	$K_{0.6}Fe_{1.7}Se_2$	AG271	27.6	297.5
AG281_1	$K_{0.9}Fe_{1.55}Se_2$	AG276	35.7	247.3
AG282_1	$K_{1.0}Fe_{1.5}Se_2$	AG272	37.0	228.7
AG295_1	$K_{0.8}Fe_{1.675}Se_2$	AG294	28.6	225.1
AG298_1	$K_{0.8}Fe_{1.84}Se_2$	AG256	30.2	244.2
AG300_1	$K_{0.8}Fe_{2.04}Se_2$	AG254	28.7	244.2
AG306_1	$K_{0.7}Fe_{1.728}Se_2$	AG302	30.2	278.0
AG307_1	$K_{0.85}Fe_{1.728}Se_2$	AG302	35.0	265.7
AG308_1	$K_{0.75}Fe_{1.702}Se_2$	AG303	31.5	269.2
AG309_1	$K_{0.9}Fe_{1.702}Se_2$	AG303	37.3	268.2
AG310_1	$K_{0.85}Fe_{1.649}Se_2$	AG305	35.7	268.6
AG311_1	$K_{0.75}Fe_{1.781}Se_2$	AG304	29.8	261.6
AG315_1	$K_{0.9}Fe_{1.625}Se_2$	AG290	33.2	234.6
AG321_1	$K_{0.7}Fe_{1.897}Se_2$	AG313	28.5	273.8
AG322_1	$K_{0.7}Fe_{1.808}Se_2$	AG317	28.3	267.3
AG323_1	$K_{0.75}Fe_{1.868}Se_2$	AG318	31.0	276.9
AG326_1	$K_{0.85}Fe_{1.810}Se_2$	AG317	36.1	279.9
AG327_1	$K_{0.7}Fe_{1.728}Se_2$	AG302	110.0	1022.6
AG332_1	$K_{0.65}Fe_{1.754}Se_2$	AG328	33.2	334.3
AG333_1	$K_{0.65}Fe_{1.868}Se_2$	AG318	31.8	325.9
AG334_1	$K_{0.65}Fe_{1.925}Se_2$	AG330	29.8	307.1
AG335_1	$K_{0.75}Fe_{1.625}Se_2$	AG290	29.8	253.4
AG336_1	$K_{0.8}Fe_{1.6}Se_2$	AG286	34.8	275.1
AG337_1	$K_{0.5}Fe_2Se_2$	AG254	22.8	314.5
AG350_1	$K_{0.6}Fe_{1.925}Se_2$	AG330	25.3	286.3
AG351_1	$K_{0.55}Fe_{1.897}Se_2$	AG313	25.6	314.1
AG352_1	$K_{0.6}Fe_{1.868}Se_2$	AG318	27.6	308.5
AG353_1	$K_{0.6}Fe_{1.808}Se_2$	AG317	27.3	301.3
AG354_1	$K_{0.6}Fe_{1.781}Se_2$	AG304	26.9	295.1
AG422_1	$K_{0.75}Fe_2Se_2$	AG254	29.7	273.1
AG424_1	$K_{0.8}Fe_{1.754}Se_2$	AG328	35.3	288.7
AM70_1	$K_{0.5}Fe_{1.836}Se_2$	AG329	22.0	293.3
AM71_1	$K_{0.5}Fe_{1.925}Se_2$	AG330	22.1	300.2
AM72_1	$K_{0.55}Fe_{1.925}Se_2$	AG330	23.5	290.3

4.2.2.1. Quenched protocol

Two additional annealing protocols were carried out in order to obtain superconducting samples. For the first method, dubbed the quenched protocol, $K_xFe_ySe_2$ (typically *ca*. 80 mg) was pre-loaded into an alumina crucible and the mass of crucible was recorded before it was carefully loaded into a silica ampoule (12 mm OD) (Table 4.3). The ampoule was then connected to a dual vacuum manifold and sealed under a low pressure of argon gas (0.5 atm). The ampoule was then placed into a calibrated furnace at room temperature before being heated to 750 °C at 1 °C min^{-1} and held there for three days. After the holding time had elapsed the ampoule was removed from the furnace using metal tongs and placed on a heat proof mat. No evidence for the reaction of the product with the container was observed. The ampoule was then opened in an argon filled glove box and the samples mass recorded by weighting the mass of the crucible. A small amount (~8 mg) of material was loaded into a capillary for X-ray diffraction.

Table 4.3 Summary of $K_xFe_ySe_2$ material prepared by the following quenched protocol

ID	Target Composition	Composition ICP
AG277_3	$K_{0.7}Fe_{1.65}Se_2$	$K_{0.685(9)}Fe_{1.699(8)}Se_{2.00(2)}$
AG278_3	$K_{0.784}Fe_{1.608}Se_2$	$K_{0.722(6)}Fe_{1.65(2)}Se_{2.00(3)}$
AG279_2	$K_{0.6}Fe_{1.7}Se_2$	$K_{0.52(2)}Fe_{1.70(5)}Se_{2.000(7)}$
AG281_3	$K_{0.9}Fe_{1.55}Se_2$	$K_{0.82(1)}Fe_{1.58(2)}Se_{2.000(8)}$
AG282_4	$K_{1.0}Fe_{1.5}Se_2$	$K_{0.93(2)}Fe_{1.56(5)}Se_{2.00(1)}$
AG295_3	$K_{0.8}Fe_{1.675}Se_2$	$K_{0.77(2)}Fe_{1.66(1)}Se_{2.000(8)}$
AG298_3	$K_{0.8}Fe_{1.84}Se_2$	$K_{0.832(4)}Fe_{1.1.870(7)}Se_{2.00(1)}$
AG300_2	$K_{0.8}Fe_{2.04}Se_2$	
AG306_2	$K_{0.7}Fe_{1.728}Se_2$	$K_{0.710(4)}Fe_{1.78(3)}Se_{2.00(1)}$
AG307_3	$K_{0.85}Fe_{1.728}Se_2$	$K_{0.844(5)}Fe_{1.780(4)}Se_{2.00(2)}$
AG308_3	$K_{0.75}Fe_{1.702}Se_2$	$K_{0.70(6)}Fe_{1.68(10)}Se_{2.00(3)}$
AG309_2	$K_{0.9}Fe_{1.702}Se_2$	$K_{0.85(8)}Fe_{1.71(4)}Se_{2.00(4)}$
AG310_2	$K_{0.85}Fe_{1.649}Se_2$	$K_{0.80(2)}Fe_{1.70(1)}Se_{2.00(1)}$
AG311_2	$K_{0.75}Fe_{1.781}Se_2$	$K_{0.70(8)}Fe_{1.80(2)}Se_{2.00(3)}$
AG315_2	$K_{0.9}Fe_{1.625}Se_2$	$K_{0.86(2)}Fe_{1.58(2)}Se_{2.00(1)}$
AG321_2	$K_{0.7}Fe_{1.897}Se_2$	$K_{0.702(5)}Fe_{1.95(2)}Se_{2.000(9)}$
AG322_2	$K_{0.7}Fe_{1.808}Se_2$	$K_{0.695(4)}Fe_{1.87(1)}Se_{2.00(2)}$
AG323_2	$K_{0.75}Fe_{1.868}Se_2$	$K_{0.740(4)}Fe_{1.92(2)}Se_{2.00(1)}$
AG324_2	$K_{0.85}Fe_{1.524}Se_2$	$K_{0.82(8)}Fe_{1.56(2)}Se_{2.00(4)}$
AG326_2	$K_{0.85}Fe_{1.810}Se_2$	$K_{0.79(12)}Fe_{1.80(7)}Se_{2.00(6)}$
AG332_2	$K_{0.65}Fe_{1.754}Se_2$	$K_{0.605(7)}Fe_{1.82(1)}Se_{2.0(1)}$
AG333_2	$K_{0.65}Fe_{1.868}Se_2$	$K_{0.669(4)}Fe_{1.882(8)}Se_{2.00(2)}$
AG334_2	$K_{0.65}Fe_{1.925}Se_2$	$K_{0.658(5)}Fe_{1.93(2)}Se_{2.00(2)}$
AG335_3	$K_{0.75}Fe_{1.625}Se_2$	$K_{0.70(2)}Fe_{1.65(3)}Se_{2.00(1)}$
AG336_3	$K_{0.8}Fe_{1.6}Se_2$	$K_{0.76(4)}Fe_{1.65(1)}Se_{2.000(3)}$
AG337_3	$K_{0.5}Fe_2Se_2$	
AG350_2	$K_{0.6}Fe_{1.925}Se_2$	
AG351_2	$K_{0.55}Fe_{1.897}Se_2$	$K_{0.512(2)}Fe_{1.88(3)}Se_{2.00(1)}$
AG352_2	$K_{0.6}Fe_{1.868}Se_2$	$K_{0.55(1)}Fe_{1.87(3)}Se_{2.00(5)}$
AG353_2	$K_{0.6}Fe_{1.808}Se_2$	$K_{0.66(4)}Fe_{1.89(7)}Se_{2.00(6)}$
AG354_2	$K_{0.6}Fe_{1.781}Se_2$	$K_{0.61(6)}Fe_{1.80(6)}Se_{2.00(5)}$
AG422_2	$K_{0.75}Fe_2Se_2$	$K_{0.62(9)}Fe_{2.04(2)}Se_{2.00(6)}$
AG424_2	$K_{0.8}Fe_{1.754}Se_2$	$K_{0.73(8)}Fe_{1.79(13)}Se_{2.00(5)}$
AM70_2	$K_{0.5}Fe_{1.836}Se_2$	$K_{0.45(14)}Fe_{1.90(2)}Se_{2.00(7)}$
AM71_2	$K_{0.5}Fe_{1.925}Se_2$	$K_{0.45(3)}Fe_{1.97(3)}Se_{2.00(2)}$
AM72_2	$K_{0.55}Fe_{1.925}Se_2$	$K_{0.50(2)}Fe_{1.92(5)}Se_{2.00(2)}$

4.2.2.2. Slow cooled protocol

The second annealing protocol, dubbed the slow cooled protocol, performed was performed in an identical fashion as described for the quenched protocol except for the cooling protocol. The ampoules containing $K_xFe_ySe_2$, once sealed, were heated from room temperature to 750 °C at a rate of 2 °C min^{-1} and held at that temperature for 3 days. The ampoules were then cooled to room temperature at a rate of 2 °C min^{-1} within the furnace. These materials were taken to an argon filled glove box and treated in an identical way to the materials produced by the quenched protocol.

The materials produced by the quenched protocol were superior in quality, gauged by the higher crystallinity of the powder patterns and larger SFs, than those made by the slow cooled protocol. Due to the large numbers of samples and analytical data involved in the production of the phase diagram for this material the quenched protocol materials are focused on in this work. The reasons for focusing on the quenched protocol materials are discussed in more detail in section 4.4.

4.2.3. Method: Powder X-ray diffraction

High resolution synchrotron powder X-ray diffraction (SPXRD) data were collected for selected samples at beamlines I11 (Diamond Light Source, λ = 0.826141, 0.827146 and 0.827153 Å), ID31 (ESRF, λ = 0.49937 Å) and BL44B2 (SPring-8, λ = 0.49937 Å). Capillary OD was selected depending on wavelength in order to allow enough X-ray transmission to keep the absorption correction within sensible limits.

Samples were collected at I11 on both the MAC and PSD detectors. Data collected on the PSD detector exhibited anomalous peaks at high angles. On observing the two separate detector scans it was noticed that the anomalous peaks occurred in different positions indicating that it is a fixed artefact and not part of the sample itself. This could be the result of a detector intensity calibration problem or particular silicon strips on the detector could be faulty. Fortunately the anomalous peaks occur in a region of the pattern which is not vital to the refinement and so the peaks were excluded.

4.3. Room temperature synchrotron x-ray analysis refinement model

4.3.1. $K_xFe_ySe_2$ *I*4/*m* structural model

In the following subsection a detailed description is given of the methods used to develop the best model for the *I*4/*m* phase for use in Rietveld refinement. The refinement model for the *I*4/*m* phase was developed on the AG278_3 material chosen due to its purity and crystallinity. The refinement model for the *I*4/*mmm* phase was refined against material which also gave the highest crystallinity for this phase (AG308_3). The effects of axial divergence were modeled by a single refined parameter using the "simple axial model" within TOPAS V5.

TOPAS does not automatically calculate the anomalous scattering factors (*f'* and *f''*) for energies above 30 KeV, so values obtained from the NIST X-ray form factor, attenuation and scattering tables (Table 4.4) were entered manually.[11, 12]

Table 4.4 Anomalous dispersion coefficients as calculated from the NIST X-ray form factor, attenuation and scattering tables.

Coefficient / Atom	*f'*	*f''*
K	0.1119	0.084188
Fe	0.2618	0.30571
Se	0.4171	0.85771

Inspection of the synchrotron powder X-ray diffraction (SPXRD) profiles of the $K_xFe_{2-x/2}Se_2$ series indicated the presence of multiple phases in various combinations. These phases correspond to $K_xFe_ySe_2$ (SG = *I*4/*m*), $K_xFe_2Se_2$ (SG = *I*4/*mmm*), FeSe (SGs = *P*4/*nmmz* and *P*63/*mmc*) and Fe (SG = $Im\bar{3}\,m$). Irrespective of the sample composition, the majority phase present in these $K_xFe_{2-x/2}Se_2$ materials always has the space group *I*4/*m* and therefore its refinement model will be discussed first.

The initial structural model used to refine the *I*4/*m* phase is based upon a fivefold *ab* plane expansion of the *I*4/*mmm* unit cell, equivalent to the $ThCr_2Si_2$-structure type, which then allows the accommodation of the required Fe and K vacancies.[7] The diffraction pattern of the *I*4/*m* phase contains superstructure reflections associated with Fe-vacancy ordering within Fe-Se layer, in addition to subcell reflections of the parent *I*4/*mmm* unit cell.[7, 13]

Analysis of the diffraction pattern obtained from the material synthesized at a nominal composition of $K_{0.784}Fe_{1.608}Se_2$ (designation AG278_2; analyzed composition $K_{0.722(6)}Fe_{1.65(2)}Se_{2.00(3)}$) reveals a high purity *I*4/*m* sample that presents complex microstructural effects. A Williamson-Hall plot reveals that the Bragg reflections are anisotropically broadened as the integral breadth values for each reflection are randomly scattered rather than lying along a straight line (Figure 4.3).

The instrumental contribution to the integral breadths (IB) were determined using a silicon standard (SRM 640c); a single pseudo-Voigt peak shape with three contributions (varying linearly with θ, varying as a function of 1/cosθ and tanθ, respectively) to both Gaussian and Lorentzian functions was used to obtain the instrument broadening contribution as a function of 2θ in radians (Equation 4-1). Equation 4-1 is the quadratic equation used to calculate the instrumental integral breadth (IB_{inst}) where a = 1.97 x 10^{-3}, b = 8.49 x10^{-5}, c = 2.88 x10^{-3} and x corresponds to 2θ in radians.

$$ax^2 + bx + c = \mathbf{IB_{inst}} \qquad \textbf{(4-1)}$$

The calculated IB due to instrument broadening from this function was then subtracted from the observed IB values for each Bragg reflection of the *I*4/*m* phase (figure 4.3). The profile of the *I*4/*m* phase is complex with anisotropic broadening of both the supercell and subcell reflections. Anisotropic peak width broadening is normally an indication of microstructure, such as anisotropic size or strain along different crystal directions.[14] This is not a surprising observation as the potassium iron selenide structure is based on layers of FeSe separated by potassium ions and so the FeSe layers are susceptible to stacking faults.[5, 7, 15]

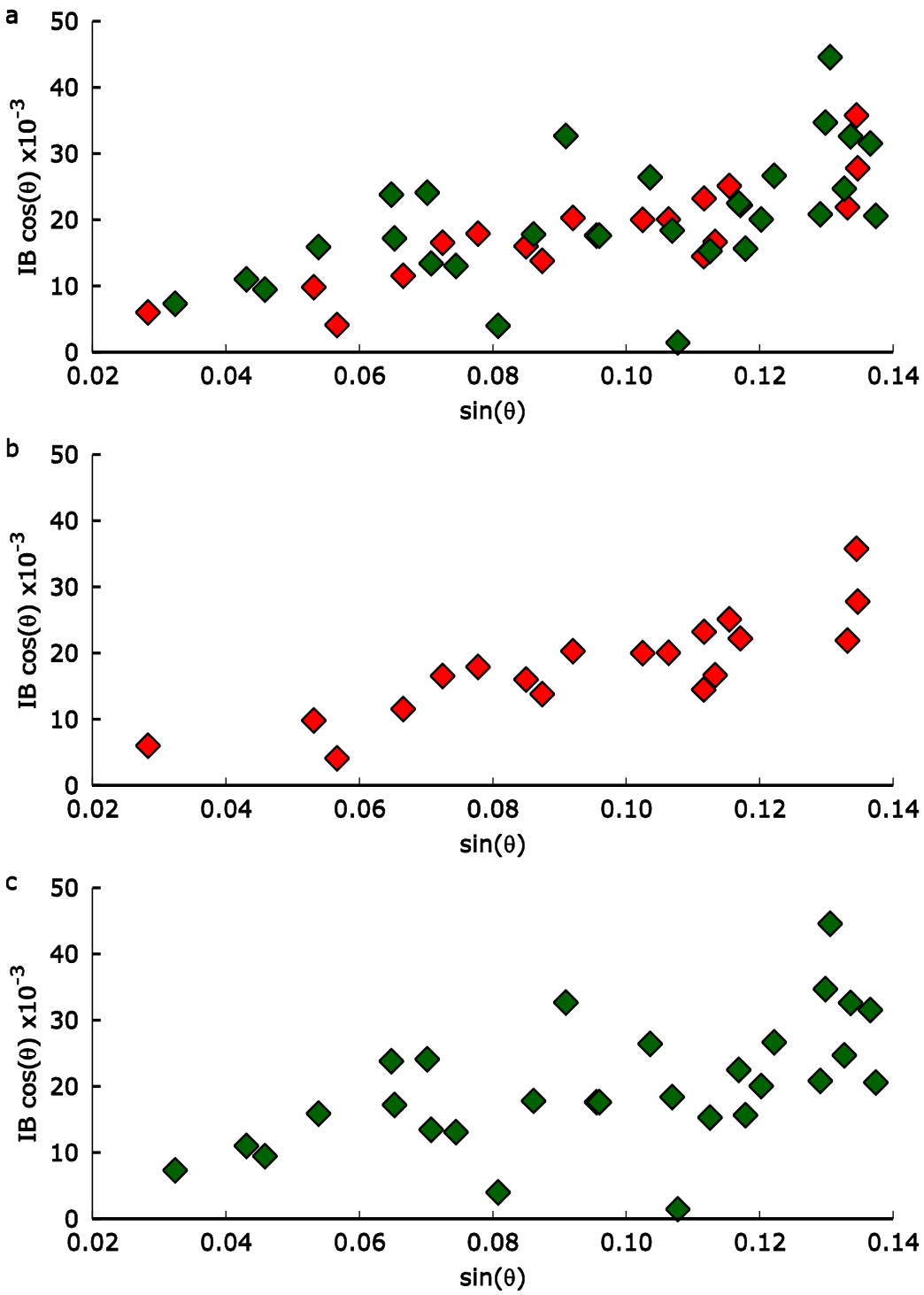

Figure 4.3. Williamson-Hall plots for the *I*4/*m* phase from material AG278_3 ($K_{0.784}Fe_{1.608}Se_2$) utilising integral breath (IB) cos(θ) vs. sin(θ) to display any trends in peak broadening with increasing θ. The errors are set at 5σ but are contained underneath the points. An ideal case of isotropic strain would produce a straight line with a positive gradient. A silicon standard was used to calculate the instrumental contribution which was subsequently removed from the *I*4/*m* IB values. (a) Shows a plot including both subcell and supercell peaks. (b) Displays the plot for the subcell reflections only and (c) gives the plot for the supercell reflections in isolation.

Initial Rietveld refinements models failed to generate acceptable fits to the observed data. This was due to the profile widths of the *I*4/*m* phase being poorly described by the peak shapes initially used (Thompson-Cox-Hastings (TCHZ) and Stephens' anisotropic peak shape). Therefore the next step was to obtain an acceptable fit to the sample peak shape, so that the structure factors can be reliably determined for each Bragg reflection.

The simplest method of determining a suitable peak shape function is to use a Pawley refinement, so that the peak profile can be determined in the absence of structural considerations. The cell parameters published in Bacsa *et.al.* provides a good starting point for this task.[7] For the initial Pawley fit the background, zero offset, axial divergence and cell parameters were refined along with a pseudo-Voigt (PV) peak shape for the *I*4/*m* phase. Although it converged quickly the refinement was highly unstable due to the poor fit produced by the description of the profile using the PV peak type. The most noticeable mis-matches are for the (002) and (123) reflections at Q of 0.890 and 2.092 $Å^{-1}$ respectively (Figure 4.4). The presence of anisotropy is best shown by the difference between isotropic and anisotropic PV peak shapes after full refinement of all parameters.

The inclusion of an anisotropic tensor (400, 004, 220, 202 and 310 directional strain terms were used in a Stephens anisotropic peak shape style[14]). This yields a drop in R_{wp} of 0.75 % and gives a significantly improved fit for the (002) and (123) reflections (Figure 4.4). Further improvements in the fit to the observed peak shape can be achieved through the introduction of peak asymmetry via the implementation of a split pseudo-Voigt (SPV). The improvement is most noticeable on the reflections (002), (110) and (123) (Figure 4.5) and results in a further drop in R_{wp} of 0.5 %.

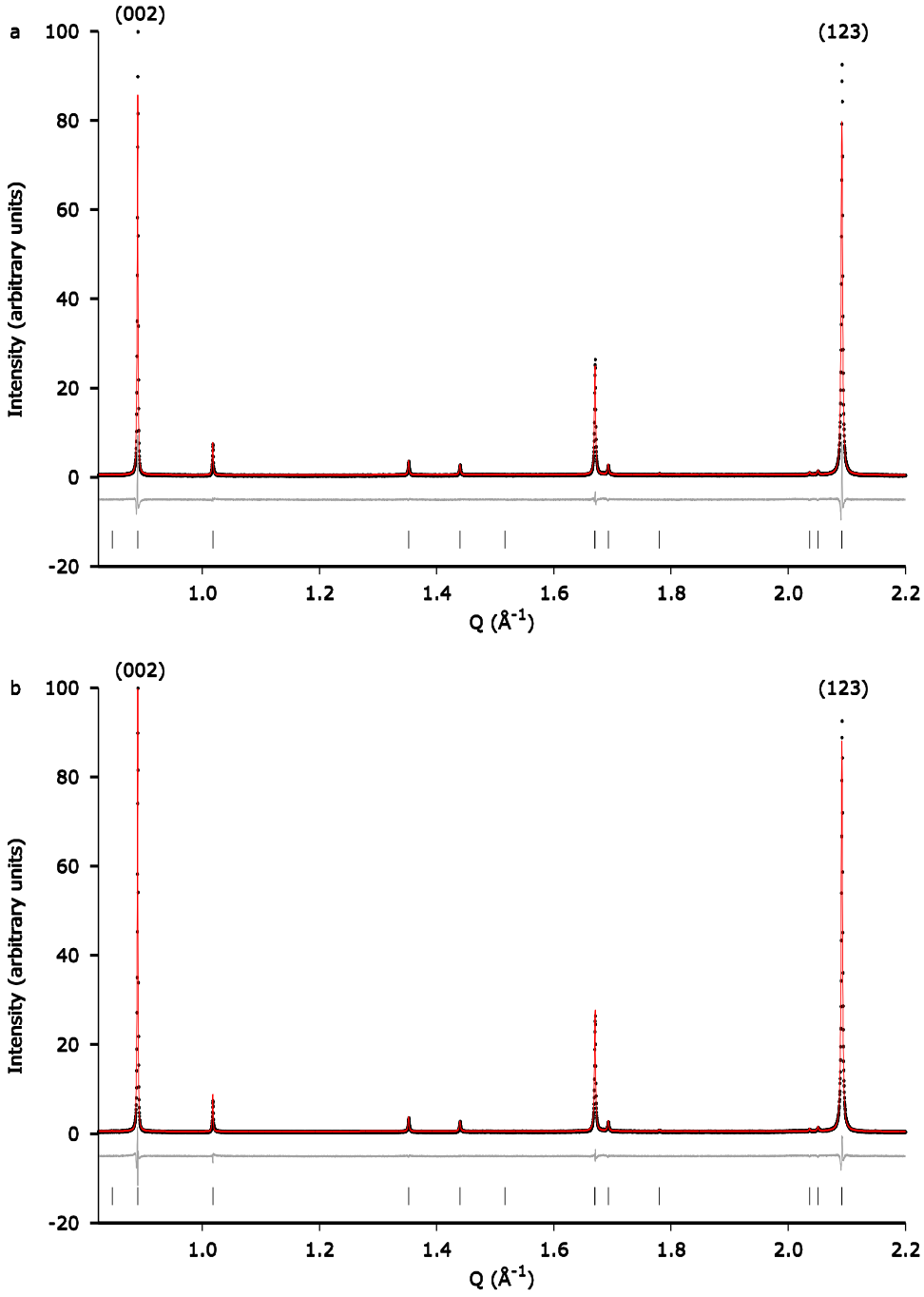

Figure 4.4. Pawley refinement plot for the material produced with the composition $K_{0.784}Fe_{1.608}Se_2$(AG278_3). The model was refined against SPXRD data at a wavelength of λ = 0.399892 Å. Observed (black dots), calculated (red line) and difference (grey line) data are shown. The tic marks represent Bragg reflection positions of the *I*4/*m* (black) phase. (a) This fit was produced using a pseudo-Voigt peak shape. R_{wp} = 7.94, R_{exp} = 5.85, number of refined parameters 703. (b) This fit was produced using a pseudo-Voigt peak shape including peak width anisotropy. R_{wp} = 7.19, R_{exp} = 5.80, number of refined parameters 709.

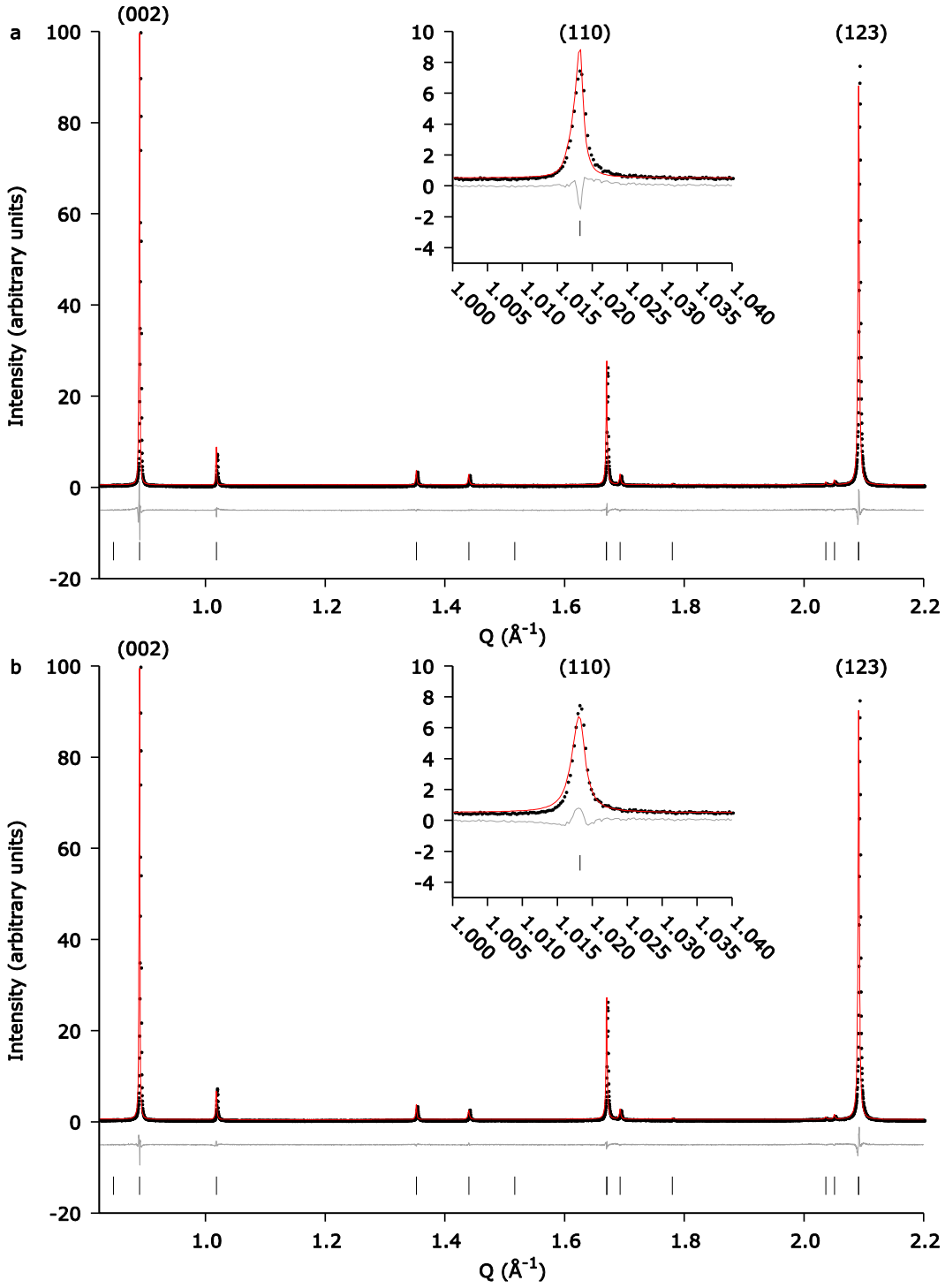

Figure 4.5. Pawley refinement plot for the material produced with the composition $K_{0.784}Fe_{1.608}Se_2$(AG278_3). The model was refined against SPXRD data at a wavelength of λ = 0.399892 Å. Observed (black dots), calculated (red line) and difference (grey line) data are shown. The tic marks represent Bragg reflection positions of the *I*4/*m* (black) phase and the insets are an enlargement of the (110) reflections. (a) This fit was produced using a pseudo-Voigt peak shape including peak width anisotropy. R_{wp} = 7.19, R_{exp} = 5.80, number of refined parameters 709. (b) This fit was produced using a pseudo-Voigt peak shape including peak width anisotropy and asymmetry. R_{wp} = 6.61, R_{exp} = 5.77, number of refined parameters 715.

The final Pawley fit (Figure 4.5 b) has a total of 715 independent parameters taking part in the refinement. The majority of these (681 parameters) are the integrated intensities for each of the possible reflections between Q = 0.8125 and 8.125 Å. The remaining 34 parameters correspond to the 13 Chebyshev polynomial background parameters; axial divergence; zero point error; 2 lattice parameters (*a* and *c*) and 17 peak shape parameters.

The breakdown of the 17 peak shape parameters are given in tables 4.5-4.7. The peak shape parameters consist of 2θ independent, 1/cos(θ) dependent and tan(θ) terms for both sides of the peaks and for the FWHM and PV mixing parameters. The tan(θ) dependent terms are then broken down into directional quantities which are refined for the whole profile. The profile widths relationship with 2θ reveals a strong dependency on tan(θ) terms indicating that the *I*4/*m* phase is heavily strained (Table 4.6). The anisotropic strain terms in table 4.7 indicate that the strain is distributed primarily along the *ab* plane.

Table 4.5 Summary of the refined parameters for the SPV peak shapes mixing parameters used to calculate the profile widths of the *I*4/*m* phase in a Rietveld refinement.

Parameter / Side	PV mixing parameters		
	Independent	**1/cos(θ)**	**tan(θ)**
Left	0.684(2)	0.341(2)	5.0(2)
Right	1.038(2)	0.017(2)	5.0(2)

Table 4.6 Summary of the refined parameters for the SPV peak shapes FWHM used to calculate the profile widths of the *I*4/*m* phase in a Rietveld refinement.

Parameter / Side	FWHM		
	2θ Independent	**size**	**strain**
Left	0	0.0006(1)	0.970(2)
Right	0	0	0.974(2)

Table 4.7 Summary of the refined parameters (contribution to the FWHM in radians) for the anisotropic strain profile shape restrained to tetragonal symmetry.

Direction	**400**	**004**	**220**	**202**	**310**
value	2.70(2)	0.220(2)	8.45(14)	1.52(2)	-4.16(6)

Once the peak shape is defined a full Rietveld refinement can be performed yielding structural information which is crucial to determining the role of this phase in the superconducting materials. The Rietveld refinement of the *I4/m* phase uses the "final" Pawley fit shown in figure 4.5 b as a starting point. The structural information provided by Bacsa *et.al.* was used as a starting point for the atom positions, occupancies and thermal parameters. Initially the peak

shape was fixed and only the scale factor was refined in addition to the parameters indicated in the Pawley fit.

Once converged the other parameters were then refined in the following sequence; atomic positions; occupancies (Se occupancies were fixed at 1) and finally displacement parameters. This allowed the refinement to converge to chemically sensible values for the occupancies and displacement parameters. The peak shape was then allowed to refine to accommodate the change in peak intensity due to calculation from structure factors (in the Rietveld refinement) rather than as a free parameter (in the Pawley refinement). Great care was taken to refine the peak shape by refining the terms one by one, so that the simultaneous refinement of highly correlated parameters would not result in unrealistic values. The peak shape was once again fixed to allow the occupancies and displacement parameters to be refined sequentially to their final values. The fit produced from the Rietveld refinement of the *I*4/*m* phase has an R_{wp} which was only 0.63 % larger than that obtained from the Pawley fit, indicating that the refined model is acceptable (Figure 4.6, Table 4.8 and 4.9).

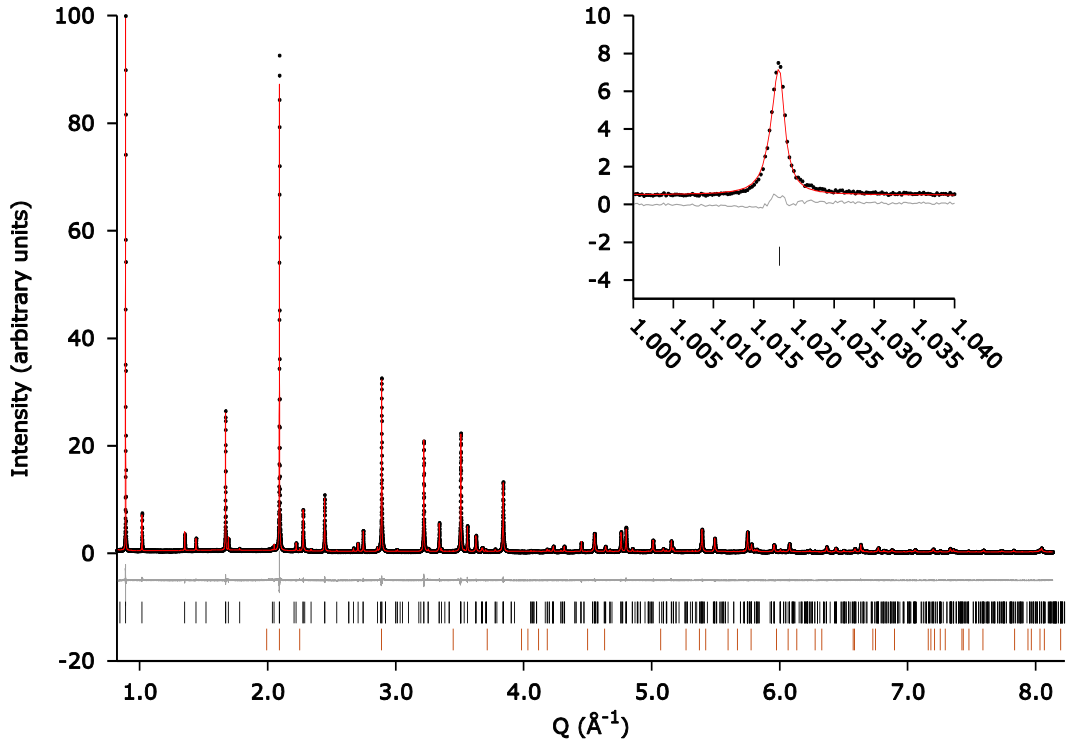

Figure 4.6. Rietveld refinement plot for the material produced with the composition $K_{0.784}Fe_{1.608}Se_2$ (AG278_3). The model was refined against SPXRD data at a wavelength of λ = 0.399892 Å. This fit was produced using a pseudo-Voigt peak shape including anisotropy and asymmetry. Observed (black dots), calculated (red line) and difference (grey line) data are shown. The tic marks represent Bragg reflection positions of the *I4/m* (black) and *δ*-FeSe (orange) phases. The inset shows an expansion of the (110) reflection of the *I*4/*m* phase. R_{wp} = 7.24, R_{exp} = 5.84 and number of refined parameters 57.

Table 4.8. Details from the Pawley and Rietveld refinement of the data displayed in Figures 4.5 and 4.6 respectively.

ID / Parameter	*AG278_3*	*AG278_3*
Refinement	Rietveld	Pawley
R_{wp} **(%)**	7.24	6.61
R_{exp} **(%)**	5.84	5.77
λ (Å)	0.399892	0.399892
***I4/m* (%)**	99.982(2)	N/A
δ-FeSe (%)	0.018(2)	N/A
***I4/m* (V/√5) (Å^3)**	215.0311(8)	215.0228(9)
***I4/m* xrd composition**	$K_{0.785(3)}Fe_{1.587(3)}Se_2$	N/A

Table 4.9 Summary of the results of the RT refinement on AG278_3 with the composition of $K_{0.784}Fe_{1.608}Se_2$ for the *I4/m* phase.

Atom	*x/a*	*y/b*	*z/c*	*N*	B_{Iso} (Å^2)
K1	0.5	0.5	0	0.94(1)	5.3(3)
K2	0.30055(6)	0.8972(4)	0	0.745(3)	2.39(6)
Fe1	0.3011(2)	0.4081(1)	0.2472(3)	0.962(2)	1.24(2)
Fe2	0.5	0	0.25	0.117(3)	0.36(5)
Se1	0	0	0.1387(1)	1	1.13(4)
Se2	0.3896(1)	0.2005(1)	0.14539(4)	1	1.36(1)

The quality of fit for the SPXRD data of this material is very good, indicating that the calculated model should be representative of the average structure. This is further confirmed in the overall refined composition which is calculated to be $K_{0.785(5)}Fe_{1.587(3)}Se_2$ is close to the nominal composition of $K_{0.784}Fe_{1.608}Se_2$ and the analyzed composition of $K_{0.722(6)}Fe_{1.65(2)}Se_{2.00(3)}$. This indicates that the structural model is good, however, there are some discrepancies in several of the peaks which are most noticeable in the (123) and (420) reflections (Table 4.10 and Figure 4.7). This deviation is typical of the Bragg reflection not being in the correct position, but other peaks such as that of the (312) reflection (Q = 2.44 $Å^{-1}$) do not suffer from this problem. There are two possible explanations for such a deviation; an anisotropic peak shift due to stacking faults or an incommensurate modification to the average structure. Both possibilities are valid for this system where the possibility of an incommensurate structure is based upon the fact that if the iron composition was to change the commensurate modulations could become incommensurate.[7]

The other possibility of stacking faults was noted by Bacsa *et.al*. in 2011 as extensions of the reflections along *c** in the observed single crystal data. In addition to this the potassium iron selenide materials were observed using TEM to have inhomogeneous microstructure along the *c*-axis.[5] These observations support the use of peak shapes that can model asymmetry and anisotropic peak widths as they are a common problem in materials with stacking faults.[15]

Table 4.10 Summary of hkl positions were the Bragg reflection is shifted off the peak maxima.

hkl	Bragg position shift	Q ($Å^{-1}$)
(123)	Lower Q	2.09
(312)	Lower Q	2.45
(134)	Lower Q	2.89
(420)	Lower Q	3.22

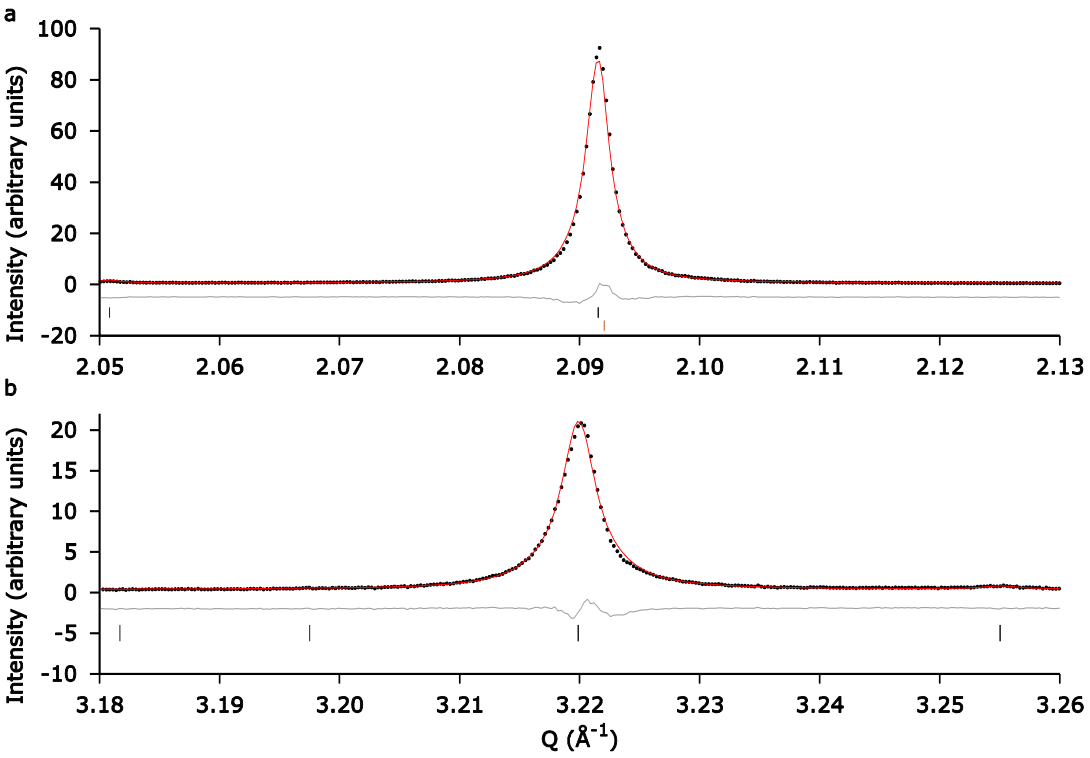

Figure 4.7 Rietveld refinement plots for the material produced with the composition $K_{0.784}Fe_{1.608}Se_2$ (AG278_3). The model was refined against SPXRD data at a wavelength of λ = 0.399892 Å. Enlarged images of the (123) and (240) reflections of the *I4/m* phase where the black and orange hkl ticks represent the *I4/m* and *δ*-FeSe phases respectively. (a) Displays the (123) reflection and the difference line a calculated peak position that is at a higher Q position than the observed peak. (b) Shows the (240) reflection suffers from the same calculated peak position issue as the (123) peak.

An anisotropic peak shift was tested for Bragg reflections which have a contribution in the basal *ab* plane and in the (00*l*) direction as the inhomogeneous microstructure was observed along this direction.[5] In addition to testing the anisotropic shift generally across all reflections the correction was also applied to the supercell and subcell reflections individually. However, no combination of peak shift corrections could account for the observed anomalous peak shifts within a reasonable number of parameters. The inability to model the peak shifts suggests that the anomalous peak shifts are unlikely to be due to stacking faults alone. Another possible source of the peak shifts could be due to the commensurate supercell modulations becoming incommensurate for certain iron compositions as suggested by Bacsa *et.al.*[7]

4.3.2. $K_xFe_2Se_2$ *I*4/*mmm* structural model

The second structure that requires detailed study is the *I*4/*mmm* structure which is based upon $ThCr_2Si_2$ structure. The best example, with the largest number of non-overlapped reflections, of the *I*4/*mmm* structure is the material with the composition $K_{0.75}Fe_{1.702}Se_2$ (AG308_3, Figure 4.8 and Table 4.11 to 4.13). The *I*4/*mmm* phase is the minority potassium-intercalated iron selenide phase, and the challenges of defining its structure are twofold. Firstly, due to the similarity of the *I*4/*mmm* structure to that of the *I*4/*m* phase, all but two of the Bragg reflections are overlapped to some degree. This means that it is much more difficult to extract meaningful and reliable information from the peak shape using Williamson-Hall plots and Pawley fits.

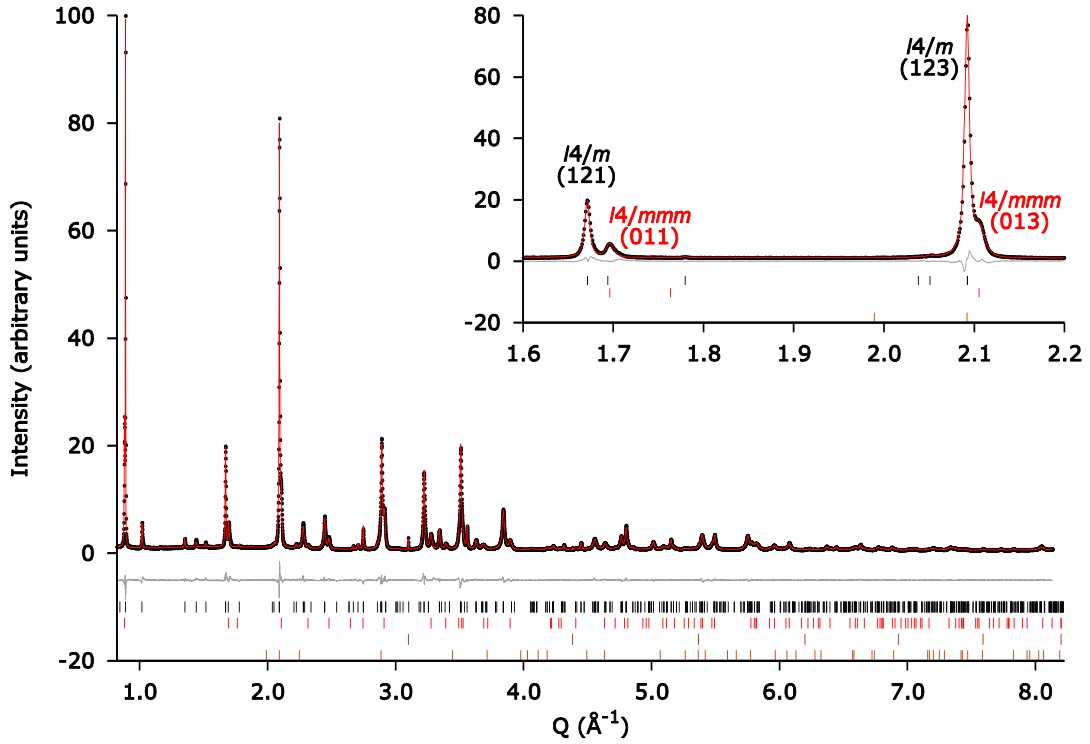

Figure 4.8 Rietveld refinement plot for the material produced with the composition $K_{0.75}Fe_{1.702}Se_2$ (AG308_3). The model was refined against SPXRD data at a wavelength of λ = 0.399892 Å. Observed (black dots), calculated (red line) and difference (grey line) data are shown. The tic marks represent Bragg reflection positions of the *I*4/*m* (black), *I*4/*mmm* (red), Fe (brown) and *δ*-FeSe (dark orange) phases. The insert shows the presence of both the *I*4/*m* and *I*4/*mmm* phases and the extent of the overlap between the two, in particular the *I*4/*m* (123) and *I*4/*mmm* (013) reflections. R_{wp} = 5.62, R_{exp} = 2.83, number of refined parameters 91.

Table 4.11 Summary of the phase fractions and cell parameters calculated from the RT refinement on AG308_3 with the composition of $K_{0.75}Fe_{1.702}Se_2$.

Parameter / Phase	Phase Fraction vol.%	*a*	*c*	Volume
I4/m	16.1983(951)	8.71912(7)	14.1204(1)	1073.48(2)
I4/mmm	83.6918(951)	3.83600(7)	14.2523(4)	209.72(1)
Fe	0.1022(3)	2.86710(5)	N/A	23.568(1)
***δ*-FeSe**	0.0077(2)	3.6472(6)	6.007(2)	69.20(3)

Table 4.12 Summary of the structural results of the RT refinement on AG308_3 with the composition of $K_{0.75}Fe_{1.702}Se_{2\ for}$ the *I4/m* phase.

Atom	*x/a*	*y/b*	*z/c*	*N*	B_{Iso} (Å^2)	$U_{11}=U_{22}$ (Å^2)	U_{33} (Å^2)
K1	0.5	0.5	0	0.84(1)		0.037(8)	0.42(3)
K2	0.2752(9)	0.897(1)	0	0.858(4)		0.030(3)	0.015(2)
Fe1	0.3021(4)	0.4091(3)	0.2470(3)	0.885(2)		0.0019(6)	0.031(1)
Fe2	0.5	0	0.25	0.204(4)	0.7(1)		
Se1	0	0	0.1386(3)	1	1.5(1)		
Se2	0.3939(3)	0.2030(4)	0.14472(9)	1		0.0113(5)	0.0303(7)

Table 4.13 Summary of the structural results of the RT refinement on AG308_3 with the composition of $K_{0.75}Fe_{1.702}Se_{2\ for}$ the *I4/mmm* phase.

Atom	*x/a*	*y/b*	*z/c*	*N*	B_{Iso} (Å^2)	$U_{11}=U_{22}$ (Å^2)	U_{33} (Å^2)
K1	0	0	0	0.576(8)	5.3(3)		
Fe1	0	0.5	0.25	1.000(5)	0.99(6)		
Se1	0	0	0.3573(2)	1		0.0085(8)	0.013(1)

The second challenge is the peak shape, which for some reflections is heavily asymmetric and super-Lorentzian. This means that the use of a split-Pearson VII (SPVII) type peak shape will be required as this type models the super-Lorentzian components better than a SPV peak shape. The super-Lorentzian line shape can be due to a wide distribution of crystallite sizes, strains or compositions. It is apparent from figure 4.9 that the right component of the peak shape has a larger super-Lorentzian component than the left and taking the values from the refinement this component is primarily 2θ independent but also has a tan(θ) contribution (Tables 4.14 and 4.15). Taking into account this misfit the main body of each peak is calculated with a good Bragg position and intensity, leading to the conclusion that although the fit is not perfect, the average structure determined from the structure factors form the achieved peak fit will be good.

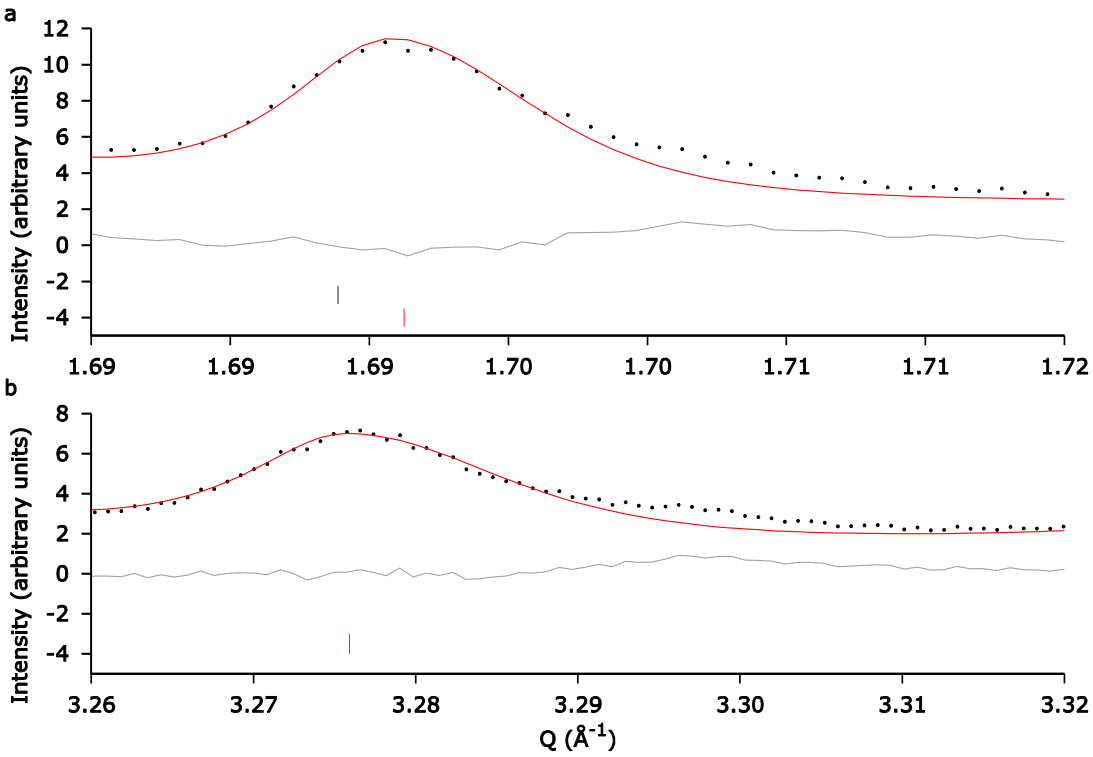

Figure 4.9 Rietveld refinement plot for the material produced with the composition $K_{0.75}Fe_{1.702}Se_2$ (AG308_3). The model was refined against SPXRD data at a wavelength of λ = 0.399892 Å. (a) The expanded view of the (011) and (b) the expanded view of the (020) peak show the high level of asymmetry and the super-Lorentzian nature of the line shapes for these reflections.

Table 4.14 Summary of the refined parameters for the SPVII peak shapes exponents used to calculate the profile widths of the *I*4/*mmm* phase in a Rietveld refinement.

Parameter / Side	Exponents for the composite functions		
	2θ Independent	**Size**	**Strain**
Left	0.31(2)	0.36(2)	0.55(31)
Right	0.35(9)	0	1.63(9)

Table 4.15 Summary of the refined parameters for the SPVII peak shapes FWHM used to calculate the profile widths of the *I*4/*mmm* phase in a Rietveld refinement.

Parameter / Side	FWHM		
	2θ Independent	**Size**	**Strain**
Left	0.0008(1)	0.269(3)	0.0006(1)
Right	0.0010(2)	0.349(3)	0.0011(2)

Due to the *I*4/*mmm* phase being heavily overlapped with the *I*4/*m* phase (11 peaks have a clear maxima in the best cases, but none of these peaks are entirely free of overlap) the number of refined parameters should be kept as small as possible. Refinement models which included two *I*4/*mmm* phases were trialled in order to determine if the super-Lorentzian tails on the right side of the peak could be modelled. The two *I*4/*mmm* phase refinement model failed to produce a better fit as on refinement the *I*4/*mmm* phases either became equivalent or one refined to a fraction of 0 %. The fits as displayed in figures 4.8 and 4.9 represent the best that could be obtained without going to the extreme of giving each peak its own shape (which would sacrifice the integrity of the information obtained from the refined structure).

The *I*4/*m* phase in this refinement has two additional slight misfits. Firstly, there is an under calculation of the intensity for the (134) reflection and secondly there is an under calculation of the (240) reflection FWHM. The misfits in FWHM and intensity for this pattern are not present in the Pawley fit, leading to the conclusion that there is a deficiency in the structural model for this phase. This is more evidence for the presence of structural features beyond an average unit cell description, which may be indicative of a slightly incommensurate structure. In an incommensurate description anisotropic strain could be applied along the modulation vectors, which may simultaneously provide a more accurate description of the FWHM while modelling structural features present beyond a unit cell description. The total refined composition over all phases for this material is $K_{0.820(5)}Fe_{1.609(5)}Se_2$ which is very close to the analysed composition of $K_{0.70(6)}Fe_{1.68(10)}Se_{2.00(3)}$ indicating that the structural models used

to fit the data are chemically sound. Considering the imperfect fit on the *I*4/*m* phase and the super-Lorentzian tails on the *I*4/*mmm* phase the conclusions will be made based on errors of 3 standard deviations representing the 99.7 % confidence level. This will enable the identification of the strongest correlations and allow the focus of improved structural models to be targeted in the correct direction.

4.4. K-Fe-Se phase diagram

4.4.1. The effect of the different annealing protocols on the crystalline phases

The phase equilibrium in the K-Fe-Se system was investigated by studying polycrystalline powder samples synthesised using a subsolidus reaction method. To ensure all samples adhered to the subsolidus reaction scheme the annealing temperature of 750 °C was used throughout the experiments. This temperature (750 °C) was the highest reaction temperature that could be safely achieved without any samples melting. Additionally the transition point of the $K_xFe_ySe_2$ phases contained within these materials occurs between 225 °C and 300 °C (Figure 4.10 and 4.11). The annealing temperature of 750 °C provides the optimum conditions for diffusion of potassium to occur and the ability to kinetically control the decomposition pathway of the single ternary phase on cooling.

An important point to note is that samples made where x in $K_xFe_ySe_2$ is less than 0.75 at high temperature have a phase assembly consisting of $K_xFe_ySe_2$, FeSe phases and in some cases a small amount of Fe present in the PXRD pattern (Figure 4.11). The samples where x in $K_xFe_ySe_2$ is equal to or greater than 0.75 only have the ternary $K_xFe_ySe_2$ phase and an Fe impurity at high temperature (Figure 4.10). This produces two different environments for samples above and below the x = 0.75 line which could affect how the high temperature ternary phase decomposes into its room temperature constituents.

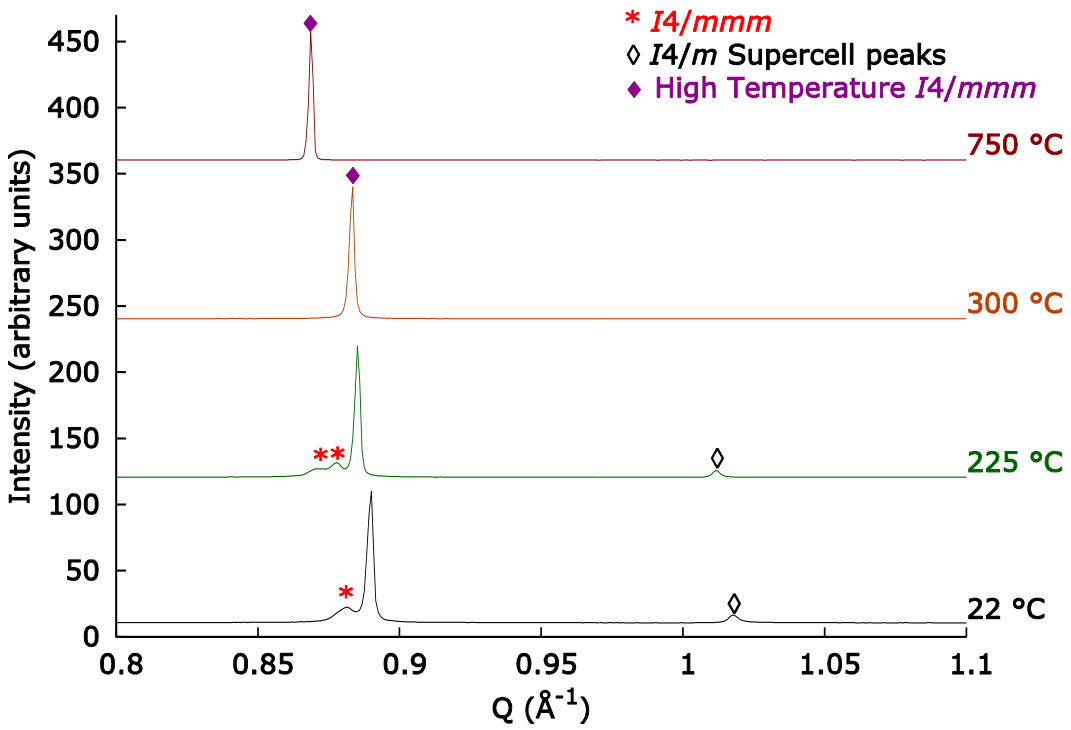

Figure 4.10 Comparison of patterns collected during the VT experiment run on AG311_3 $K_{0.75}Fe_{1.781}Se_2$ produced using the slow cooled protocol (section 4.2.2.2.) where the heating protocol used for the VT experiment was RT→2 °C min^{-1}, 750 °C. The unmarked peaks are the subcell reflections of the *I*4/*m* phase which are present below the transition temperature. As the temperature increases from 225 °C to 300 °C the supercell peaks of the *I*4/*m* phase disappear as the iron vacancies become disordered and its space group changes to *I*4/*mmm*. At this point both ternary $K_xFe_ySe_2$ (*I*4/*m* and *I*4/*mmm*) phases combine into a single ternary phase referred to as the high temperature *I*4/*mmm* phase.

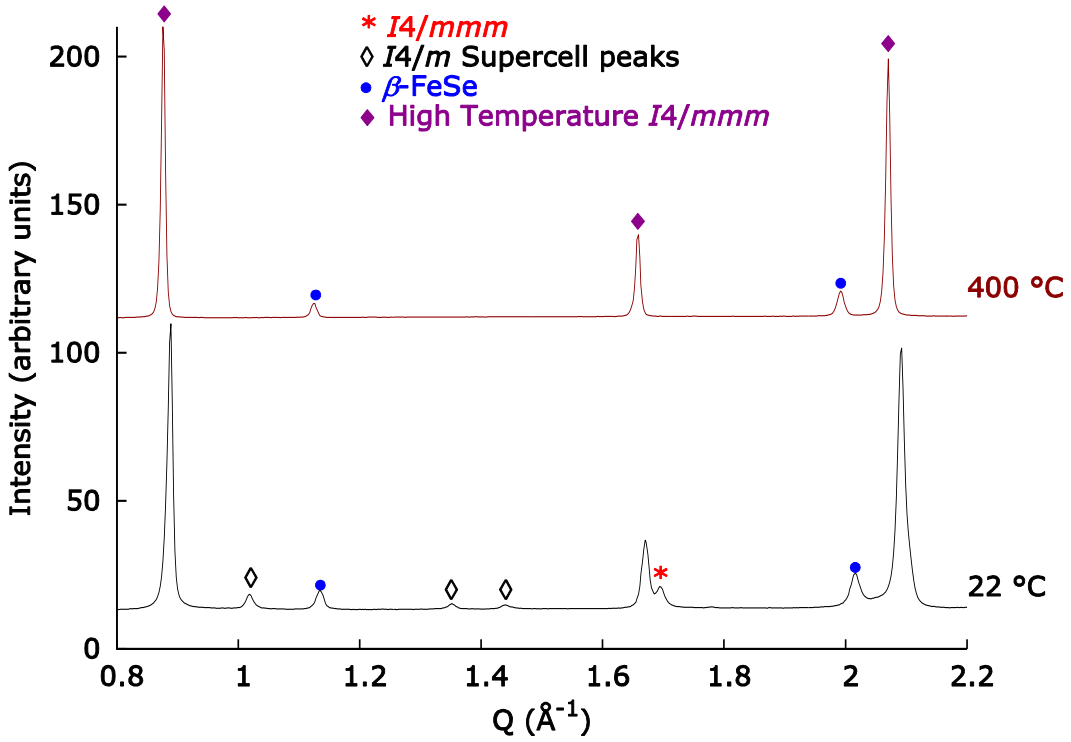

Figure 4.11 Comparison of patterns collected at room temperature and 400 °C for the AG332_2 $K_{0.65}Fe_{1.754}Se_2$ sample produced using the quenched protocol (section 4.2.2.1.). The unmarked peaks represent the subcell reflections of the *I*4/*m* phase. At 400 °C the supercell peaks of the *I*4/*m* phase have disappeared as the iron vacancies become disordered. Since 400 °C is past the transition point for this material both ternary $K_xFe_ySe_2$ phases combine into a single ternary phase referred to as the high temperature *I*4/*mmm* phase.

The initial reaction and the two subsequent cooling protocols all produced different materials for the same nominal composition, $K_{0.75}Fe_{1.781}Se_2$, when investigated by X-ray diffraction and SQUID magnetometry. The initial reaction produced a material that displayed no superconducting properties at all. The PXRD pattern for the initial reaction to form $K_{0.75}Fe_{1.781}Se_2$ showed the presence of three $K_xFe_ySe_2$ phases corresponding to one *I*4/*m* phase and two poorly crystalline *I*4/*mmm* phases. The slow cooled protocol, at the $K_{0.75}Fe_{1.781}Se_2$ composition, gave a superconducting material with a T_c of 31.5 K and a shielding fraction of 3 %. The PXRD pattern of the $K_{0.75}Fe_{1.781}Se_2$ material produced after the slow cooled protocol exhibits the same phase composition as that of the material produced after the initial reaction. The difference between the material produced by the initial reaction and slow cooled protocol is that the *I*4/*mmm* phases are much more crystalline (Figure 4.12). The $K_{0.75}Fe_{1.781}Se_2$ sample produced by the quenched protocol is a far superior superconductor to the material obtained from the slow cooled protocol. The shielding fraction of the

$K_{0.75}Fe_{1.781}Se_2$ material produced by the quenched protocol shows a T_c of 33 K and an SF of 19 %. In addition to the improvements in the T_c and SF the PXRD pattern of the $K_{0.75}Fe_{1.781}Se_2$ quenched material shows only one *I*4/*mmm* phase in addition to the *I*4/*m*. Also the *I*4/*mmm* material produced by the quenched protocol is far more crystalline than either of the materials produced after the initial reaction or slow cooled protocol. The higher quality of material produced by the quenched protocol gave the best chance for determining which of the ternary phases is responsible and any critical criteria that need to be met in order to observe superconductivity in these samples. Therefore, the materials produced by the quenched method will be studied in more detail.

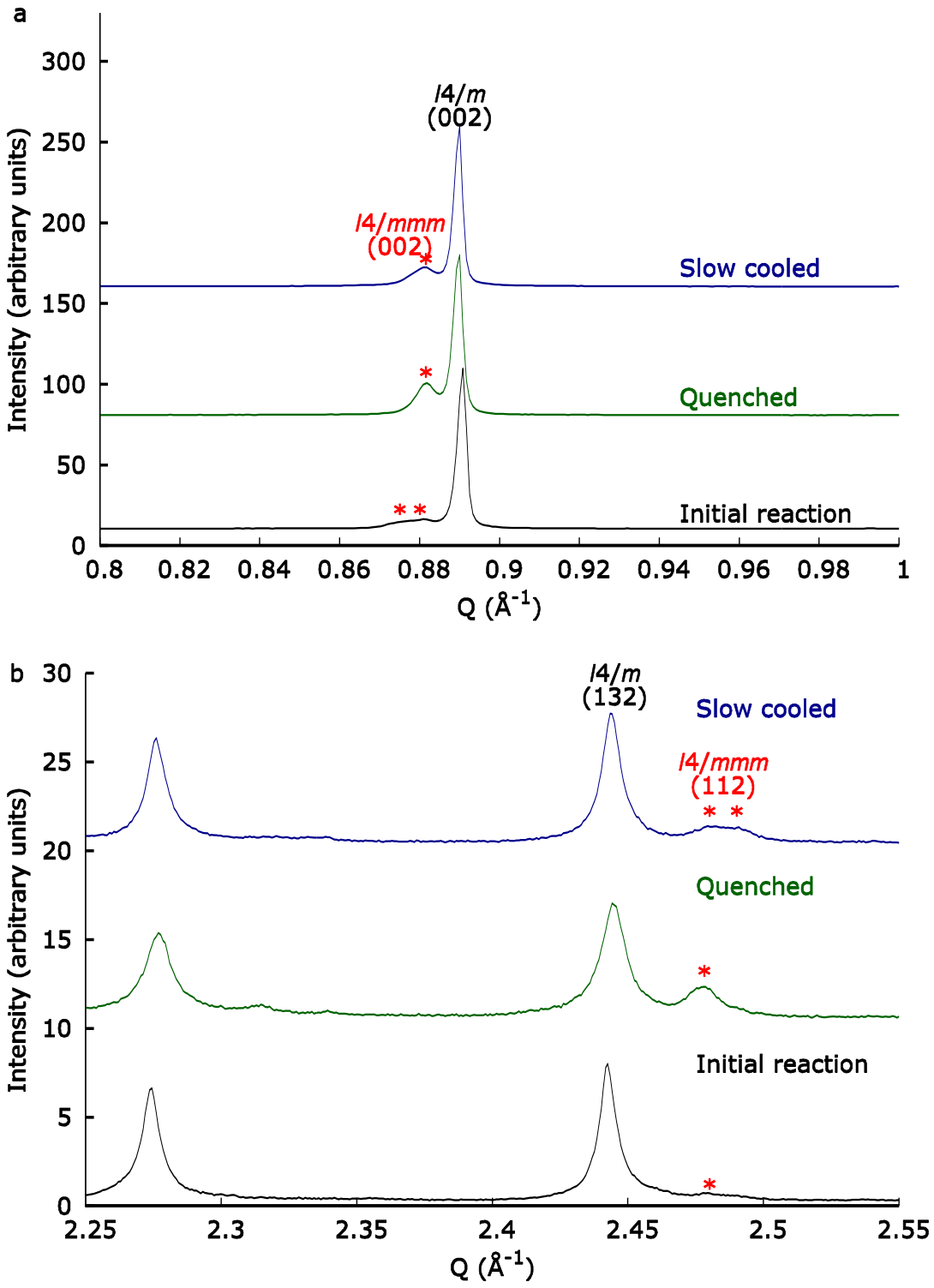

Figure 4.12 Comparison of the PXRD patterns of AG311_1 (Initial reaction), AG311_2 (Quenched) and AG311_3 (Slow cooled (section 4.2.2.2.)) produced at a nominal composition of $K_{0.75}Fe_{1.781}Se_2$. The red * represents the *I4/mmm* peaks. (a) The comparison of the *I4/m* and *I4/mmm* (002) reflections for the initial reaction, quenched protocol and slow cooled protocol. (b) The comparison of the *I4/m* (132) and *I4/mmm* (112) reflections of the materials produced using the initial, quenched and slow cooled protocols.

4.4.2. K-Fe-Se phase diagram for quenched samples

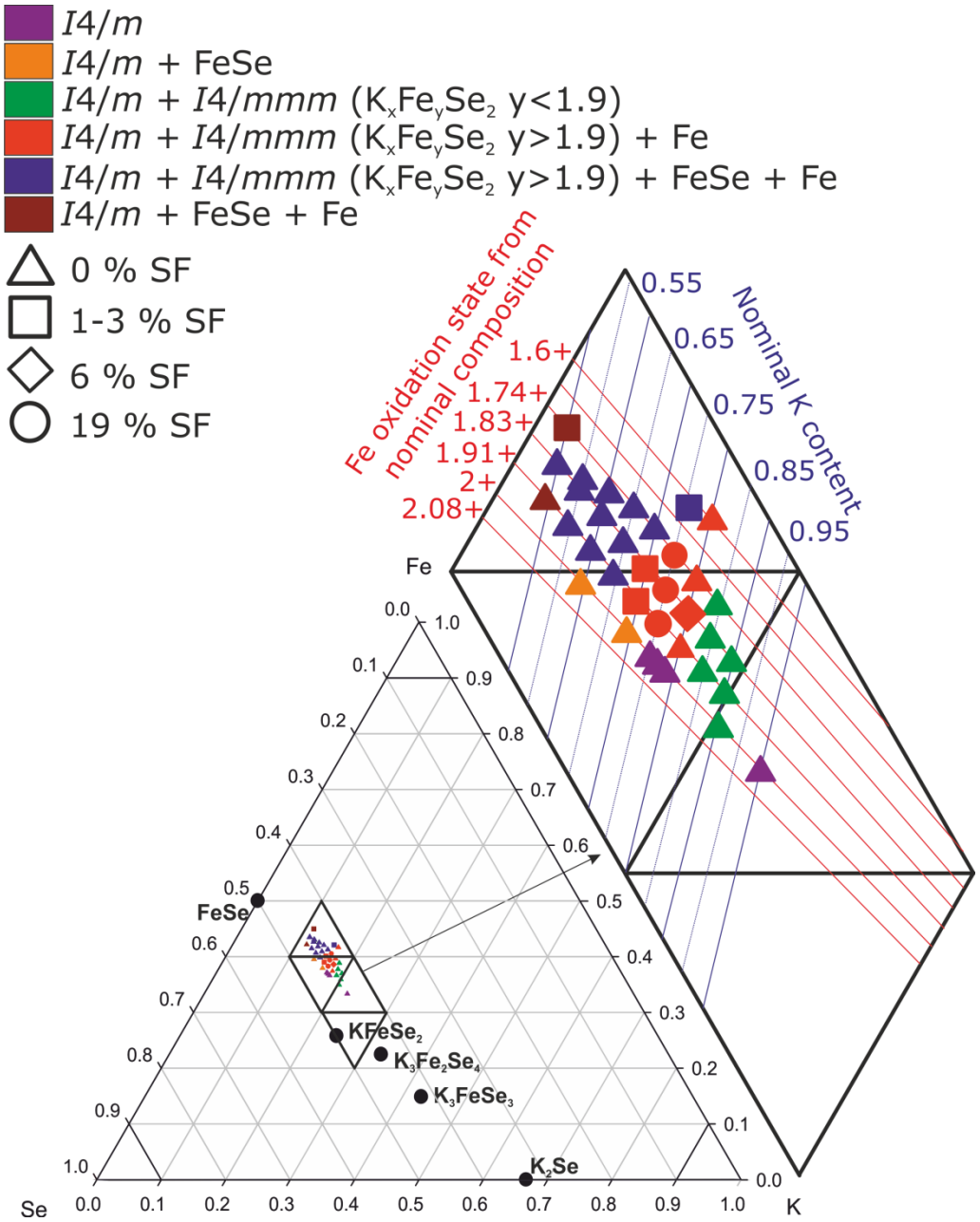

Figure 4.13 Phase diagram of K – Fe – Se system derived from the samples prepared at 750 °C using the quenched protocol (section 4.2.2.1.) and the relationship between observed phases and superconductivity. In the zoom region: The red lines guide for the Fe oxidation state targeted by nominal composition. Blue lines define K nominal content. Superconductivity from SQUID measurements: triangles - 0 %; squares - 1-3 %; diamonds - 6 %; circles – 19 %. The colour of the markers define the following regions: (1) dark purple - $K_xFe_{2-x/2}Se_2$ (x=0.75-1.0), single-phase *I4/m* phase; (2) orange - $K_xFe_{2-x/2}Se2$ (x=0.6-0.7), *I4/m* + FeSe; (3) green - $K_xFe_ySe_2$ (x=0.85-0.9; y=1.625-1.810), *I4/m* + *I4/mmm* (refined composition: $K_xFe_ySe_2$ y<1.9); (4) red - $K_xFe_ySe_2$ (x=0.7-0.8; y=1.675-2) *I4/m* + *I4/mmm* (refined composition: $K_xFe_ySe_2$ y>1.9) + Fe; (5) blue - $K_xFe_ySe_2$ (x=0.5-0.75; y=1.754-2.0): *I4/m* + *I4/mmm* + FeSe + Fe; (6) brown - $K_xFe_ySe_2$ (x=0.5; y=1.83 and 2.0): *I4/m* + FeSe + Fe.

The phase diagram (Figure 4.13 for the summary of the studied compositions) contains several distinct regions which are composed of different phase assemblies. Each of these regions was examined for superconductivity and the presence of this phenomenon was then rationalized by the use of Rietveld analysis on the produced powder X-ray patterns. First the phase composition and superconducting properties of each region will be discussed which enables the identification of critical superconducting compositions. Once the importance of these materials is established the detailed discussion of the results obtained by Rietveld analysis will then be dealt with and any correlations found can be put into context.

The $K_xFe_ySe_2$ phase diagram contains five different crystallographic phases which have varying phase fractions present depending upon the targeted nominal composition. The first phase has the general formula $K_xFe_ySe_2$ (SG = *I*4/*m*) where ordering of the tetrahedral site vacancies gives rise to a superstructure based upon a five-fold expansion in the *ab* plane of the $ThCr_2Si_2$ unit cell. The tetragonal cell produced by this *I*4/*m* phase maintains the square planar arrangement of tetrahedral iron centres common to the $Fe_{1.01}Se$ and other iron based superconductors.[4, 16]

The second notable phase is the $K_xFe_ySe_2$ (SG = *I*4/*mmm*, $ThCr_2Si_2$ structure type, Figure 4.1) phase which can be assigned as crystallizing in a tetragonal symmetry where the [FeSe] layers are separated by potassium.[2] This phase comes in two variants of an iron rich and iron deficient form.[2] The lack of the superstructure reflections associated with the iron deficient phase supports a crystal structure model based on random distribution of Fe cations within the [FeSe] plane.

The third phase is *β*-FeSe which is again based upon a tetragonal unit cell (SG = *P*4/*nmmz*) and has the composition $Fe_{1.01}Se_1$ where it has the superconducting transition temperature of 8 K.[4] The fourth possible phase is the *δ*-FeSe which presents with a hexagonal unit cell (SG = *P*63/*mmc*). The fifth and final phase is elemental iron (SG = $Im\bar{3}\,m$) which, depending on the targeted nominal composition, is present in amounts from 0 to 4.3 vol.%.

The phase diagram also identifies the compositions at which bulk superconductivity occurs. Superconducting fractions of 19 % and T_cs of 33 K were observed for samples with the compositions $K_{0.75}Fe_ySe_2$ (y = 1.868, 1.781 and 1.702). One other notable sample has a nominal composition of $K_{0.8}Fe_{1.753}Se_2$ and a SF of 6.3 % shown by the red diamond in Figure 4.13. The 6.3 % SF material could have many similar features with the 19 % material and the optimal parameters which give rise to this phenomenon. Any correlation

between the materials presenting with an SF of 19 % and the presence of superconductivity could be strengthened by this material if it is indeed similar. All other samples that have a T_c above 8 K have SFs of ~1 % meaning that the superconducting phase in these materials will be impossible to assign.

Either of the *I*4/*m* and *I*4/*mmm* phases could be responsible for the superconductivity displayed in these materials. The other phases in the material are either non superconducting (Fe and *δ*-FeSe) or their superconductivity is known (*β*-FeSe, T_c 8 K). In order to decipher which phase and its property (or properties) is responsible an in-depth analysis of the powder x-ray diffraction patterns produced by these materials, both superconducting and not, is required.

4.4.3. Region 1 (deep purple markers): $K_xFe_{2-x/2}Se_2$ (x=0.75-1.0) single-phased material with ordering of iron vacancies in the iron-selenium layer.

The first region (purple markers Figure 4.13) represents materials which lie along the Fe^{+2} oxidation state line in the compositional range of $K_xFe_{2-x/2}Se_2$ (x=0.75-1.0). Without exception the materials contained within this range are dominated by the *I*4/*m* phase which is clearly identifiable by the presence of strong supercell reflections. With the exception of one composition ($K_{0.9}Fe_{1.55}Se_2$) they are ≥99.99 % pure *I*4/*m* material (Figure 4.14 and Table 4.16 to 4.18). The material with the nominal composition of $K_{0.9}Fe_{1.55}Se_2$ contains two intercalated phases corresponding to the *I*4/*m* and iron deficient *I*4/*mmm* phase and as such will be discussed with the materials contained within the green coloured markers. The SQUID magnetometry data for region 1 materials revealed no superconducting transition for any of the studied samples which is in line with the recent literature observations (Figure 4.15).[2, 7]

The *I*4/*m* $K_xFe_ySe_2$ phases of region 1 hint at the presence of interesting trends within their lattice parameters. There is a large change in the *a* and *c* axis between x = 0.8 and 1.0 but with so few data points for this region it is impossible to determine if this is a trend or an outlier. Therefore the cell parameters will be discussed in section 4.4.4. with the other points lying along the Fe^{2+} oxidation state line of the phase diagram.

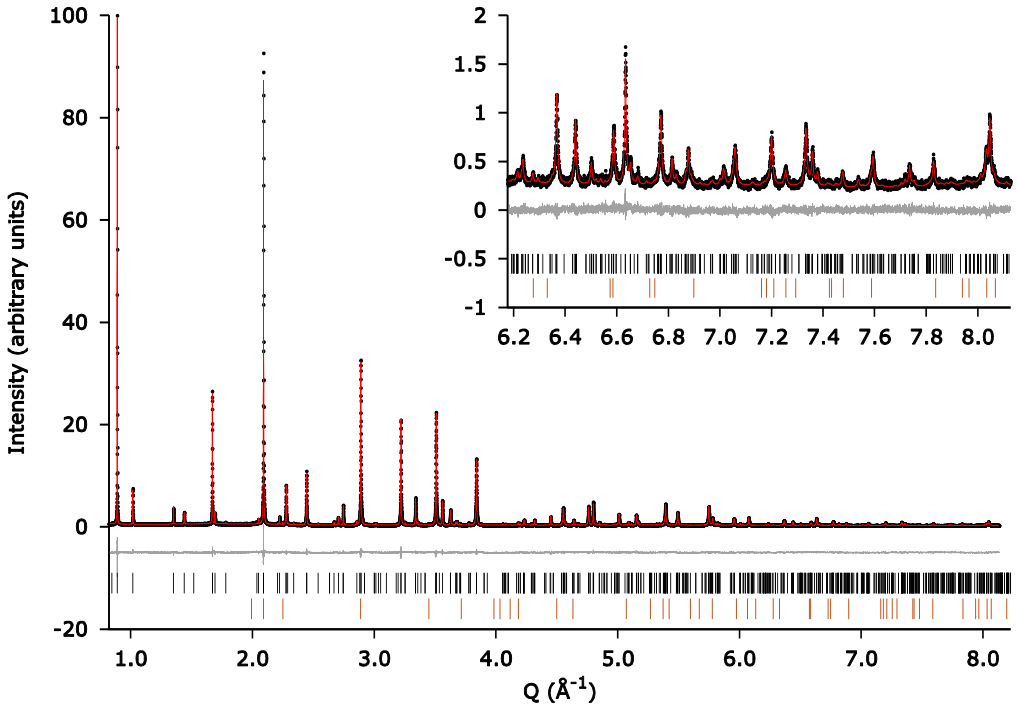

Figure 4.14 A typical Rietveld refinement plot for the material from region 1 with the composition $K_{0.784}Fe_{1.608}Se_2$ (AG278_3). The multiphase model was refined against SPXRD data at a wavelength of λ = 0.399892 Å. Observed (black dots), calculated (red line) and difference (grey line) data are shown. The tic marks represent Bragg reflection positions of the *I*4/*m* (black) and *δ*-FeSe (dark orange) phases. A summary of the refined parameters are presented in Tables 4.16, 4.17 and 4.18. R_{wp} = 7.24, R_{exp} = 5.84 and number of refined parameters 57.

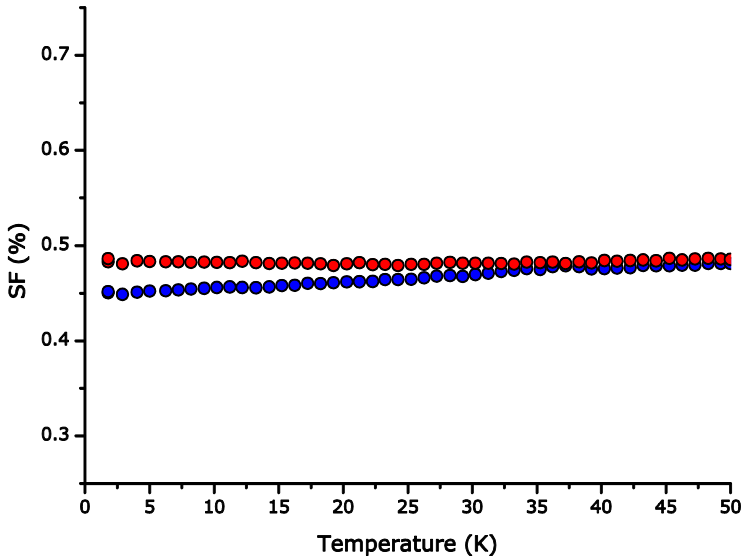

Figure 4.15 The magnetisation as a function of temperature measurements done on AG278_3 ($K_{0.784}Fe_{1.608}Se_2$). Where the red and blue circles correspond to the field cooled and zero field cooled experiments respectively. The magnetic measurements were taken in an applied field of 10 Oe with a sample mass of 31.5 mg.

Table 4.16 The phase assembly from the Rietveld analysis of the PXRD data for materials shown by the purple markers in Figure 4.13.

Parameter / Label	SF (%) @ 10 K	*I*4/*m* (vol. %)	*β*-FeSe (vol. %)	*δ*-FeSe (vol. %)	Fe (vol. %)
AG335_2($K_{0.75}Fe_{1.625}Se_2$)	0	100	0	0	0
AG278_3($K_{0.784}Fe_{1.608}Se_2$)	0	99.9945(40)	0	0.0055(6)	0
AG336_3($K_{0.8}Fe_{1.6}Se_2$)	0	100	0	0	0
AG282_4($K_{1.0}Fe_{1.5}Se_2$)	0	100	0	0	0

Table 4.17 The lattice parameters of the *I*4/*m* phase as obtained from the Rietveld analysis of the PXRD data for materials shown by the purple markers in Figure 4.13.

Parameter / Label	SF (%) @ 10 K	*a*/√5 (Å)	*c* (Å)	V/5 (Å^3)	√5 *c*/*a*
AG335_2($K_{0.75}Fe_{1.625}Se_2$)	0	3.90131(3)	14.1134(2)	214.810(4)	3.61761(5)
AG278_3($K_{0.784}Fe_{1.608}Se_2$)	0	3.902748(4)	14.11768(3)	215.0325(8)	3.61737(1)
AG336_3($K_{0.8}Fe_{1.6}Se_2$)	0	3.89934(4)	14.1212(2)	214.710(5)	3.62143(6)
AG282_4($K_{1.0}Fe_{1.5}Se_2$)	0	3.94491(7)	13.8898(3)	216.157(9)	3.5209(1)

Table 4.18 The refined compositions and individual site occupancies of the *I*4/*m* phase obtained from the Rietveld analysis of the PXRD data for materials shown by the purple markers in Figure 4.13.

Parameter / Label	SF (%) @ 10 K	Refined Composition	K1 *2b*	K2 *8h*	Fe1 *16i*	Fe2 *4d*
AG335_2($K_{0.75}Fe_{1.625}Se_2$)	0	$K_{0.737(8)}Fe_{1.704(8)}Se_2$	1.00(3)	0.671(7)	0.996(4)	0.274(8)
AG278_3($K_{0.784}Fe_{1.608}Se_2$)	0	$K_{0.785(3)}Fe_{1.587(3)}Se_2$	0.943(8)	0.745(2)	0.962(1)	0.117(3)
AG336_3($K_{0.8}Fe_{1.6}Se_2$)	0	$K_{0.73(1)}Fe_{1.597(9)}Se_2$	0.85(5)	0.70(1)	0.981(5)	0.07(1)
AG282_4($K_{1.0}Fe_{1.5}Se_2$)	0	$K_{0.973(8)}Fe_{1.418(7)}Se_2$	0.86(2)	1.000(6)	0.886(4)	0

4.4.4. Region 2 (orange markers): $K_xFe_{2-x/2}Se_2$ (x=0.6-0.7) *I4/m* and FeSe.

In comparison to the single phase materials of region 1, the region 2 materials have more iron and less potassium present in their nominal compositions. The lower potassium to iron ratio leads to multiphase samples where three phases are present within the PXRD phase assembly. These phases correspond to $K_xFe_ySe_2$ (SG = *I*4/*m*), *β-FeSe* and *δ*-FeSe (Figure 4.16 and Table 4.19).[7, 13] Increasing x from 0.6 to 0.7 ($K_xFe_{2-x/2}Se_2$) results in the fractions of FeSe reducing by 54.6 % and 95.0 % for the *β* and *δ* variants respectively (Table 4.19). The reason for this large decrease in the FeSe impurity fractions is due to the lower nominal iron composition. This drop in iron is coupled with an increase in nominal potassium composition which allows the formation of additional $K_xFe_ySe_2$ material without sacrificing the stability of the +2 iron oxidation state. Both samples showed a superconducting response only below T_c = 10 K in the SQUID which could be associated only with the presence of *β*-FeSe (Figure 4.17). As no other superconducting transition was found in the system we conclude that the *I*4/*m* phase at this level of K doping is non-superconducting.

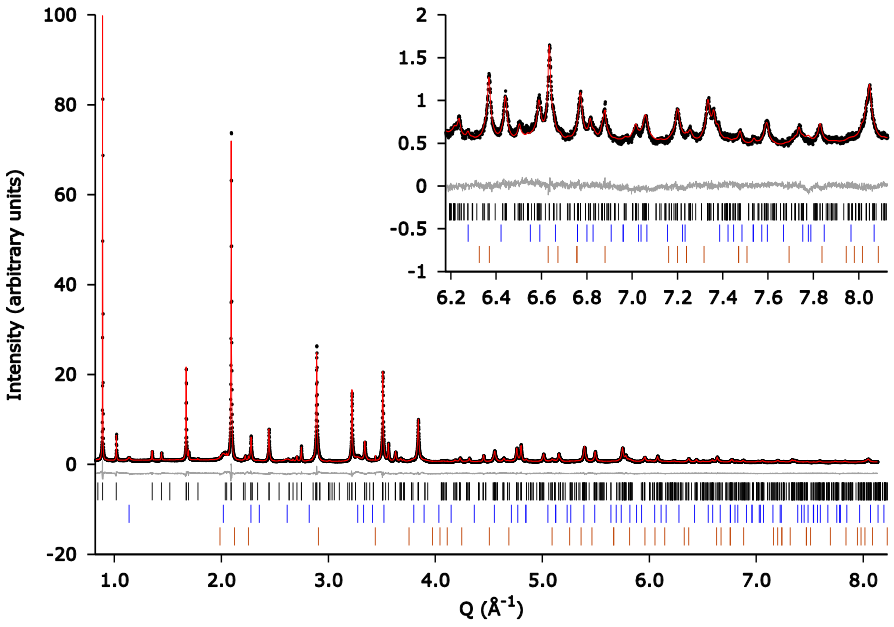

Figure 4.16 A typical Rietveld refinement plot for the, region 2, material produced with the composition $K_{0.7}Fe_{1.65}Se_2$ (AG277_3). The model was refined against SPXRD data at a wavelength of λ = 0.399892 Å. Observed (black dots), calculated (red line) and difference (grey line) data are shown. The tic marks represent Bragg reflection positions of the *I*4/*m* (black), *β*-FeSe (blue) and *δ*-FeSe (dark orange) phases. A summary of the refined phase

fractions are presented in tables 4.19, 4.20 and 4.21. R_{wp} = 5.96, R_{exp} = 2.71 and number of refined parameters 59.

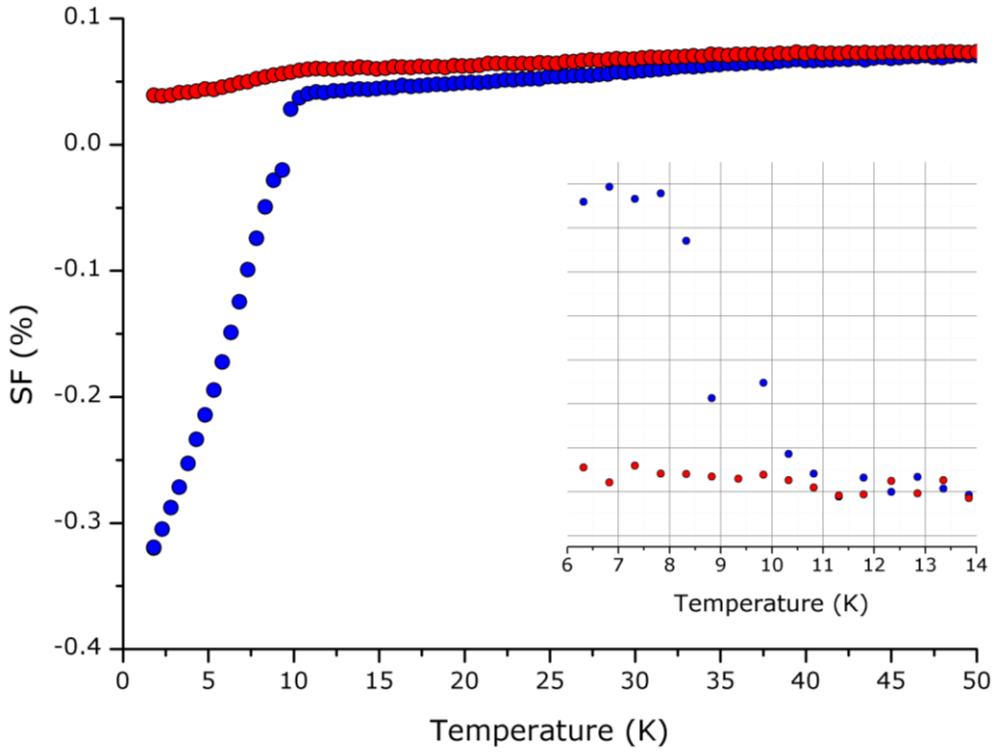

Figure 4.17 The magnetisation as a function of temperature measurements done on AG277_3 ($K_{0.7}Fe_{1.65}Se_2$). Where the red and blue circles correspond to the field cooled and zero field cooled experiments respectively. The inset is *d*M/*d*T and shows the onset of superconduction at a T_c of 10 K and a SF of 0.4 %. The magnetic measurements were taken in an applied field of 10 Oe with a sample mass of 30.7 mg. The superconducting phase in this material is *β*-FeSe.

Table 4.19 The phase assembly from the Rietveld analysis of the PXRD data for materials shown by the orange markers in Figure 4.13.

Parameter / Label	SF (%) @ 10 K	*I*4/*m* (vol. %)	*β*-FeSe (vol. %)	*δ*-FeSe (vol. %)
AG279_2($K_{0.6}Fe_{1.7}Se_2$)	0	79.07(2)	19.84(20)	1.09(2)
AG277_3($K_{0.7}Fe_{1.65}Se_2$)	0	90.935(7)	9.010(70)	0.054(2)

Table 4.20 The lattice parameters of the *I*4/*m* phase as obtained from the Rietveld analysis of the PXRD data for materials shown by the orange markers in Figure 4.13.

Parameter / Label	SF (%) @ 10 K	$a/\sqrt{5}$ (Å)	*c* (Å)	V/5 (Å^3)	$\sqrt{5}\,c/a$
AG279_2($K_{0.6}Fe_{1.7}Se_2$)	0	3.9011(1)	14.1167(7)	214.83(2)	3.6187(2)
AG277_3($K_{0.7}Fe_{1.65}Se_2$)	0	3.90218(3)	14.1166(1)	214.954(4)	3.61762(4)

Table 4.21 The refined compositions and individual site occupancies of the *I*4/*m* phase obtained from the Rietveld analysis of the PXRD data for materials shown by the orange markers in Figure 4.13.

Parameter / Label	SF (%) @ 10 K	Refined Composition	K1 *2b*	K2 *8h*	Fe1 *16i*	Fe2 *4d*
AG279_2($K_{0.6}Fe_{1.7}Se_2$)	0	$K_{0.83(1)}Fe_{1.35(1)}Se_2$	0.73(3)	0.85(1)	0.845(6)	0
AG277_3($K_{0.7}Fe_{1.65}Se_2$)	0	$K_{0.780(6)}Fe_{1.576(5)}Se_2$	0.87(2)	0.757(6)	0.951(3)	0.139(5)

Examination of the results produced from Rietveld refinement using the SPXRD patterns reveals some differences between the two $K_xFe_{2-x/2}Se_2$ materials (Tables 4.19-4.21). The *I*4/*m* phase of the AG277_3 has a larger *a* parameter, cell volume and refined iron content than that found in the *I*4/*m* phase of AG279_2 (Table 4.21). However, the lattice parameters, cell volumes and refined potassium contents fall within the spread of data observed for the *I*4/*m* phases of region 1 specifically for $K_xFe_{2-x/2}Se_2$ where $x<0.8$. Interestingly the refined iron content for AG279_2 is the lowest for the entire series along the Fe^{2+} line despite having the largest nominal iron composition.

The lattice parameters of the $K_xFe_{2-x/2}Se_2$ *I*4/*m* phases for regions 1 and 2 show two different trends as a function of x. For nominal potassium compositions up to x = 0.8 the *a* axis shows a distribution of points between the values of 3.89934(4) and 3.94491(7) Å. The *c* axis in the same compositional range also has a narrow distribution of points when compared to values of x greater than 0.8. When the nominal potassium composition increases to 1 a large change in the lattice parameters is observed where the *c* axis is decreased by 1.6 % and the *a* axis increased by 1.1 % (Figure 4.18). The cell volumes of the *I*4/*m* phases increase with the refined potassium composition (Figure 4.19). The point that lies outside of this trend corresponds to AG279_2 which has the lowest iron composition out of all the examined *I*4/*m* phases. This indicates that the cell volume of the *I*4/*m* phases may be affected by its refined iron composition when it decreases below $K_xFe_{1.4}Se_2$. The trend in lattice parameters identifies a compositional range where x is less than 0.8 in which the *I*4/*m* phase is least affected by compositional changes. The trend in cell volumes with refined potassium composition identify that the largest cell volumes occur for the largest refined potassium compositions.

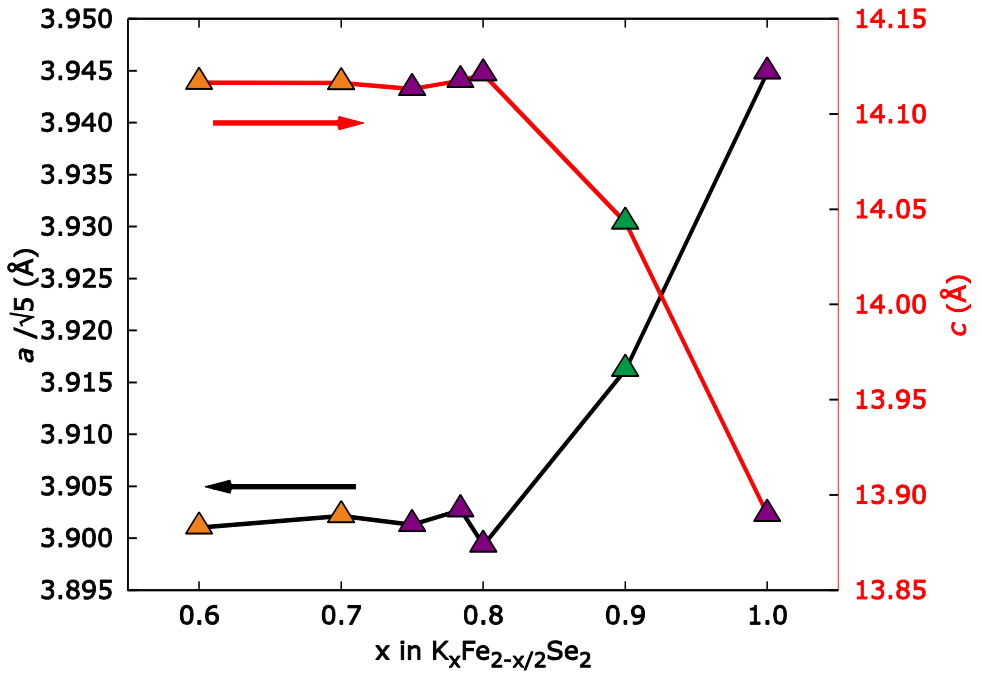

Figure 4.18 The lattice parameters of the *I*4/*m* phases as a function of nominal potassium composition. The markers correspond to the regions (1) dark purple; (2) orange and (3) green. The green point corresponds to the anomalous point on the Fe^{+2} line that contains two intercalated $K_xFe_ySe_2$ phases. The error bars are set at 3σ but are contained within the points.

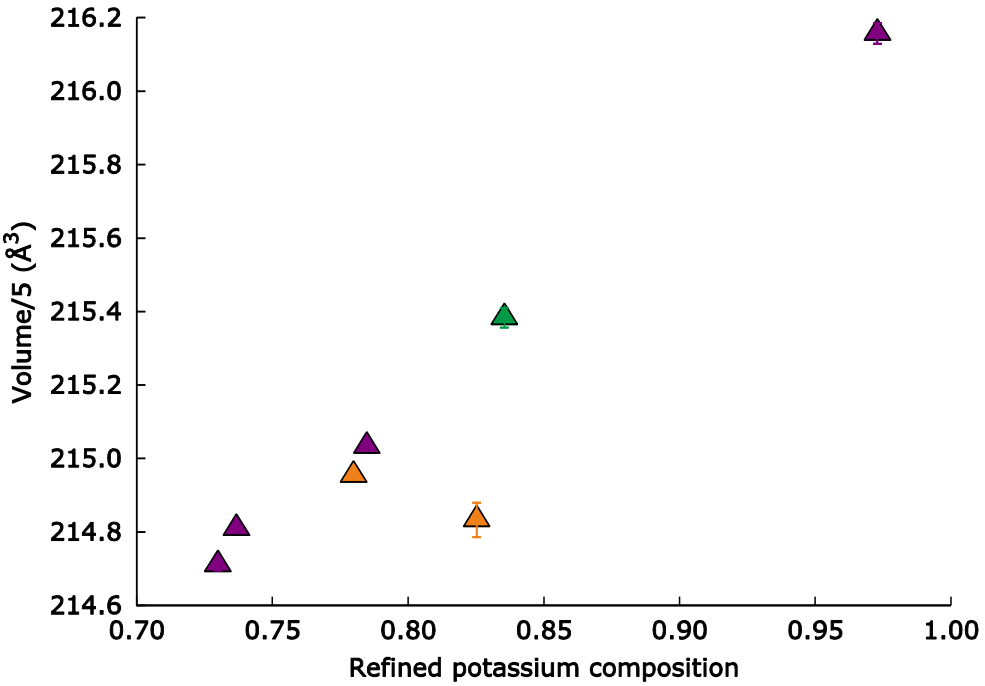

Figure 4.19 Refined potassium composition and normalised cell volumes for the $K_xFe_{2-x/2}Se_2$ materials as determined by Rietveld analysis. The markers correspond to the regions (1) dark purple; (2) orange and (3) green. The green point corresponds to the anomalous point on the Fe^{+2} line that contains two intercalated $K_xFe_ySe_2$ phases. The error bars are set at 3σ but are contained within the points.

The refined K content of the *I*4/*m* phases along the Fe^{+2} line in figure 4.13 does not drop below 0.73 even when the nominal composition is significantly smaller (Figure 4.20). In fact the sample with the lowest refined potassium composition, AG336_3, has a nominal potassium composition of 0.8. As previously stated the region 2 materials contain significant amounts of FeSe along with the *I*4/*m* phase which indicates that single phase *I*4/*m* materials with K contents of 0.6 and 0.7 are unfavourable. This combined with the fact that the refined potassium compositions for the *I*4/*m* phase do not drop below 0.73 means that the *I*4/*m* phase is not stable at refined potassium compositions of less than 0.73.

The refined iron composition calculated for the *I*4/*m* phases shows a maximum at x = 0.75 (Figure 4.20) which corresponds to a refined composition of $K_{0.737(8)}Fe_{1.704(8)}Se_2$ (AG335_2). This composition is close to that found for the *I*4/*m* phase containing 20 % of tetrahedral vacancies.[7] It is strange that as the nominal iron is increased from x = 0.6 to 0.75 that the amount of refined iron in the *I*4/*m* phases should decrease. This drop in refined iron content also corresponds to an increase in the amount of FeSe present in the materials. It would appear that the extra amount of nominal iron in the region 2 samples is used to form FeSe. A likely reason for the production of FeSe in the region 2 samples is that *I*4/*m* phase is unable to adopt compositions where the refined potassium composition is below 0.73. In order to keep this constraint in place some non-intercalated FeSe must be formed.

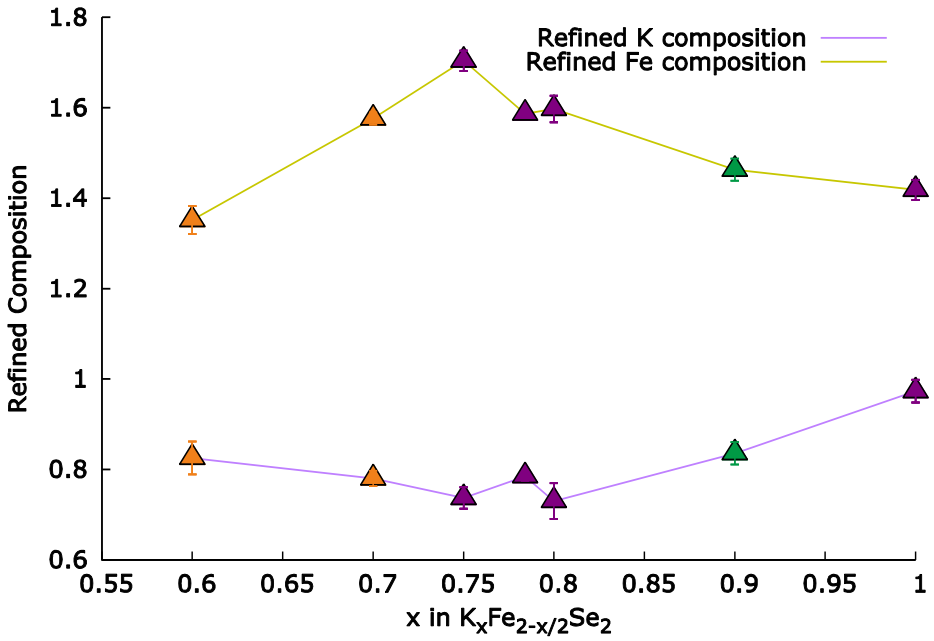

Figure 4.20 Refined potassium and iron compositions for the *I*4/*m* phases as determined by Rietveld analysis. The colour of the markers corresponds to the region of the phase diagram were the data was obtained; (1) dark purple; (2) orange and (3) green. The green point corresponds to the anomalous point on the Fe^{+2} line that contains two intercalated $K_xFe_ySe_2$ phases. The error bars are displayed at 3σ.

When the iron occupancies of region 1 and 2 are taken together it reveals the point at which the *I*4/*m* phase becomes unstable with respect to increasing levels of iron occupancy (Figure 4.21). While the Fe1(16*i*) site is stable with varying x in $K_xFe_{2-x/2}Se_2$, the Fe2(4*d*) site shows the same trend as the refined iron composition as a function of x. The Fe2(4*d*) site increases from 0 at x = 0.69 to a maximum at x = 0.75 and then decreases back to 0 at x = 1. For x values of less than 0.75 FeSe impurities are present in the materials. This trend in Fe2(4*d*) site occupancies gives another possible reason for the formation of FeSe in region 2 as it could be unfavourable to form an *I*4/*m* phase with significantly less vacancies than 20 % as found for the composition $K_{0.8}Fe_{1.6}Se_2$.[7]

The potassium site occupancies of the *I*4/*m* phases also give insight into the driving forces behind the phase assembly in the phase diagram (Figure 4.21). For all the samples along the Fe^{+2} line on the phase diagram the potassium occupancies never drop below ~0.75. As with the refined potassium composition the site occupancies of K1(2*a*) and K2(8*h*) have a limit of ~0.7 which they do not drop below. This observation reinforces the conclusion made using the refined potassium composition where it appears that *I*4/*m* phases with refined potassium compositions of less than 0.73 are unstable with respect to the formation of material containing the phases $K_{0.8}Fe_ySe_2$ and FeSe.

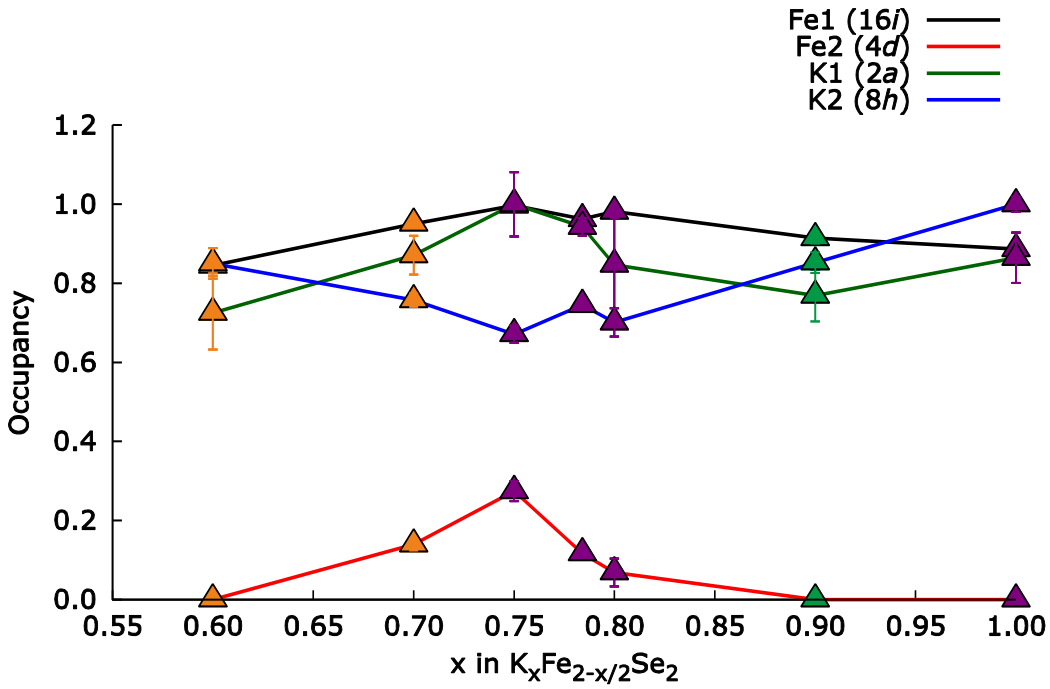

Figure 4.21 The occupancies of the potassium and iron sites as a function of x show that the *I*4/*m* phase with 20 % iron vacancies is located at x = 0.75. The colour of the markers corresponds to the region of the phase diagram were the data was obtained; (1) dark purple; (2) orange and (3) green. The green point corresponds to the anomalous point on the Fe^{+2} line that contains two intercalated $K_xFe_ySe_2$ phases. The error bars are displayed at 3σ.

4.4.5. Region 3 (green markers): $K_xFe_ySe_2$ (x=0.85-0.9; y=1.625-1.810) *I*4/*m*, *I*4/*mmm* and bulk Fe metal

The samples produced in region 3 have, in terms of nominal composition, more iron and relatively less selenium when compared to region 1. When examining regions 2 and 3 there is an increase in nominal potassium content between the two. We know that from regions 1 and 2 that extra iron is initially dealt with by increasing the Fe2 occupancy of the *I*4/*m* phase but ultimately leads to the production of FeSe. However for the region 3 samples because they have relatively less selenium to iron, rather than producing FeSe they precipitate elemental iron on cooling instead. What is not certain is how the extra potassium in comparison to the region 2 samples will be dealt with.

The region three (green markers Figure 4.13) materials contain the phases *I*4/*m*, *I*4/*mmm* and Fe (Figure 4.22). The overwhelmingly dominant phase is the $K_xFe_ySe_2$ *I*4/*m* as evident by the presence of superstructure reflections and confirmed by Rietveld refinement (Figure 4.22 and Table 4.22).

The *I*4/*mmm* phase produced for the samples with the nominal potassium composition of 0.85 is only present in very small amounts (~3 %). Once the nominal potassium composition is increased to 0.9 the fraction of *I*4/*mmm* jumps to ~11 vol.%. The samples at the nominal potassium composition of 0.9 have enough potassium and iron present in the material to form *I*4/*mmm* and *I*4/*m* phases. This means that the extra iron and extra potassium, when compared to regions 1 and 2, is combined to form an *I*4/*mmm* $K_xFe_ySe_2$ phase. It should be noted that the sample corresponding to the composition $K_{0.9}Fe_{1.702}Se_2$ (AG309_2) was exposed to air on recording its PXRD pattern but did have its magnetization data successfully recorded. Therefore results from PXRD are not presented but the sample is included in the phase diagram to show that this composition was tested and found to be non-superconducting.

Magnetization measurements using SQUID showed that none of the synthesized samples from this region were superconducting (Figure 4.23). This re-confirms that superconductivity is unlikely to originate from the vacancy-ordered *I*4/*m* phase.[2, 7] In addition to this conformation this also demonstrates that certain forms of the *I*4/*mmm* phase are also non-superconducting. It is therefore crucially important that this non-superconducting *I*4/*mmm* phase is analysed and put into context with the *I*4/*m* phase.

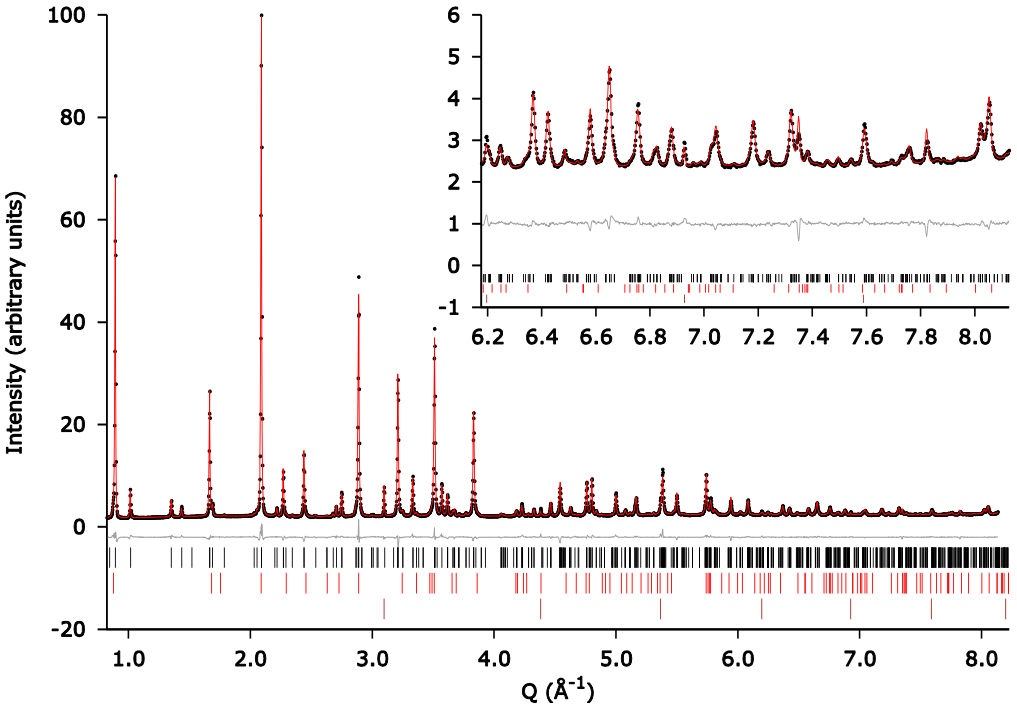

Figure 4.22 A typical Rietveld refinement plot for the material, region 3, produced with the composition $K_{0.85}Fe_{1.74}Se_2$ (AG326_2). The model was refined against SPXRD data at a wavelength of λ = 0.49937 Å. Observed (black dots), calculated (red line) and difference (grey line) data are shown. The tic marks represent Bragg reflection positions of the *I*4/*m* (black), *I*4/*mmm* (Red) and Fe (brown) phases. A summary of the refined phase fractions are presented in tables 4.22-4.26. R_{wp} = 3.33, R_{exp} = 2.71 and number of refined parameters 69.

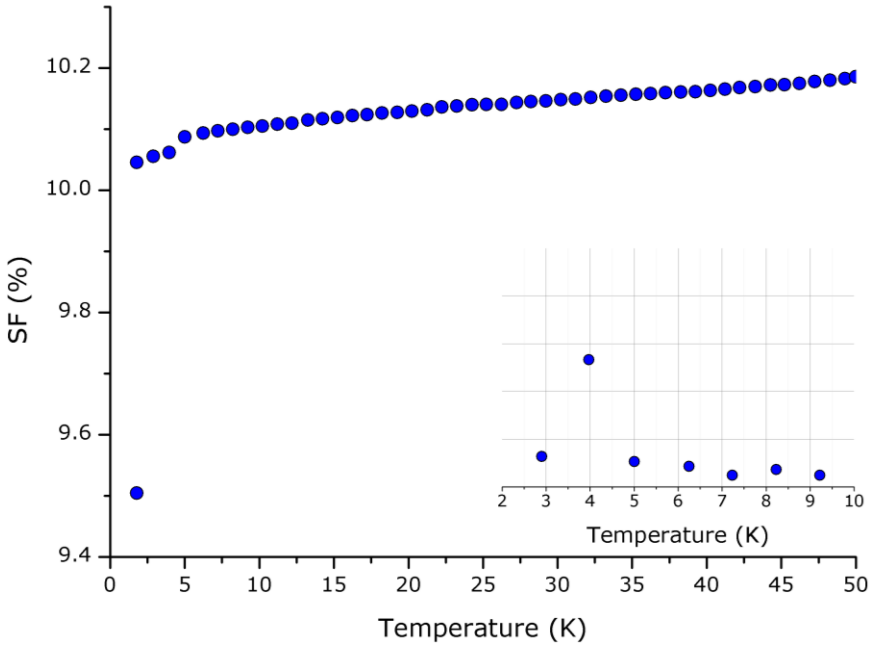

Figure 4.23 The magnetisation as a function of temperature measurements (zero field cooled) done on AG326_2 ($K_{0.85}Fe_{1.74}Se_2$). The inset is *d*M/*d*T and shows that there is no superconductivity present. The magnetic measurements were taken in an applied field of 10 Oe with a sample mass of 30.6 mg. The superconducting phase in this material is unidentifiable due to the small SF.

Table 4.22 The phase assembly from the Rietveld analysis of the PXRD data for materials shown by the green markers in Figure 4.13.

Parameter / Label	SF (%) @ 10 K	*I*4/*mmm* (vol. %)	*I*4/*m* (vol. %)	Fe (vol. %)
AG310_2($K_{0.85}Fe_{1.649}Se_2$)	0	3.558(109)	95.726(109)	0.717(7)
AG307_3($K_{0.85}Fe_{1.728}Se_2$)	0	0	98.52(2)	1.48(2)
AG326_2($K_{0.85}Fe_{1.810}Se_2$)	0	3.34(26)	95.46(25)	1.20(2)
AG281_3($K_{0.9}Fe_{1.55}Se_2$)	0	11.1(3)	88.9(3)	0
AG315_2($K_{0.9}Fe_{1.625}Se_2$)	0	11.3(3)	88.7(3)	0

Table 4.23 The lattice parameters of the *I*4/*m* phase as obtained from the Rietveld analysis of the PXRD data for materials shown by the green markers in Figure 4.13.

Parameter / Label	SF (%) @ 10 K	$a/\sqrt{5}$ (Å)	*c* (Å)	V/5 (Å^3)	$\sqrt{5}\,c/a$
AG310_2($K_{0.85}Fe_{1.649}Se_2$)	0	3.912810(9)	14.06345(4)	215.313(1)	3.59420(1)
AG307_3($K_{0.85}Fe_{1.728}Se_2$)	0	3.914443(4)	14.05564(4)	215.3728(9)	3.59071(1)
AG326_2($K_{0.85}Fe_{1.810}Se_2$)	0	3.91221(5)	14.0718(2)	215.374(6)	3.59688(7)
AG281_3($K_{0.9}Fe_{1.55}Se_2$)	0	3.91626(6)	14.0433(3)	215.383(9)	3.5859(1)
AG315_2($K_{0.9}Fe_{1.625}Se_2$)	0	3.9255(1)	13.9813(5)	215.45(1)	3.5617(2)

Table 4.24 The refined compositions and individual site occupancies of the *I*4/*m* phase obtained from the Rietveld analysis of the PXRD data for materials shown by the green markers in Figure 4.13.

Parameter / Label	SF (%) @ 10 K	Refined composition	K1 *2b*	K2 *8h*	Fe1 *16i*	Fe2 *4d*
AG310_2($K_{0.85}Fe_{1.649}Se_2$)	0	$K_{0.832(3)}Fe_{1.562(3)}Se_2$	0.928(8)	0.806(3)	0.937(1)	0.153(3)
AG307_3($K_{0.85}Fe_{1.728}Se_2$)	0	$K_{0.883(5)}Fe_{1.464(4)}Se_2$	1.00(1)	0.854(4)	0.915(2)	0
AG326_2($K_{0.85}Fe_{1.810}Se_2$)	0	$K_{0.772(6)}Fe_{1.612(5)}Se_2$	1.00(1)	0.868(4)	0.931(2)	0.134(4)
AG281_3($K_{0.9}Fe_{1.55}Se_2$)	0	$K_{0.835(8)}Fe_{1.463(8)}Se_2$	0.77(1)	0.852(9)	0.914(5)	0
AG315_2($K_{0.9}Fe_{1.625}Se_2$)	0	$K_{0.88(1)}Fe_{1.341(9)}Se_2$	0.81(3)	0.89(1)	0.838(4)	0

Table 4.25 The lattice parameters of the *I*4/*mmm* phase as obtained from the Rietveld analysis of the PXRD data for materials shown by the green markers in Figure 4.13.

Parameter / Label	SF (%) @ 10 K	*a* (Å)	*c* (Å)	V (Å^3)	*c*/*a*
AG310_2($K_{0.85}Fe_{1.649}Se_2$)	0	3.8767(3)	14.345(1)	215.59(4)	3.7004(4)
AG326_2($K_{0.85}Fe_{1.810}Se_2$)	0	3.8708(7)	14.327(5)	214.7(1)	3.701(3)
AG281_3($K_{0.9}Fe_{1.55}Se_2$)	0	3.9673(8)	13.754(4)	216.5(1)	3.467(1)
AG315_2($K_{0.9}Fe_{1.625}Se_2$)	0	3.9682(4)	13.773(2)	216.88(6)	3.4707(7)

Table 4.26 The refined compositions of the *I*4/*mmm* phases with a phase fraction over 10 vol.% obtained from the Rietveld analysis of the PXRD data for materials shown by the green markers in Figure 4.13.

Parameter / Label	SF (%) @ 10 K	Refined composition
AG281_3($K_{0.9}Fe_{1.55}Se_2$)	0	$K_{0.88(3)}Fe_{1.47(4)}Se_2$
AG315_2($K_{0.9}Fe_{1.625}Se_2$)	0	$K_{0.94(3)}Fe_{1.36(4)}Se_2$

Due to the narrow range of compositions and small number of samples the only trend observed for the *I*4/*m* phase of these materials is between the *c* and *a* axis (Figure 4.24). This shows a decrease in the *c* axis as the *a* axis increases. This observation fits in very well with the trends observed in the *c* and *a* axes for the *I*4/*m* phases in regions 1 and 2. The *I*4/*m* phases in regions 1 and 2 shows an inverse proportionality between the *c* and *a* axes for samples where x>0.8 for $K_xFe_{2-x/2}Se_2$. The materials in region 3 all have a nominal potassium composition greater than 0.8 as well and display the same inverse relationship between the *c* and *a* axes of the *I*4/*m* phase. Another observation comes from the occupancies of the iron sites where in the *I*4/*m* phase the Fe2 site is depleted before iron is removed from the Fe2 site (Table 4.24).

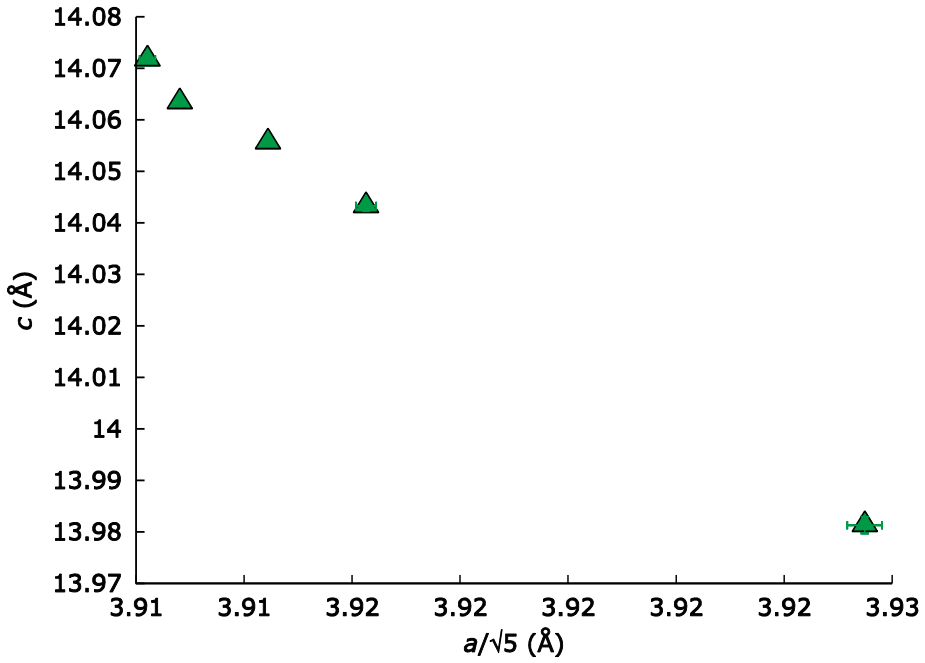

Figure 4.24 The lattice parameters of the *I*4/*m* phases as calculated by the Rietveld refinement of the *I*4/*m* structural model against the multiphase PXRD data of region 3. The error bars are displayed at 3σ.

The second ternary phase present in the region 3 samples presents with no supercell peaks and is described by the $ThCr_2Si_2$ (SG = *I*4/*mmm*) structure. The refined composition of this phase, from the two materials with high enough fractions of this phase, show that this *I*4/*mmm* phase is heavily iron deficient but potassium rich (Table 4.26). A similarity between the *I*4/*mmm* phases in the region 3 materials and the *I*4/*m* phases in the regions 1,2 and 3 is that although their space group differs their cell volumes fall within the spread of normalised cell volumes of the *I*4/*m* phases (Figure 4.25). The difference between the *c*/*a* parameters for the *I*4/*mmm* phases in the region 3 materials and the normalised *c*/*a* parameters for the *I*4/*m* phases for the regions 1,2 and 3 supports the

conclusion that this form of the *I*4/*mmm* phase is distinct from the *I*4/*m* phases. This additional potassium rich phase is how the extra potassium metal is accommodated for in these samples when compared to the region 2 materials.

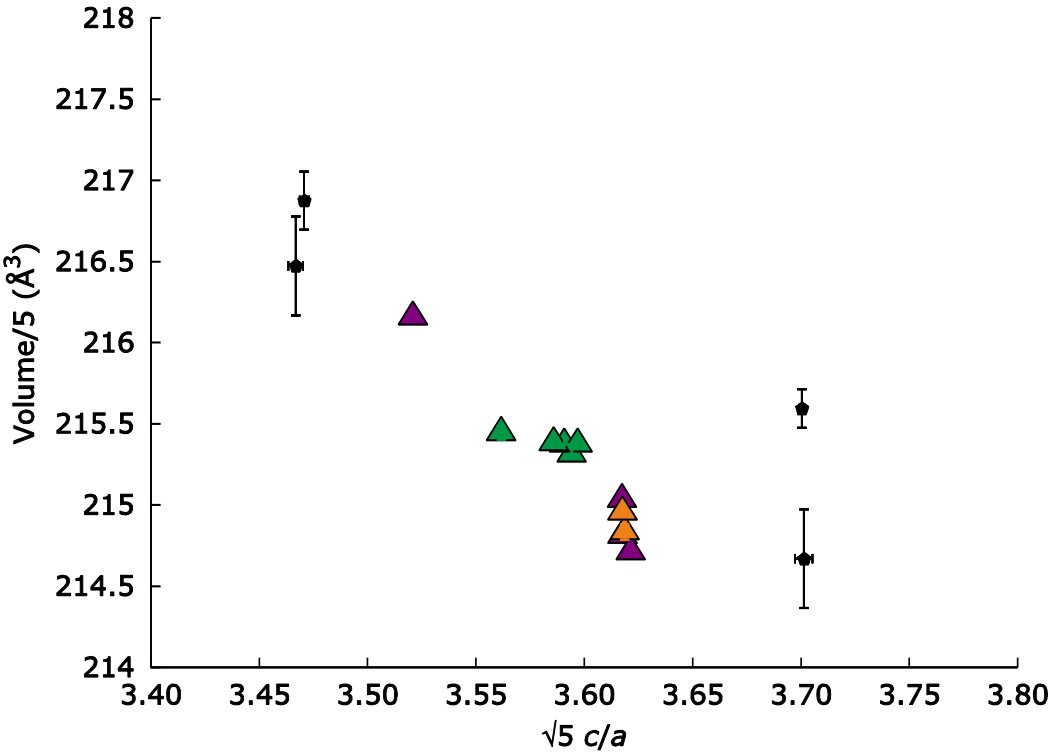

Figure 4.25 Normalised cell volume as a function of the *c*/*a* ratio. These values are calculated by the Rietveld refinement of the *I*4/*m* structural model against the PXRD data of region 1,2 and 3. Also included in this plot are the corresponding values of the *I*4/*mmm* phase from the region 3 materials. The black hexagons represent the *I*4/*mmm* phase of the region 3 materials. The colour of the markers corresponds to the region of the phase diagram were the data was obtained; (1) dark purple; (2) orange and (3) green. The error bars are displayed at 3σ.

4.4.6. Region 4 (red markers): $K_xFe_ySe_2$ (x=0.7-0.8; y=1.675-1.868) *I*4/*m*, *I*4/*mmm* and bulk Fe metal

In comparison to region 1 the materials the samples produced in region 4 (red markers Figure 4.13) have, in terms of nominal composition, more iron and relatively less selenium. So, like in region 3, elemental iron forms as a method of dealing with excess iron in the presence of relatively less selenium when compared to region 1. When region 3 materials are compared to those of region 4 the change in nominal composition is an increase in iron and a decrease in potassium content. This means that the phase assembly is identical to that of the region 3 giving *I*4/*m*, *I*4/*mmm* and Fe phases (Figure 4.26 and Table 4.27). A minor impurity detected in some patterns was also attributed to the *δ*-FeSe phase. The major difference between region 4 materials and all others is that they give a totally different picture in terms of superconductivity.

The phase fractions reveal the intolerance of the *I*4/*m* phase with respect to increasing iron content. As expected when more iron is added to the system, decreasing the nominal iron oxidation state, an increase in the elemental iron fraction is observed (Table 4.27). Interestingly two samples showed the presence of two *I*4/*mmm* type phases, these materials had the nominal compositions of $K_{0.7}Fe_{1.808}Se_2$ and $K_{0.8}Fe_{1.84}Se_2$. The *I*4/*mmm* phases produced from these two compositions will be discussed in terms of their cell parameters as all other parameters are heavily correlated with the respective values in the opposing *I*4/*mmm* phase.

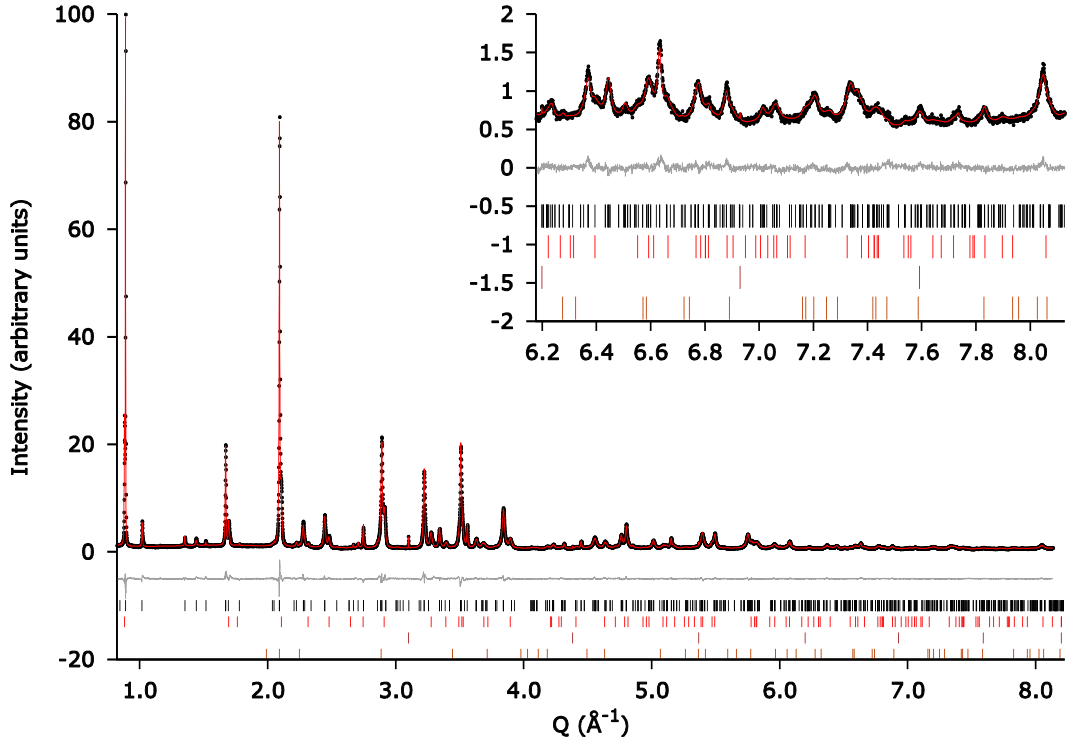

Figure 4.26 Rietveld refinement plot for the, region 4, material produced with the composition $K_{0.75}Fe_{1.702}Se_2$ (AG308_3) which gives a T_c = 33 K and an SF of 19 %. The model was refined against SPXRD data at a wavelength of λ = 0.399892 Å. Observed (black dots), calculated (red line) and difference (grey line) data are shown. The tic marks represent Bragg reflection positions of the *I*4/*m* (black), *I*4/*mmm* (red), Fe (brown) and *δ*-FeSe (dark orange) phases. A summary of the refined phase fractions are presented in tables 4.27-4.29. R_{wp} = 5.62, R_{exp} = 2.83, number of refined parameters 91.

Low-field (10 Oe) zero-field-cooling and field-cooling SQUID d.c.-magnetization measurements reveal that samples with the K-doping level targeted by the nominal composition close to 0.75 produces bulk superconductivity with shielding fraction of 19% (Figures 4.27, 4.28 and 4.29; Table 4.27). The identical superconducting properties of the three samples AG308_3, AG311_2 and AG323_2 indicate that the phases responsible for the superconductivity should be identical in each case (Figure 4.30). Interestingly the examination of the PXRD patterns for the AG308_3, AG311_2 and AG323_2 samples shows that the *I*4/*mmm* phases in these samples are all very similar (Figure 4.31). The structural property responsible for the superconductivity should be identifiable by Rietveld analysis of appropriate structural models against high resolution powder X-ray patterns.

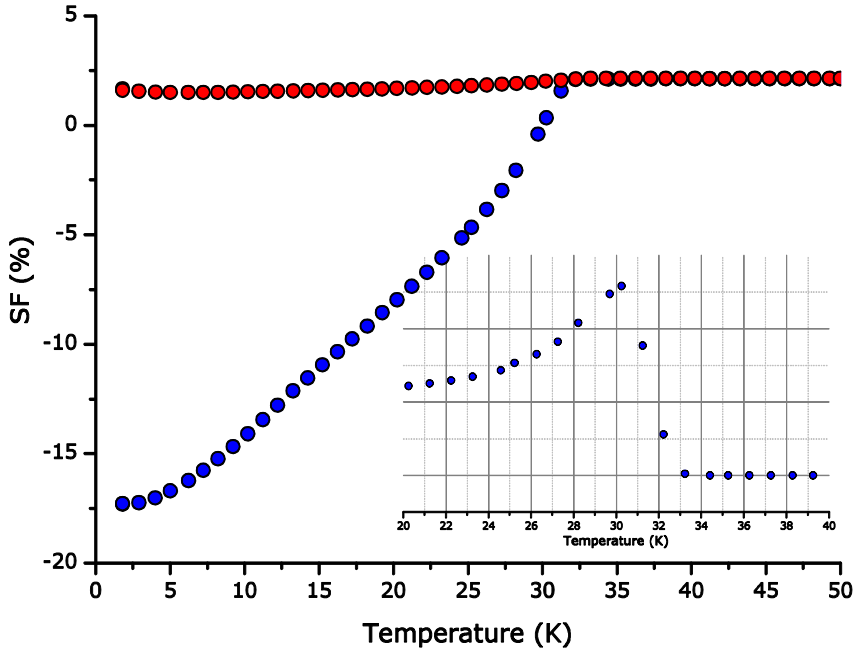

Figure 4.27 The magnetisation as a function of temperature measurements done on AG308_3 ($K_{0.75}Fe_{1.702}Se_2$). Where the red and blue circles correspond to the field cooled and zero field cooled experiments respectively. The inset is *d*M/*d*T and shows the onset of superconduction at a T_c of 33 K which rises to a shielding fraction of 19 % at 2 K. The magnetic measurements were taken in an applied field of 10 Oe with a sample mass of 30.7 mg.

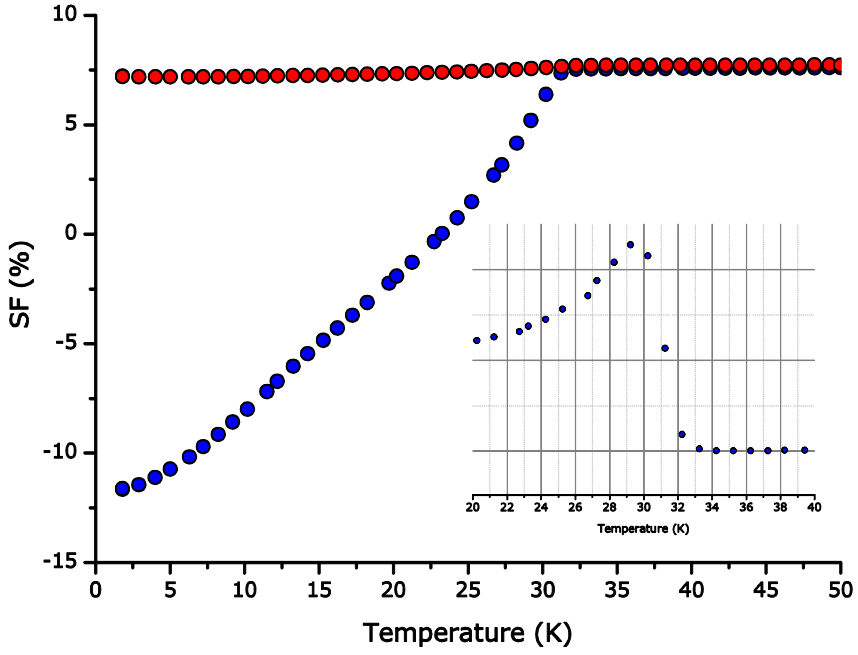

Figure 4.28 The magnetisation as a function of temperature measurements done on AG311_2 ($K_{0.75}Fe_{1.781}Se_2$). Where the red and blue circles correspond to the field cooled and zero field cooled experiments respectively. The inset is *d*M/*d*T and shows the onset of superconduction at a T_c of 33 K which rises to a shielding fraction of 19 % at 2 K. The magnetic measurements were taken in an applied field of 10 Oe with a sample mass of 31.4 mg.

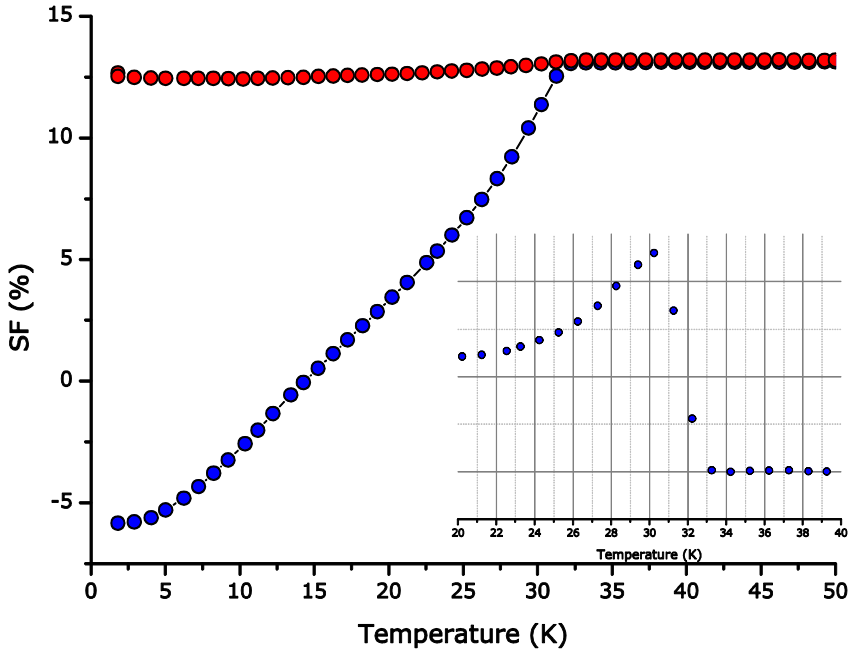

Figure 4.29 The magnetisation as a function of temperature measurements done on AG323_2 ($K_{0.75}Fe_{1.868}Se_2$). Where the red and blue circles correspond to the field cooled and zero field cooled experiments respectively. The inset is *d*M/*d*T and shows the onset of superconduction at a T_c of 33 K which rises to a shielding fraction of 19 % at 2 K. The magnetic measurements were taken in an applied field of 10 Oe with a sample mass of 30.2 mg.

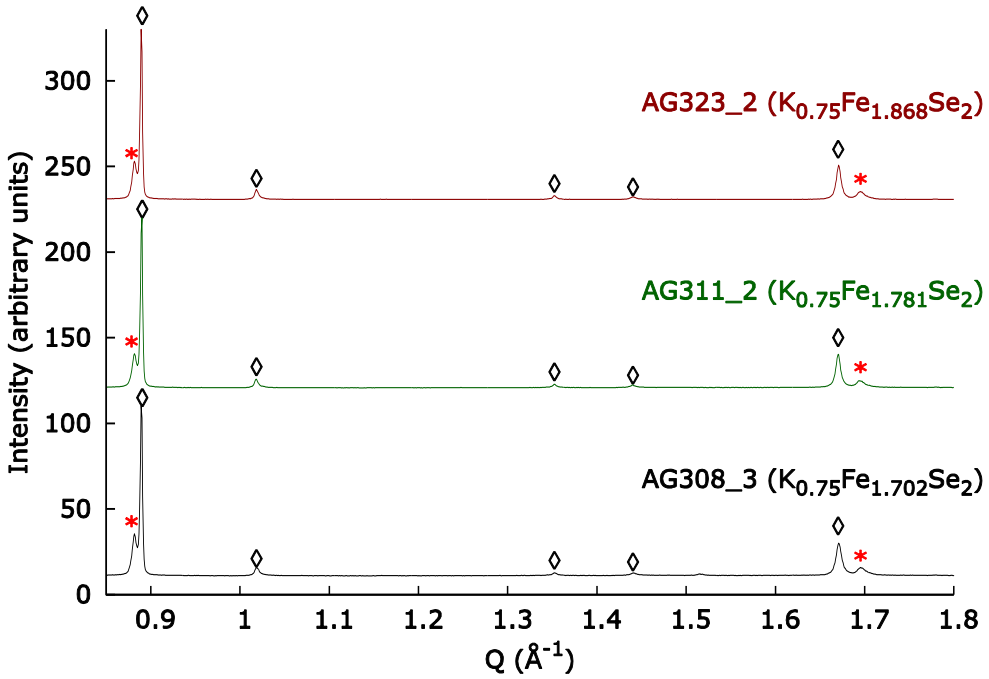

Figure 4.30 Comparison of patterns collected at room temperature for the materials with nominal compositions of AG308_3($K_{0.75}Fe_{1.702}Se_2$), AG311_2($K_{0.75}Fe_{1.781}Se_2$) and AG323_2($K_{0.75}Fe_{1.868}Se_2$) made using the quenched protocol. The black hollow diamonds represents the peaks of the *I*4/*m* phase; the red * represents the *I*4/*mmm* peaks. The comparison of the three patterns of the materials which display SFs of 19 % shows that the *I*4/*mmm* phase for these materials appears identical.

Table 4.27 The phase assembly from the Rietveld analysis of the PXRD data for materials shown by the red markers in Figure 4.13.

Parameter / Label	SF (%) @ 2 K	*I*4/*mmm* (vol. %)	*I*4/*mmm*(a) (vol. %)	*I*4/*m* (vol. %)	Fe (vol. %)	*β*-FeSe (vol. %)	*δ*-FeSe (vol. %)
AG306_2($K_{0.7}Fe_{1.728}Se_2$)	2	18.7340(1801)	0	81.1557(1780)	0.1103(4)	0	0
AG322_2($K_{0.7}Fe_{1.808}Se_2$)	1	14.428(214)	14.848(209)	69.979(248)	0.663(8)	0	0.083(2)
AG323_2($K_{0.75}Fe_{1.868}Se_2$)	19	15.41(12)	0	82.69(12)	1.90(2)	0	0
AG311_2($K_{0.75}Fe_{1.781}Se_2$)	19	15.673(118)	0	83.389(117)	0.938(9)	0	0
AG308_3($K_{0.75}Fe_{1.702}Se_2$)	19	16.1983(951)	0	83.6918(951)	0.1022(3)	0	0.0077(2)
AG300_2($K_{0.8}Fe_{2.04}Se_2$)	0	2.85(18)	0	92.88(19)	4.27(7)	0	0
AG298_3($K_{0.8}Fe_{1.84}Se_2$)	0	11.43(16)	0.36(4)	86.31(16)	1.90(1)	0	0
AG424_2($K_{0.8}Fe_{1.754}Se_2$)	6.3	17.58(56)	0	81.03(56)	1.39(1)	0	0
AG295_3($K_{0.8}Fe_{1.675}Se_2$)	0	9.604(104)	0	90.282(104)	0.114(4)	0	0

Table 4.28 The lattice parameters of the *I*4/*m* phase as obtained from the Rietveld analysis of the PXRD data for materials shown by the red markers in Figure 4.13.

Parameter / Label	SF (%) @ 2 K	$a/\sqrt{5}$ (Å)	c (Å)	V/5 (Å^3)	$\sqrt{5}\,c/a$
AG306_2($K_{0.7}Fe_{1.728}Se_2$)	2	3.89742(4)	14.1253(2)	214.561(5)	3.62426(6)
AG322_2($K_{0.7}Fe_{1.808}Se_2$)	1	3.89881(5)	14.1120(2)	214.634(4)	3.62162(5)
AG323_2($K_{0.75}Fe_{1.868}Se_2$)	19	3.90011(2)	14.1228(1)	214.820(3)	3.62113(4)
AG311_2($K_{0.75}Fe_{1.781}Se_2$)	19	3.90137(2)	14.1165(1)	214.862(3)	3.61835(3)
AG308_3($K_{0.75}Fe_{1.702}Se_2$)	19	3.89931(3)	14.1204(1)	214.695(3)	3.62126(4)
AG300_2($K_{0.8}Fe_{2.04}Se_2$)	0	3.90778(8)	14.1005(4)	215.33(1)	3.6083(1)
AG298_3($K_{0.8}Fe_{1.84}Se_2$)	0	3.90398(3)	14.1088(1)	215.033(3)	3.61394(4)
AG424_2($K_{0.8}Fe_{1.754}Se_2$)	6.3	3.90340(2)	14.10424(9)	214.899(2)	3.61333(3)
AG295_3($K_{0.8}Fe_{1.675}Se_2$)	0	3.907627(9)	14.09331(4)	215.199(1)	3.60662(1)

Table 4.29 The refined compositions and individual site occupancies of the *I*4/*m* phase obtained from the Rietveld analysis of the PXRD data for materials shown by the red markers in Figure 4.13.

Parameter / Label	SF (%) @ 2 K	Refined Composition	K1 *2b*	K2 *8h*	Fe1 *16i*	Fe2 *4d*
AG306_2($K_{0.7}Fe_{1.728}Se_2$)	2	$K_{0.742(8)}Fe_{1.613(8)}Se_2$	0.82(2)	0.723(8)	0.950(4)	0.23(1)
AG322_2($K_{0.7}Fe_{1.808}Se_2$)	1	$K_{0.810(7)}Fe_{1.677(7)}Se_2$	0.92(2)	0.782(7)	0.987(4)	0.248(8)
AG323_2($K_{0.75}Fe_{1.868}Se_2$)	19	$K_{0.831(6)}Fe_{1.523(5)}Se_2$	1.00(2)	0.789(6)	0.922(3)	0.119(6)
AG311_2($K_{0.75}Fe_{1.781}Se_2$)	19	$K_{0.801(5)}Fe_{1.522(5)}Se_2$	0.88(2)	0.781(5)	0.914(2)	0.148(6)
AG308_3($K_{0.75}Fe_{1.702}Se_2$)	19	$K_{0.868(6)}Fe_{1.527(5)}Se_2$	0.86(2)	0.870(5)	0.898(3)	0.226(7)
AG300_2($K_{0.8}Fe_{2.04}Se_2$)	0	$K_{0.79(2)}Fe_{1.61(1)}Se_2$	0.89(5)	0.77(1)	0.979(6)	0.10(2)
AG298_3($K_{0.8}Fe_{1.84}Se_2$)	0	$K_{0.847(7)}Fe_{1.46(5)}Se_2$	1.00(2)	0.808(6)	0.879(3)	0.138(6)
AG424_2($K_{0.8}Fe_{1.754}Se_2$)	6.3	$K_{0.713(6)}Fe_{1.681(5)}Se_2$	0.90(2)	0.667(5)	1.000(3)	0.204(7)
AG295_3($K_{0.8}Fe_{1.675}Se_2$)	0	$K_{0.822(3)}Fe_{1.621(2)}Se_2$	0.905(8)	0.801(3)	0.972(1)	0.162(3)

As indicated by the region 1 and 2 materials the 0.8 nominal potassium doping level is a critical point after which the intercalated phase's lattice parameters begin to change significantly (Figure 4.31). The corresponding critical nominal potassium level above the +2 iron oxidation state line is at a nominal potassium composition of 0.75. The lattice parameters of the *I*4/*m* phase between 0.7 and 0.75 nominal potassium composition show, generally, a small drop in *c* coupled with a small increase in *a*. However, the change in the *I*4/*m* phases lattice parameters between the 0.75 and 0.8 nominal potassium levels is much more obvious. There is a significant drop in the *c* axis coupled with a large increase in the *a* axis between the nominal potassium levels 0.75 and 0.8 (Figure 4.31). The spread in lattice parameters of the *I*4/*m* phases at each potassium level in figure 4.31 has no trend with refined or nominal iron composition. This is the identical trend to what was observed for the region 1 and 2 *I*4/*m* phases where the presence of less iron and more potassium in the system caused drastic changes in lattice parameters after x exceeded 0.8 in $K_xFe_{2-x/2}Se_2$.

In order to assign the superconducting behaviour found in some of these materials to a particular phase in their PXRD there needs to be an agreement between the three samples AG308_3, AG311_2 and AG323_2. What the lattice parameters of the *I*4/*m* phases produced by materials in region 4 do demonstrate is that the *I*4/*m* phases of the three samples with a SF of 19 % are significantly different to each other (Figure 4.31). Not only are the region 4 *I*4/*m* phases different from each other they also fall within the spread of points generated by *I*4/*m* phases from non-superconducting samples for all parameters directly derived from the lattice parameters (Figure 4.31 and 4.32). The lack of correlation between the *I*4/*m* phases within superconducting samples and the overlap of their cell parameters with *I*4/*m* phases from non-superconducting materials is very strong evidence to conclude that the *I*4/*m* phase in these materials is not responsible for superconductivity.

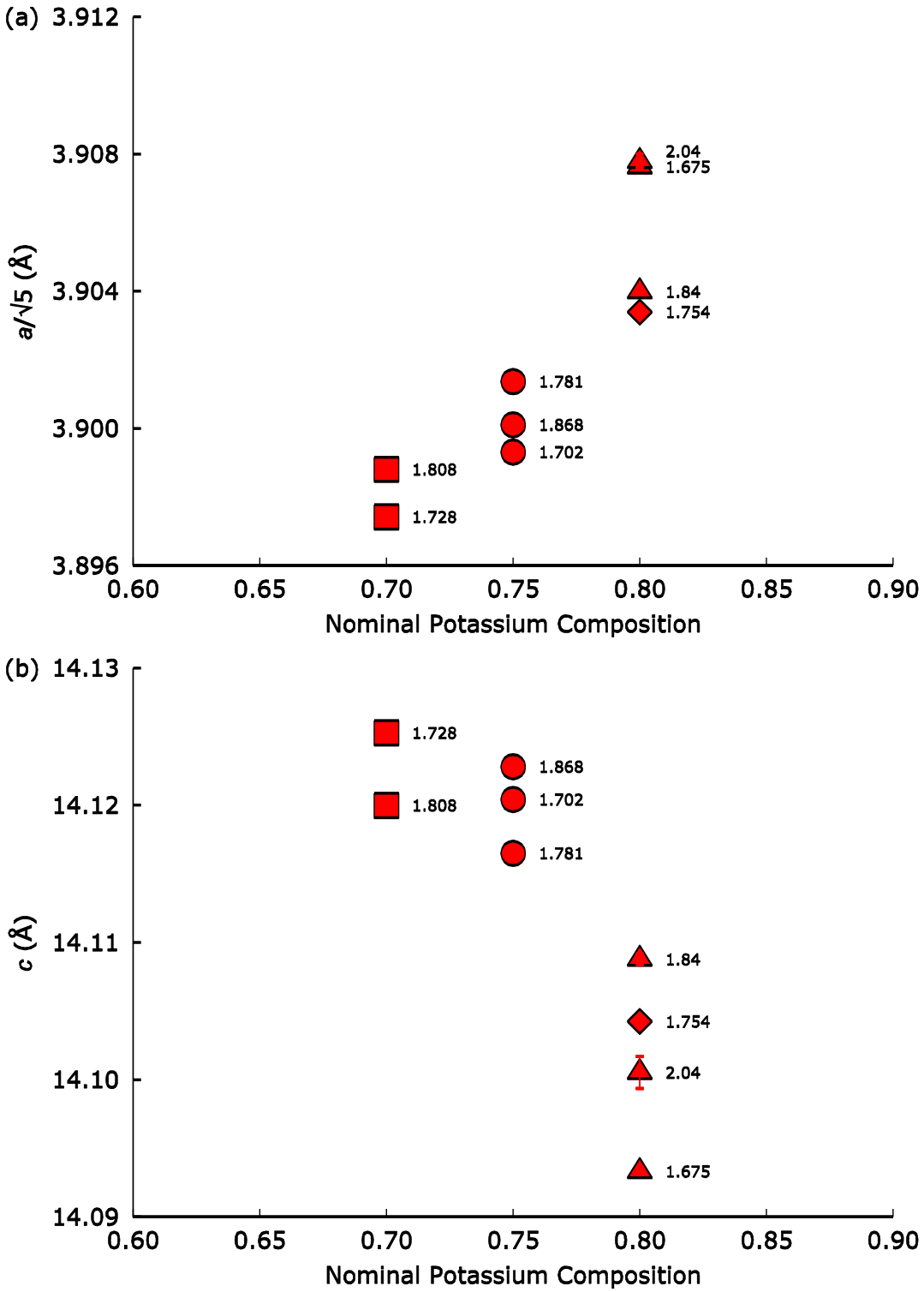

Figure 4.31 The lattice parameters where (a) $a/\sqrt{5}$ and (b) c of the $I4/m$ phase as a function of nominal potassium composition. The numbers beside each point correspond to the nominal iron compositions. Superconductivity from SQUID measurements: triangles - 0 %; squares - 1-3 %; diamonds - 6 %; circles – 19 %. The error bars are displayed at 3σ.

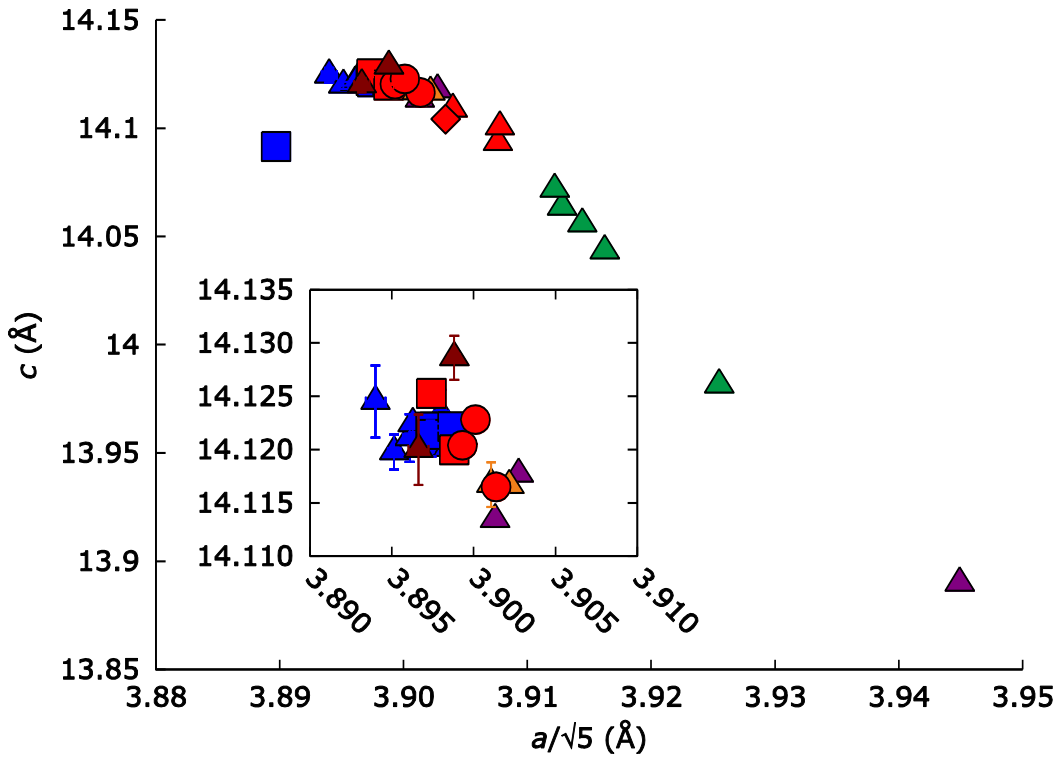

Figure 4.32 The lattice parameters of *I*4/*m* phases as determined from Rietveld analysis. Superconductivity from SQUID measurements: triangles - 0 %; squares - 1-3 %; diamonds - 6 %; circles – 19 %. The colour of the markers corresponds to the region of the phase diagram were the data was obtained; (1) dark purple; (2) orange; (3) green; (4) red; (5) blue and (6) brown. The insert is an enlargement of the densely populated region of the plot that contains the values produced by the materials with SFs of 19 %. The error bars are displayed at 3σ.

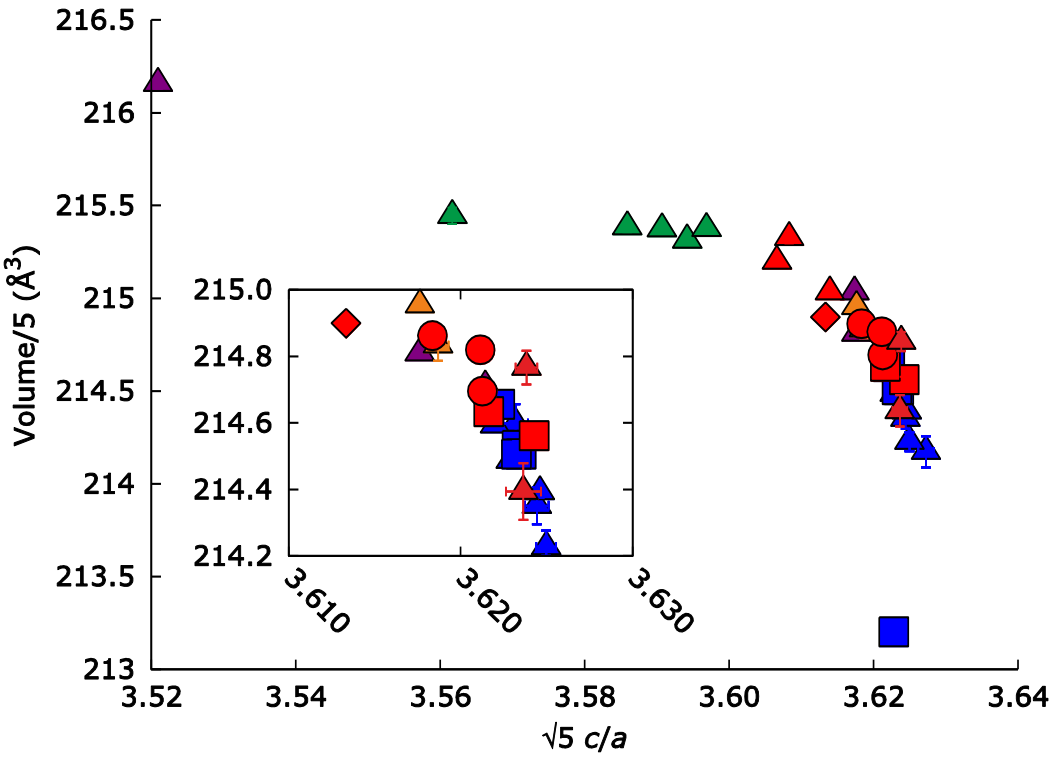

Figure 4.33 Normalised cell volume as a function of the √5 *c*/*a* ratio of the *I*4/*m* phases. Superconductivity from SQUID measurements: triangles - 0 %; squares - 1-3 %; diamonds - 6 %; circles – 19 %. The colour of the markers corresponds to the region of the phase diagram were the data was obtained; (1) dark purple; (2) orange; (3) green; (4) red; (5) blue and (6) brown. The insert is an enlargement of the densely populated region of the plot that contains the values produced by the materials with SFs of 19 %. The error bars are displayed at 3σ.

The composition of the *I*4/*m* phases from the region 4 materials also supports the conclusion that the *I*4/*m* phase is not responsible for superconductivity. The spread of the refined potassium compositions for the *I*4/*m* phases belonging to the samples AG308_3, AG311_2 and AG323_2 are such that the refined potassium composition of the *I*4/*m* phase from the AG308_3 sample is significantly different to the others in that series (Figure 4.34). This means that the refined potassium composition of the *I*4/*m* phases is not a key parameter for the presence of superconductivity. The refined iron compositions of the *I*4/*m* phases from the AG308_3, AG311_2 and AG323_2 materials, red circle markers, are identical within one standard deviation (Figure 4.35). Although the materials presenting with an SF of 19 % have an *I*4/*m* phase with identical refined iron compositions they are not unique and fall within the spread of refined iron compositions obtained from *I*4/*m* phases of non-superconducting samples. The lack of agreement that is unique, with respect to non-superconducting materials, between the refined compositions of the *I*4/*m*

phases of the AG308_3, AG311_2 and AG323_2 samples means that this phase is not responsible for superconductivity in the $K_xFe_ySe_2$ materials.

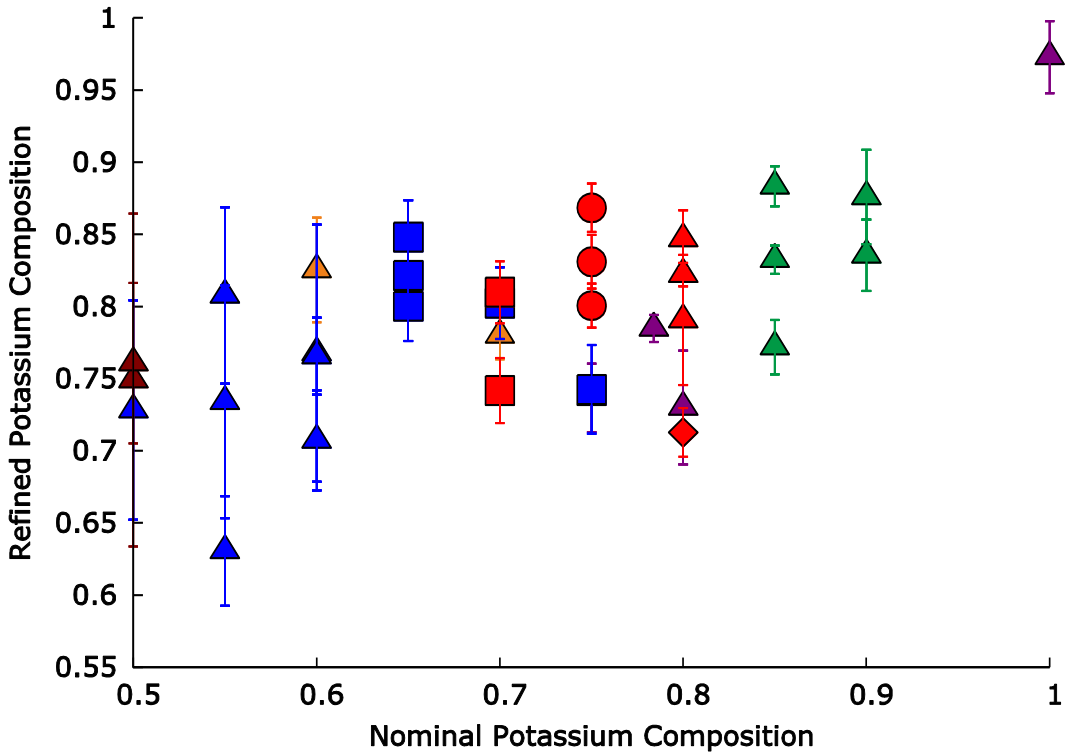

Figure 4.34 Refined potassium content of the *I*4/*m* phases plotted vs. nominal potassium content. Superconductivity from SQUID measurements: triangles - 0 %; squares - 1-3 %; diamonds - 6 %; circles – 19 %. The colour of the markers corresponds to the region of the phase diagram were the data was obtained; (1) dark purple; (2) orange; (3) green; (4) red; (5) blue and (6) brown. The error bars are displayed at 3σ.

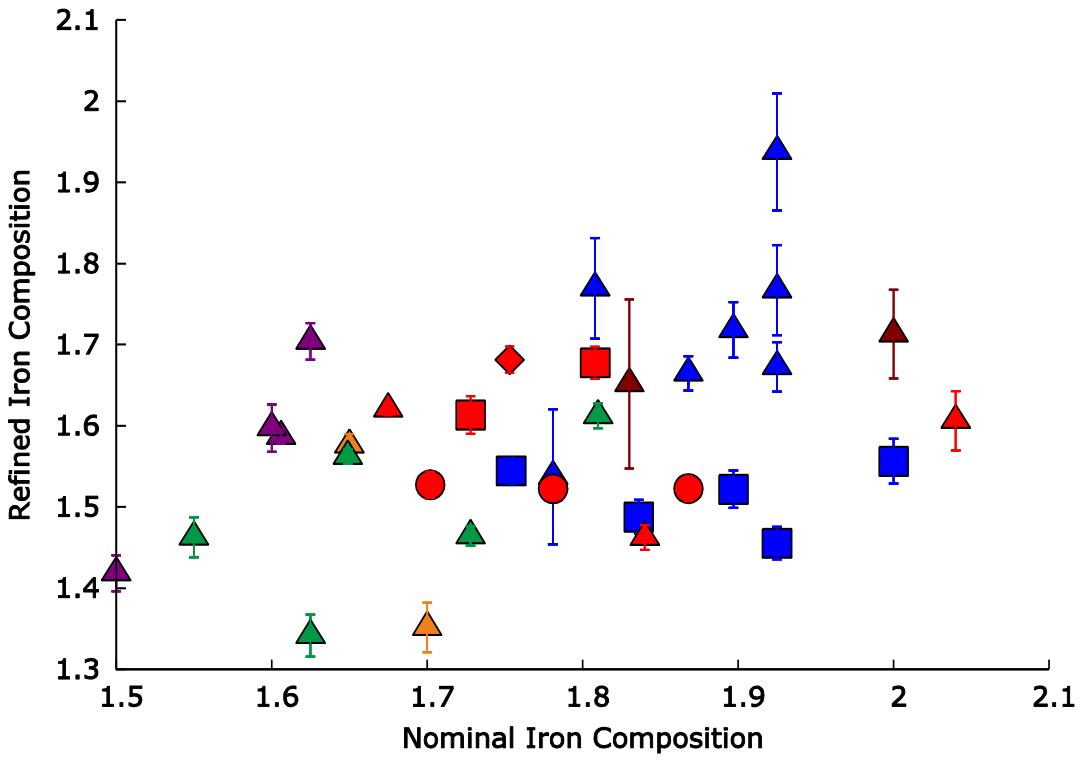

Figure 4.35 Refined iron content of the *I*4/*m* phase plotted vs. nominal iron content. Superconductivity from SQUID measurements: triangles - 0 %; squares - 1-3 %; diamonds - 6 %; circles – 19 %. The colour of the markers corresponds to the region of the phase diagram were the data was obtained; (1) dark purple; (2) orange; (3) green; (4) red; (5) blue and (6) brown. The error bars are displayed at 3σ.

An obvious possible source for the cause of superconductivity comes from the iron rich *I*4/*mmm* phases present in the materials at the nominal potassium composition of 0.75. There is only a small difference between the refined phase fractions and the actual superconducting fractions for these materials. Unlike the *I*4/*m* phase the iron rich *I*4/*mmm* phases share many structural similarities to other iron based superconductors. For example $Ba_{1-x}K_xFe_2As_2$ material which has the same basic $ThCr_2Si_2$ structure.[17] Ascertaining the role of the *I*4/*mmm* phase is complicated by the presence of significant amounts of this phase in non-superconducting materials. As stated before, the superconducting phases in these materials should be identical to each other and unique from all other non-superconducting forms of the material. Superconductors with a similar $ThCr_2Si_2$ (*I*4/*mmm*) structure highlight the following properties as important to the presence of superconductivity in their samples, bond angles, anion height, *c*/*a* ratio, cell volume and composition.[2, 17-19]

Table 4.30 The lattice parameters of the *I*4/*mmm* phase as obtained from the Rietveld analysis of the PXRD data for materials shown by the red markers in Figure 4.13.

Parameter / Label	SF (%)	*I*4/*mmm* *a* Å	*I*4/*mmm* *c* Å	*I*4/*mmm* V Å^3	*I*4/*mmm* *c*/*a*	*I*4/*mmm*(a) *a* Å	*I*4/*mmm*(a) *c* Å	*I*4/*mmm*(a) V Å^3	*I*4/*mmm(a)* *c*/*a*
AG306_2($K_{0.7}Fe_{1.728}Se_2$)	2	3.8330(1)	14.2423(6)	209.24(1)	3.7157(2)	0	0	0	0
AG322_2($K_{0.7}Fe_{1.808}Se_2$)	1	3.8207(2)	14.2576(9)	208.13(3)	3.7316(3)	3.8344(1)	14.278(1)	209.91(2)	3.7236(3)
AG323_2($K_{0.75}Fe_{1.868}Se_2$)	19	3.83626(7)	14.2508(4)	209.73(1)	3.7148(1)	0	0	0	0
AG311_2($K_{0.75}Fe_{1.781}Se_2$)	19	3.83643(8)	14.2504(3)	209.74(1)	3.7145(1)	0	0	0	0
AG308_3($K_{0.75}Fe_{1.702}Se_2$)	19	3.83600(7)	14.2523(4)	209.72(1)	3.7154(1)	0	0	0	0
AG300_2($K_{0.8}Fe_{2.04}Se_2$)	0	3.8673(6)	14.411(5)	215.5(1)	3.726(2)	0	0	0	0
AG298_3($K_{0.8}Fe_{1.84}Se_2$)	0	3.8385(2)	14.253(1)	210.01(3)	3.765(1)	3.8081(2)	14.338(4)	207.93(6)	3.71313(1)
AG424_2($K_{0.8}Fe_{1.754}Se_2$)	6.3	3.8371(2)	14.2518(6)	209.84(2)	3.7142(2)	0	0	0	0
AG295_3($K_{0.8}Fe_{1.675}Se_2$)	0	3.8671(1)	14.3471(4)	214.56(1)	3.7100(2)	0	0	0	0

Table 4.31 The bond angles and refined compositions as obtained from the Rietveld refinement of *I*4/*mmm* phase over 10 vol.% in the materials shown by the red markers in Figure 4.13. Due to the complete overlap of all peaks between the *I*4/*mmm* and *I*4/*mmm*(a) phases the compositions and bond angles of AG322_2 (K0.7Fe1.808Se2) and AG298_3 ($K_{0.8}Fe_{1.84}Se_2$) are not considered.

Parameter / Label	SF (%)	*I*4/*mmm* bond angle Se-Fe-Se		Refined Composition	Se layer height Å
		2 fold axis	4 fold axis		
AG306_2($K_{0.7}Fe_{1.728}Se_2$)	2	103.2(1)	112.72(6)	$K_{0.52(2)}Fe_{2.00(2)}Se_2$	1.520(2)
AG323_2($K_{0.75}Fe_{1.868}Se_2$)	19	103.33(9)	112.63(5)	$K_{0.53(2)}Fe_{2.00(1)}Se_2$	1.517(1)
AG311_2($K_{0.75}Fe_{1.781}Se_2$)	19	103.23(8)	112.68(4)	$K_{0.54(1)}Fe_{1.98(1)}Se_2$	1.520(1)
AG308_3($K_{0.75}Fe_{1.702}Se_2$)	19	102.89(8)	112.86(4)	$K_{0.55(1)}Fe_{1.97(1)}Se_2$	1.529(1)
AG424_2($K_{0.8}Fe_{1.754}Se_2$)	6.3	105.1(2)	111.7(1)	$K_{0.59(2)}Fe_{2.00(3)}Se_2$	1.469(3)
AG295_3($K_{0.8}Fe_{1.675}Se_2$)	0	102.477(9)	113.08(5)	$K_{0.62(1)}Fe_{1.90(2)}Se_2$	1.552(2)

The *I*4/*mmm* phases in region 4 (shown by the red markers in Figure 4.13) are for the majority of cases very similar. What jumps out immediately is that the *I*4/*mmm* phases at the K = 0.75 level have identical (within 3 standard deviations) lattice parameters (Figure 4.36 and 4.37). As one would expect from the lattice parameters they have, within error, identical compositions with an average composition of $K_{0.54}Fe_{1.983}Se_2$. The average composition corresponds to a formal iron oxidation state of $Fe^{1.75+}$, representing a very reduced form of iron which is considerably less stable than Fe^{2+}. The implication of this is that based on first principals the *I*4/*mmm* phase should be less stable than the *I*4/*m* phase which contains Fe with a charge state close to 2+. The X-ray data across the entire phase diagram and at high temperature supports this conclusion as on cooling the *I*4/*mmm* high temperature phase decomposes into two ternary phases where in all cases the *I*4/*m* phases is the majority phase. These observations indicate that isolation of the *I*4/*mmm* phase with a composition of $K_{0.54}Fe_{1.983}Se_2$ is going to be difficult without decomposition into the *I*4/*m* phase.

Another point is that although the *I*4/*mmm* phases belonging to the AG308_3, AG311_2 and AG323_2 materials are identical, other materials have *I*4/*mmm* phases which have similar lattice parameters and compositions as well. An interesting observation is displayed by figure 4.36 there is one *I*4/*mmm* phase which lies which is very close to the points described by the 19 % SF materials *I*4/*mmm* phases. This phase belongs to the sample with the nominal composition of $K_{0.8}Fe_{1.753}Se_2$ which incidentally has a SF of 6.3 %. This material has 17.6 vol.% of the *I*4/*mmm* phase and considering that 6.3 % of that is superconducting we would expect this sample to be very close to that of the AG308_3, AG311_2 and AG323_2 *I*4/*mmm* phases. Despite the observation that the *I*4/*mmm* phases belonging to the AG308_3, AG311_2 and AG323_2 materials are identical, there needs to be another defining property which sets them aside from the non-superconducting *I*4/*mmm* phases represented by the blue triangle in the inset of figure 4.36.

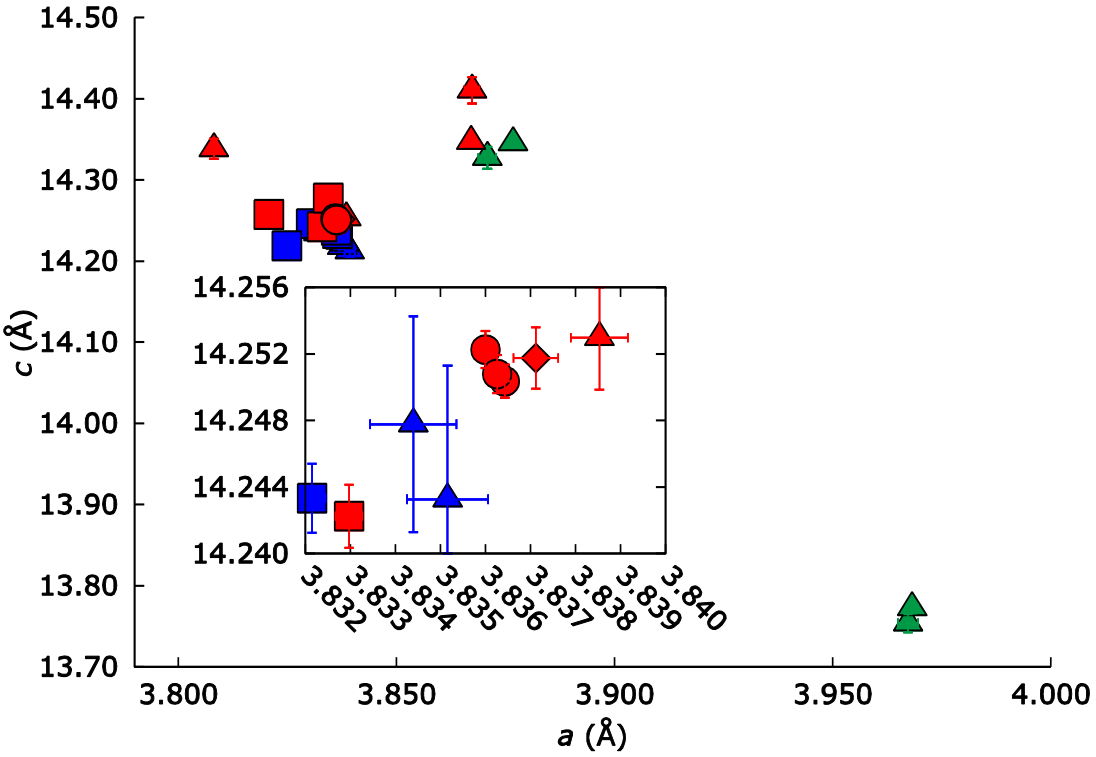

Figure 4.36 The lattice parameters of the *I*4/*mmm* phase as obtained from Rietveld refinement. The inset is an enlarged view of the region around the red circle markers. Superconductivity from SQUID measurements: triangles - 0 %; squares - 1-3 %; diamonds - 6 %; circles – 19 %. The colour of the markers corresponds to the region of the phase diagram where the data was obtained; (3) green; (4) red and (5) blue. The insert is an enlargement of the densely populated region of the plot that contains the values produced by the materials with SFs of 19 %. The error bars are displayed at 3σ.

The similarities between the 19 and 6.3 % SF materials are further reinforced by the measure of tetragonality (*c*/*a*) and cell volume (Figure 4.37). The *I*4/*mmm* phases generated from the nominal composition $K_{0.75}Fe_{1.702}Se_2$ and $K_{0.75}Fe_{1.781}Se_2$ have a *c*/*a* ratios but identical volumes. This indicates that the superconducting phase has a tolerance for different *c* and *a* parameters if the calculated cell volume is within error of 209.73(1) $Å^3$. The *I*4/*mmm* cell volumes obtained from the AG308_3, AG311_2 and AG323_2 materials when compared to all other *I*4/*mmm* phases are significantly different from each other.

A reassuring observation is that the cell volume of the 6.3 % SF material is larger than the AG308_3, AG311_2 and AG323_2 materials *I*4/*mmm* phases but is the closest point to them. The likely reason for the lower SF in the $K_{0.8}Fe_{1.754}Se_2$ material is that there are two closely related overlapping *I*4/*mmm* phases one has the correct cell volume and the other, being the majority, is skewing the cell volume to significantly higher values. With the I4/mmm phases being heavily strain broadened (section 4.3.2.) the resolution of these theoretical phases would be difficult unless they both had high phase fractions. The conclusions from figure 4.37 are that the cell volume is the critical value for

the superconducting *I*4/*mmm* phases. This is not a surprising outcome as the role of volume has been noted in systems such as $BaFe_2(As_{1-x}P_x)_2$.[20]

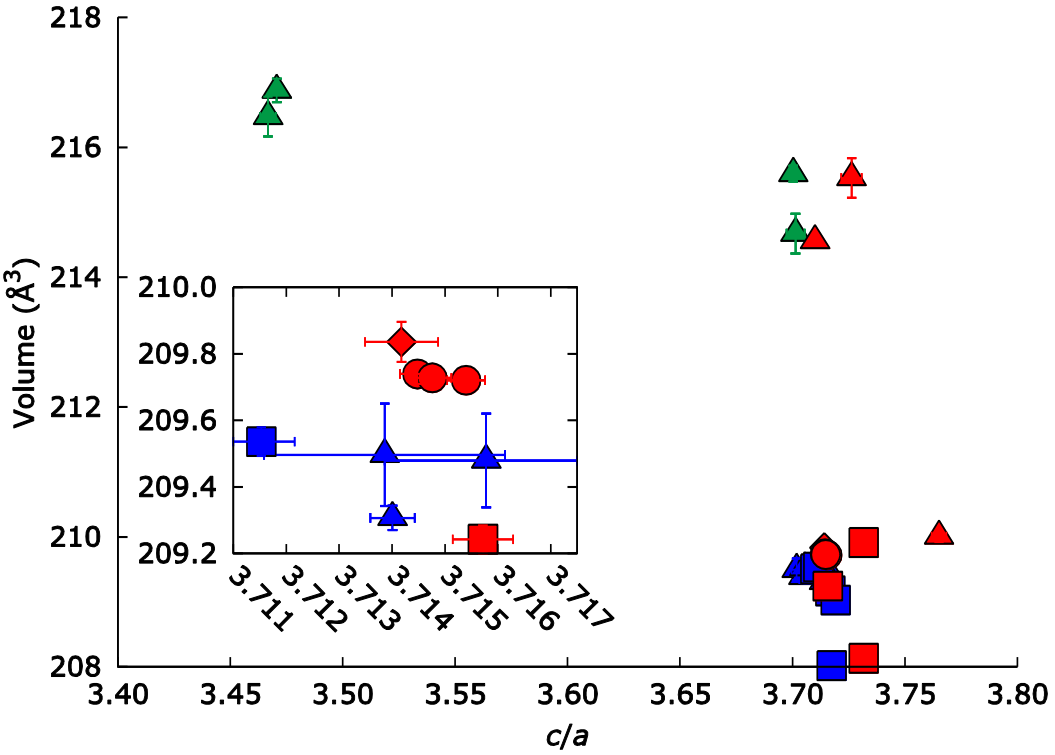

Figure 4.37 Normalised cell volume as a function of the *c/a* ratio of the *I*4/*mmm* phases. Superconductivity from SQUID measurements: triangles - 0 %; squares - 1-3 %; diamonds - 6 %; circles – 19 %. The colour of the markers corresponds to the region of the phase diagram were the data was obtained; (3) green; (4) red and (5) blue. The insert is an enlargement of the densely populated region of the plot that contains the values produced by the materials with SFs of 19 %. The error bars are displayed at 3σ.

This leaves two other prominent properties with which to investigate the ideal *I*4/*mmm* superconducting phase. These are the Se-Fe-Se bond angles and the selenium layer height above the planar iron layer. These parameters have been linked to T_c in systems like $Ba_{1-x}K_xFe_2As_2$ where the closer the average angle is to the ideal tetrahedral angle (109.47 °) the higher the T_c becomes.[21] Considering that the materials AG308_3, AG311_2 and AG323_2 all have a T_c of 33 K critical parameters, like the Se-Fe-Se bond angles, should still be identical. The relationship between volume and Se layer height is displayed in figure 4.38 and shows no correlation between the AG308_3, AG311_2 and AG323_2 materials *I*4/*mmm* phases within 3 standard deviations. The lack of agreement for the selenium layer height values of the materials with a SF of 19 % and a T_c of 33 K means that this parameter is not important to obtaining superconducting material.

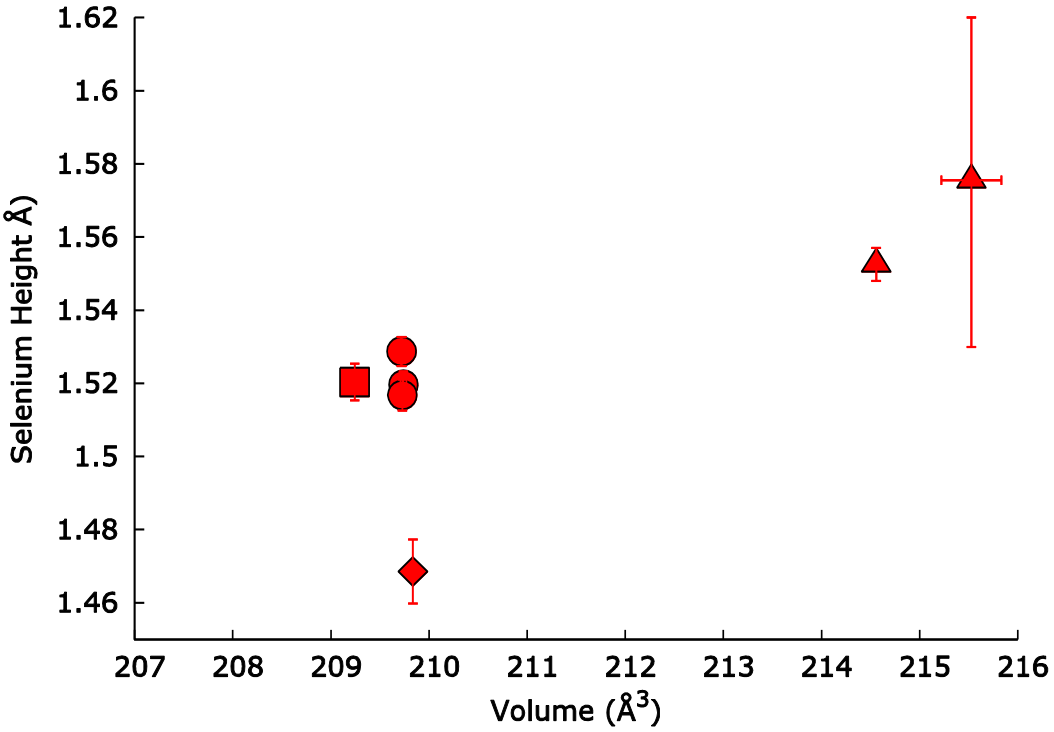

Figure 4.38 The change in selenium layer height of the *I*4/*mmm* phase as a function of unit cell volume. Superconductivity from SQUID measurements: triangles - 0 %; squares - 1-3 %; diamonds - 6 %; circles – 19 %. The error bars are displayed at 3σ.

In the *I*4/*mmm* structure there are two distinct bond angles one corresponding to a twofold bond angle between the Se atoms on the same side of the Fe layer and a fourfold bond angle between Se atoms on opposite sides of the same layer. Plotting both the angles vs cell volume reveals a strong agreement between the AG308_3, AG311_2 and AG323_2 *I*4/*mmm* phases, which are identical within one standard deviation (Figure 4.39). It also shows that the 6.3 % SF materials *I*4/*mmm* phase is different, outside of 3 standard deviations, but very close. This further supports the conclusion that the superconductivity is due to the *I*4/*mmm* phase. Since the Se-Fe-Se bond angles of the *I*4/*mmm* phases of the AG308_3, AG311_2 and AG323_2 materials do fall within the spread of the other *I*4/*mmm* phases of materials with SFs of less than 19 % it can be said that the cell volume is the most influential parameter in determining the materials superconducting properties. Interestingly this average bond angle corresponds to the same angle in the $Ba_{1-x}K_xFe_2As_2$ system which produces a T_c of ~30 K.[22]

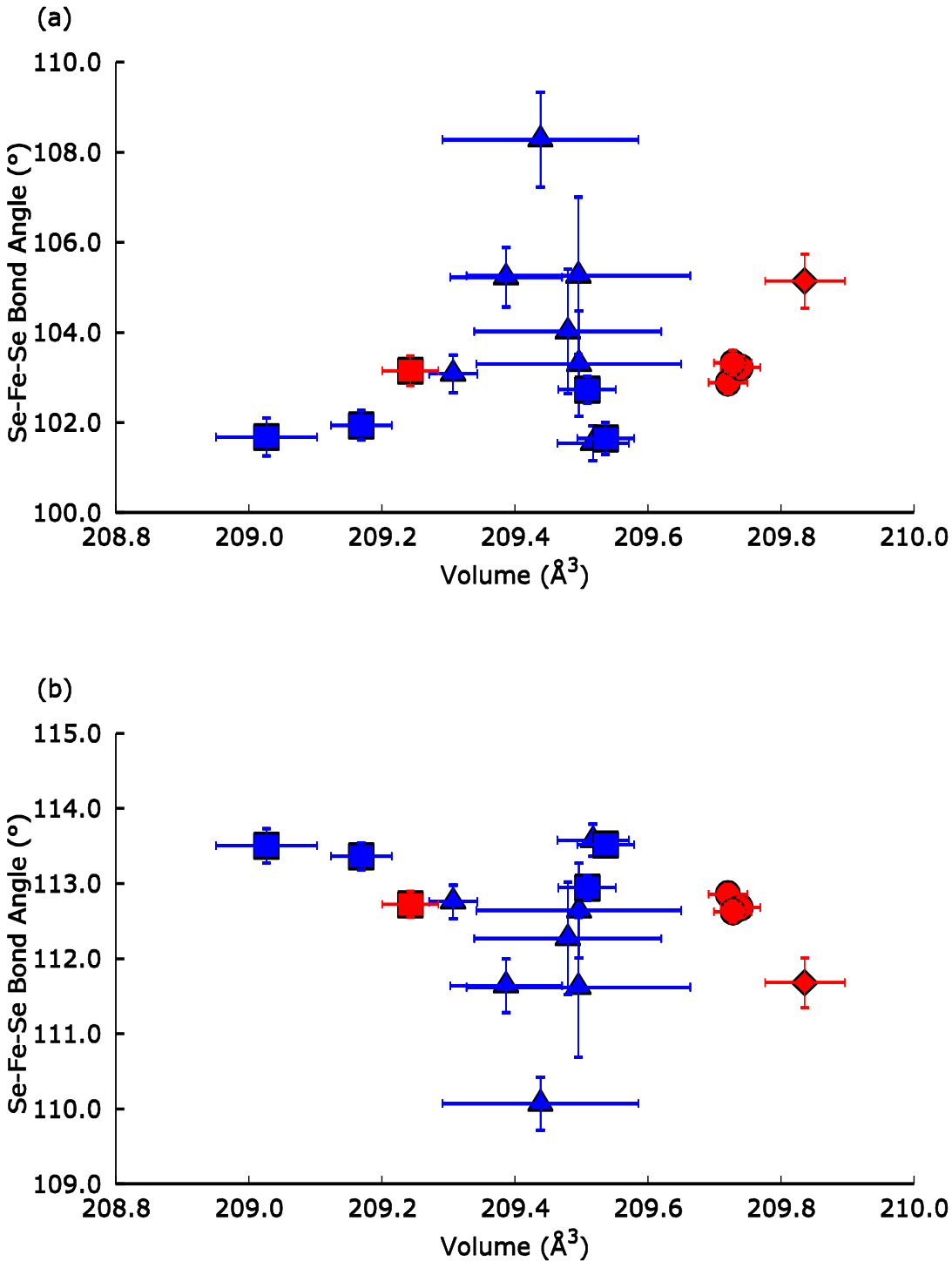

Figure 4.39 The change in Se-Fe-Se bond angles for the *I*4/*mmm* phase as a function of unit cell volume. (a) The bond angles here correspond to the twofold bond angle. (b) The bond angles correspond to the four fold bond angle. Superconductivity from SQUID measurements: triangles - 0 %; squares - 1-3 %; diamonds - 6 %; circles – 19 %. The colour of the markers corresponds to the region of the phase diagram were the data was obtained (4) red and (5) blue. The error bars are displayed at 3σ.

4.4.7. Region 5 (blue markers): $K_xFe_ySe_2$ (x=0.5-0.75; y=1.754-2.0) *I*4/*m*, *I*4/*mmm*, FeSe and bulk Fe metal

The samples produced in region 5 have less nominal potassium, more iron present when compared to the single phase region 1 and the multiphase region 4 materials. The increased nominal iron content for materials made with a nominal potassium content of less than 0.75 causes the formation of *β*-FeSe. This is the same effect as observed in the comparison of regions 1 and region 2 materials and the iron selenide remains present in the phase assembly up to 750 °C creating a different environment during cooling to that of the $K_xFe_ySe_2$ (x≥0.75) samples (Figure 4.13). Comparing regions 2 to region 5 also involves an increase in nominal iron composition and an increase in the potassium to selenium ratio as well. This relative increase in potassium metal available causes the precipitation of a ternary *I*4/*mmm* phase as well as the *β*-FeSe.

The materials produced in region five (blue markers Figure 4.13) are similar to that of region four in that they contain the phases *I*4/*m*, *I*4/*mmm* and Fe. However, like all materials produced with potassium content of 0.7 and under they also contain *β*-FeSe (Figure 4.40 and Table 4.32). A minor impurity detected in some patterns was also attributed to the *δ*-FeSe phase.

Magnetization measurements in the SQUID showed only traces of superconductivity in five of the blue region materials (Figure 4.41 and Table 4.32). These five materials have nominal potassium compositions of 0.65 up to 0.75 which puts them closest to the border between the blue and red regions. This group complicates the picture by containing *I*4/*mmm* in fractions similar to that shown by the AG308_3, AG311_2 and AG323_2 materials in region four. This means that there is an array of $K_xFe_2Se_2$ (SG = *I*4/*mmm*) in which only a small range of x produces superconducting material.

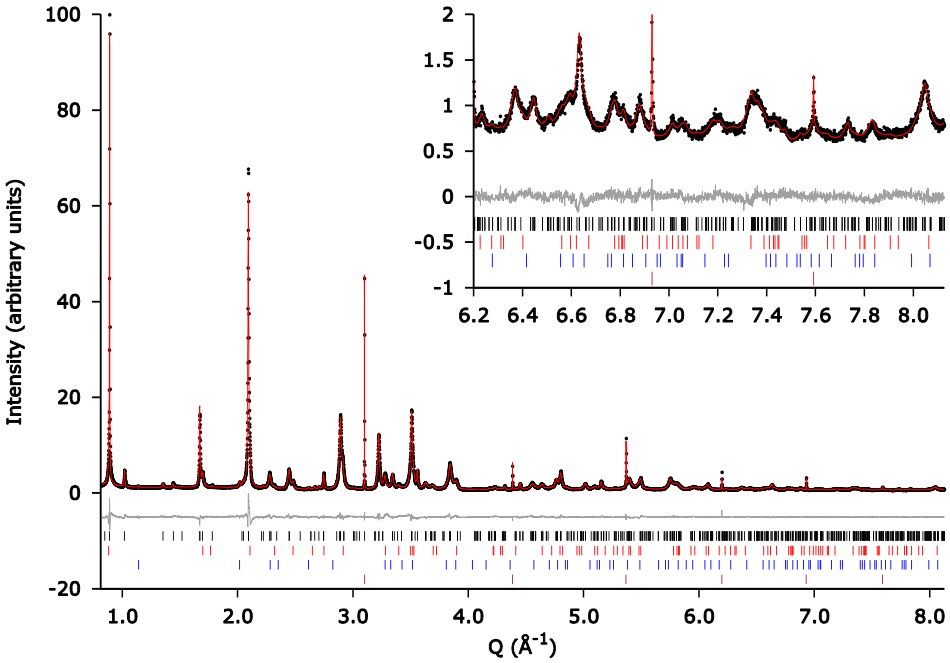

Figure 4.40 Rietveld refinement plot for the material produced with the composition $K_{0.7}Fe_{1.897}Se_2$ (AG321_2). The model was refined against SPXRD data at a wavelength of λ = 0.399892 Å. Observed (black dots), calculated (red line) and difference (grey line) data are shown. The tic marks represent Bragg reflection positions of the *I*4/*m* (black), *I*4/*mmm* (red), *β*-FeSe (blue), Fe (brown) phases. A summary of the refined phase fractions are presented in table 4.32-4.36. R_{wp} = 6.67, R_{exp} = 3.17, number of refined parameters 96.

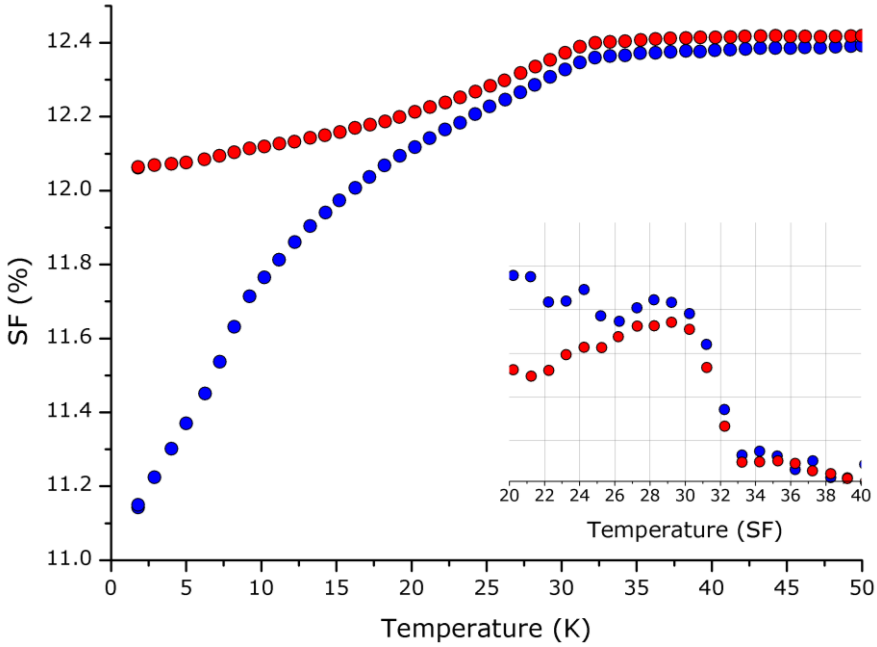

Figure 4.41 The magnetisation as a function of temperature measurements done on AG321_2 ($K_{0.7}Fe_{1.897}Se_2$). Where the red and blue circles correspond to the field cooled and zero field cooled experiments respectively. The inset is *d*M/*d*T and shows the onset of superconduction at a T_c of 33 K which rises to a shielding fraction of 1 % at 10 K. The magnetic measurements were taken in an applied field of 10 Oe with a sample mass of 31.3 mg.

Table 4.32 The phase assembly from the Rietveld analysis of the PXRD data for materials shown by the blue markers in Figure 4.13.

Parameter / Label	SF (%) @ 10 K	*I*4/*mmm* (vol. %)	*I*4/*m* (vol. %)	Fe (vol. %)	*β*-FeSe (vol. %)	*δ*-FeSe (vol. %)
AM72_2($K_{0.55}Fe_{1.925}Se_2$)	0	8.75(23)	74.20(41)	1.86(7)	14.06(36)	1.12(2)
AG353_2($K_{0.6}Fe_{1.808}Se_2$)	0	16.62(32)	78.11(36)	0.74(4)	4.54(20)	0
AG351_2($K_{0.55}Fe_{1.897}Se_2$)	0	15.59(28)	70.09(26)	1.69(2)	11.76(9)	0.87(4)
AM71_2($K_{0.5}Fe_{1.925}Se_2$)	0	8.55(17)	76.32(24)	1.68(3)	12.39(16)	1.06(2)
AG354_2($K_{0.6}Fe_{1.781}Se_2$)	0	21.23(46)	69.26(45)	0.33(6)	9.18(19)	0
AG352_3($K_{0.6}Fe_{1.868}Se_2$)	0	12.25(14)	76.93(14)	1.13(1)	9.51(6)	0.19(1)
AG350_3($K_{0.6}Fe_{1.925}Se_2$)	0	14.37(16)	65.76(15)	1.80(2)	17.60(7)	0.47(1)
AG332_2($K_{0.65}Fe_{1.754}Se_2$)	0.3	21.927(2)	69.327(2)	0.133(1)	8.468(1)	0.145(1)
AG333_2($K_{0.65}Fe_{1.868}Se_2$)	0.3	18.187(170)	74.289(171)	0.94(1)	5.84(7)	0.75(3)
AG334_2($K_{0.65}Fe_{1.925}Se_2$)	0.3	19.956(214)	73.611(207)	1.818(15)	4.576(45)	0.037(1)
AG321_2($K_{0.7}Fe_{1.897}Se_2$)	1.0	17.98(23)	78.99(23)	2.12(3)	0.91(4)	0
AG422_2($K_{0.75}Fe_{2.0}Se_2$)	1.3	13.499(217)	78.885(222)	2.686(34)	4.843(97)	0.088(4)

Table 4.33 The lattice parameters of the *I*4/*m* phase as obtained from the Rietveld analysis of the PXRD data for materials shown by the blue markers in Figure 4.13.

Parameter / Label	SF (%) @ 10 K	$a/\sqrt{5}$ (Å)	c (Å)	V/5 (Å^3)	$\sqrt{5}\,c/a$
AM72_2($K_{0.55}Fe_{1.925}Se_2$)	0	3.8940(2)	14.125(1)	214.17(3)	3.6273(4)
AG353_2($K_{0.6}Fe_{1.808}Se_2$)	0	3.8951(1)	14.1198(6)	214.22(2)	3.6250(2)
AG351_2($K_{0.55}Fe_{1.897}Se_2$)	0	3.89745(4)	14.1201(2)	214.486(6)	3.62291(7)
AM71_2($K_{0.5}Fe_{1.925}Se_2$)	0	3.8980(1)	14.1233(8)	214.60(2)	3.6232(2)
AG354_2($K_{0.6}Fe_{1.781}Se_2$)	0	3.8961(1)	14.1211(8)	214.35(2)	3.6244(2)
AG352_3($K_{0.6}Fe_{1.868}Se_2$)	0	3.89843(2)	14.1201(2)	214.593(3)	3.62199(5)
AG350_3($K_{0.6}Fe_{1.925}Se_2$)	0	3.89628(4)	14.1224(3)	214.392(6)	3.62460(7)
AG332_2($K_{0.65}Fe_{1.754}Se_2$)	0.3	3.89760(4)	14.1221(1)	214.533(4)	3.62328(4)
AG333_2($K_{0.65}Fe_{1.868}Se_2$)	0.3	3.89736(4)	14.1221(2)	214.507(5)	3.62351(6)
AG334_2($K_{0.65}Fe_{1.925}Se_2$)	0.3	3.89746(4)	14.1214(1)	214.507(4)	3.62324(5)
AG321_2($K_{0.7}Fe_{1.897}Se_2$)	1.0	3.89871(5)	14.1222(2)	214.656(6)	3.62227(6)
AG422_2($K_{0.75}Fe_{2.0}Se_2$)	1.3	3.88970(6)	14.0916(3)	213.203(9)	3.6228(1)

Table 4.34 The refined compositions and individual site occupancies of the *I*4/*m* phase obtained from the Rietveld analysis of the PXRD data for materials shown by the blue markers in Figure 4.13.

Parameter / Label	SF (%) @ 10 K	Refined composition	K1 *2b*	K2 *8h*	Fe1 *16i*	Fe2 *4d*
AM72_2($K_{0.55}Fe_{1.925}Se_2$)	0	$K_{0.73(3)}Fe_{1.94(2)}Se_2$	0.78(8)	0.72(3)	0.99(1)	0.87(3)
AG353_2($K_{0.6}Fe_{1.808}Se_2$)	0	$K_{0.73(3)}Fe_{1.77(2)}Se_2$	0.44(9)	0.81(3)	0.89(1)	0.87(3)
AG351_2($K_{0.55}Fe_{1.897}Se_2$)	0	$K_{0.63(1)}Fe_{1.72(1)}Se_2$	0.56(4)	0.65(1)	0.995(6)	0.32(2)
AM71_2($K_{0.5}Fe_{1.925}Se_2$)	0	$K_{0.81(2)}Fe_{1.77(2)}Se_2$	0.88(6)	0.79(2)	0.855(9)	1.00(2)
AG354_2($K_{0.6}Fe_{1.781}Se_2$)	0	$K_{0.77(3)}Fe_{1.54(3)}Se_2$	0.72(9)	0.78(3)	0.72(1)	0.98(5)
AG352_3($K_{0.6}Fe_{1.868}Se_2$)	0	$K_{0.766(9)}Fe_{1.665(7)}Se_2$	0.85(3)	0.744(8)	1.000(4)	0.162(9)
AG350_3($K_{0.6}Fe_{1.925}Se_2$)	0	$K_{0.71(1)}Fe_{1.67(1)}Se_2$	0.58(4)	0.74(1)	0.998(5)	0.19(1)
AG332_2($K_{0.65}Fe_{1.754}Se_2$)	0.3	$K_{0.822(8)}Fe_{1.544(5)}Se_2$	0.95(2)	0.791(8)	0.930(3)	0.143(7)
AG333_2($K_{0.65}Fe_{1.868}Se_2$)	0.3	$K_{0.800(8)}Fe_{1.488(7)}Se_2$	0.98(3)	0.755(9)	0.909(4)	0.084(9)
AG334_2($K_{0.65}Fe_{1.925}Se_2$)	0.3	$K_{0.848(9)}Fe_{1.455(7)}Se_2$	0.98(2)	0.814(9)	0.910(4)	0
AG321_2($K_{0.7}Fe_{1.897}Se_2$)	1.0	$K_{0.802(8)}Fe_{1.522(8)}Se_2$	0.88(2)	0.786(8)	0.916(4)	0.14(1)
AG422_2($K_{0.75}Fe_{2.0}Se_2$)	1.3	$K_{0.74(1)}Fe_{1.556(9)}Se_2$	1.00(4)	0.678(9)	0.944(5)	0.114(9)

Table 4.35 The lattice parameters of the *I*4/*mmm* phase as obtained from the Rietveld analysis of the PXRD data for materials shown by the blue markers in Figure 4.13

Parameter / Label	SF (%) @ 10 K	*I*4/*mmm* *a* Å	*I*4/*mmm* *c* Å	*I*4/*mmm* V Å^3	*I*4/*mmm* *c*/*a*
AM72_2($K_{0.55}Fe_{1.925}Se_2$)	0	3.8393(4)	14.213(3)	209.50(6)	3.7019(8)
AG353_2($K_{0.6}Fe_{1.808}Se_2$)	0	3.8372(4)	14.224(2)	209.44(5)	3.7069(6)
AG351_2($K_{0.55}Fe_{1.897}Se_2$)	0	3.8376(2)	14.218(1)	209.39(3)	3.7049(3)
AM71_2($K_{0.5}Fe_{1.925}Se_2$)	0	3.8344(3)	14.2478(2)	209.48(5)	3.7158(6)
AG354_2($K_{0.6}Fe_{1.781}Se_2$)	0	3.8352(3)	14.243(3)	209.50(5)	3.7139(8)
AG352_3($K_{0.6}Fe_{1.868}Se_2$)	0	3.8340(1)	14.2394(4)	209.31(1)	3.7140(1)
AG350_3($K_{0.6}Fe_{1.925}Se_2$)	0	3.8382(1)	14.2219(8)	209.52(2)	3.7053(2)
AG332_2($K_{0.65}Fe_{1.754}Se_2$)	0.3	3.8365(1)	14.2341(6)	209.51(1)	3.7102(2)
AG333_2($K_{0.65}Fe_{1.868}Se_2$)	0.3	3.8322(1)	14.2433(7)	209.17(2)	3.7168(2)
AG334_2($K_{0.65}Fe_{1.925}Se_2$)	0.3	3.83621(8)	14.2382(7)	209.54(1)	3.7115(2)
AG321_2($K_{0.7}Fe_{1.897}Se_2$)	1.0	3.8305(2)	14.246(1)	209.03(3)	3.7192(4)
AG422_2($K_{0.75}Fe_{2.0}Se_2$)	1.3	3.8249(2)	14.219(1)	208.02(2)	3.7174(3)

Table 4.36 The bond angles and refined compositions as obtained from the Rietveld refinement of *I*4/*mmm* phases in the materials shown by the blue markers in Figure 4.13. AM72_2 and AM71_2 have less than 9 vol.% of the *I*4/*mmm* phase present this low fraction combined with the heavy overlap of the *I*4/*mmm* peaks with the *I*4/*m* phase the compositions of the *I*4/*mmm* phases were fixed at $K_{0.5}Fe_2Se_2$.

Parameter / Label	SF (%)	*I*4/*mmm* bond angle Se-Fe-Se		Refined composition	Se layer height Å
		2 fold axis	4 fold axis		
AM72_2($K_{0.55}Fe_{1.925}Se_2$)	0	105.3(6)	111.6(3)	$K_{0.5}Fe_2Se_2$	1.466(8)
AG353_2($K_{0.6}Fe_{1.808}Se_2$)	0	108.3(4)	110.1(1)	$K_{0.12(4)}Fe_{2.00(5)}Se_2$	1.387(5)
AG351_2($K_{0.55}Fe_{1.897}Se_2$)	0	105.2(2)	111.6(1)	$K_{0.41(2)}Fe_{1.98(4)}Se_2$	1.466(3)
AM71_2($K_{0.5}Fe_{1.925}Se_2$)	0	104.0(5)	112.27(3)	$K_{0.5}Fe_2Se_2$	1.498(7)
AG354_2($K_{0.6}Fe_{1.781}Se_2$)	0	103.3(4)	112.6(2)	$K_{0.40(3)}Fe_{1.97(5)}Se_2$	1.562(6)
AG352_3($K_{0.6}Fe_{1.868}Se_2$)	0	103.1(1)	112.76(7)	$K_{0.48(1)}Fe_{2.00(2)}Se_2$	1.523(2)
AG350_3($K_{0.6}Fe_{1.925}Se_2$)	0	101.5(1)	113.58(7)	$K_{0.48(1)}Fe_{2.00(3)}Se_2$	1.567(2)
AG332_2($K_{0.65}Fe_{1.754}Se_2$)	0.3	102.7(1)	112.94(6)	$K_{0.50(1)}Fe_{2.00(1)}Se_2$	1.533(2)
AG333_2($K_{0.65}Fe_{1.868}Se_2$)	0.3	101.9(1)	113.36(6)	$K_{0.53(2)}Fe_{1.95(2)}Se_2$	1.553(2)
AG334_2($K_{0.65}Fe_{1.925}Se_2$)	0.3	101.7(1)	113.52(4)	$K_{0.58(2)}Fe_{1.94(2)}Se_2$	1.563(2)
AG321_2($K_{0.7}Fe_{1.897}Se_2$)	1.0	101.7(1)	113.50(8)	$K_{0.52(2)}Fe_{2.00(3)}Se_2$	1.560(2)
AG422_2($K_{0.75}Fe_{2.0}Se_2$)	1.3	103.5(2)	112.5(1)	$K_{0.40(3)}Fe_{2.00(3)}Se_2$	1.506(3)

The two potassium intercalated phases produced by materials contained within the blue region show no obvious trends in their lattice parameters as a function of nominal potassium composition (Figure 4.42 and 4.43). For the *I*4/*m* phase this is expected by taking into account regions 1, 2, 3 and 4 where the largest changes in lattice parameters are only encountered in samples after a nominal potassium composition of 0.75. It would appear that in addition to this the *I*4/*mmm* phases also share a similar trend to that of the *I*4/*m* phase. The lattice parameters of the *I*4/*mmm* phases, when region 5 samples are looked at alongside the *I*4/*mmm* phases from all other materials, are stable and show very little change up to the nominal potassium composition of 0.75 (Figure 4.42). At nominal potassium compositions of 0.85 and higher the *a* axis increases and the *c* axis drops which corresponds to the formation of the *I*4/*mmm* phase which is based upon an iron vacancy disordered structure which is heavily iron deficient.

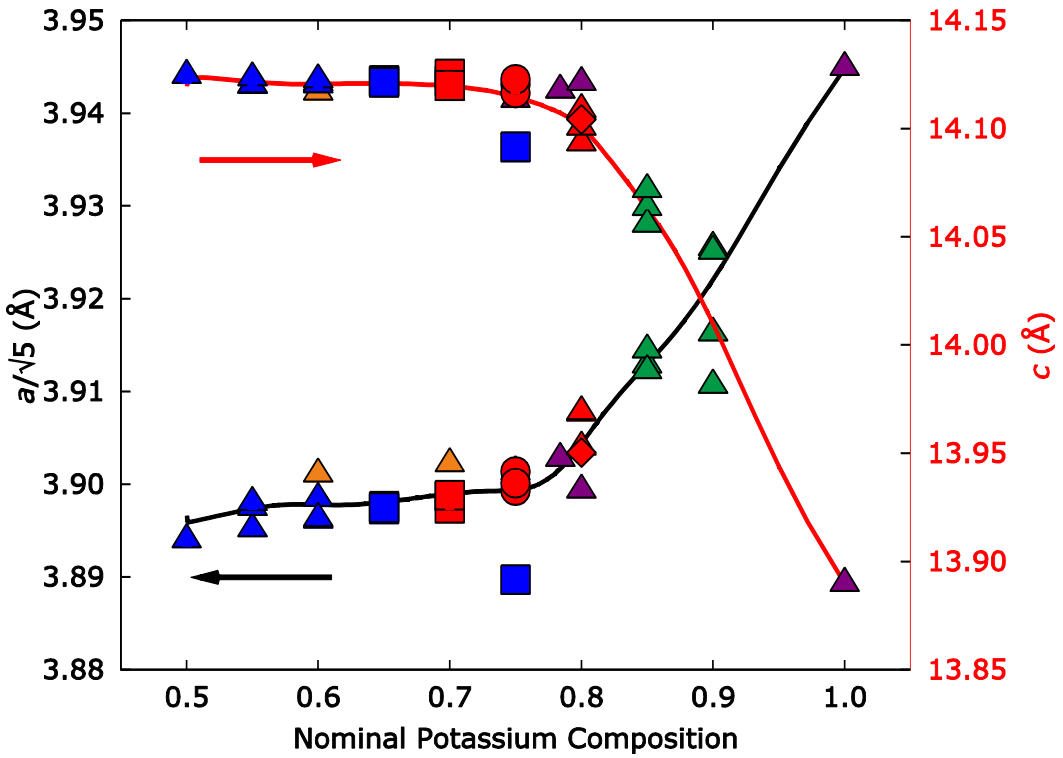

Figure 4.42 The lattice parameters *of* the *I*4/*m* phase as a function of nominal potassium composition. Superconductivity from SQUID measurements: triangles - 0 %; squares - 1-3 %; diamonds - 6 %; circles – 19 %. The colour of the markers corresponds to the region of the phase diagram were the data was obtained; (1) dark purple; (2) orange; (3) green; (4) red; (5) blue and (6) brown. The error bars are displayed at 3σ.

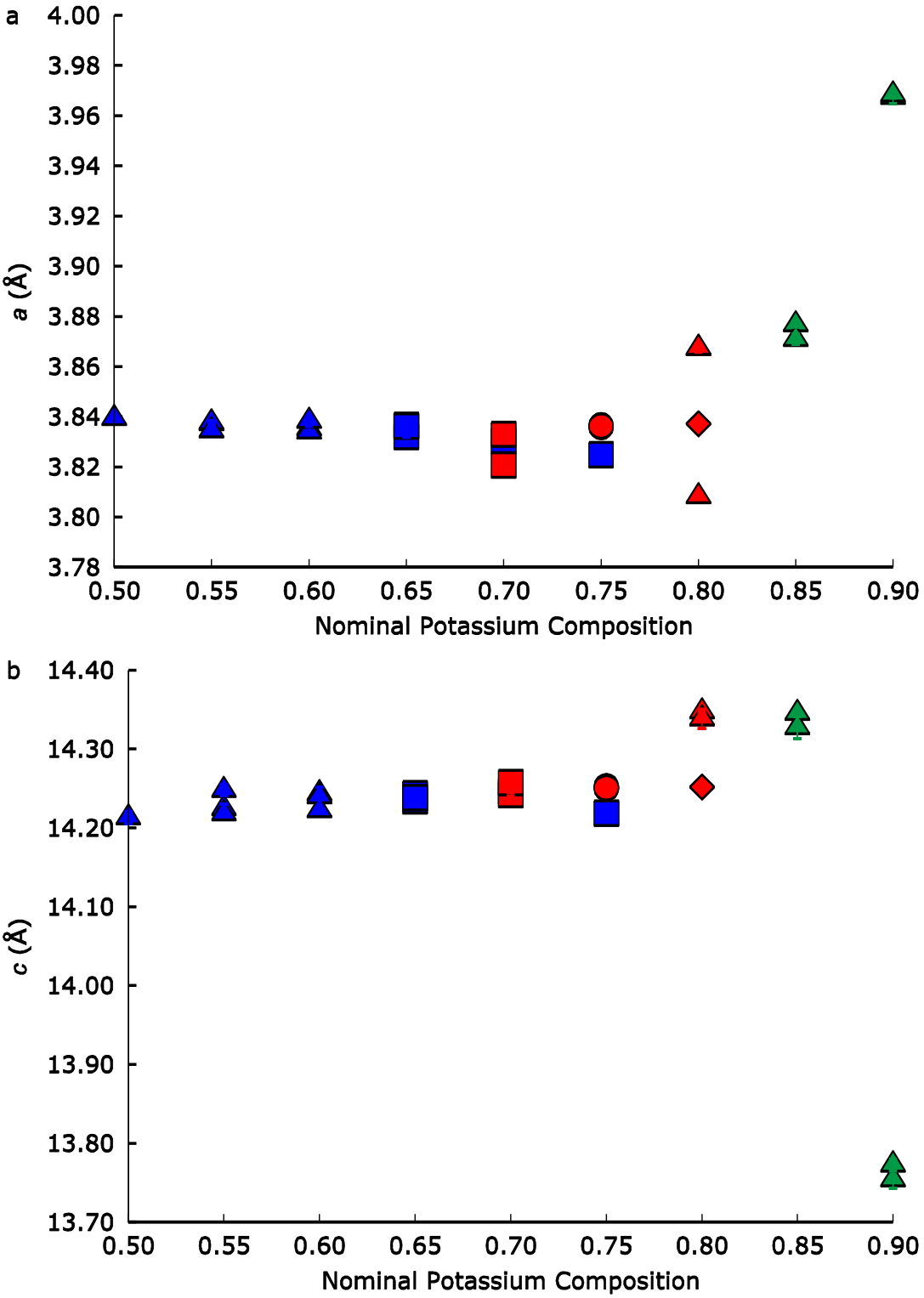

Figure 4.43 The lattice parameters of the *I*4/*mmm* phase as a function of nominal potassium composition. Superconductivity from SQUID measurements: triangles - 0 %; squares - 1-3 %; diamonds - 6 %; circles – 19 %. The colour of the markers corresponds to the region of the phase diagram were the data was obtained; (3) green; (4) red and (5) blue. The error bars are displayed at 3σ.

4.4.8. Region 6 (brown markers): $K_xFe_ySe_2$ (x=0.5; y=1.83 and 2.0) *I*4/*m*, FeSe and bulk Fe metal

The samples produced in region 6 have less nominal potassium and more iron present when compared to the majority of the neighbouring region 5 samples. The decrease in nominal potassium content between region 5 and region 6 means that all of the potassium is taken up by the *I*4/*m* phase to maintain the stable Fe^{+2} oxidation state within this phase. This means that there is insufficient potassium in the materials to form an observable *I*4/*mmm* phase and the extra iron is accommodated by the *β*-FeSe phase solely.

The material produced in region six (brown markers Figure 4.13) contain the phases *I*4/*m,* Fe and FeSe (Figure 4.44 and Tables 4.37-4.39). This region contains the important material with the "nominal" composition $K_{0.5}Fe_{2.0}Se_2$. The importance of this material is that it forms the lower potassium limit of the refined composition of the *I*4/*mmm* phases responsible for superconductivity in these materials.

This particular nominal composition exemplifies the problems in synthesising the *I*4/*mmm* phase at this composition. The material with the nominal composition of $K_{0.5}Fe_2Se_2$ shows no sign of the critical *I*4/*mmm* phase in its powder pattern. The problem with these systems is that an impure sample containing the *I*4/*m* phase with a high refined potassium content is more stable than a pure sample of *I*4/*mmm* $K_{0.5}Fe_2Se_2$. At K = 0.5 levels all of the potassium in the system can be easily accommodated by the *I*4/*m* phase by the production of FeSe phases to allow the *I*4/*m* phase to have a refined potassium composition greater than 0.73. This means that any technique that favours the thermodynamic product will not produce phase pure superconducting material.

This idea is highlighted by the first annealing step in this synthesis where potassium and the iron selenide precursor are heated to 750 °C and then cooled at 2 °C min^{-1} to room temperature. The first annealing step, even for the K = 0.75 materials does not produce superconducting material. It is only when these materials are quenched from 750 °C to room temperature in air that the superconducting products are isolated. This particular nuance is indicative of a kinetically stable material being responsible for superconductivity. For region six SQUID magnetometry revealed only one sample with trace superconductivity with a T_c of 33 K and an SF of 1 % (Figure 4.45).

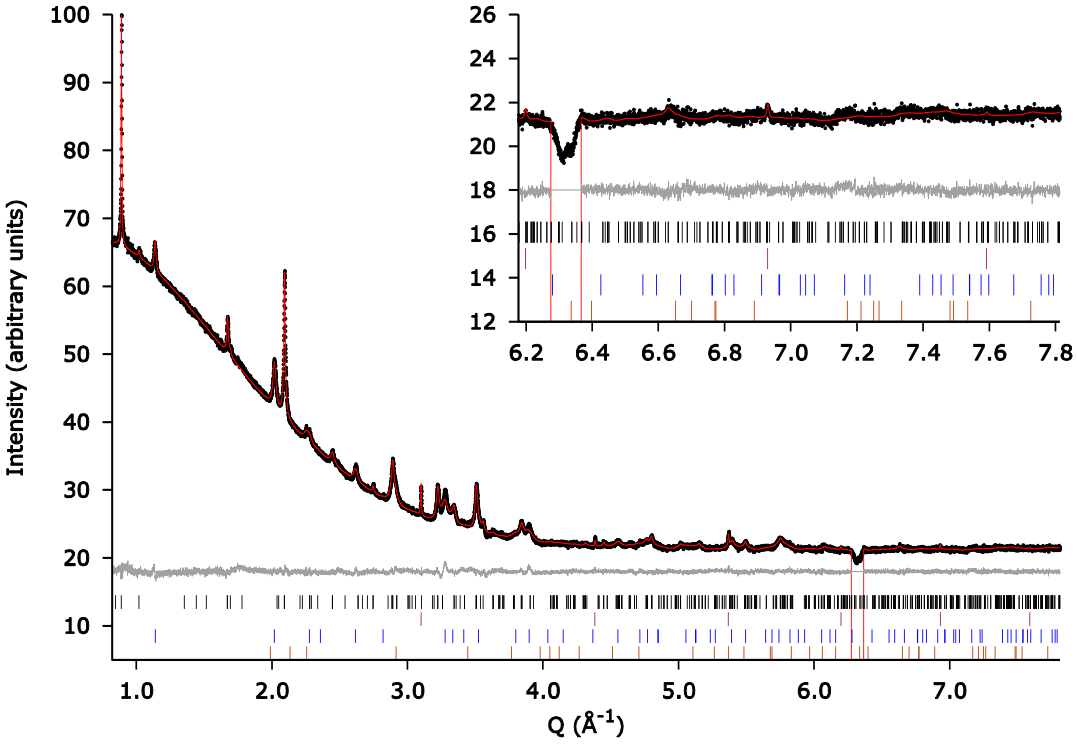

Figure 4.44 Rietveld refinement plot for the material produced with the composition $K_{0.5}Fe_{2.0}Se_2$ (AG337_3). The model was refined against SPXRD data at a wavelength of λ = 0.827153 Å. Observed (black dots), calculated (red line) and difference (grey line) data are shown. The tic marks represent Bragg reflection positions of the *I*4/*m* (black), Fe (brown), *β*-FeSe (blue) and *δ*-FeSe phases (dark-orange). A summary of the refined phase fractions are presented in table 4.37, 4.38 and 4.39. The red columns are the positions in the pattern where the anomalous peaks occur due to the PSD detector at Diamond I-11 beam line described in the experimental section. R_{wp} = 0.72, R_{exp} = 0.57, number of refined parameters 71.

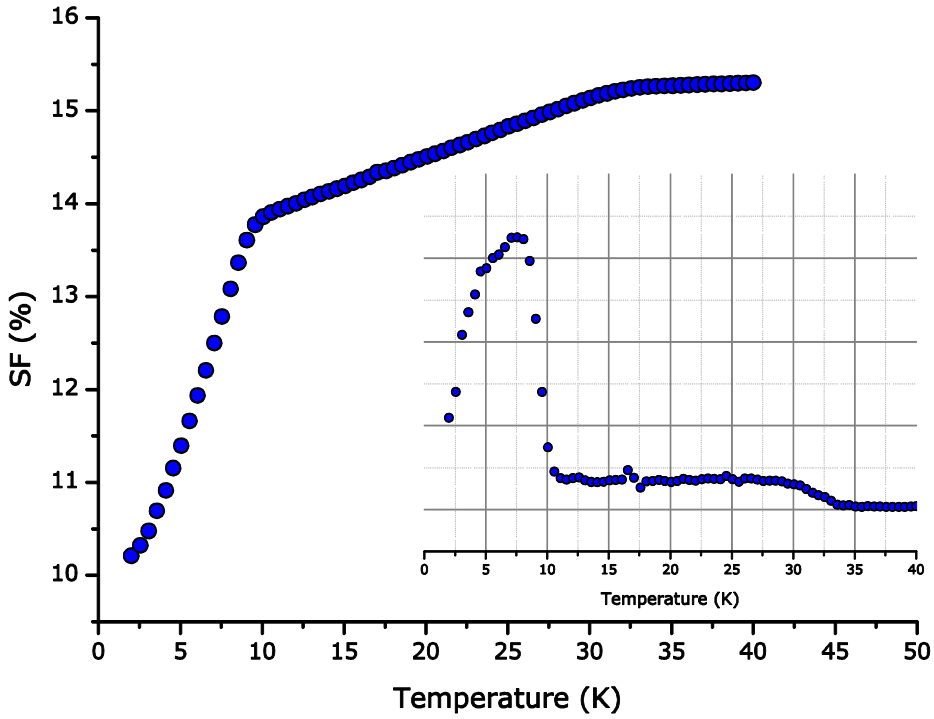

Figure 4.45 The magnetisation as a function of temperature measurements (zero field cooled) done on AG337_3 ($K_{0.5}Fe_{2.0}Se_2$). The inset is dM/dT and shows the onset of superconduction at a Tc of 33 K which rises to a shielding fraction of 1 % at 10 K. The magnetic measurements were taken in an applied field of 10 Oe with a sample mass of 31.3 mg.

Table 4.37 The phase assembly from the Rietveld analysis of the PXRD data for materials shown by the brown markers in Figure 4.13.

Parameter / Label	SF (%) @ 10 K	*I*4/*m* (vol. %)	*β*-FeSe (vol. %)	*δ*-FeSe (vol. %)	Fe (vol. %)
AM70_2($K_{0.5}Fe_{1.836}Se_2$)	0	76.62(30)	0.71(5)	22.02(23)	0.65(4)
AG337_3($K_{0.5}Fe_{2.0}Se_2$)	1	73.22(19)	1.68(6)	24.39(18)	0.70(2)

Table 4.38 The lattice parameters of the *I*4/*m* phase as obtained from the Rietveld analysis of the PXRD data for materials shown by the brown markers in Figure 4.13.

Parameter / Label	SF (%) @ 10 K	*a*/√5 (Å)	*c* (Å)	V/5 (Å^3)	√5 *c*/*a*
AM70_2($K_{0.5}Fe_{1.836}Se_2$)	0	3.8966(2)	14.120(1)	214.39(3)	3.6236(3)
AG337_3($K_{0.5}Fe_{2.0}Se_2$)	1	3.8988(1)	14.1286(7)	214.77(2)	3.6238(2)

Table 4.39 The refined compositions and individual site occupancies of the *I*4/*m* phase obtained from the Rietveld analysis of the PXRD data for materials shown by the brown markers in Figure 4.13.

Parameter / Label	SF (%) @ 10 K	Refined Composition	K1 *2b*	K2 *8h*	Fe1 *16i*	Fe2 *4d*
AM70_2($K_{0.5}Fe_{1.836}Se_2$)	0	$K_{0.75(4)}Fe_{1.65(3)}Se_2$	0.7(1)	0.77(4)	0.79(2)	0.99(6)
AG337_3($K_{0.5}Fe_{2.0}Se_2$)	1	$K_{0.76(2)}Fe_{1.71(2)}Se_2$	1.00(6)	0.70(2)	0.973(8)	0.39(2)

4.5. Conclusions

The aim of assembling this phase diagram was to obtain bulk superconducting powders, ascertain the phase responsible and obtain the parameters which are important for superconductivity. The choice of a subsolidus method of synthesis was an important one allowing the assessment of the average structure and properties of the entire system. Due to the highly sensitive nature of these materials techniques like energy dispersive X-ray (EDX) or electron microscopy are not ideal due to the requirement of exposing the samples to air during sample preparation. This means that obtaining the composition of each phase, to support the Rietveld refinement, is impossible.

This means that every effort to maintain the nominal composition is critical to these experiments. Part of these efforts is the subsolidus method which allows the synthesis of these materials without risk of the material reacting with the reaction vessel. In addition to this, because the materials prepared in this work have not been subject to melting (melting point >800 °C depending on composition) during the reaction no material is lost to the porous alumina crucible. This then allows superior control over the composition of the product where the products total composition to be determined by bulk techniques like ICP and powder diffraction.

The first objective of obtaining bulk superconducting material was achieved immediately with the completion of the phase diagram. SQUID magnetometry confirmed the presence of three superconducting materials with a T_c of 33 K and an SF of 19 %. The three materials had the nominal compositions of $K_{0.75}Fe_{1.868}Se_2$, $K_{0.75}Fe_{1.781}Se_2$ and $K_{0.75}Fe_{1.702}Se_2$ which quickly established the K = 0.75 line as a critical region of the phase diagram. The fact that these materials displayed identical superconducting properties indicated that these materials must have a special aspect that none of the other materials possess. The material with the nominal composition $K_{0.8}Fe_{1.753}Se_2$ gave a T_c of 33 K with an SF of 6.3 % meaning that it may be possible to extract the identity of the superconducting phase in addition to that of the AG308_3, AG311_2 and AG323_2 materials. Trace superconductivity (0-3 % SF) was also detected in some samples in the blue and red regions of the phase diagram. These materials gave T_cs between 30 and 32 K but due to the very low SFs it is unlikely that the origin of superconductivity can be determined for these samples. Therefore, the focus will lie on the samples showing bulk superconductivity and the comparison of these materials to each other and all other materials within the phase diagram.

Within the phase diagram there are five different crystallographic phases which vary depending upon the targeted nominal composition. These phases include the intercalated phase $K_xFe_ySe_2$ (SG = *I*4/*m*) which has a √5x√5 cell expansion of the $ThCr_2Si_2$ crystal structure due to iron vacancy ordering; the second intercalated phase $K_xFe_2Se_2$ (SG = *I*4/*mmm*); an a vacancy disordered variant of the first phase $K_xFe_ySe_2$ (SG = I4/mmm); elemental Fe; tetragonal *β*-FeSe and lastly the *δ*-FeSe hexagonal variant.

The second objective was the identity of the superconducting phase which became clear on the Rietveld analysis of the powder X-ray diffraction patterns of the three AG308_3, AG311_2 and AG323_2 materials. Within these three samples are the phases, *I*4/*m*, $K_xFe_2Se_2$ *I*4/*mmm* and Fe. Considering that the *I*4/*m* and *I*4/*mmm* phases in the three bulk superconducting samples are present at ~80 vol.% and ~16 vol.% fractions it is logical to assume that the *I*4/*mmm* phase is therefore responsible for the superconductivity. However, the *I*4/*mmm* phases in these samples are present in lower amounts than those suggested by the SQUID data (19 % SF). One possible explanation for this anomaly is that if the *I*4/*mmm* phase forms around the surface of an *I*4/*m* crystallite then that entire volume will be seen as superconducting. This is due to the exclusion of a magnetic field within a superconductor beyond the London penetration depth. Although this behaviour can be explained a more concrete correlation is critical to the identification of the correct phase.

The analysis of the Rietveld refinement of the structural models against the powder diffraction data reveals that the *I*4/*m* phase is not responsible for superconduction. The only correlation found within the *I*4/*m* phases of the three AG308_3, AG311_2 and AG323_2 samples displaying an SF of 19 % was their refined iron compositions which are identical. Although the refined iron compositions of the *I*4/*m* phases for the AG308_3, AG311_2 and AG323_2 are identical they are not unique. For example the *I*4/*m* phase produced by the nominal composition $K_{0.7}Fe_{1.897}Se_2$ also has an identical refined iron composition but has a T_c of 32 K and a SF of 1 %. The *I*4/*m* materials were also found to be significantly different in lattice parameters, cell volumes, tetragonality (*c*/*a*) and refined potassium composition. The lack of unique agreements between any of the *I*4/*m* phase parameters is conclusive evidence to show that this phase is not responsible for the observed superconductivity in the $K_xFe_ySe_2$ system.

Even though the *I*4/*m* phase was ruled out as the phase responsible for the presence of superconductivity some interesting trends were observed in this phase. The results of the Rietveld analysis reveal that the *I*4/*m* phase has an obvious region where it remains almost constant with respect to changing

nominal potassium and iron compositions. This region is between K = 0.5 and 0.75 and here the *I*4/*m* phase is most stable. This is because phases like $K_xFe_2Se_2$, FeSe and Fe can precipitate out of the material as it cools after reaction. This means that the *I*4/*m* phase can adopt its most stable compositions as the excess elements are taken up by the impurity phases. After the nominal potassium composition level of 0.75 is exceeded the lower nominal iron content coupled with higher levels of potassium prevents the formation of the *β*-FeSe impurity resulting in the *I*4/*m* phase changing. This change manifests itself as a dramatic increase in the *a* axis by 1.1 % coupled with a decrease in the *c* parameter of 1.6 % (Figure 4.46).

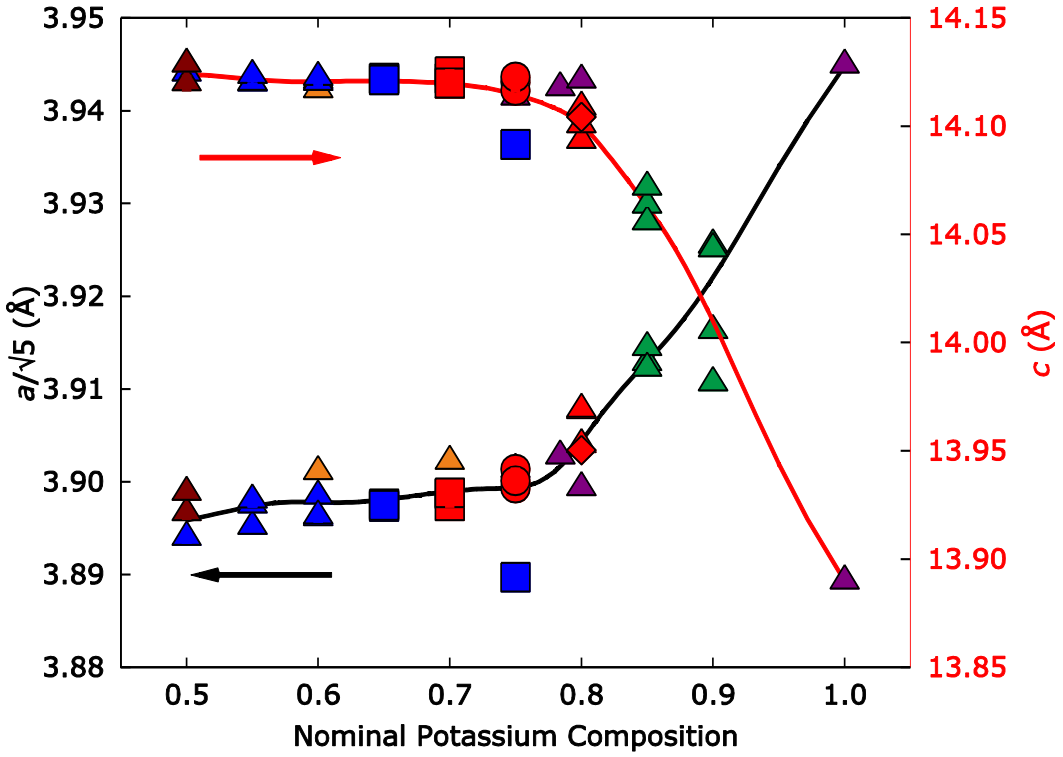

Figure 4.46 The *I*4/*m* lattice parameters as a function of potassium content. Superconductivity from SQUID measurements: triangles - 0 %; squares - 1-3 %; diamonds - 6 %; circles – 19 %. The colour of the markers corresponds to the region of the phase diagram were the data was obtained; (1) dark purple; (2) orange; (3) green; (4) red; (5) blue and (6) brown. The error bars are displayed at 3σ.

The *I*4/*m* phase is an interesting material due to its structural complexity. It contains elements of local effects like stacking faults and may become incommensurate when the iron composition is varied. The development of an incommensurate structural model based upon a 5-dimensional system would allow the complete characterisation of this phase by Rietveld refinement. This in turn would yield more accurate information about where this phase is at its most

stable and how the conditions under which this phase precipitates affects its bond angles. This information could then be used to target compositions in between those of the AG308_3, AG311_2 and AG323_2 materials producing higher quantities of the *I*4/*mmm* phase.

The results of the Rietveld refinements confirm that the $K_xFe_2Se_2$ *I*4/*mmm* phase is responsible for the superconductivity in these systems. There are two *I*4/*mmm* phases present in the system; one that is iron rich and based upon the $ThCr_2Si_2$ structure and the second which is iron deficient is based on an iron vacancy disordered *I*4/*m* structure. The iron deficient *I*4/*mmm* phase is only present at nominal potassium doping levels of K = 0.85 and above. The samples prepared at nominal potassium levels of above 0.85 are completely non-superconducting which excludes the iron deficient *I*4/*mmm* phase as the one responsible for the superconductivity. This then leaves the iron rich $K_xFe_2Se_2$ phase as the superconducting material.

The dependency of the *I*4/*mmm* lattice parameters as a function of potassium composition shows the progression of the *I*4/*mmm* iron rich phase into the deficient variant at nominal potassium doping levels of above K = 0.8 (Figure 4.47). The broad distribution of lattice parameters along the K = 0.8 line is likely to be a result of the iron rich phase becoming close to its limit before losing iron. Critically, the iron rich *I*4/*mmm* phase with SF 6 % has very similar lattice parameters. This gives us the first starting point with which to construct a picture of what characteristics are important for this iron rich *I*4/*mmm* phase to have in order for it to express superconductivity.

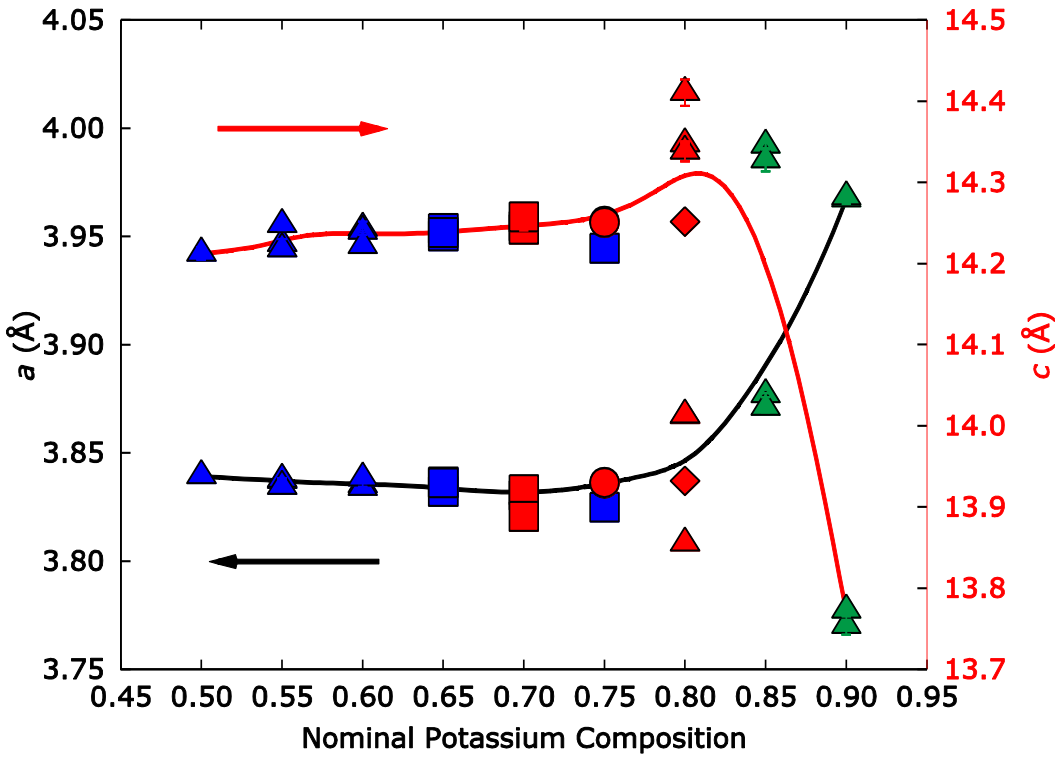

Figure 4.47 The lattice parameters of the I4/mmm phase as a function of nominal potassium composition. Superconductivity from SQUID measurements: triangles - 0 %; squares - 1-3 %; diamonds - 6 %; circles – 19 %. The colour of the markers corresponds to the region of the phase diagram were the data was obtained; (3) green; (4) red and (5) blue. The error bars are displayed at 3σ.

The third objective is met by the detailed analysis of the refinement parameters for the *I*4/*mmm* phases. By eliminating parameters of high importance, with respect to superconductivity, which have no correlations the critical characteristics can then be extracted. The critical parameters considered were the bond angles, selenium height above the iron layer, *c*/*a* ratio, cell volume and composition. No unique, with respect to all *I*4/*mmm* phases, correlation between the AG308_3, AG311_2 and AG323_2 *I*4/*mmm* phases were found for the selenium height, *c*/*a* ratio and composition within an error of 3 standard deviations.

However, strong correlations were found for the cell volumes of the *I*4/*mmm* phase in the AG308_3, AG311_2 and AG323_2 materials were the values are identical to each other (209.73 $Å^3$) but unique with respect to all other *I*4/*mmm* phases. This specific cell volume (209.73 $Å^3$) is likely to be due to the *I*4/*mmm* phases of the AG308_3, AG311_2 and AG323_2 having a very specific composition. Unfortunately, due to the heavy overlap between the *I*4/*m* and *I*4/*mmm* peaks in the X-ray diffraction patterns, the uncertainty in the

refined compositions is too large to define this specific composition as different from the composition of all other non-superconducting *I*4/*mmm* phases.

The Se-Fe-Se bond angles are expected to be definitive due to observations in systems like $Ba_{1-x}K_xFe_2As_2$ where the T_c is optimised when the average angle tends to the ideal tetrahedral angle (109.47 °). The AG308_3, AG311_2 and AG323_2 materials all share the same, with in 3 σ errors, bond angles but are significantly different from the ideal angle. In addition to this is that the bond angles for the *I*4/*mmm* phases of the AG308_3, AG311_2 and AG323_2 19 % SF materials are contained within the spread of data produced by the non-superconducting materials. This means that the cell volume of the *I*4/*mmm* phase is the overriding factor in determining if a sample superconducts or not.

4.6. References

1. R. Guo, Y. Song, G. L. Wang and R. W. Murray, *Journal of the American Chemical Society*, 2005, **127**, 2752-2757.
2. D. P. Shoemaker, D. Y. Chung, H. Claus, M. C. Francisco, S. Avci, A. Llobet and M. G. Kanatzidis, *Physical Review B*, 2012, **86**.
3. J. Guo, S. Jin, G. Wang, S. Wang, K. Zhu, T. Zhou, M. He and X. Chen, *Physical Review B*, 2010, **82**, 180520.
4. T. M. McQueen, Q. Huang, V. Ksenofontov, C. Felser, Q. Xu, H. Zandbergen, Y. S. Hor, J. Allred, A. J. Williams, D. Qu, J. Checkelsky, N. P. Ong and R. J. Cava, *Physical Review B*, 2009, **79**.
5. Z. Wang, Y. J. Song, H. L. Shi, Z. W. Wang, Z. Chen, H. F. Tian, G. F. Chen, J. G. Guo, H. X. Yang and J. Q. Li, *Physical Review B*, 2011, **83**.
6. Z.-W. Wang, Z. Wang, Y.-J. Song, C. Ma, Y. Cai, Z. Chen, H.-F. Tian, H.-X. Yang, G.-F. Chen and J.-Q. Li, *The Journal of Physical Chemistry C*, 2012, **116**, 17847-17852.
7. J. Bacsa, A. Y. Ganin, Y. Takabayashi, K. E. Christensen, K. Prassides, M. J. Rosseinsky and J. B. Claridge, *Chemical Science*, 2011, **2**, 1054-1058.
8. D. M. Wang, J. B. He, T. L. Xia and G. F. Chen, *Physical Review B*, 2011, **83**.
9. X. W. Yan, M. Gao, Z. Y. Lu and T. Xiang, *Physical Review B*, 2011, **83**, 4.
10. G. Huan, M. Greenblatt and M. Croft, *European Journal of Solid State and Inorganic Chemistry*, 1989, **26**, 193-220.
11. C. T. Chantler, *Journal of Physical and Chemical Reference Data*, 1995, **24**, 71-591.
12. C. T. Chantler, *Journal of Physical and Chemical Reference Data*, 2000, **29**, 597-1048.
13. W. Bao, Q.-Z. Huang, G.-F. Chen, M. A. Green, D.-M. Wang, J.-B. He and Y.-M. Qiu, *Chinese Physics Letters*, 2011, **28**, 086104.
14. P. W. Stephens, *Journal of Applied Crystallography*, 1999, **32**, 281-289.
15. T. Ungar and J. Gubicza, *Zeitschrift Fur Kristallographie*, 2007, **222**, 114-128.
16. D. C. Johnston, *Advances in Physics*, 2010, **59**, 803-1061.
17. J. T. Park, D. S. Inosov, C. Niedermayer, G. L. Sun, D. Haug, N. B. Christensen, R. Dinnebier, A. V. Boris, A. J. Drew, L. Schulz, T. Shapoval,

U. Wolff, V. Neu, X. P. Yang, C. T. Lin, B. Keimer and V. Hinkov, *Physical Review Letters*, 2009, **102**.
18. Y. Mizuguchi, Y. Hara, K. Deguchi, S. Tsuda, T. Yamaguchi, K. Takeda, H. Kotegawa, H. Tou and Y. Takano, *Superconductor Science & Technology*, 2010, **23**.
19. K. Kuroki, H. Usui, S. Onari, R. Arita and H. Aoki, *Physical Review B*, 2009, **79**.
20. S. Jiang, H. Xing, G. F. Xuan, C. Wang, Z. Ren, C. M. Feng, J. H. Dai, Z. A. Xu and G. H. Cao, *Journal of Physics-Condensed Matter*, 2009, **21**.
21. Z. W. Wang, H. X. Yang, C. Ma, H. F. Tian, H. L. Shi, J. B. Lu, L. J. Zeng and J. Q. Li, *Journal of Physics-Condensed Matter*, 2009, **21**.
22. S. A. J. Kimber, A. Kreyssig, Y. Z. Zhang, H. O. Jeschke, R. Valenti, F. Yokaichiya, E. Colombier, J. Yan, T. C. Hansen, T. Chatterji, R. J. McQueeney, P. C. Canfield, A. I. Goldman and D. N. Argyriou, *Nature Materials*, 2009, **8**, 471-475.

5. Synthesis of $K_{0.5}Fe_2Se_2$ using room temperature "wet" methods.

5.1. Introduction

The identification of the superconducting phase responsible for superconductivity in $K_xFe_ySe_2$ systems as the $K_{0.55}Fe_2Se_2$ (SG = *I*4/*mmm*, 209.73(1) Å^3, Figure 5.1) phase allows the targeting of this material (Chapter 4).[1] Since materials of this composition when made by subsolidus reactions quenched from 750 °C do not produce superconductivity or significant amounts of *I*4/*mmm* material we must turn to milder methods to produce this metastable phase (Chapter 4). One applicable set of techniques involves the intercalation of alkali metals at room or low temperature into layered materials and these methods could yield a synthetic protocol capable of obtaining pure *I*4/*mmm* material.

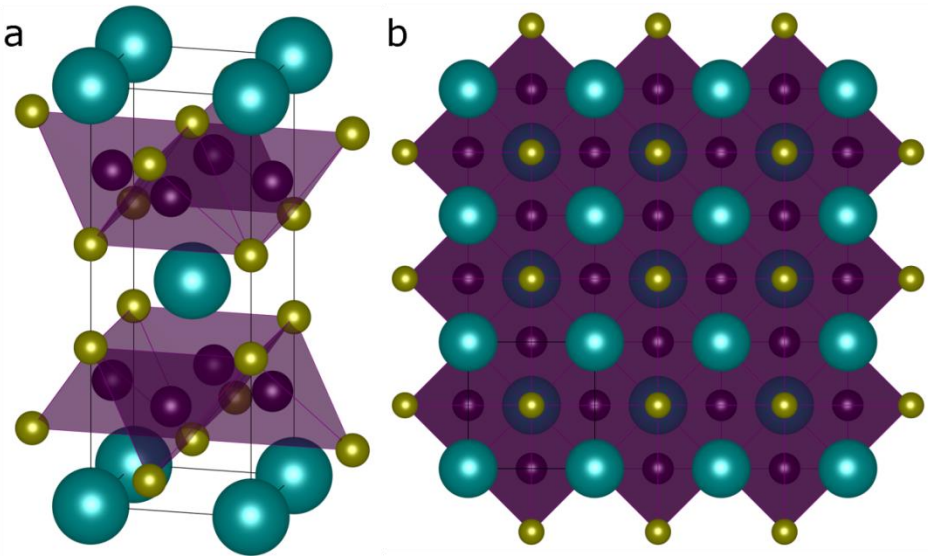

Figure 5.1 Structure of $A_xFe_2Se_2$ (tetragonal, SG = *I*4/*mmm*) where the selenium anions are yellow, the iron cations are purple, the A cation is in turquoise and the unit cell is outlined in black. The two diagrams are (a) viewed along the *ab* plane and (b) the view along the *c*-axis.

5.1.1. Solution approach to $A_xFe_2Se_2$ intercalation

The intercalation of cation species into host layered materials is a vast and diverse subject. The methods used range from standard solid state chemical

techniques, Schlenk procedures, and electrochemical intercalation to exotic methods utilising microwaves and liquid ammonia in autoclaves.[2-9] Low or ambient temperature methods are often used to isolate unstable phases or compositions of transition metal dichalcogenides (TMDC) that are prone to liberating the transitions metal (TM) on reduction.[2] These methods use an array of reaction media including liquid ammonia (LA), hexamethyl phosphotriamide (HMPT), acetonitrile, pyridine, hexane, tetrahydrofuran (THF), glyme and mercury amalgams.[2, 6, 8, 10-19] The wide range of reaction methods and media available to form alkali metal TMDCs gives a huge scope for finding a method sufficient to isolate high purity $K_xFe_2Se_2$ (SG = *I*4/*mmm*) materials capable of superconduction.

The history of combining alkali metals and liquid ammonia for synthesising intercalation compounds started 54 years ago with the intercalation of alkali metals into MoS_2 and WS_2.[20] The reason for this combination is due to the compatibility between LA and alkali metals[21] and this has led to the publication of some fascinating and relevant methods.[6, 7, 22] An important issue to consider with the use of ammonia is the potential to intercalate the solvent along with the cation. An example of the effect of co-intercalating ammonia with the alkali metals on superconductivity is demonstrated by the tri-alkali metal fullerenes. These simple cubic systems highlight the significance of the role of ammonia where the inclusion of the solvent can result in changes in structural and physical properties.[23, 24] The presence of ammonia in tri-alkali metal fullerenes or layered TMDCs is not necessarily undesirable where in both example systems increases in critical temperature T_c have been observed.[6, 7, 22, 25, 26]

Considering the past role of ammonia in both intercalation chemistry and superconductivity utilising alkali metals it is no surprise, even in such early developmental stages, that the alkali metal doped iron selenide materials have been subject to ammonia based synthesis. The synthesis of iron selenides with a focus on superconductivity using ammonia has thus far been limited to intercalation of alkaline earths, lithium, sodium and potassium metals.[6, 7, 22] The lack of reports on solid state methods producing $A_xFe_2Se_2$ (A= Li and Na) could be due to the reactivity of those alkali metals towards glass. The problems of these metals reacting with glass has been observed for other TMDCs such as Na_xNbS_2 and Na_xTaS_2 in the range of $x > 0.7$ where the lattice parameters of the intercalated materials do not change significantly after $x = 0.7$ and the excess alkali metal is observed to react with the sealed glass tube.[27]

5.2.1.1. Methods of producing $A_xFe_2Se_2$ utilising amine solvents

Focusing on the solvent containing alkali metal variants of $A_xFe_2Se_2(NH_3)_y$ (A = Li, Na and K) superconductivity was found for all of the materials (Table 5.1). These materials were synthesised using an ammonothermal method where LA, *β*-FeSe and the alkali metal were sealed together in an autoclave (in a bath of LA) before being reacted for 2-17 days at room temperature.[7] The products were then washed with LA and were not subject to heating above room temperature. The indexing performed on the Li and Na materials powder X-ray diffraction (PXRD) pattern gave body centred tetragonal (BCT) cell corresponding to *I*4/*mmm* symmetry. The X-ray diffraction patterns of both the Li and Na were refined using models based on $K_{0.8}Fe_2Se_2$[28] and $Li_x(NH_2)y(NH3)_{1-y}Fe_2Se_2$[6] where it was found that the inclusion of solvent as a co-intercalate did not significantly improve the refinement. Initially it was thought that solvent did not intercalate into the materials along with the alkali metal as the $K_{0.8}Fe_2Se_2$ refinement model did not indicate the presence of solvent in the structure. However, it was later found that ammonia did co-intercalate and a tentative structure was suggested.[29]

Table 5.1 Summary of compositions, T_cs and SFs from ref 7

Nominal Composition	T_c (K)	SF (%)
$LiFe_2Se_2$	44	32
$NaFe_2Se_2$	46	40
$K_{0.5}Fe_2Se_2$	29	1.5
KFe_2Se_2	40	11

The two BCT cells indexed from the powder X-ray patterns of $K_{1.0}Fe_2Se_2$ yielded *c*-axes which are significantly larger than those obtained for superconducting *I*4/*mmm* phases made using solid state methods (Table 5.2).[1] The $K_{1.0}Fe_2Se_2$ material produced using the ammonothermal route gave a T_c 7 K higher than that of the superconducting phase in the materials described by Shoemaker *et.al.* and chapter 4 indicating the superconducting phases are completely different. Since a structural model for the potassium iron selenide superconductor with a T_c of 40 K could not be ascertained the reason for the hyper-expanded *c*-axis is uncertain. The two most likely reasons for hyper-expansion of the *c*-axis are firstly that ammonia has co-intercalated along with the potassium metal or secondly there is more potassium in between the layers.

Table 5.2 Cell parameters as determined by indexing for the $K_{1.0}Fe_2Se_2$ material made using the ammonothermal route.

Composition	*a* Å	*c* Å	Ref
$K_{1.0}Fe_2Se_2$ phase 1	3.755(2)	20.48(1)	7
$K_{1.0}Fe_2Se_2$ phase 2	3.79(2)	16.16(5)	7
$K_{0.55(1)}Fe_{2.00(2)}Se_2$	3.82803(23)	14.2634(1)	1
$K_{0.54(1)}Fe_{1.98(1)}Se_2$	3.83643(8)	14.2504(3)	Chapter 4

The later expansion of the $K_xFe_2Se_2$ ammonothernal system in 2013 showed that the $K_xFe_2Se_2(NH_3)_y$ (x =0.1 to 1, 0.3<y<0.5) material produced can yield single phase material for x > 0.6 and multiphase material for x<0.5.[29] Two superconducting phases were identified based on composition which were determined to be $K_{0.3}Fe_2Se_2(NH_3)_{0.47}$ (T_c = 30 K) and $K_{0.6}Fe_2Se_2(NH_3)_{0.37}$ (T_c = 30 K).[29] Both phases were identified as being free of iron vacancies and containing no anti-ferromagnetic ordering. During these experiments it was demonstrated that a large range of T_cs were possible for the $K_xFe_2Se_2$ system from 30 to 44 K.[29] The structure of these superconducting phases were indexed to be BCT where each phase had a similar *a* parameter but with a large variance in the *c* parameter of up to 1 Å. Considering the wide range of compositions and solvent contents for these materials The observation of a wide range of *c* parameter confirms the dependence of this parameter on the intercalated species.[29]

The range of T_cs for the $K_xFe_2Se_2$ material produced using the ammonothermal route indicates that controlling the solution reaction to get a specific T_c could be difficult. The $K_{0.5}Fe_2Se_2$ composition produced by the ammonothermal route was observed to have a T_c of 29 K and an SF of 1.5 % both of which are considerably lower than that of the $K_{1.0}Fe_2Se_2$ material (Table 5.1). The T_c of the $K_{0.5}Fe_2Se_2$ material indicates that the origin of superconductivity in this sample is similar to that observed for the $K_xFe_ySe_2$ materials produced at high temperature.[1] This observation is good evidence for targeting the $K_{0.5}Fe_2Se_2$ composition so comparisons to other $K_xFe_ySe_2$ superconducting materials made using high temperature routes can be made. The presence of superconductivity in the $K_xFe_2Se_2$ (x = 0.5 and 1.0) systems demonstrates the validity of room temperature synthesis for these materials.

The $Li_xFe_2Se_2$ (x=0.5) systems have had further study in the form of reactions that produce material where ammonia is co-intercalated with the alkali metal. These materials were synthesised using LA, *β*-FeSe and lithium metal in Schlenk vessels. The reaction mixture was then stirred and reacted at temperatures between -75 to -78 °C for the duration of the reaction. The LA was

then removed by evaporation which allowed the isolation of the solvent rich products of $Li_{0.6}(NH2)_{0.2}(NH3)_{0.8}Fe_2Se_2$, $Li_{0.9}Fe_2Se_2(NH_3)_{0.5}$ and $Li_{1.8}Fe_2Se_2(NH_3)[Li(NH_2)]_{0.5}$.[6, 22] The $Li_xFe_2Se_2$ products here crystallise within the $ThCr_2Si_2$ type structure (SG = *I*4/*mmm*) and show a heavy dependence of the *c*-axis on the amount and type of intercalated species. The exact composition of the material presenting with a T_c of 44(1) K and SFs up to 80 %[22] is currently contested.[6, 22]

Scheidt *et.al.* also described a material with the composition $Li_{1.8}Fe_2Se_2(NH_3)[Li(NH_2)]_{0.5}$[22] which has *c*-axis 2.8 % larger than the $Li_{0.6}(NH_2)_{0.2}(NH_3)_{0.8}Fe_2Se_2$[6] composition. This increase in *c*-axis is accompanied by a decrease in the T_c by 4 K and a large increase in magnetic impurities. This increase in magnetic impurities could indicate the liberation of iron and a deviation away from the $Li_xFe_2Se_2$ composition to one with much less iron.[30] Another important point to note is that thermal treatment (400 °C under vacuum) to remove the solvent from these structures results in the decomposition of the material to FeSe and Li_2Se.[6] This has considerable impact for methods targeting non-solvent containing alkali metal iron selenide superconductors. If the solvent cannot be removed without decomposition of the material the isolation of pure $K_{0.5}Fe_2Se_2$ by will have to be performed with methods utilising alternate solvents.

The intercalation of lithium into FeSe is not without its difficulties. An example of this is the lithium rich $Li_{1.8}Fe_2Se_2(NH_3)[Li(NH_2)]_{0.5}$[22]. This material exhibits increased magnetic impurities indicating the decomposition of FeSe by lithium.[2] The issue of Li and TMDCs reactions proceeding past the intercalation stage and producing the elemental transition metal is due to the activities for alkali metals dissolved in ammonia being close to that of bare alkali metal.[2, 31] Although the $A_xFe_2Se_2$ (A = Li, Na and K) ammonia methods have met with success, in the case of $Li_xFe_2Se_2$[6] and $Na_xFe_2Se_2$[7], if they are to be used to make pure $K_{0.5}Fe_2Se_2$ material great care will have to be taken to make sure the material does not decompose on removal of the co-intercalated ammonia.

Although ammonia has been used in the majority of work it should be noted that $A_x(C_5H_5N)_yFe_{2-z}Se_2$(A = Li, Na, K and Rb) material has also been produced.[18] These materials were produced by the reaction of FeSe powders with the alkali metal dissolved in pyridine and reacted at 40 °C. Using this method superconductivity was only observed in the lithium material at 45 K.

The lithium material produced using pyridine differs from those made using ammonia as it is not a high purity material (characterised by powder x-ray diffraction (PXRD)). In the powder pattern of $Li_x(C_5H_5N)_yFe_{2-z}Se_2$ there were

multiple unidentified peaks which the authors assigned to Li(CN). The $Li_x(C_5H_5N)_yFe_{2-z}Se_2$ peaks were defined using BCT cell metrics, however, they were unable to fit a structural model to the powder pattern as the *I*4/*mmm* models described by Burrard-Lucas *et.al.*, Scheidt*et.al.* and Ying *et.al.* resulted in an inadequate fit of the intensities of the $Li_x(C_5H_5N)_yFe_{2-z}Se_2$ reflections.[6, 7, 18, 22]

Interestingly the $K_{1.15(2)}Fe_{2.02(3)}Se_2$ (analytical composition) material produced in pyridine at 40 °C resulted in the formation of the *I*4/*m* phase with the √5x√5 superstructure reflections due to the ordering of iron vacancies within the $K_xFe_ySe_2$ lattice.[32]

This $K_{1.15(2)}Fe_{2.02(3)}Se_2$ material reinforces the conclusions presented in chapter 4 where potassium compositions greater than $K_{0.8}Fe_ySe_2$ result in the formation of *I*4/*m* and a very iron deficient *I*4/*mmm* phase. In addition to this is the fact that the potassium material produced in pyridine is non-superconducting and considering that the crystalline phase in its PXRD was assigned to the *I*4/*m* phase this further reinforces the conclusions presented in chapter 4 that the *I*4/*m* phase is not responsible for superconductivity. The implication of the reactions of alkali metals and iron selenide in pyridine at 40 °C is that if phase pure $A_xFe_2Se_2$ material is to be obtained this method is unsuitable.

5.1.2. Characteristics of potential reducing agents for the synthesis of $A_xFe_2Se_2$

5.1.2.1. N-Butyl lithium

Although methods of producing $A_xFe_2Se_2$ (A = Li, Na, K and Rb) have focused on the use of amines there still exists the potential for utilising alternate methods for intercalating guest species into layered materials. One such method is the reaction between n-butyl lithium (BuLi) and TMDCs in hexane. Examples of layered materials intercalated with Li using BuLi are $Ta_xMo_{1-x}S_2$ (x>0.5), $PbNb_2S_5$, $SnNb_2Se_5$, SnVSe, ZrNCl and HfNCl.[11, 33-36] The use of BuLi to form intercalation compounds of TMDCs is based upon the fact that BuLi is less aggressive than the bare alkali metal.[2, 31] This means that unlike the alkali metal dissolved in ammonia, BuLi is less likely to reduce the parent TMDC so far as to produce the elemental transition metal.[2, 31] However, BuLi is still a powerful reducing agent capable of highly exothermic reactions with TMDCs to the extent of boiling the reaction solution.[2]

The reactive nature of BuLi ($E^{o'}$ = -2.7 V[31]) means that care must be exercised when using it to intercalate TMDCs if a specific composition is needed as BuLi is more than capable of fully saturating the parent material with lithium.[2, 11, 37] An additional benefit of using BuLi is that the typical hexane solvent is not intercalated with the lithium so unlike ammonia much more gentle drying protocols can be utilised.[2] Reassuringly the intercalation of Li into layered materials by BuLi in hexane has been used to produce the superconductor $Li_{0.16}ZrNCl$ which has a T_c of 12.5 K. Considering the general applicability of the BuLi/hexane systems to intercalating layered materials, even producing superconductors, and that n-butylpotassium (BuK) is obtainable[38] the use of these methods to form $K_{0.5}Fe_2Se_2$ is a possibility but a more gentle approach may be better.

5.1.2.2. Alkali metal acenes

The minimisation of the risk of reducing the transition metal in a TMDC to its elemental form is important if high purity alkali metal intercalated TMDCs are to be obtained. An interesting way of doing this is to use organometallic reducing agents such as alkali metal naphthalenides. The solubility of naphthalene in solvents such as ethers and alkanes makes it a very attractive reducing agent.[31] Where the reaction between the naphthalenide reducing agent and the starting material can be done in easy-to-use solvent like THF.[31]

Naphthalenide reducing agents have been used in layered systems such as the nitrides A_xZrNCl (A = Li, Na and K)[14, 36] and LiHfN[39] as well as the TMDC systems A_xMS_2 (A = Li, Na and K; M = Ti, Mo and W)[2, 40]. The application of these naphthalenide reducing agents to TMDCs is not straight forward because for the Li and sodium variants the risk of over reducing the parent material is great.[2, 41] This is due to the ion paring between naphthalene and the alkali metal increasing in strength as group 1 is descended which has been observed by electron paramagnetic resonance (EPR) spectroscopy.[31, 42] This means that the formal potentials of the alkali metal naphthalenides will increase in the same manner as the ion paring. The effect of increasing formal potentials from Li[Naphthalene] to K[Naphthalene] means that the latter is a weaker reducing agent.

Naphthalene forms part of a larger group of molecules called the acenes where the commonality that they all share is conjugated benzene rings making them excellent electron acceptors (Figure 5.1 and Table 5.1). As the number of rings is increased in the molecules their ability to stabilise their radical anion increases due to the increase in the number of possible molecular resonance

forms. So as the acenes molecular weight increases their reductive potential decreases.[31] This generates the possibility to use the acenes to pick a reduction potential that will not cause any over reduction of a TMDC system.

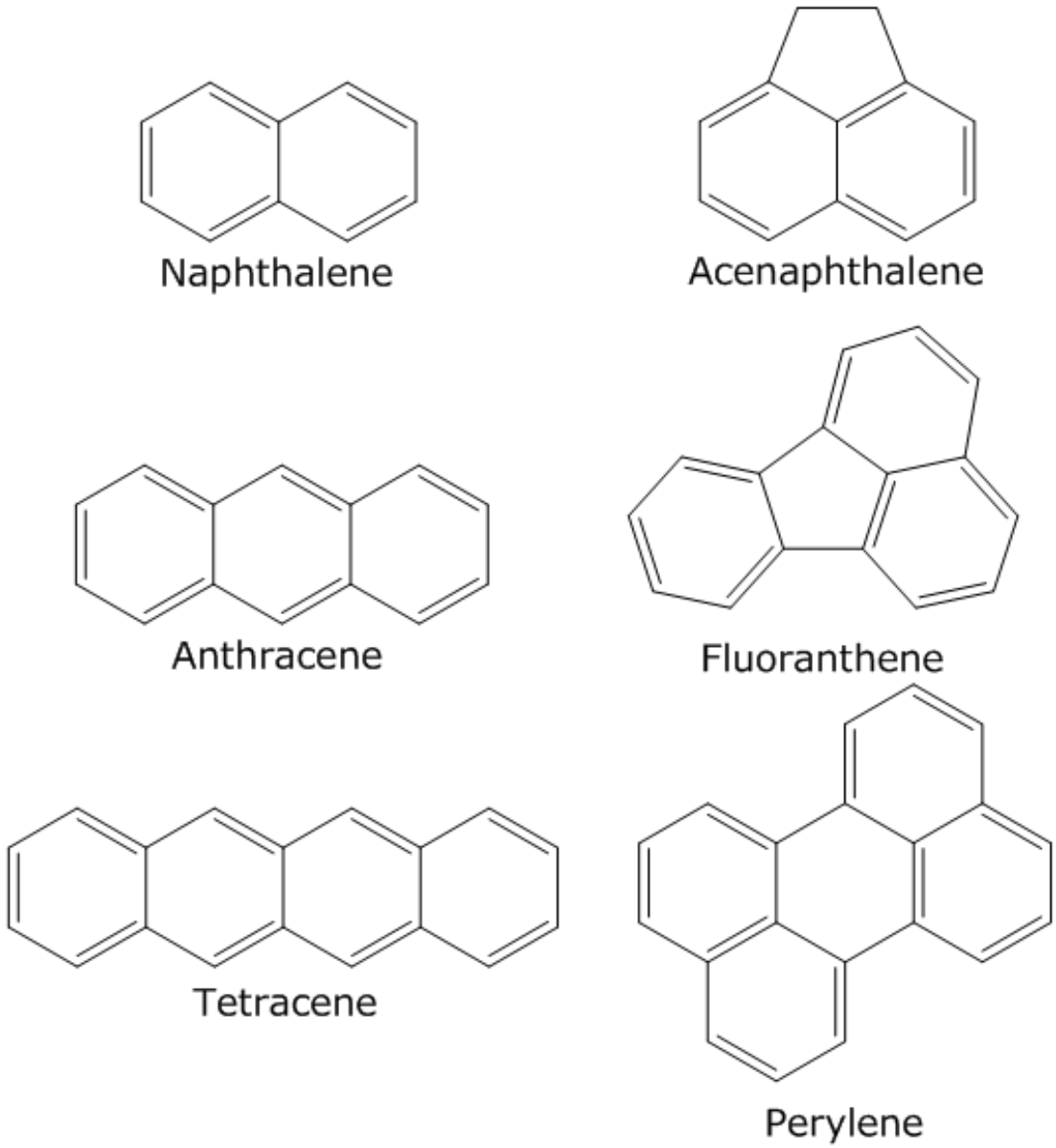

Figure 5.2 Graphical representations of several common acenes. The redox potential for the anion radicals of these molecules follows the following trend; naphthalene (NP)>acenaphthalene (ANP) >anthracene (AN) >fluoranthene (FA)>perylene (PY)>tetracene (TA).

Table 5.3 Summary of reduction potentials Vs SCE in DMF for the acenes in figure 5.1.[43]

Acene	E_{red} (V)
Naphthalene (NP)	-2.79
Acenaphthalene (ANP)	-2.67
Anthracene (AN)	-1.96
Fluoranthene (FA)	-1.74

Perylene (PY)	-1.67
Tetracene (TA)	-1.64

This work assesses the viability of acenes being used as reducing agents to form high quality $K_{0.5}Fe_2Se_2$ superconducting material. This work will be carried out solely in the ether solvent THF primarily because of its compatibility with powerful reducing agents, ease of handling (boiling point 66 °C) and the high solubility of the acene molecules in this solvent.[31, 44] Also the method of drying THF to the degree required here is well known, rigorous and the risks well understood (method described in chapter 2).[44] Due to the heterogeneous nature of the reaction, as TMDCs are not soluble in THF,[2] the potassium acene can be prepared, used and then washed away in THF. The ease of handling THF coupled with the insolubility of the TMDC in this solvent means that the manipulations required during these reactions can be minimised and performed rigorously. The air and moisture sensitive nature of the $K_xFe_2Se_2$ product makes the added simplicity of using a THF system an asset.

5.2. Synthesis of solid state FeSe precursors

The synthesis of the FeSe precursor followed the method outlined in chapter 2 section 4.2.1 with the following differences (masses and target compositions are given in Table 5.4):

Once the furnace reached 1075 °C the samples were held for 24 hours before the ampoule being cooled at a rate of 20 °C min^{-1} to 410 °C. After that temperature was held for 120 hours the ampoule was quenched to ice/water mixture. This annealing protocol served the purpose of achieving a homogeneous precursor while the purpose of quenching was to minimise the presence of a competing hexagonal FeSe phase.

The samples in table 5.5 were subject to additional annealing due to the presence of higher levels of the hexagonal FeSe phase (Table 5.4). The samples AG360_1 and AG361_1 were combined and designated AG364_1 which was then sealed in a silica ampoule (12 OD). The annealing was carried out by placing the ampoules directly into an oven preheated to 300 °C for 48 hours followed by quenching them into ice/water. The sample AG364_1 was subjected to the above treatment one more time to improve its phase composition generating the product AG364_2.

The products mass was recorded before it was ground with a pestle and mortar. A small sample was loaded into a capillary (0.2 mm) tube and sealed using a micro torch. The materials PXRD pattern was recorded on a Bruker Advance D8 lab diffractometer using Mo $K_{\alpha 1}$ radiation.

Table 5.4 Reactant amounts, phase composition and superconducting properties of FeSe materials prepared by following the reaction protocol: RT →@2°C/min, 750°C, 72h →@1°C/min, 1075°C, 24h→ @20°C/min, 410°C, 120h→Quench to ice/water.

ID	Fe mass /g	Se mass /g	Phase fractions (%) *β*-FeSe/ *δ*-FeSe/ Bulk Fe	SF @2 K	T_c (K)
AG338_1	0.8449	1.1945	95.6(9)/ 4.0(9)/ 0.4(9)	-	
AG349_1	0.8494	1.2009	97.6(3) / 1.5(3) / 0.9(3)	62%	8
AG360_1	1.3320	1.8816	97.0(3)/2.55(30)/0.45(30)	-	
AG361_1	1.3582	1916.1	98(2) / 2(2) / 0	-	

Table 5.5 Reactant amounts, phase composition and superconducting properties of FeSe materials prepared by following the reaction protocol: direct 300°C, 48h → Quench to ice/water (AG364_2 was subject to annealing/quenching twice)

ID	Phase fractions (%) *β*-FeSe/ *δ*-FeSe/ Bulk Fe	Precursor mass, g	Superconducting fraction	T_c (K)
AG338_2	97.8(4) / 1.6(4) /0.6(4)	1.1023	65%	8
AG364_1	97.6(2) /1.7(2) / 0.7(2)	6.0112	55%	
AG364_2	98.1(2) / 1.1 (2) / 0.8(2)	5.8912	96%	

5.3. Preparation of $K_{1.0}$[Acene] solution for use as a reducing agent

Fresh solutions of reducing agent was prepared for each reaction as per the following method. Potassium metal (Aldrich, 99.95%, 14.9 mg, 0.382 mmol) was loaded into a silica glass insert (8 mm outer diameter (OD)) and put into a round bottomed Schlenk flask. A slight excess of acene (0.384 mmol), to ensure all potassium metal can be reacted, was then loaded into the flask using a funnel and a magnetic glass stir was carefully added before the flask was closed. The flask was then taken to a dual manifold Schlenk line and connected via PVC

vacuum tubing along with another flask containing dry THF. Both sets of tubing were then evacuated and purged with argon 3 times before the flasks were opened to the line under positive argon pressure. The dry THF (30 ml) was then transferred through a cannula into the flask containing K and acene by establishing a positive over-pressure of argon. Both of the flasks were then isolated from the Schlenk line by closing the PTFE high vacuum taps on each vessel and the THF flask removed. The K and acene was then reacted for at least 12 hours in the THF forming an opaque coloured solution (Table 5.6).

Table 5.6 Summary of the acenes used in this work, the amount of acene (1:1.005 acene to K ratio) required to form the reducing solutions and the colour of the THF solutions of these solutions.

Acene	Mass used (mg)	Radical colour
Naphthalene	49.4	Green
Acenaphthalene	59.5	Green
Fluoranthene	78.0	Green
Perylene	96.6	Blue
Tetracene	88.0	Green

5.4. Synthesis of $K_{0.5}Fe_2Se_2$ using $K_{1.0}$[Acene] and FeSe in THF

5.4.1. Experimental method for the synthesis of $K_{0.5}Fe_2Se_2$ in THF using $K_{1.0}$[Acene] and FeSe

In the argon glove box iron selenide precursor (207 mg, 1.53 mmol) was loaded into the flask using a funnel and a magnetic glass stir was carefully added before the flask was closed (Table 5.3). The flask was then taken to the Schlenk line and connected via PVC vacuum tubing with another flask containing fresh dry THF. The tubing was then evacuated and purged with argon gas 3 times before all three of the vessels were re-opened to the Schlenk line. Dry THF (5 ml) was then transferred via cannula to the FeSe precursor flask and a suspension created by stirring (300 rpm). Once the transfer was complete the THF containing flask was removed from the line.

Table 5.7Summary of reaction masses for the reaction of $K_{1.0}$[Acene] and FeSe.

ID	Reaction Time / Hours	Precursor ID	Reducing agent
AM75_1	24	AG338_2	K[Naphthalene]
AM82_1	24	AG338_2	K[Acenaphthalene]
AM87_1	24	AG338_2	K[Perylene]
AM88_1	24	AG338_2	K[Fluoranthene]
AM89_1	24	AG338_2	K[Tetracene]
AM94_1	168	AG338_2	K[Perylene]
AM127_1	3	AG364_2	K[Perylene]

The $K_{1.0}$[Acene] reducing solution (30 ml) was then transferred drop-wise via a cannula to the FeSe suspension over 5 minutes. In order to determine the best K[Acene] reducing agent each one was tested over 24 hours. It was noted that only the K[NP] and K[ANP] were completely exhausted and the other three showed a green colouration to their solutions indicating the presence of unreacted radical anions. Once the reactions were completed the product was isolated from the supernatant by filtration through a Schlenk frit. The materials were then washed with THF (3 x 20 ml) to remove the acene starting material from the product. The washed product was then dried under low vacuum ($1x10^{-3}$ mbar) before being transferred to an argon glove box. The best reducing agent was determined to be K[PY] by the use of PXRD and will be discussed briefly in the next section.

Two additional reactions were performed to explore the effect of reaction time on the $K_xFe_2Se_2$ product. The first reaction (AM127_1) was performed over 3 hours and the second (AM94_1) for 168 hours. These materials were subjected to the same isolation, washing and drying protocol as the reactions lasting 24 hours.

The recovered materials were removed from the Schlenk frit using a long titanium spatula. The materials weight was recorded before it was ground in a pestle and mortar. The ground material was then loaded into a capillary for PXRD.

5.4.2. Results and Discussion for the synthesis of $K_{0.5}Fe_2Se_2$ in THF using $K_{1.0}$[Acene] and FeSe

The heterogeneous reaction between $K_{1.0}$[Acene] and FeSe successfully forms ternary $K_xFe_2Se_2$ phases (Figure 5.3). However, there are at least two sets of peaks in the PXRD patterns of the products, the first corresponds to $K_xFe_2Se_2$ *I*4/*mmm* and the second corresponds to unreacted *β*-FeSe (Figure 5.3). It is observable from the PXRD patterns that the stronger the reducing agent the more of the FeSe is reacted. It is also clear that the material produced by using K[Naphthalene (NP)] has multiple $K_xFe_2Se_2$ phases. PXRD also reveals the unsuitability of K[Tetracene (TA)] as a reducing agent as the presence of TA in the final product indicated that the washing protocol was inadequate (Figure 5.4). Although all the reducing agents are capable of making $K_xFe_ySe_2$ material it is unclear which is best.

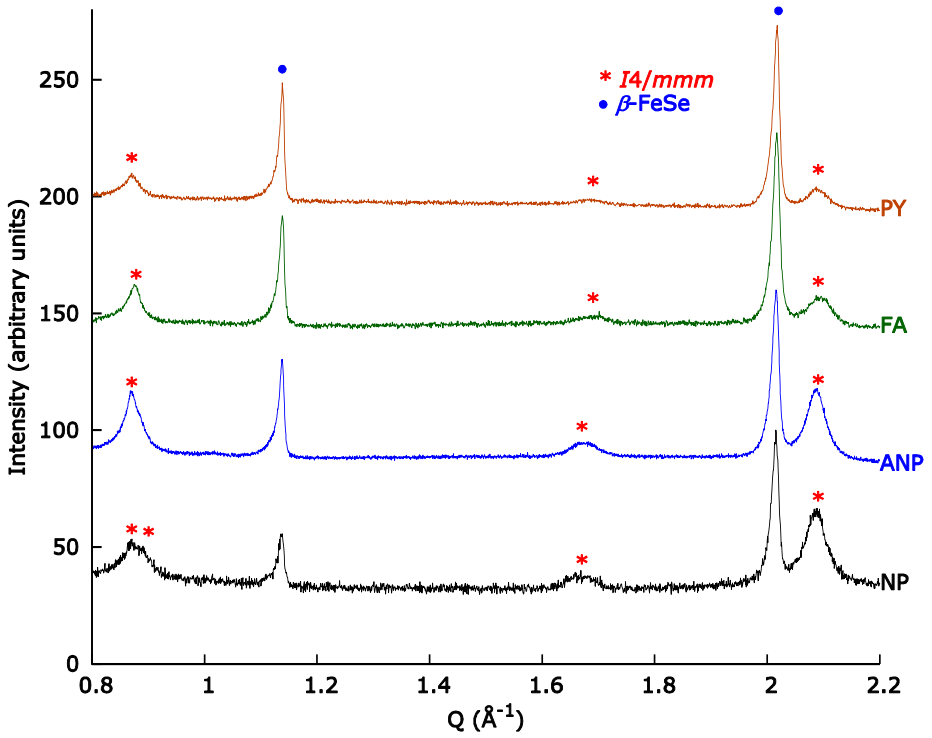

Figure 5.3 Comparison of the PXRD patterns of AM75_1 (NP), AM82_1 (ANP), AM87_1 (PY) and AM88_1 (FA) where the red * represents the *I*4/*mmm* peaks and the blue circles represent the *β*-FeSe.

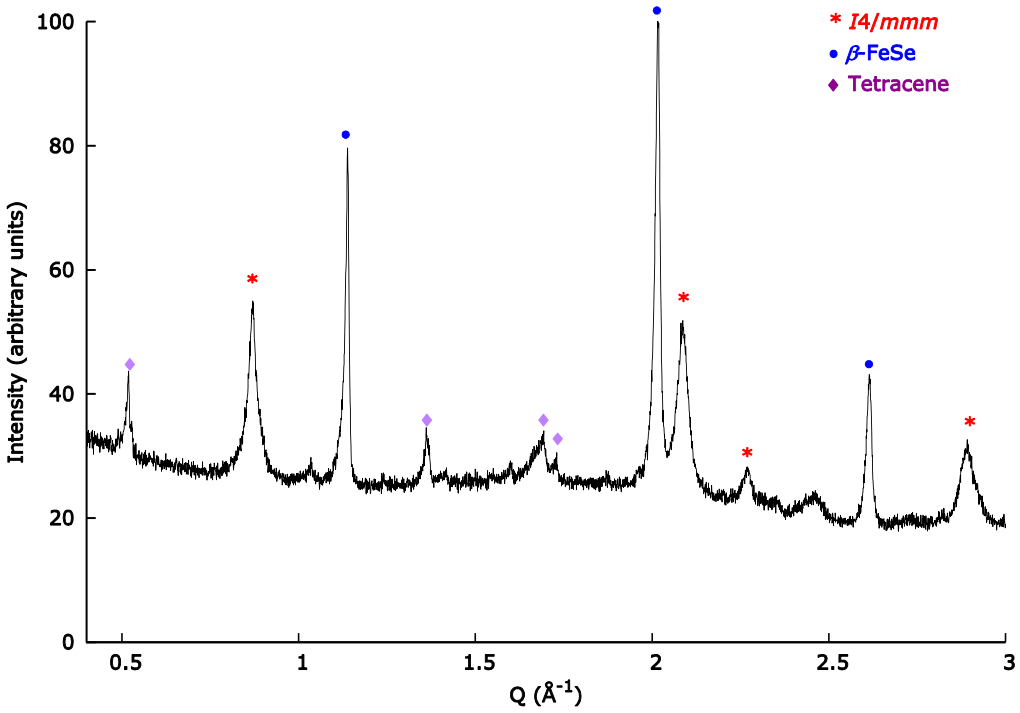

Figure 5.4 PXRD pattern recorded for the material produced using the reducing agent K[Tetracene] and FeSe. The lilac diamonds are tetracene, the red * are *I4/mmm* peaks and the blue circles are *β*-FeSe peaks.

The Rietveld analysis of AM75_1, AM82_1, AM87_1 and AM88_1 yields a phase assembly that is inconsistent with the $K_{0.5}Fe_2Se_2$ material discussed in chapter 4. It would be expected that at this composition, from the solid state work in the previous chapter, the phases present would be *I*4/*m* ($K_xFe_ySe_2$), FeSe and Fe. Instead we see a unique phase assembly consisting of two *I*4/*mmm* phases, *β*-FeSe and Fe (Figure 5.5 and Table 5.8-10). Interestingly there is no sign of the superstructure reflections associated with the iron vacancy ordered *I*4/*m* phase which was common place throughout the materials in chapter 4. The reaction of $K_{1.0}$[Acene] and FeSe therefore promotes the formation of the *I*4/*mmm* phases over that of the more stable *I*4/*m* phase.

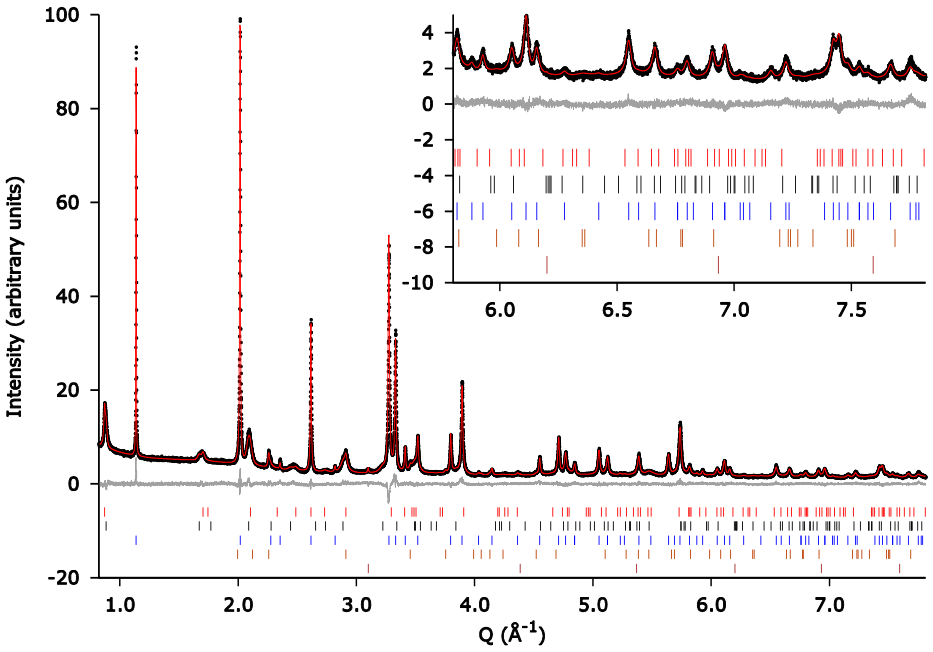

Figure 5.5 A typical Rietveld refinement plot for $K_{0.5}Fe_2Se_2$ materials produced by using 0.5 K[Acene] + 2Fe_2Se_2. The presented refinement was done on the material AM87_1 with the nominal composition of $K_{0.5}Fe_2Se_2$. The multiphase model was refined against SPXRD data at a wavelength of λ = 0.826141 Å. Observed (black dots), calculated (red line) and difference (grey line) data are shown. The tic marks represent Bragg reflection positions of the *I*4/*mmm* (red), *I*4/*mmm*2 (black), *β*-FeSe (Blue); *δ*-FeSe (dark orange) and Fe (Brown) phases. A summary of the refined parameters are presented in Tables 5.8 to 5.10. R_{wp} = 5.01, R_{exp} = 2.88, number of refined parameters 71.

Table 5.8 The shielding and phase fractions as obtained from the Rietveld analysis of the powder x-ray diffraction (pxrd) obtained from materials produced by the reaction of $K_{1.0}$[Acene] and FeSe in THF.

Parameter / Label	acene	*I*4/*mmm* (wt. %)	*I*4/*mmm*2 (wt. %)	*β*-FeSe (wt. %)	*δ*-FeSe (wt. %)	Fe (wt. %)
AM75_1	NP	19.0(10)	46.5(9)	29.3(5)	0	5.2(1)
AM82_1	ANP	22.34(27)	33.34(25)	41.75(21)	0	2.57(5)
AM87_1	PY	15.68(22)	15.77(22)	67.20(25)	0.80(2)	0.56(2)
AM88_1	FA	17.40(61)	18.97(58)	61.90(63)	1.01(3)	0.73(5)

Table 5.9 The cell parameters of the *I*4/*mmm* phases as obtained from the Rietveld analysis of the pxrd obtained from materials produced by the reaction of $K_{1.0}$[Acene] and FeSe in THF. In addition to materials described in this chapter some important materials from chapter 4 are included for reference.

Parameter / Label	acene	*I*4/*mmm* *a* Å	*I*4/*mmm* *c* Å	*I*4/*mmm* V Å^3	*I*4/*mmm* *c*/*a*	*I*4/*mmm*2 *a* Å	*I*4/*mmm*2 *c* Å	*I*4/*mmm*2 V Å^3	*I*4/*mmm*2 *c*/*a*
AM75_1	NP	3.851(3)	14.38(1)	213.3(1)	3.735(4)	3.929(1)	13.990(8)	216.0(2)	3.561(2)
AM82_1	ANP	3.8419(5)	14.393(2)	212.44(6)	3.7464(7)	3.9172(4)	14.085(2)	216.13(5)	3.5957(6)
AM87_1	PY	3.8194(5)	14.409(2)	210.19(6)	3.7725(7)	3.9021(5)	14.185(3)	215.98(7)	3.6352(8)
AM88_1	FA	3.816(1)	14.316(4)	208.5(2)	3.751(2)	3.892(1)	14.215(9)	215.3(2)	3.652(3)
AG323_2($K_{0.75}Fe_{1.868}Se_2$)	N/A	3.83626(7)	14.2508(4)	209.73(1)	3.7148(1)	0	0	0	0
AG311_2($K_{0.75}Fe_{1.781}Se_2$)	N/A	3.83643(8)	14.2504(3)	209.74(1)	3.7145(1)	0	0	0	0
AG308_3($K_{0.75}Fe_{1.702}Se_2$)	N/A	3.83600(7)	14.2523(4)	209.72(1)	3.7154(1)	0	0	0	0
AG424_2($K_{0.8}Fe_{1.753}Se_2$)	N/A	3.8371(2)	14.2518(6)	209.84(2)	3.7142(2)	0	0	0	0
AG281_3($K_{0.9}Fe_{1.55}Se_2$)	N/A	0	0	0	0	3.9673(8)	13.754(4)	216.5(1)	3.467(1)
AG315_2($K_{0.9}Fe_{1.625}Se_2$)	N/A	0	0	0	0	3.9682(4)	13.773(2)	216.88(6)	3.4707(7)

Table 5.10 A summary of the compositions of the materials produced using $K_{1.0}$[Acene] and FeSe in THF obtained by Rietveld analysis.

Parameter / Label	Acene	Nominal Composition	Overall Refined Composition	Refined *I*4/*mmm* composition	Refined *I*4/*mmm*2 composition
AM75_1	NP	$K_{0.5}Fe_2Se_2$	$K_{0.63(2)}Fe_{1.91(2)}Se_2$	$K_{0.71(5)}Fe_{1.90(7)}Se_2$	$K_{1.00(2)}Fe_{1.24(2)}Se_2$
AM82_1	ANP		$K_{0.43(1)}Fe_{1.95(1)}Se_2$	$K_{0.45(1)}Fe_{1.99(2)}Se_2$	$K_{0.95(1)}Fe_{1.99(2)}Se_2$
AM87_1	PY		$K_{0.218(5)}Fe_{1.983(5)}Se_2$	$K_{0.38(2)}Fe_{1.81(2)}Se_2$	$K_{0.98\ (1)}Fe_{1.39(2)}Se_2$
AM88_1	FA		$K_{0.24(1)}Fe_{1.90(2)}Se_2$	$K_{0.23(4)}Fe_{2.00(5)}Se_2$	$K_{0.97(4)}Fe_{0.93(4)}Se_2$

The two ternary $K_xFe_ySe_2$ phases are both based upon the $ThCr_2Si_2$ (SG = *I*4/*mmm*, Figure 5.1) structure type. The first phase (labelled as *I*4/*mmm*) corresponds to the general composition of $K_xFe_2Se_2$.[1] The second $K_xFe_ySe_2$ phase (labelled as *I*4/*mmm*2) crystallises in the same space group as $ThCr_2Si_2$ but is based upon an iron vacancy disordered *I*4/*m* ($K_xFe_ySe_2$) structure. This *I*4/*mmm*2 phase displays much larger cell volume (~216.0 Å^3) when compared to that of the *I*4/*mmm* (~210.0 Å^3) as observed by Shoemaker *et.al.* and in the subsolidus reactions of chapter 4.[1] The presence of the *I*4/*mmm*2 phase, which is heavily iron deficient showing compositions of $K_{0.94(3)}Fe_{1.36(4)}Se_2$ (Chapter 4), within the materials produced using the K[Acene] reducing agents indicates that all of these reagents are capable of liberating iron from the parent material.

The phase fractions obtained from the Rietveld analysis of PXRD data recorded on the samples show that NP and ANP are unsuitable for producing $K_xFe_2Se_2$ materials. The significant increase of elemental iron between the iron selenide precursors and the products after intercalation by K[NP] and K[Acenaphthalene (ANP)] is a clear indication that the parent material is being destroyed by these reducing agents (Figure 5.6 and Table 5.8). The effects of over reduction are much less evident for the materials produced using K[PY] and K[Fluoranthene (FA)] which only show a minuscule increase in elemental iron levels. The decision to use K[PY] as the reducing agent over that of K[FA] was based on the fact that due to PY having more conjugated benzene rings that FA it is the weaker reducing agent. In addition to this the difference between the products of the two reducing agents when reacted with FeSe are very similar and it was hoped that the milder nature of K[PY] could be capitalised on by controlling the reaction time.

The cell volumes of the *I*4/*mmm* phase also reflect the aggressive nature of the K[NP] and K[ANP] reducing agents both producing the largest cell volumes of the entire data set (Table 5.9). This also corresponds with the overall refined composition and the observations made during the experiments where the K[NP] and K[ANP] completely intercalate all of their potassium into the FeSe (Table 5.10). The other two viable reducing agents K[PY] and K[FA] do not fully intercalate the FeSe starting material during the 24 hour reaction period and this is reflected in the overall refined potassium content as well as the fact that the *I*4/*mmm* and *I*4/*mmm*2 cell volumes are much smaller than those found in the products of reactions using K[NP] and K[ANP].

The *I*4/*mmm*2 phase is undesirable in these materials as it interferes with the identification of any possible superconducting *I*4/*mmm* phases. Since the largest fraction of the *I*4/*mmm*2 phase was shown to be in the material

intercalated using the strongest reducing agent, K[NP], the mildest reducing agent was used to investigate the time dependence of the phase assembly of these materials.

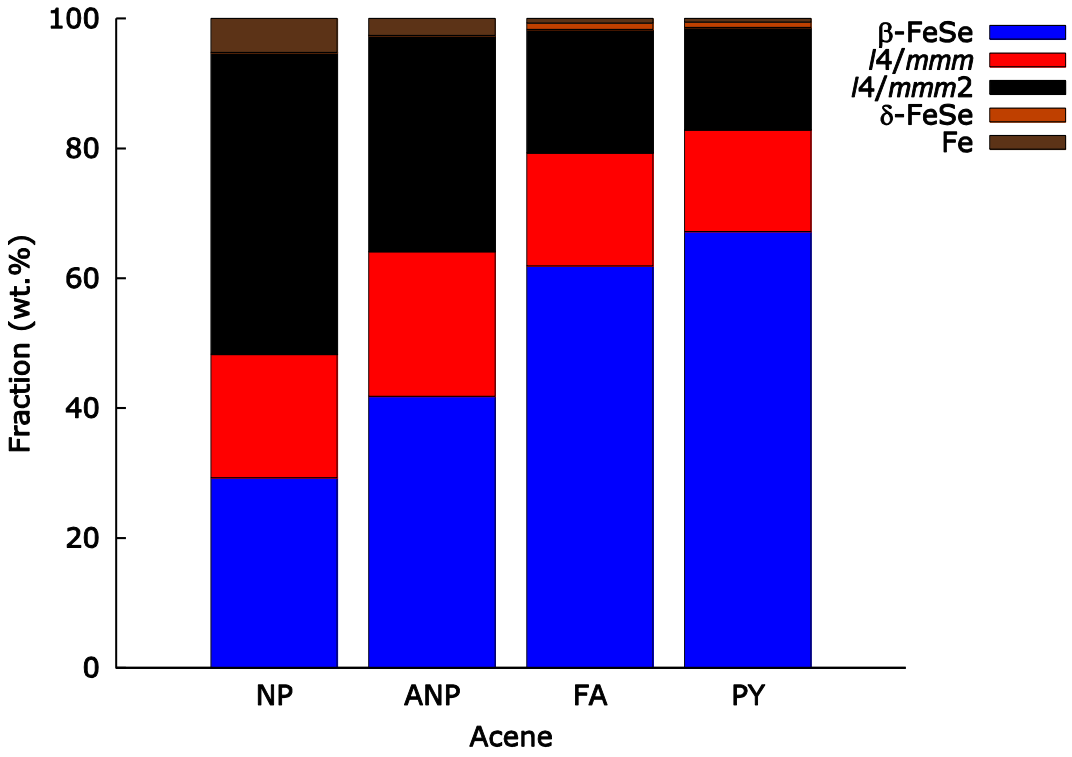

Figure 5.6 Phase fractions obtained from Rietveld performed on the materials AM75_1 (NP), AM82_1 (ANP), AM87_1 (FA) and AM88_1 (PY). The x axis labels represent the acenes used to form the reductive solutions naphthalene (NP), acenaphthalene (ANP), fluoranthene (FA) and perylene (PY).

5.4.2.1. Investigation of the effect of reaction time on producing $K_{0.5}Fe_2Se_2$

It was hoped that using the mildest reducing agent K[PY] to form the $K_{0.5}Fe_2Se_2$ material would allow the isolation of materials containing a single *I*4/*mmm* phase. Initially it looked as if altering the reaction times had successfully achieved this as qualitative observations of the PXRD data did not observe any peak splitting for the material obtained after the 3 hour reaction. The true phase assembly is only revealed after Rietveld analysis which indicated the presence of two *I*4/*mmm* phases for all of the materials. Varying the reaction time between 3 and 168 hours revealed an identical phase assembly to that seen for the materials produced using the range of reducing agents (Figure

5.5, 5.7 and Table 5.11). The results of the Rietveld refinements done using the PXRD data for these materials are summarised in tables 5.11-13

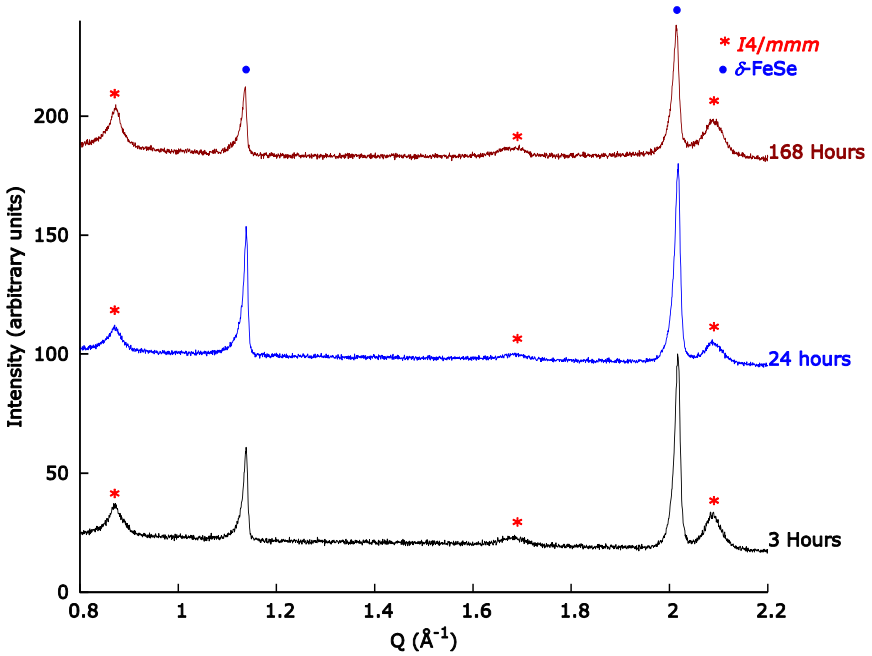

Figure 5.7 Comparison of the PXRD patterns of AM127_1 (3 Hours), AM87_1 (24 Hours) and AM94_1 (168 Hours) where the red * represents the *I*4/*mmm* peaks and the blue circles represent the *β*-FeSe.

Table 5.11 The shielding and phase fractions as obtained from the Rietveld analysis of the powder x-ray diffraction (pxrd) obtained from materials produced by the reaction of $K_{1.0}$[PY] and FeSe in THF.

Parameter / Label	Total Reaction time (Hours)	T_c (K)	SF (%)	*I4/mmm* (wt. %)	*I4/mmm*2 (wt. %)	*β*-FeSe (wt. %)	*δ*-FeSe (wt. %)	Fe (wt. %)
AM127_1	3	31.5	2.4	18.0(5)	20.6(5)	59.7(5)	0	1.7(1)
AM87_1	24	31.5	2.0	15.68(22)	15.77(22)	67.20(25)	0.80(2)	0.56(2)
AM94_1	168	32	10.4	20.3(6)	27.5(6)	46.5(5)	0	5.7(1)

Table 5.12 The cell parameters of the *I4/mmm* phases as obtained from the Rietveld analysis of the pxrd obtained from materials produced by the reaction of $K_{1.0}$[PY] and FeSe in THF. In addition to materials described in this chapter some important materials from chapter 4 are included for reference.

Parameter / Label	Total Reaction time (Hours)	SF (%)	*I4/mmm* *a* Å	*I4/mmm* *c* Å	*I4/mmm* V Å^3	*I4/mmm* *c/a*	*I4/mmm*2 *a* Å	*I4/mmm*2 *c* Å	*I4/mmm*2 V Å^3	*I4/mmm*2 *c/a*
AM127_1	3	2.4	3.836(1)	14.391(4)	211.8(1)	3.752(2)	3.915(1)	14.066(6)	215.6(1)	3.752(2)
AM87_1	24	2.0	3.8194(5)	14.409(2)	210.19(6)	3.7725(7)	3.9021(5)	14.185(3)	215.98(7)	3.6352(8)
AM94_1	168	10.4	3.824(1)	14.348(5)	209.8(2)	3.752(2)	3.907(1)	14.139(6)	215.8(2)	3.7522(2)
AG323_2($K_{0.75}Fe_{1.868}Se_2$)	N/A	19	3.83626(7)	14.2508(4)	209.73(1)	3.7148(1)	0	0	0	0
AG311_2($K_{0.75}Fe_{1.781}Se_2$)	N/A	19	3.83643(8)	14.2504(3)	209.74(1)	3.7145(1)	0	0	0	0
AG308_3($K_{0.75}Fe_{1.702}Se_2$)	N/A	19	3.83600(7)	14.2523(4)	209.72(1)	3.7154(1)	0	0	0	0
AG424_2($K_{0.8}Fe_{1.753}Se_2$)	N/A	6.3	3.8371(2)	14.2518(6)	209.84(2)	3.7142(2)	0	0	0	0
AG281_3($K_{0.9}Fe_{1.55}Se_2$)	N/A	0	0	0	0	0	3.9673(8)	13.754(4)	216.5(1)	3.467(1)
AG315_2($K_{0.9}Fe_{1.625}Se_2$)	N/A	0	0	0	0	0	3.9682(4)	13.773(2)	216.88(6)	3.4707(7)

Table 5.13 A summary of the compositions of the materials produced using $K_{1.0}$[PY] and FeSe in THF obtained by Rietveld analysis.

Parameter Label	Total Reaction time (Hours)	Nominal Composition	Analysed Composition	Overall Refined Composition	Refined *I*4/*mmm* composition	Refined *I*4/*mmm*2 composition
AM127_1	3	$K_{0.5}Fe_2Se_2$	$K_{0.35(4)}Fe_{2.10(2)}Se_{2.00(2)}$	$K_{0.28(1)}Fe_{1.97(1)}Se_2$	$K_{0.60(2)}Fe_{1.83(3)}Se_2$	$K_{0.99(4)}Fe_{1.30(4)}Se_2$
AM87_1	24		$K_{0.21(3)}Fe_{2.05(2)}Se_{2.000(9)}$	$K_{0.218(5)}Fe_{1.983(5)}Se_2$	$K_{0.38(2)}Fe_{1.91(2)}Se_2$	$K_{0.99(2)}Fe_{1.39(2)}Se_2$
AM94_1	168		$K_{0.552(4)}Fe_{2.12(2)}Se_{2.00(2)}$	$K_{0.40(1)}Fe_{2.16(2)}Se_2$	$K_{0.49(3)}Fe_{1.99(4)}Se_2$	$K_{1.00(3)}Fe_{1.30(3)}Se_2$

Despite the disappointing phase assembly the analysis of their superconducting properties using SQUID magnetometry showed that all of them have superconducting behaviour. The samples AM127_1 and AM87_1 showed trace superconductivity (SF ~2 %) at a T_c of 31.5 but AM94_1 gave a SF of 10.4 % coupled with a T_c of 32 K (Figure 5.8). This demonstrates that the superconducting *I*4/*mmm* phase identified in chapter 4 exists within these materials. Therefore Rietveld analysis of their PXRD patterns is necessary to test the validity of the conclusions of chapter 4.

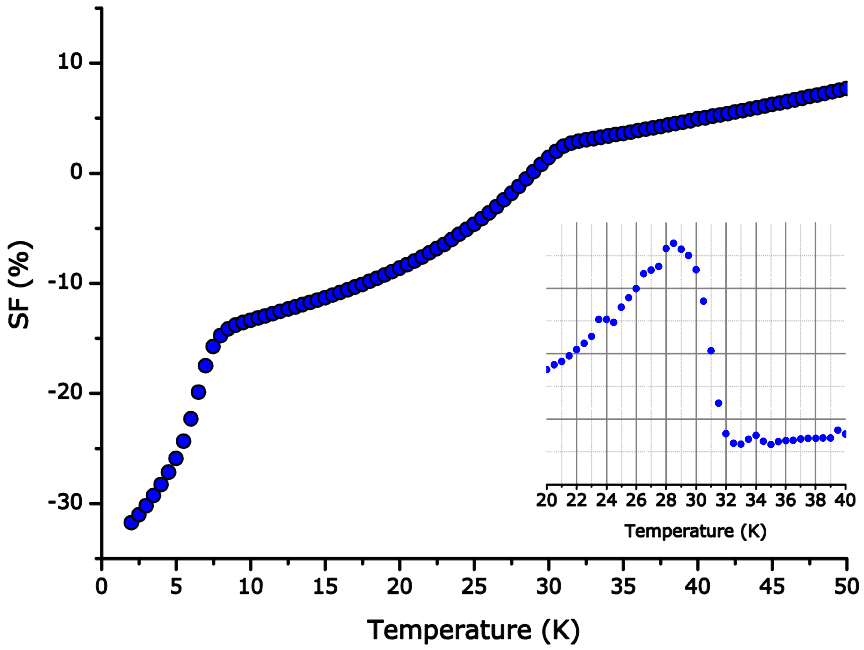

Figure 5.8 The magnetisation as a function of temperature measurements (zero field cooled) done on AM94_1 ($K_{0.5}Fe_2Se_2$). The inset is *d*M/*d*T and shows the onset of superconduction at a T_c of 32 K and a SF of 10.4 %. The magnetic measurements were taken in an applied field of 10 Oe with a sample mass of 15.5 mg.

The phase fractions of these materials show no trend with reaction time. This is unexpected as the extent of reaction is observable by a colour change of blue to yellow when the reducing agent is exhausted. Observation of the colour changes as the reaction time progresses showed that the reaction is complete under these conditions after three days. The colour of the supernatant liquid after filtration at each of the reaction times is opaque blue (3 hours), clear green/yellow (24 hours) and finally clear yellow (168 hours). These observations, however, present a problem as the AM87_1 overall refined composition and amount of β-FeSe is not what is expected from the observation of the reactions as time progresses. For AM87_1 more of the reducing agent has

reacted than in AM127_1 but there is less intercalation (Table 5.13). Considering that AM94_1 is observed to have complete reaction of the reducing agent, lowest fraction of *β*-FeSe and highest refined overall composition it is logical to conclude that AM87_1 is anomalous. The comparison of the analytical composition $K_{0.552(4)}Fe_{2.12(2)}Se_{2.00(2)}$ to the overall refined composition ($K_{0.5}Fe_2Se_2$) reveal that for AM94_1 there is a discrepancy between the potassium compositions calculated by the two methods. This could potentially be due to the formation of amorphous K_2Se_4[45] as the reaction progresses.

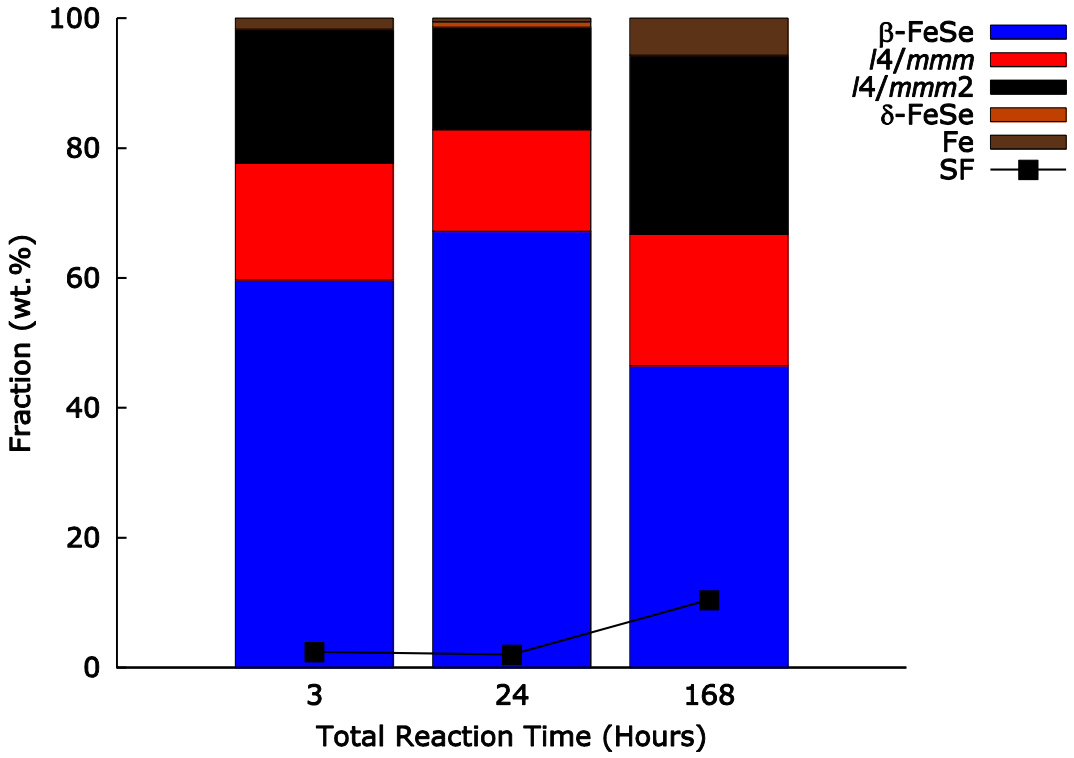

Figure 5.9 Phase and superconducting fractions obtained from Rietveld analysis and SQUID magnetometry performed on the materials AM87_1 (24 hours), AM94_1(168 hours) and AM127_1 (3 hours).

The presence of the *I*4/*mmm* and *I*4/*mmm*2 phases within all of the materials poses the same problem as the materials made using solid state methods; the intercalated phase responsible for superconductivity is unknown (Figure 5.9). The two *I*4/*mmm* phases are distinctly different with cell volumes corresponding to the $K_xFe_2Se_2$ (which is iron rich and has a cell volume of <214 Å^3) and $K_xFe_ySe_2$ (which is iron deficient and has a range of cell volumes 215-217 Å^3) (Table 5.12). Of these two compositions it was shown that the *I*4/*mmm* variant with a cell volume of 209.73 Å^3 was responsible for the expression of superconducting properties (Chapter 4). In the materials produced using $K_{1.0}$[PY] in THF the *I*4/*mmm*2 phases have identical cell volumes to each other but are

clearly different from the smaller *I*4/*mmm* variants (Table 5.12). The fact that all the *I*4/*mmm*2 phases have identical cell volumes coupled with the presence of a significant change in SF between AM87_1 (24 hours total reaction time) and AM94_1 (168 hours total reaction time) means that this particular phase is non-superconducting. The conclusion that *I*4/*mmm*2 phases with cell volumes of ~215.8 $Å^3$ are non-superconducting further supports the conclusions of chapter 4 where samples containing this form of *I*4/*mmm* material were found to have no superconducting properties.

The presence of superconductivity in the AM94_1 sample (T_c = 32 K, SF = 10 %) confirms that the *I*4/*mmm* phase is responsible for this phenomenon in these materials (Figure 5.9 and Table 5.11). The largest SF is expressed by the material which was reacted for the longest time (AM94_1 168 hours) and the other two samples reacted for 3 and 24 hours exhibit only trace superconductivity. As discussed in chapter 4 the volume of the *I*4/*mmm* phase is critically important in determining whether or not a particular material superconducts. The cell volume is especially useful due to the fact that even for phases that experience heavy overlap in an X-ray pattern, like the two forms of the *I*4/*mmm* phases, it is readily and accurately attainable. In the case of the three samples made by the reaction between $K_{1.0}$[PY] and FeSe only AM94_1 (168 hours total reaction time) has a cell volume identical to the critical value of 209.73 $Å^3$ identified in chapter 4 (Table 5.12).

This material then reinforces the conclusions stated in chapter 4, that the *I*4/*mmm* phase with the general composition of $K_xFe_2Se_2$ is responsible for the superconducting properties of these materials. However, only half of the produced *I*4/*mmm* phase is superconducting. This indicates that the *I*4/*mmm* phase present in AM94_1 has more in common with the AG424_2 ($K_{0.8}Fe_{1.753}Se_2$, SF = 6 %) material rather than those displaying an SF of 19 %.

As a proof of concept the production of $K_{0.5}Fe_2Se_2$ material by the reaction of FeSe with $K_{1.0}$[PY] was successful in demonstrating that this ambient temperature route can give shielding fractions comparable to those produced by the solid state methods in chapter 4. The results from these experiments reinforces the work in chapter 4 by showing that the material with the highest SF has *I*4/*mmm* material with a cell volume identical to that of the three samples with an SF of 19 %. The other two samples (AM127_1 and AM87_1) do not have *I*4/*mmm* phases with similar cell volumes to that shown in the *I*4/*mmm* phase of AM94_1 demonstrating again the importance of the cell volume in determining when shielding fractions above trace amounts are observed.

The next iteration of these reactions should include a method of increasing the homogeneity of intercalation as well as reducing the time it takes to complete the reaction. The timescale that these reactions are performed over is an important parameter to reduce purely because of the highly air sensitive nature both the reducing agent and product. Due to the anomalous nature of the phase fractions of AM87_1 the reaction time will be revisited in the next section.

5.5. Synthesis of $K_{0.5}Fe_2Se_2$ using $K_{1.0}$[Perylene], FeSe and sonication in THF

The inability of the K[Acene] reducing agents to fully react all of the FeSe starting material may be due to the inaccessibility of the FeSe material in the centre of the starting materials crystallites. This would lead to over reduced $K_xFe_ySe_2$ phases whilst leaving unreacted material even after extended reaction times. One possible method of overcoming this problem is the exfoliation of the FeSe layers so that they are then well dispersed. This dispersion of FeSe layers would then produce a reaction where all of the FeSe is exposed to the reducing agent creating allowing an even intercalation upon flocculation.

The most expedient method of exfoliation for layered materials is the use of ultrasonic baths and has been successfully used upon TMDCs such as MoS_2 and TaS_2.[46, 47] These methods utilised a wide variety of solvents combined with sonication creating suspensions of highly exfoliated material.[46] These solvents consist of amines, ethers and alcohols to name a few, with each having a unique effect on the stability of the suspensions dependant on what TMDC was being used.[46, 47]

Before trying to find the ideal solvent for the intercalation of potassium into iron selenide it is essential to determine the effect, if any, that sonication has on the system. A control reaction of FeSe in THF using the sonication protocol showed only a slight broadening of all the FeSe peaks which is expected from exfoliation of materials such as MT_2 (M = Mo, W; T = S, Se) (Figure 5.10).[48]

It is important to gauge what impact the energy imparted from the sonic bath has on iron selenide, for example, does the material degrade faster under the reaction conditions with sonication. In order to obtain this information the reaction of K[PY] and FeSe in THF will be adapted to include the sonication step. In this manner the applicability of sonication can be determined before a large amount of time and effort are expended in searching for alternate solvents.

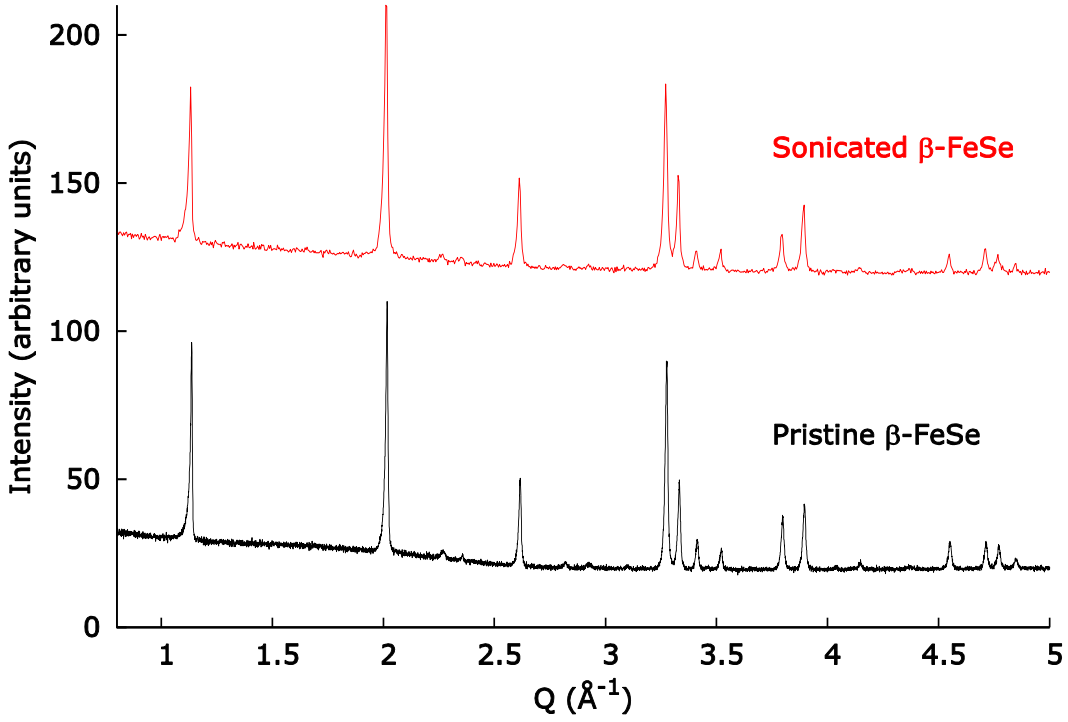

Figure 5.10 Comparison of *β*-FeSe materials AG364_2 before and after sonication.

5.5.1. Experimental method for the synthesis of $K_{0.5}Fe_2Se_2$ in THF using $K_{1.0}$[Perylene] and FeSe with sonication

In an argon glove box iron selenide (207 mg, 1.53 mmol) was loaded into the flask, containing a magnetic glass stir, using a funnel (Table 5.14). The flask was then taken to the Schlenk line and connected via PVC vacuum tubing with flasks containing fresh dry THF and the reducing agent. The tubing was then evacuated and purged with argon gas 3 times before the vessels were opened to the Schlenk line. Dry THF (5 ml) was then transferred via cannula to the FeSe precursor flask and a suspension created by stirring (300 rpm). Once the transfer was complete the THF containing flask was removed from the line.

The K[PY] reducing solution was then transferred drop-wise via a cannula to the FeSe suspension over 5 minutes. The reaction mixture was then subject to 10 minutes of sonication in a sonic bath (100 W) followed by 50 minutes of stirring; this sequence was repeated 3 times. Due to the insoluble iron selenide settling out during the sonication (stirring was unavailable during sonication) the repetition of sonication and stirring step ensured that the energy from sonication was applied evenly throughout the solid iron selenide. The first reaction (AM144_1) was performed for 3 hours; the second (AM101_1) for 24 hours and the third (AM124_1) for 72 hours. Once their respective reaction times were

completed the product was isolated from the supernatant by filtration through a Schlenk frit. The material was then washed with THF (3 x 20 ml) to remove the PY starting material from the product. The washed product was then dried under low vacuum ($1x10^{-1}$ mbar) before being transferred to an argon glove box.

A control reaction was carried out following the above protocol over 24 hours except that THF (35 ml) was added without any reducing agent dissolved within it. This allowed the effect of sonication on FeSe to be assessed to see if any decomposition was observed.

The recovered material was removed from the Schlenk frit using a long titanium spatula. The materials weight was recorded before it was ground in a pestle and mortar. The ground material was then loaded into a capillary for PXRD.

Table 5.14 Summary of reaction times for the reaction of $K_{1.0}$[PY] and FeSe using sonication.

ID/ hours	Total Reaction time/ Hours	Precursor ID
AM101_1	24	AG349_1
AM124_1	72	AG364_2
AM147_1	3	AG364_2
AM151_1	24	AG364_2

5.5.1.1. Method of obtaining amorphous content via X-ray analysis

The lack of a trend in the phase fractions over time (Figure 5.4) could potentially be due to the formation of an amorphous phase as time progresses. This quantity can be determined by the use of internal standards ground into the material before X-ray analysis. Laboratory powder X-ray diffraction (PXRD) patterns were collected on a Bruker D8 Advance diffractometer in capillary geometry mode with a Ge crystal monochromator and molybdenum X-ray source supplying $K\alpha_1$ at a wavelength of 0.70930 Å. Analysis of the amorphous contents of the $K_{0.5}Fe_2Se_2$ materials produced by low temperature methods was achieved by grinding the product with a known amount of anhydrous KBr (*ca*. 15 wt.%). This provided a highly crystalline phase of a known quantity with which to calculate the total amount of the sample which scatters x-rays.[49]

5.5.2. Results and Discussion for the synthesis of $K_{0.5}Fe_2Se_2$ in THF using $K_{1.0}$[Perylene] and FeSe with sonication

The inclusion of sonication to both stimulate the formation of, and homogenise, the final product fails to produce fully reacted material. The PXRD patterns collected for each of the materials shows significant amounts of unreacted β-FeSe (Figure 5.11 and 5.12). Like the materials produced using K[PY] at reaction times of 3, 24, 168 hours the sonicated materials appear to have only one *I*4/*mmm* phase at first glance. The true phase assembly only becomes clear on Rietveld analysis where for the 24 and 72 hour samples there are 2 *I*4/*mmm* phases present. An additional similarity between the materials made with and without sonication is that the samples exhibit superconducting properties (Figure 5.13 and Table 5.15). For the samples made using the sonication step the samples AM101_1 and AM124_1 show SFs of 11 and 6 % respectively where the T_c is at 33 K (Figure 5.13). This indicates that the sonication step facilitates the formation of the superconducting material. The results of the Rietveld analysis and SQUID magnetometry of these materials are presented in tables 5.15 to 5.17.

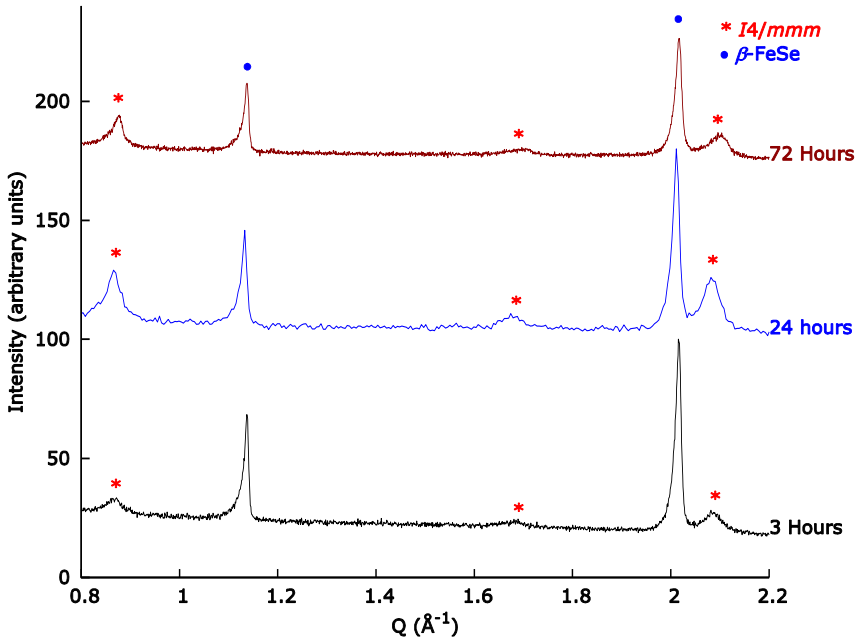

Figure 5.11 Comparison of the PXRD patterns of AM147_1 (3 Hours), AM101_1 (24 Hours) and AM124_1 (72 Hours) where the red * represents the *I*4/*mmm* peaks and the blue circles represent the β-FeSe.

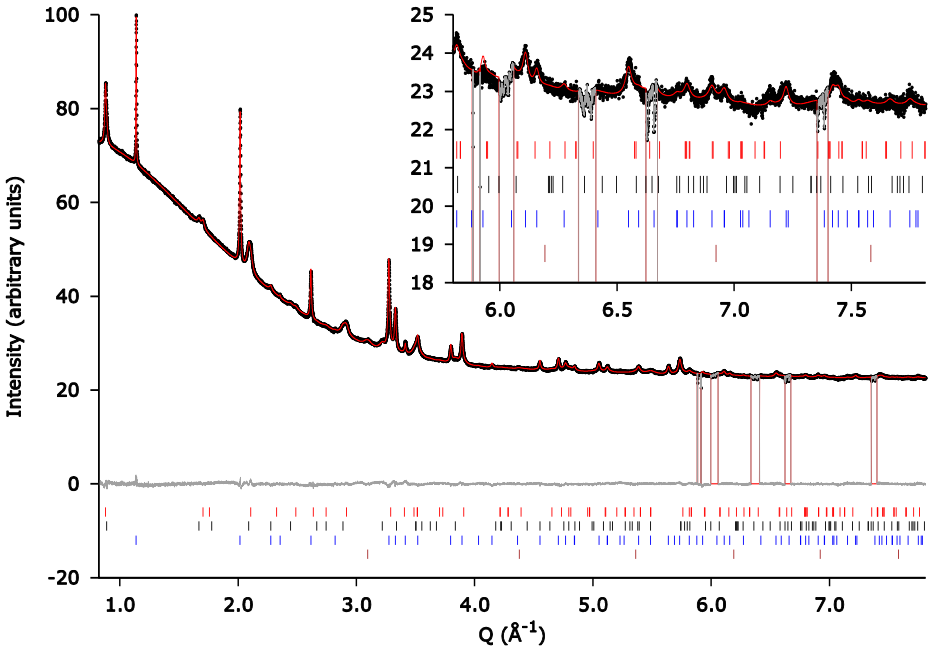

Figure 5.12 A typical Rietveld refinement plot for the materials made using the sonication step in section 5.2.1. The presented refinement was done on the material AM101_1 (24 hours) with the composition $K_{0.5}Fe_2Se_2$. The multiphase model was refined against SPXRD data at a wavelength of λ = 0.827157 Å. Observed (black dots), calculated (red line) and difference (grey line) data are shown. The tic marks represent Bragg reflection positions of the *I*4/*mmm* (red), *I*4/*mmm*2 (black), *β*-FeSe (Blue) and Fe (Brown) phases. A summary of the refined parameters are presented in Tables 5.15 to 5.17. R_{wp} = 0.56, R_{exp} = 0.26, number of refined parameters 51.

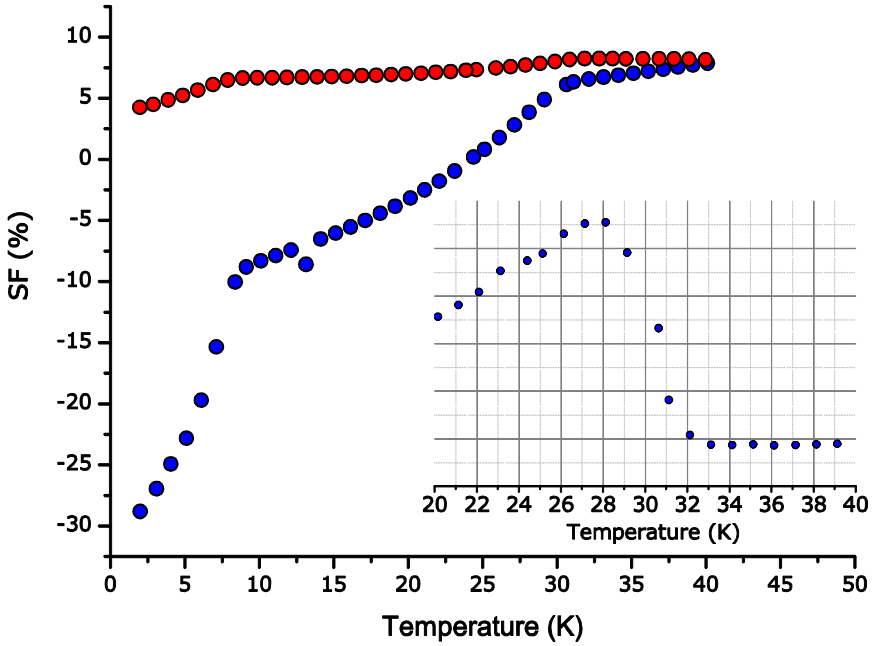

Figure 5.13 The magnetisation as a function of temperature measurements done on AM101_1 ($K_{0.5}Fe_2Se_2$). The blue and red circles are the ZFC and field cooled experiments respectively. The inset is *d*M/*d*T and shows the onset of superconduction at a T_c of 33 K and a SF of 11.2 %. The magnetic measurements were taken in an applied field of 10 Oe with a sample mass of 15.1 mg.

Table 5.15 The T_cs, shielding and phase fractions as obtained from the Rietveld analysis of the pxrd obtained from materials produced by the reaction of $K_{1.0}$[PY] and FeSe in THF using sonication. The errors are displayed at one standard deviation.

Parameter / Label	Total Reaction time (Hours)	T_c (K)	SF (%)	*I*4/*mmm* (wt. %)	*I*4/*mmm*2 (wt. %)	*β*-FeSe (wt. %)	*δ*-FeSe (wt. %)	Fe (wt. %)
AM147_1	3	N/A	0	29.75(39)	0	69.40(44)	0.84(5)	0
AM101_1	24	33(5)	11.2	20.38(26)	26.16(25)	51.15(25)	0	2.31(5)
AM124_1	72	33(5)	6.1	22.7(5)	14.3(5)	57.2(6)	0	5.8(6)

Table 5.16 The cell parameters of the *I*4/*mmm* phases as obtained from the Rietveld analysis of the pxrd obtained from materials produced by the reaction of $K_{1.0}$[PY] and FeSe in THF using sonication. In addition to materials described in this chapter some important materials from chapter 4 are included for reference. The errors are displayed at one standard deviation.

Parameter / Label	Total Reaction time (Hours)	SF (%)	*I*4/*mmm* *a* Å	*I*4/*mmm* *c* Å	*I*4/*mmm* V Å^3	*I*4/*mmm* *c*/*a*	*I*4/*mmm*2 *a* Å	*I*4/*mmm*2 *c* Å	*I*4/*mmm*2 V Å^3	*I*4/*mmm*2 *c*/*a*
AM147_1	3	0	3.854(1)	14.394(8)	213.9(2)	3.734(2)	0	0	0	0
AM101_1	24	11.2	3.8192(5)	14.305(1)	208.67(5)	3.745(6)	3.9051(4)	14.160(2)	215.93(3)	3.7453(6)
AM124_1	72	6.1	3.8121(9)	14.321(3)	208.1(1)	3.757(1)	3.906(2)	14.107(9)	215.2(2)	3.757(1)
AG323_2($K_{0.75}Fe_{1.868}Se_2$)	N/A	19	3.83626(7)	14.2508(4)	209.73(1)	3.7148(1)	0	0	0	0
AG311_2($K_{0.75}Fe_{1.781}Se_2$)	N/A	19	3.83643(8)	14.2504(3)	209.74(1)	3.7145(1)	0	0	0	0
AG308_3($K_{0.75}Fe_{1.702}Se_2$)	N/A	19	3.83600(7)	14.2523(4)	209.72(1)	3.7154(1)	0	0	0	0
AG424_2($K_{0.8}Fe_{1.753}Se_2$)	N/A	6.3	3.8371(2)	14.2518(6)	209.84(2)	3.7142(2)	0	0	0	0
AG281_3($K_{0.9}Fe_{1.55}Se_2$)	N/A	0	0	0	0	0	3.9673(8)	13.754(4)	216.5(1)	3.467(1)
AG315_2($K_{0.9}Fe_{1.625}Se_2$)	N/A	0	0	0	0	0	3.9682(4)	13.773(2)	216.88(6)	3.4707(7)

Table 5.17 A summary of the compositions of the materials produced using $K_{1.0}$[PY] and FeSe in THF using sonication obtained by Rietveld analysis.

Parameter / Label	Total Reaction time (Hours)	Nominal Composition	Analysed Composition	Overall Refined Composition	Refined *I*4/*mmm* composition	Refined *I*4/*mmm*2 composition
AM147_1	3	$K_{0.5}Fe_2Se_2$	$K_{0.3(2)}Fe_{1.84(5)}Se_{2.00(2)}$	$K_{0.204(9)}Fe_{1.94(1)}Se_2$	$K_{0.84(3)}Fe_{2.00(4)}Se_2$	N/A
AM101_1	24		$K_{0.450(2)}Fe_{2.14(2)}Se_{2.00(2)}$	$K_{0.320(8)}Fe_{2.0(1)}Se_2$	$K_{0.33(2)}Fe_{1.95(3)}Se_2$	$K_{1.00(2)}Fe_{1.57(3)}Se_2$
AM124_1	72		$K_{0.39(7)}Fe_{2.10(2)}Se_{2.00(2)}$	$K_{0.25(1)}Fe_{2.14(4)}Se_2$	$K_{0.37(3)}Fe_{2.00(3)}Se_2$	$K_{1.00(5)}Fe_{1.03(5)}Se_2$

The phase assembly of the materials produced using the sonication step consists of two *I*4/*mmm* phases, *β*-FeSe and elemental iron (Figure 5.14 and Table 5.15). The sonication creates a significant difference between the two three hour reaction products produced with sonication (AM147_1) and without (AM127_1). The sonicated material at a reaction time of three hours shows the presence of only one *I*4/*mmm* phase at a fraction of 29.75(39) % which is one of the highest fractions produced for these materials (including samples in chapter 4).

At reaction times of 24 and 72 hours the PXRD shows the presence of the *I*4/*mmm*2 phase in addition to the *I*4/*mmm* and FeSe phases. Intriguingly the phase fractions here, like those of the un-sonicated materials, show no trend where the amount of unreacted FeSe increases between 24 and 72 hours (Figure 5.14). One possible reason for this behaviour is if an amorphous material is present which can cause inaccuracies in the calculation of phase fractions from PXRD.[49]

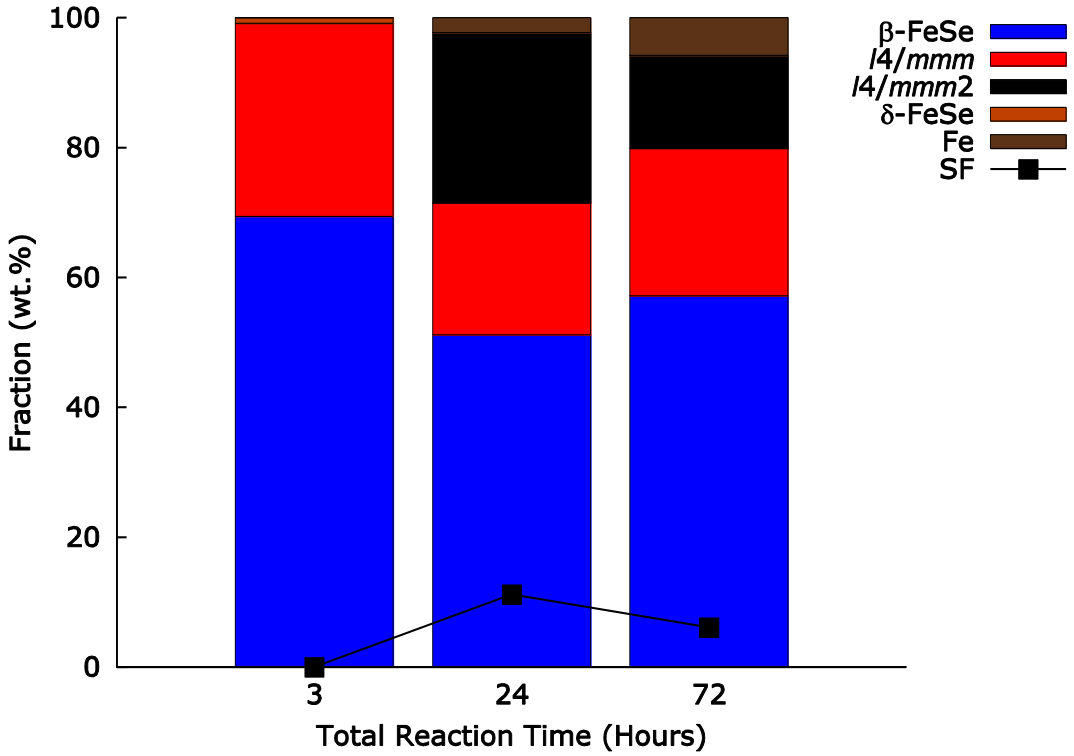

Figure 5.14 Phase and superconducting fractions obtained from Rietveld analysis and SQUID magnetometry performed on the materials AM101_1 (24 hours), AM124_1 (72 hours) and AM147_1 (3 hours).

The materials produced using the sonication step have refined compositions that are inconsistent with the nominal composition and observations made during the reactions. Observing the colour change (from opaque blue to clear yellow) during the reactions over 72 hours revealed that the reducing agent was used up after 5 hours consistent with the ICP analysis of AM101_1 (total reaction time of 24 hours) gave $K_{0.45(2)}Fe_{2.15(1)}Se_{2.00(1)}$. The compositional anomaly between the results of Rietveld refinement and nominal composition is most severe in the sample reacted for 72 hours where the Rietveld calculated composition is only 50 % of the nominal value. This is a strong indication of the formation of an amorphous phase which could potentially be taking up the missing potassium

5.5.2.1. Analysis of amorphous content

Rietveld analysis of PXRD patterns spiked with KBr reveals the presence of significant amorphous material in AM124_1 (72 hours total reaction time, Figure 5.15 and Table 5.18). This explains the increase in FeSe fraction in the unspiked samples when AM124_1 is compared to AM101_1. It also helps to explain where the low overall refined potassium composition in AM124_1 (Table 5.17). The undetected amorphous phase results in the incorrect phase fractions being calculated and therefore the global composition is also incorrect.[49] So taking into account the revised fractions, calculated by Rietveld refinement against the spiked PXRD, it is clear that the majority of the reaction is done in the first 3 hours (Figure 5.15). The issue with such a quick reaction is that the initial intercalated material must then contain considerable amounts of potassium.

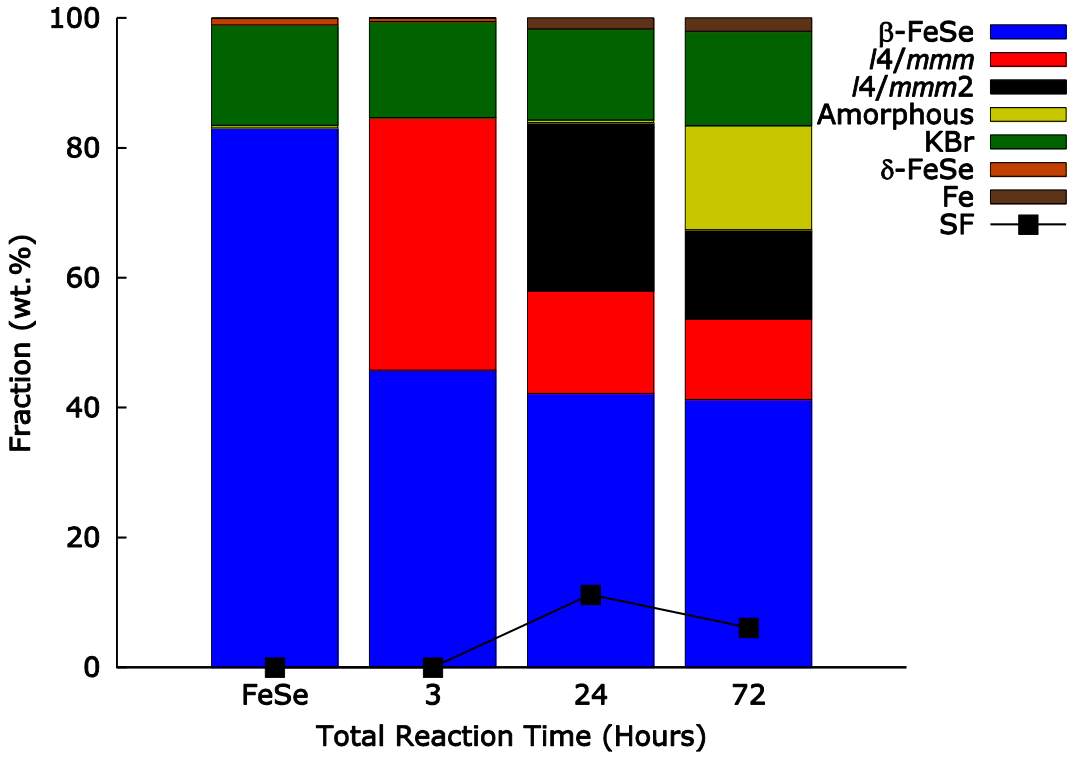

Figure 5.15 Results of determination of amorphous content by Rietveld analysis using material spiked with an internal reference (KBr) and superconducting fractions obtained from SQUID magnetometry performed on the materials AM101_1, AM124_1 and AM147_1.

Table 5.18 The phase fractions as obtained from the Rietveld analysis of the pxrd patterns obtained from materials produced by the reaction of $K_{1.0}$[PY] and FeSe in THF using sonication and spiked with an internal standard (KBr). The errors are displayed at one standard deviation.

Parameter / Label	Total Reaction time (Hours)	*I*4/*mmm* (wt. %)	*I*4/*mmm*2 (wt. %)	*β*-FeSe (wt. %)	*δ*-FeSe (wt. %)	Fe (wt. %)	KBr (wt. %)	Amorphous (wt. %)
FeSe	N/A	0	0	83.1(10)	1.01(4)	0	15.5	0.37(103)
AM147_1	3	38.86(81)	0	45.78(80)	0.54(7)	0	14.80	0.03(178)
AM101_1	24	15.8(3)	25.9(5)	42.2(2)	0	1.9(1)	14.0	0.4(11)
AM124_1	72	12.38(70)	13.77(75)	41.27(59)	0	2.05(3)	14.50	16.02(135)

The initial presence of a single *I*4/*mmm* phase with the refined composition of $K_{0.84(3)}Fe_{2.00(4)}Se_2$ means that the reaction is likely to progress by first intercalating the surface of the *β*-FeSe crystallites. This would create the observed *I*4/*mmm* phase in AM147_1 where the majority of the potassium is intercalated into a small amount of FeSe creating an iron and potassium rich *I*4/*mmm* phase. This iron and potassium rich *I*4/*mmm* phase is then intercalated further causing the loss of iron in the most external regions (of the crystallites) creating the *I*4/*mmm*2 phase. As shown in chapter 4 this iron deficient phase can accommodate much more potassium, up to $K_{0.9}Fe_ySe_2$, depending on how much iron is lost.

The creation of this layer of iron deficient $K_xFe_ySe_2$ then protects the inner iron rich phase as the remaining potassium is taken up by the now sacrificial *I*4/*mmm*2 phase. This process continues through to 72 hours where the elemental iron content is at its highest and the *I*4/*mmm*2 phase loses more iron and becomes amorphous. In support of this we can see that the iron deficient phase (*I*4/*mmm*2) drops by 12.1 % between 24 and 72 hours. This is accompanied by the appearance of an amorphous contribution to the pattern indicating that the *I*4/*mmm*2 phase is being converted into the amorphous phase. This indicates that the best reaction time to operate within is 3 hours; this would give the maximum amount of iron rich *I*4/*mmm* material.

The examination of the cell volumes of the intercalated phases reveals a similar theme as described in the previous section; the presence of an iron rich *I*4/*mmm* phase with a smaller cell volume and an iron deficient *I*4/*mmm*2 phase with a larger cell volume (Tables 5.16 and 5.17). As demonstrated in chapter 4 and in section 5.1 *I*4/*mmm* phases with cell volumes of ~215 $Å^3$ are non-superconducting. This leaves the *I*4/*mmm* phase with cell volumes of less than 214 $Å^3$ to be responsible for superconductivity (Tables 5.16 and 5.17). Interestingly for the superconducting materials here (AM101_1 and AM124_1) the T_cs are observed at 33 K (Figure 5.13). This means that the superconducting phase here is likely to be the same as the superconducting materials of chapter 4. However, the analysis of the materials in this chapter is hampered by the fact that not all of the *I*4/*mmm* phase is superconducting and is heavily overlapped by the *I*4/*mmm*2 phase in the PXRD data.

The cell volumes of the *I*4/*mmm* phases of the two superconducting materials (AM101_1 and AM124_1) are over 1 $Å^3$ smaller than those of AG308_3, AG311_2 and AG323_2 (Table 5.17). However, this value may be untrue for the superconducting material as only 70 % of the *I*4/*mmm* phase in AM101_1 and 40 % AM124_1 is superconducting (Table 5.16 and 5.17). This

could be due to a range of close compositions being present which could affect the position of the *I*4/*mmm* peaks. Due to the heavy overlap between the peaks of the two *I*4/*mmm* phase reliable extraction of the strain values to obtain a value for the spread of lattice parameters is impossible. The possibility of a broad range of compositions present in these materials should be considered as the material has not been equilibrated by subsequent thermal treatments. This means that conclusively linking cell volume to T_c is not sensible at this point with the quality and quantity of data from these reactions.

The reaction of 2 equivalents of FeSe with ½ K[PY] in THF using sonication has improved upon the synthesis described in section 5.1. The inclusion of the sonication step allowed the isolation of material with only one intercalated *I*4/*mmm* phase. The presence of only one *I*4/*mmm* phase at fractions of 38.86(81) wt.% is one of the highest for any of the $K_xFe_2Se_2$ materials. Unfortunately the material with a single intercalated phase (AM147_1) is non-superconducting as the cell volume is 2 % larger than the critical value of 209.73 $Å^3$ obtained from chapter 4.

5.6. Conclusions

The primary objective of this work was to ascertain the viability of a low temperature synthetic route to synthesise superconducting *I*4/*mmm* $K_{0.5}Fe_2Se_2$. The reaction of FeSe with K[Acene] (Acene = naphthalene (NP), acenaphthalene (ANP), fluoranthene (FA), perylene (PY) and tetracene(TA))produces intercalated material which shows no sign of the vacancy ordered *I*4/*m* $K_xFe_ySe_2$ phase. Instead of this there are two forms of intercalated material with crystal symmetry corresponding to the $ThCr_2Si_2$ (SG = *I*4/*mmm*). The difference between these two forms of *I*4/*mmm* material is that one has stoichiometric FeSe units (designated *I*4/*mmm*) and the other is based upon a "vacancy disordered" analogue of the *I*4/*m* phase (designated *I*4/*mmm*2). The presence of this *I*4/*mmm*2 phase and the FeSe starting material indicates that the reducing agents are not capable of evenly reducing the material which leads to over reduction and the leeching of iron from the material. The conclusions for the results presented in this chapter are:

(1) K[PY] is the best reducing agent for intercalating FeSe used in this work as it gives $K_xFe_2Se_2$ material with the least amount of the *I*4/*mmm*2 and it is uncontaminated by the organic reagent. The most noticeable reason for rejecting the reducing agents K[NP] and K[ANP] is the presence of significantly more iron than was originally present in the relevant precursor. The K[TA] reducing was further eliminated as the TA remained in the sample after washing and the qualitative assessment of the PXRD showed no significant improvement over using K[FA] or K[PY]. Differentiating between K[FA] and K[PY] came down to the fact that due to the larger number of conjugated rings in PY it is the less powerful reducing agent of the two. It was decided that the use of the K[PY] reducing agent could give greater control over how quickly the material decomposed during the reaction thereby enabling the isolation of FeSe and a single *I*4/*mmm* iron rich phase.

(2) The reaction of ½ K[PY] and 2 Fe_2Se_2 in THF is capable of producing superconducting materials where the *I*4/*mmm* phase is the likely cause. The T_cs recorded for these materials are found in the range 31.5-33 K which is consistent with those found in the subsolidus materials of chapter 4. This indicates that these materials are free from solvent. For the reactions that did not use the sonication step (section 5.1.1.1.) the superconductivity developed to

a maximum SF of 10.4 % at a reaction time of 168 hours. Samples made after reaction times of 3 and 24 hours only produced trace SFs of 2 %. Interestingly the sample showing 10 % SF at 32 K has an *I*4/*mmm* phase which has a cell volume within its error of the critical value of 209.73 Å^3. This indicates that although no match for the shielding fractions (19 %) produced by the subsolidus reactions in chapter 4 the reactions are a valid starting point with which to investigate the possibility of obtaining superconducting pure *I*4/*mmm* material.

The materials made using the sonication method achieve their maximum SF at 24 hours of 11.2 % which then decreased to 6.1 % at 72 hours. The material produced after 3 hours of reaction time using the sonication protocol was the only non-superconducting material produced using K[PY]. The cell volumes of the two superconducting samples produced by this method are ~1 Å^3 smaller than that of the *I*4/*mmm* phases with 19 % SFs (209.73 Å^3). Since less than half of the *I*4/*mmm* phase is superconducting these materials have more in common with AG424_2. The cell volume of AG424_2 is close to that of AG308_3, AG311_2 and AG323_2 but not identical which results in a significantly lower SF. This is a similar situation for AM101_1 and AM124_1 where the cell volume of the *I*4/*mmm* phase is not correct and therefore the SF is lower than that expressed for AG308_3.

(3) The *I*4/*mmm*2 phase is not responsible for the superconducting behaviour of the material. The *I*4/*mmm*2 phase is comparable to that found in region 3 of the subsolidus $K_xFe_ySe_2$ phase diagram in chapter 4. The cell parameters of the *I*4/*mmm*2 phase are identical, to within 3 standard deviations, of the iron deficient *I*4/*mmm* phase found in the region 3 materials. In addition to this is the observation that the *I*4/*mmm*2 phases for the K[PY] based synthetic methods are identical between each reaction giving a spread of cell volumes of 215.7(4) Å^3. Such that the *I*4/*mmm*2 phases in the materials showing SFs of ~10 % are identical to those showing trace superconductivity.

(4) The inclusion of the sonication step in the reaction of K[PY] and FeSe demonstrated that it is possible to obtain a single *I*4/*mmm* phase after 3 hours of reaction time. Unfortunately this sample was non-superconducting where the *I*4/*mmm* phase had a very large cell volume of 213.9(2) Å^3 and a refined composition of $K_{0.84(3)}Fe_{2.00(4)}Se_2$. Although the Rietveld refinement yields the composition of this phase because potassium scatters X-rays relatively poorly which impacts the accuracy to which the composition is known. The conclusion that superconducting *I*4/*mmm* phases have a specific cell volume of 209.73 Å^3 is

supported by this material as the *I*4/*mmm* phase here has the "wrong" cell volume.

(5) Reaction times that are longer than 24 hours produce amorphous material which means that shorter reaction times should be used to obtain high quality material. The anomalous trend in phase fractions for the materials produced by using the sonication step is resolved on spiking the materials with an internal standard (KBr). The initial anomalous trend shows a decrease in FeSe content between 3 and 24 hours followed by an increase between 24 and 72 hours. Once spiked the Rietveld analysis show a more logical trend in the phase fraction of *β*-FeSe where it initially decreases and finally plateaus out after 24 hours.

At a reaction time of 72 hours the Rietveld analyses of the spiked materials show the presence of an amorphous material at a fraction of 16 %. This is coupled with a reduction in the SF of 4.9 % lower when compared to the material isolated at 24 hours reaction time. This indicates that the amorphous material is not responsible for superconductivity here. Therefore if high shielding fractions are to be obtained then the room temperature reactions between K[PY] and FeSe should be done at 24 hours or less.

(6) This work shows that it is possible to produce superconducting potassium iron selenide from a K[PY] and FeSe system. Sonication speeds up the rate of reaction which gives the benefit of reducing the risk that the sample is exposed to atmosphere and considering the possibility of the negative effect of stirring minimises this as well. In addition to this the use of sonication promotes the formation of one single *I*4/*mmm* phase whereas in the absence of this additional step two *I*4/*mmm* phases are always observed. Most importantly this work clearly shows that the FeSe material shows no adverse reaction to sonication under the conditions presented here. This means that it is a worthwhile endeavour to pursue more ideal solvents than THF which promote layer exfoliation and allow the formation of stable colloidal solutions of the FeSe layers.

5.7. References

1. D. P. Shoemaker, D. Y. Chung, H. Claus, M. C. Francisco, S. Avci, A. Llobet and M. G. Kanatzidis, *Physical Review B*, 2012, **86**.

2. M. S. Whittingham, *Progress in Solid State Chemistry*, 1978, **12**, 41-99.
3. S. W. Muir, O. D. Rachdi and M. A. Subramanian, *Materials Research Bulletin*, 2012, **47**, 798-800.
4. F. C. Hsu, J. Y. Luo, K. W. Yeh, T. K. Chen, T. W. Huang, P. M. Wu, Y. C. Lee, Y. L. Huang, Y. Y. Chu, D. C. Yan and M. K. Wu, *Proceedings of the National Academy of Sciences of the United States of America*, 2008, **105**, 14262-14264.
5. Y. Kamihara, T. Watanabe, M. Hirano and H. Hosono, *Journal of the American Chemical Society*, 2008, **130**, 3296.
6. M. Burrard-Lucas, D. G. Free, S. J. Sedlmaier, J. D. Wright, S. J. Cassidy, Y. Hara, A. J. Corkett, T. Lancaster, P. J. Baker, S. J. Blundell and S. J. Clarke, *Nature Materials*, 2013, **12**, 15-19.
7. T. P. Ying, X. L. Chen, G. Wang, S. F. Jin, T. T. Zhou, X. F. Lai, H. Zhang and W. Y. Wang, *Sci. Rep.*, 2012, **2**.
8. W. P. F. A. M. Omloo and F. Jellinek, *Journal of the Less Common Metals*, 1970, **20**, 121-129.
9. J. K. Chen, Y. J. Zhu, N. F. Chen, X. L. Liu, Z. L. Sun, Z. H. Huang, F. Y. Kang, Q. M. Gao, J. Jiang and L. D. Chen, *Journal of Nanoparticle Research*, 2011, **13**, 6569-6578.
10. B. M. L. Rao and R. W. Francis, *Journal of Physics and Chemistry of Solids*, 1976, **37**, 345-345.
11. L. Hernán, J. Morales, J. Pattanayak and J. L. Tirado, *Journal of Solid State Chemistry*, 1992, **100**, 262-271.
12. J. S. O. Evans, S. J. Price, H. V. Wong and D. O'Hare, *Journal of the American Chemical Society*, 1998, **120**, 10837-10846.
13. L. F. Nazar and A. J. Jacobson, *Journal of Materials Chemistry*, 1994, **4**, 1419-1425.
14. M. Ohashi, K. Uyeoka, S. Yamanaka and M. Hattori, *Bulletin of the Chemical Society of Japan*, 1991, **64**, 2814-2818.
15. F. R. Gamble, F. J. Disalvo, R. A. Klemm and T. H. Geballe, *Science*, 1970, **168**, 568.
16. C. A. Formstone, M. Kurmoo, E. T. Fitzgerald, P. A. Cox and D. O-hare, *Journal of Materials Chemistry*, 1991, **1**, 51-57.
17. F. R. Gamble, J. H. Osiecki, M. Cais and Pisharod.R, *Science*, 1971, **174**, 493.
18. A. Krzton-Maziopa, E. V. Pomjakushina, V. Y. Pomjakushin, F. von Rohr, A. Schilling and K. Conder, *Journal of Physics-Condensed Matter*, 2012, **24**, 6.
19. P. K. Biswas, A. Krzton-Maziopa, R. Khasanov, H. Luetkens, E. Pomjakushina, K. Conder and A. Amato, *Physical Review Letters*, 2013, **110**.

20. W. Rudorff and H. H. Sick, *Angewandte Chemie-International Edition*, 1959, **71**, 127-127.
21. J. C. Wasse, S. L. Stebbings, S. Masmanidis, S. Hayama and N. T. Skipper, *Journal of Molecular Liquids*, 2002, **96-7**, 341-352.
22. E. W. Scheidt, V. R. Hathwar, D. Schmitz, A. Dunbar, W. Scherer, F. Mayr, V. Tsurkan, J. Deisenhofer and A. Loidl, *European Physical Journal B*, 2012, **85**.
23. M. J. Rosseinsky, D. W. Murphy, R. M. Fleming and O. Zhou, *Nature*, 1993, **364**, 425-427.
24. A. Y. Ganin, Y. Takabayashi, P. Jeglic, D. Arcon, A. Potocnik, P. J. Baker, Y. Ohishi, M. T. McDonald, M. D. Tzirakis, A. McLennan, G. R. Darling, M. Takata, M. J. Rosseinsky and K. Prassides, *Nature*, 2010, **466**, 221-293.
25. O. Zhou, R. M. Fleming, D. W. Murphy, M. J. Rosseinsky, A. P. Ramirez, R. B. Vandover and R. C. Haddon, *Nature*, 1993, **362**, 433-435.
26. T. M. McQueen, Q. Huang, V. Ksenofontov, C. Felser, Q. Xu, H. Zandbergen, Y. S. Hor, J. Allred, A. J. Williams, D. Qu, J. Checkelsky, N. P. Ong and R. J. Cava, *Physical Review B*, 2009, **79**.
27. W. P. F. Omloo and F. Jellinek, *Journal of the Less-Common Metals*, 1970, **20**, 121.
28. J. Guo, S. Jin, G. Wang, S. Wang, K. Zhu, T. Zhou, M. He and X. Chen, *Physical Review B*, 2010, **82**, 180520.
29. T.-P. Ying, G. Wang, S.-F. Jin, S.-J. Shen, H. Zhang, T.-T. Zhou, X.-F. Lai, W.-Y. Wang and X.-L. Chen, *Chinese Physics B*, 2013, **22**.
30. W. P. F. Omloo and F. Jellinek, *Journal of the Less-Common Metals*, 1970, **20**, 121-&.
31. N. G. Connelly and W. E. Geiger, *Chemical Reviews*, 1996, **96**, 877-910.
32. J. Bacsa, A. Y. Ganin, Y. Takabayashi, K. E. Christensen, K. Prassides, M. J. Rosseinsky and J. B. Claridge, *Chemical Science*, 2011, **2**, 1054-1058.
33. N. Lara, P. Aranda, A. I. Ruiz, V. Manriquez and E. Ruiz-Hitzky, *Journal of the Brazilian Chemical Society*, 2012, **23**, 415.
34. D. W. Murphy, F. J. Disalvo, G. W. Hull and J. V. Waszczak, *Inorganic Chemistry*, 1976, **15**, 17-21.
35. S. Yamanaka, H. Kawaji, K. Hotehama and M. Ohashi, *Advanced Materials*, 1996, **8**, 771.
36. S. Yamanaka, *Annual Review of Materials Science*, 2000, **30**, 53-82.
37. N. Lara, P. Aranda, A. I. Ruiz, V. Manriquez and E. Ruiz-Hitzky, *Journal of the Brazilian Chemical Society*, 2012, **23**, 415-+.

38. R. Pi, W. Bauer, B. Brix, C. Schade and P. V. Schleyer, *Journal of Organometallic Chemistry*, 1986, **306**, C1-C4.
39. S. Yamanaka, K. Hotehama and H. Kawaji, *Nature*, 1998, **392**, 580-582.
40. E. Bayer and W. Rudorff, *Zeitschrift Fur Naturforschung Section B-a Journal of Chemical Sciences*, 1972, **B 27**, 1336-1339.
41. *Inorganic chemistry of the main-group elements : a review of the literature*, Chemical Society, London, 1972.
42. N. Hirota, *Journal of the American Chemical Society*, 1968, **90**, 3603.
43. C. K. Mann and K. K. Barnes, *Electrochemical reactions in nonaqueous systems*, M. Dekker, New York, 1970.
44. W. L. F. Armarego and C. L. L. Chai, *Purification of laboratory chemicals*, 5th ed. edn., Butterworth-Heinemann, Amsterdam ; London, 2003.
45. J. Sangster and A. D. Pelton, *Journal of Phase Equilibria*, 1997, **18**, 177-180.
46. J. N. Coleman, M. Lotya, A. O'Neill, S. D. Bergin, P. J. King, U. Khan, K. Young, A. Gaucher, S. De, R. J. Smith, I. V. Shvets, S. K. Arora, G. Stanton, H. Y. Kim, K. Lee, G. T. Kim, G. S. Duesberg, T. Hallam, J. J. Boland, J. J. Wang, J. F. Donegan, J. C. Grunlan, G. Moriarty, A. Shmeliov, R. J. Nicholls, J. M. Perkins, E. M. Grieveson, K. Theuwissen, D. W. McComb, P. D. Nellist and V. Nicolosi, *Science*, 2011, **331**, 568-571.
47. V. Nicolosi, M. Chhowalla, M. G. Kanatzidis, M. S. Strano and J. N. Coleman, *Science*, 2013, **340**, 1420.
48. J. Y. Kim, S. M. Choi, W. S. Seo and W. S. Cho, *Bulletin of the Korean Chemical Society*, 2010, **31**, 3225-3227.
49. I. C. Madsen and N. V. Y. Scarlett, *Quantitative Phase Analysis*, Royal Society of Chemistry, Cambridge, 2008.

6. Conclusions and future work

6.1. Overview of the literature background

The discovery of superconductivity and its properties of zero electrical resistance and the Meissner effect led to a huge interest in materials that exhibited this phenomenon and their potential applications. This driving force has encouraged the investigation of increasingly more exotic superconductors with higher and higher critical temperatures (T_c). This interest has generated a multitude of superconductor classes from conventional low temperature superconductors like NbTi to unconventional high superconductors such as $YBa_2Cu_3O_{7-x}$. The generation of such a wide array of superconducting materials with diverse properties and structures has led to difficulties in defining the important structural aspects of some of the superconductor classes.

Out of all the different classes of superconductors only the superconductivity displayed by the conventional class is fully understood. The conventional superconductors are described by the Bardeen-Cooper-Schrieffer (BCS) theory which links the lattice vibrations to the formation of Cooper pairs by the generation of a weak attraction between electrons. High T_c superconductors are not accounted for by the BCS theory and their properties are not fully understood. The general problem with high T_c superconductors, for example the cuprates, is that they have very complex structures with high levels of disorder coupled with complex superconductivity.

A possible method to help resolve the lack of understanding in the most complex superconductors is to investigate complex unconventional superconductivity in structurally more simplistic materials. A classic example of such a system containing simple structures coupled with unconventional superconductivity is the A_3C_{60} (A = alkali metal) materials. The superconducting forms of these materials are either face centred cubic (FCC) or primitive cubic ("A15"). These materials show no transition to another phase on cooling through the T_c. This means that they undergo a totally electronic transition into the superconducting state. Their status as unconventional superconductors was confirmed when both polymorphs of Cs_3C_{60} FCC and "A15" demonstrated a relationship between T_c and Mott-metal insulator transition.

One of the most powerful aspects of these superconductors is their simplicity which offers a clear view of the superconducting properties but the best samples to date of Cs_3C_{60} still contain impurities of ~20 %. The presence of these

impurities hampers the analysis of the physical properties of this important material. Therefore improvements in the synthetic protocols could still benefit the field of superconductivity.

The iron selenide based superconductors are a much newer class of superconductor offering the same range of alkali metal intercalation compounds that the fullerenes have. The iron selenide superconductors have strong structural links with the iron pnictides and cuprate unconventional superconductors as all of these classes are composed of layers. These layers are thought to be crucial to the superconducting properties of these materials. For the iron based superconductors the layers are composed of [FeX] (X = pnictide or chalcogenide) tetrahedra which can host guest species in between the layers. Therefore the investigation of the iron selenide based superconductors represents an important link between many high temperature superconductors.

Of particular interest is the alkali metal intercalates of the FeSe superconductor. These materials yield a large increase in T_c from 8 K for the FeSe parent material to 46 K for a sodium intercalate. For the $A_xFe_ySe_2$ superconducting (T_c = 33 K) system both the composition and identity of the superconducting phase are in question. The multiphasic nature of these materials makes the interpretation of data concerning their structure difficult and therefore a synthetic answer is required to produce material that can be used to identify the critical phase within this system.

6.2. Overview of the results for this work

6.2.1. The synthesis and characterisation of Cs_3C_{60}

The best samples of the face centred cubic (FCC) and primitive cubic ("A15") Cs_3C_{60} polymorphs have only been obtained in purities of ~80 %. The synthetic methods producing these two polymorphs utilise the hazardous and dangerous solvents methylamine and ammonia. Using these two solvents limits the control over the initial formative step where the Cs metal and C_{60} are reacted. The repeated annealing of these materials fails to improve the purity and therefore the best way of obtaining pure material would be preventing the formation of the impurities at the start. Before this can be done an investigation of the temperature dependency of the phase assembly in methylamine (MA) is necessary to determine if a simple change in protocol is all that is required.

6.2.1.1. Reaction of Cs_3C_{60} precursor in methylamine

Five reactions were carried out in MA using a Cs_3C_{60} solid state precursor which was prepared at 350 °C in a sealed ampoule using stoichiometric amounts of Cs and C_{60}. These reactions were performed in the temperature range of -40 to 40 °C at 20 °C intervals whilst stirring at 300 rpm. The as made product was studied using variable temperature (VT) powder X-ray diffraction (PXRD) experiments. The products of these reactions were subjected to two different annealing protocols where the first was done at 120 °C under dynamic vacuum and the second was done under 300 mbar of He at 180 °C in a sealed ampoule. The products were investigated using PXRD and data was used to perform Rietveld analysis.

(1) The formation of the "A15" Cs_3C_{60} polymorph is favoured by reactions in methylamine performed at 40 °C over those at lower temperatures. The reaction of a Cs_3C_{60} solid state precursor in methylamine at a reaction temperature of 40 °C produces 25 % more of the "A15" phase than the reaction at -40 °C after annealing in at 180 °C. The increase in the phase fraction of the "A15" polymorph is accompanied by a proportional decrease in the fractions of Cs_1C_{60} and the BCO (Cs_4C_{60}) impurity phases. Considering that the precursors used contained none of the "A15" polymorph we can conclude that the BCO and Cs_1C_{60} phases combine to form the "A15" material when reacted in MA.

(2) Additional quantities of "A15" Cs_3C_{60} material are produced during annealing by the reaction of Cs_1C_{60} and the BCO phase. The investigation of the as made materials using variable temperature (VT) PXRD confirmed the relationship between BCO, Cs_1C_{60} and the "A15" Cs_3C_{60} polymorph. The Rietveld analysis of the VT data revealed that as the "A15" phase grew (starting at 60 °C) the BCO and Cs_1C_{60} phases diminished at a similar rate. The analysis of the VT data produced from the as made material of -40 °C reaction the "A15" phase fractions showed that initially the rate increased quickly between 60 and 100 °C by 20 %. The rate of increase in the phase fraction for the "A15" phase decreased showing only a ~8 % increase in the fraction between 100 and 140 °C. This indicates that an optimal annealing protocol would operate between 60 and 100 °C which could potentially maximise the amount of "A15" material produced during future reactions.

6.2.1.2. Production of Cs_3C_{60} using THF as a solvent

The experiments designed to control the initial reaction step were performed in THF rather than ammonia or methylamine as this had the benefit of being able to operate without the use of cryogens. Initially the effect of using THF was assessed by reacting stoichiometric amounts of Cs metal and C_{60} in the solvent. This was performed at three individual temperatures of 20, 40 and 60 °C. The as made product of the 20 °C reaction was investigated using VT PXRD. The products were subject to an annealing protocol under dynamic vacuum at 180 °C. These materials were then investigated using PXRD and Rietveld analysis.

(1) The use of THF as a solvent for the formation of Cs_3C_{60} material favours the FCC polymorph over the "A15" when reacting at 20 °C. After reacting Cs metal and C_{60} in THF at room temperature followed by annealing under dynamic vacuum at 180 °C a product containing 58.3(2) wt.% of FCC Cs_3C_{60} and 2.3(3) wt.% of "A15" material was recovered. This same protocol when performed at a reaction temperature of 40 or 60 °C in solution produced between 32 and 40 wt.% of the "A15" phase and only ~20 wt.% of the FCC polymorph. These reactions when combined with the results of the methylamine experiments show that high temperatures favour the formation of the "A15" Cs_3C_{60} polymorph. If the formation of the impurity phases, BCO and Cs_1C_{60}, can be prevented then obtaining high purity FCC material could be possible using THF at reaction temperatures of 20 °C.

6.2.1.3. Targeted synthesis of Cs_3C_{60}

Since the reaction between stoichiometric amounts of Cs and C_{60} at 20 °C in THF was shown to be the best reaction protocol for the previous data set, this temperature was used for the next set of reactions. The organometallic precursor $Cs[Mn(Cp^*)_2]$ was prepared using a modified method of that described by Robbins et.al. in 1979 for the synthesis of $Na[Mn(Cp^*)_2]$. The modification was that the initial alkali metal naphthalenide solution was performed at 30 °C rather than room temperature in order to complete the reaction within a reasonable time frame.

Three equivalents of $Cs[Mn(Cp^*)_2]$ and C_{60} were then reacted together by adding the reducing agent dissolved in THF (80 ml) to a suspension of the C_{60} in THF (10 ml). The reaction solution was then stirred for 30 minutes before having

the volume of the solution reduced to 22 %. The Cs_3C_{60} material was then precipitated by the addition of hexane (so that there is a 1:1 ratio of THF to hexane). The as-made material was then subject to multiple annealing protocols under dynamic vacuum where the best annealing temperature was found to be 350 °C. This reaction was performed on two different scales aiming to produce 100 mg and 200 mg of Cs_3C_{60} material. The products were then investigated using PXRD, microanalysis and SQUID magnetometry.

(1) The use of the organometallic reducing agent $Cs[Mn(Cp^*)_2]$ can prevent the formation of the BCO phase giving FCC Cs_3C_{60} in purities of >96 %. The utilisation of $Cs[Mn(Cp^*)_2]$ as a reducing agent in THF greatly impedes the formation of the impurity phase BCO where products made by this method have typically less than 4 wt.% of the BCO impurity. When this reaction was performed on a small ~100 mg scale with annealing under dynamic vacuum at 350 °C it gave an analysed composition of $Cs_{3.0}C_{60}{\cdot}(THF)_{0.24}$ and contained 96.8 wt.% of the FCC phase with BCO being the remainder. Scaling this reaction up to a ~200 mg scale resulted in the formation of a material that consisted of FCC Cs_3C_{60} and a small amount of another phase which was linked to a $Cs_3C_{60}.(THF)_x$ (SG = *C*2/*m*) composition indicating that the annealing protocol used was insufficient to remove all solvent. This leads to the conclusion that although the synthesis was successful in preventing the formation of BCO, further annealing trials are required before this method can be used for physical measurements.

(2) The $Cs[Mn(Cp^*)_2]$ method produces Cs_3C_{60} material that supports the conclusions on superconductivity in these materials made by Ganin *et.al.* in 2010. The material produced by this method was investigated for superconductivity using SQUID magnetometry. The materials displayed superconducting behaviour with T_cs of 33.5 K and shielding fractions of 3-6 %. Both the T_c and shielding fractions for the materials are less than the best literature values of T_c = 35 K and shielding fractions of 80 %. Despite the differences between the T_cs and shielding fractions the materials synthesised using $Cs[Mn(Cp^*)_2]$ in THF demonstrated the same dome in the T_c vs pressure as that seen in Ganin *et.al.* in 2010. This observation supports the conclusions made by Ganin *et.al.* in 2010 that Cs_3C_{60} is an unconventional superconductor.

6.2.2. Cs_3C_{60} future work

Further work in obtaining materials with higher purity "A15" Cs_3C_{60} should take advantage of the increased yield of the "A15" phase on increasing temperature. In addition the optimal annealing protocol to maximise "A15" production seems to be between 60 and 100 °C. In this temperature range the amount of "A15" increases at its fastest rate. It would be interesting to perform a reaction in MA at 60 °C to see how much more "A15" material can be obtained. Unfortunately the pressure of MA at 60 °C exceeds the known pressure limits of the equipment used in this project. Therefore higher reaction temperatures would require considerable work in ensuring the integrity of the reaction vessels under the specified conditions.

The FCC polymorph of Cs_3C_{60} has an altogether different problem than the "A15" phase. Here the reactions are able to obtain highly pure material but the material produced is of inferior quality to the best literature values in terms of the shielding fraction. The strong points of the reaction protocol are that it is safely scalable and adjustments to the protocols could produce gram scale quantities in the future. The end quality of the material also needs to be improved by an extended annealing protocol to ensure all THF is removed. With a small amount of work the use of $Cs[Mn(Cp^*)_2]$ in THF to form Cs_3C_{60} could provide a precursor for use in the method described by Ganin *et.al.* in 2010. Without the presence of impurities from the beginning high purity material with good superconducting properties could be obtainable.

6.2.3. The synthesis and characterisation of $K_xFe_ySe_2$

The structure and composition of $K_xFe_ySe_2$ is not definitely known, it is suspected that the *I*4/*mmm* minority phase based on the direct intercalation of K into *β*-FeSe is responsible. In addition to this no superconducting materials that were prepared as powders have been found. In this work this issue was explored by the production of a $K_xFe_ySe_2$ powder phase diagram at 750 °C under a subsolidus regime. This temperature is just below the melting point of the $K_xFe_ySe_2$ materials of 800 °C and far above the transition temperature of 300 °C. The initial reaction between potassium metal and Fe_ySe_2 was performed under a 0.5 atm pressure of Ar gas in sealed ampoules at 750 °C. These reactions were then cooled at a rate of 2 °C min^{-1} to room temperature in the furnace. This protocol was then followed by two different methods of cooling by sealing ~80 mg of the materials in a silica ampoule under 0.5 atm. The first was

termed the quenching protocol and consisted of removing the ampoules from the furnace at 750 °C and placing them onto a heat proof mat. The second protocol was termed the slow cooling protocol and consisted of allowing the ampoules to cool at a rate of 2 °C min^{-1} in the furnace. The samples were investigated using SQUID magnetometry, PXRD and ICP.

(1) The phase diagram at room temperature reveals the presence of three ternary potassium iron selenide intercalated phases in the phase assembly of the materials. Using Rietveld analysis it was found that the three intercalated phases correspond to the refined general compositions of $K_xFe_ySe_2$ (space group (SG) = *I*4/*m*), $K_xFe_2Se_2$ (SG = *I*4/*mmm*) and another $K_xFe_ySe_2$ compositional phase with an SG of *I*4/*mmm*. The *I*4/*m* phase is by a √5 x √5 cell expansion of the $ThCr_2Si_2$ structure in the *ab* plane as described by Bacsa *et.al.* in 2011. The *I*4/*mmm* phase corresponding to the composition $K_xFe_ySe_2$ was observed by Shoemaker *et.al.*, is heavily iron deficient and based upon a vacancy disordered structure of the *I*4/*m* phase. The *I*4/*mmm* phase corresponding to a general refined composition of $K_xFe_2Se_2$ is a direct intercalation of potassium into *β*-FeSe.

(2) At high temperature (above 300 °C) there is only one ternary phase present which decomposes into the *I*4/*m* and *I*4/*mmm* phases on cooling. Heating the material above the transition point results in the *I*4/*m* phases iron vacancies becoming disordered which alters the symmetry of the phase to one of *I*4/*mmm* symmetry. For the samples where the nominal Fe oxidation state targeted was +2 the cooling resulted in the formation of a single ternary phase on cooling. For the nominal iron oxidation states less than this the cooling through the transition temperature ~300 °C, in general, results in two ternary phases being formed consisting of an *I*4/*m* and *I*4/*mmm* phase. A further observation is that for nominal potassium compositions less than $K_{0.75}Fe_ySe_2$ there is *β*-FeSe material present above the transition temperature due to the lack of enough potassium to intercalate this FeSe material. Above the nominal potassium composition of $K_{0.75}Fe_ySe_2$ there is only the presence of the ternary potassium iron selenide and iron at high temperature.

(3) The phase diagram of the $K_xFe_ySe_2$ system indicates that bulk superconducting powders are obtainable in the nominal compositional range of $K_{0.75}Fe_ySe_2$ (y = 1.702, 1.781 and 1.868). These three compositions produced materials that exhibited superconductivity with T_cs of 33 K and shielding

fractions of 19 %. The identical nature of the superconductivity found within these materials indicates that the phase responsible for the phenomena should be identical within these three compositions. The Rietveld analysis of synchrotron powder X-ray diffraction data revealed the presence of three distinct phases in each of the samples ($K_{0.75}Fe_ySe_2$ (y = 1.702, 1.781 and 1.868)). These phases were identified as the *I*4/*m*, *I*4/*mmm* (general refined composition $K_xFe_2Se_2$) and Fe.

(4) The *I*4/*m* and iron deficient *I*4/*mmm* phases are not responsible for superconduction in the $K_xFe_ySe_2$ system. Based upon the Rietveld analysis the *I*4/*m* phases in the samples of the $K_{0.75}Fe_ySe_2$ (y = 1.702, 1.781 and 1.868) superconducting compositions were found to have significantly different lattice parameters, cell volumes and *c*/*a* ratios. Their refined potassium and iron compositions were found to be identical to within 3 standard deviations but other *I*4/*m* phases from non-superconducting materials also had the same composition. The lack of a unique and significant result from the Rietveld analysis of the *I*4/*m* phase is strong evidence that the *I*4/*m* phases in the three superconducting compositions are not responsible for the superconducting properties.

The iron deficient *I*4/*mmm* phase was only present in non-superconducting powders where the nominal potassium composition was greater than 0.8 ($K_xFe_ySe_2$). This leads to the conclusion that the iron deficient *I*4/*mmm* phases are also not responsible for superconductivity. This conclusion was also reached by Shoemaker *et.al.* in 2011 where samples containing this material were also non-superconducting.

(5) The *I*4/*mmm* phase with the composition $K_{0.54(1)}Fe_{1.98(1)}Se_2$ and specific cell volume of 209.73(1) $Å^3$ is responsible for the superconductivity in the $K_xFe_ySe_2$ system. The direct comparison of the synchrotron powder X-ray diffraction data in three superconducting (SF = 19 %, T_c = 33 K) compositions $K_{0.75}Fe_ySe_2$ (y = 1.702, 1.781 and 1.868) led to the observation that the three *I*4/*mmm* phases present (at phase fractions of ~16 %) in these compositions were identical. This was later confirmed by Rietveld analysis of the data demonstrating that the lattice parameters, cell volumes, *c*/*a* ratios, compositions and Se-Fe-Se bond angles were all identical for the *I*4/*mmm* phases. The argument that the *I*4/*mmm* phase in these materials was responsible for superconductivity was further reinforced by the fact that their cell volumes were all identical to each other but significantly different from all other *I*4/*mmm*

phases. This led to the conclusion that the *I*4/*mmm* phase with a composition of $K_{0.54(1)}Fe_{1.98(1)}Se_2$ and specific cell volume of 209.73(1) Å^3 was critical to the presence of superconductivity in a sample.

6.2.4. Targeted synthesis of the $K_{0.5}Fe_2Se_2$ composition

The subsolidus reactions of $K_xFe_ySe_2$ were unable to produce high phase fractions of the superconducting phase meaning that the information gained on superconductivity is limited. The positive identification of the *I*4/*mmm* phase at a composition close to that of $K_{0.5}Fe_2Se_2$ enables us to attempt alternate methods of synthesising this important phase. The chosen method of doing this is the reaction of *β*-FeSe with organometallic potassium reducing agents in THF. The reducing agents used were potassium acenes and the acenes used were naphthalene, acenaphthalene, fluoranthene, tetracene and perylene. The reducing agents were produced in THF (30 ml) by the reaction of a slight excess of acene with potassium metal (~14 mg) where the slight excess ensured that all of the potassium metal was converted into the reducing agent. The reducing solution was added to a suspension of *β*-FeSe (5 ml of THF) via a cannula and the reaction stirred over 24 hours. The produced material was then washed using THF and dried under vacuum before being analysed using PXRD.

Out of all of the reducing agents used the K[Perylene] was found to produce the best $K_xFe_ySe_2$ material showing the least amount of decomposition for the FeSe material. The K[Perylene] reducing agent was reacted with *β*-FeSe using the same method as above but using two additional reaction times of 3 and 168 hours. The material was then washed and dried as previously described before being analysed using PXRD.

An additional protocol was developed to attempt to aid in the intercalation of the potassium into the *β*-FeSe material. This consisted of the implementation of a sonication step in the first three hours of the reaction. This step consisted of 3 rounds of 10 minutes sonication followed by 50 minutes of stirring. There were three individual reactions performed using this modification with the total reaction times of 3, 24 and 72 hours. The products were treated washed and dried before being analysed using PXRD.

(1) The room temperature reaction of K[Perylene] and *β*-FeSe produces a phase assembly consisting of two *I*4/*mmm* phases, unreacted *β*-FeSe and elemental iron. The phases assemble consists of the *I*4/*mmm* phases corresponding to the general refined composition of $K_xFe_2Se_2$ and the iron

deficient $K_xFe_ySe_2$ as defined in the subsolidus materials. Due to both the *I*4/*mmm* phases existing within one material the iron deficient variant is referred to as the *I*4/*mmm*2 phase.

(2) Superconducting materials can be produced by reacting *β*-FeSe with K[Perylene]. The reaction of K[Perylene] and *β*-FeSe in THF produces a material that contains the following phase assembly; *I*4/*mmm*; *I*4/*mmm*2; *β*-FeSe and Fe. When the reaction was performed without sonication the superconductivity was only observed in the product obtained after 168 hours of reaction time. The observed superconductivity in this case was at a T_c of 32 K and a shielding fraction of 10 %. Using the sonication step to facilitate the reaction between the K[Perylene] and *β*-FeSe superconductivity was observed in the products obtained after 24 hours of reaction time. The observed superconductivity in these cases had T_cs of 33 K and shielding fractions of 11.2 % and 6.1 % for the products obtained from the reactions at 24 and 72 hours respectively.

(3) The superconducting materials reinforce the conclusion that the iron rich *I*4/*mmm* phase is responsible for superconductivity. Of the phases in the phase assembly in the materials produced by the reaction of K[Perylene] and *β*-FeSe only the superconducting properties of the *I*4/*mmm* and *I*4/*mmm*2 phases are unknown. The Rietveld analysis of the PXRD patterns obtained for all materials shows that the *I*4/*mmm*2 phases are identical to each other both for superconducting and non-superconducting materials. The spread in the *I*4/*mmm*2 cell volumes is 215.7(4) $Å^3$ where samples containing superconducting material have *I*4/*mmm*2 cell volumes within one standard deviation of the cell volumes of *I*4/*mmm*2 phases in materials with trace superconductivity. In comparison to the *I*4/*mmm*2 phase of the subsolidus reactions the *I*4/*mmm*2 phases of the reaction between K[Perylene] and *β*-FeSe have volumes that are identical to within three standard deviations of each other. This reinforces the conclusion that the *I*4/*mmm*2 phase, corresponding to the iron deficient I4/mmm phase based on a vacancy disordered *I*4/*m* phase, is non-superconducting.

The *I*4/*mmm* phases produced by the reaction of K[Perylene] and *β*-FeSe have unit cell volumes close to those observed for the three *I*4/*mmm* phases of the superconducting (SF = 19 %) materials synthesised by the subsolidus reactions. The materials showing superconductivity with the highest shielding fractions (10 and 11 %) made from the reaction of K[Perylene] and *β*-FeSe have the closest cell volumes to the *I*4/*mmm* phases of the three materials showing

shielding fractions of 19 % in the subsolidus reaction. Unfortunately due to the heavy overlap between the *I*4/*mmm* and *I*4/*mmm*2 phases for the materials made using of K[Perylene] and *β*-FeSe a definitive cell volume could not be obtained. However, the phase fractions, from Rietveld analysis, of the superconducting materials are twice the size of the shielding fractions, obtained from SQUID magnetometry. This indicates that these materials have more in common with another sample from the subsolidus reactions with a nominal composition of $K_{0.8}Fe_{1.754}Se_2$; a shielding fraction of 6.3 %; *I*4/*mmm* phase fraction of 18.4(6) wt.% and a *I*4/*mmm* cell volume of 209.84(2) $Å^3$. This sample from the subsolidus reactions is the only other material in that data set that has more than trace superconductivity and has a cell volume that is very close to the ideal. These comparisons make it likely that the *I*4/*mmm* phases that have volumes close to the ideal value of 209.73(1) $Å^3$ are responsible for superconductivity in the materials made using K[Perylene] and *β*-FeSe.

(4) The inclusion of a sonication step at the start of the reaction enables the isolation of a material with only one *I*4/*mmm* phase. The effect of the sonication step during the first 3 hours of the reaction speeds up the time it takes to fully exhaust the reducing agent. Without the sonication step the reducing agent was observed to be depleted at 72 hours by the complete change in colour from blue to yellow. The inclusion of the sonication step reduces this time to 5 hours. This is observable by the analytical composition (obtained from ICP) after 24 hours for of $K_{0.45(2)}Fe_{2.15}Se_{2.00}$. This is also observable from the phase fraction of unreacted *β*-FeSe which is 67.2(3) wt.% at 24 hours without sonication and 51.2(3) wt.% at 24 hours with sonication.

As a result of this faster reaction time a material with a single *I*4/*mmm* phase was obtained from the reaction at 3 hours. The *I*4/*mmm* phase of this material has the following parameters; *a* 3.854(1) Å; *c* 14.394(8) Å; cell volume 213.9(2) $Å^3$; *c*/*a* ratio 3.734(2) and it has a refined composition of $K_{0.84(3)}Fe_{2.00(4)}Se_2$. These values are far away from those obtained from the three materials showing shielding fractions of 19 % obtained from the subsolidus reactions ($K_{0.75}Fe_ySe_2$ (y = 1.702, 1.781 and 1.868)). Therefore it is no surprise that the material produced after a 3 hour reaction using the sonication step is non-superconducting. This observation also reinforces the conclusion that an *I*4/*mmm* phase with a specific cell volume is required in order for a sample to display superconductivity.

(5) Reaction times in excess of 24 hours produce amorphous material indicating that short reaction times are preferable. An anomalous trend in phase fractions was observed for the materials produced by the reaction of K[Perylene] and *β*-FeSe where sonication was applied during the first 3 hours of the reaction time. The anomaly was that the amount of *β*-FeSe starting material, obtained from Rietveld analysis, dropped between the reaction times of 3 and 24 hours. The amount of *β*-FeSe was then observed to increase between 24 and 72 hours reaction time. It would be expected that the amount of starting material would either decrease with reaction time or initially decrease and then plateau out. The materials were then investigated for amorphous content by spiking the material with KBr ~15 %. The Rietveld analysis of the resulting powder X-ray data showed the presence of 16.0(1) % of an amorphous material. It was also observed that the *I*4/*mmm*2 phase decreased by 12 % between 24 and 72 hours reaction time. It would seem that the reaction progresses in the following fashion; *I*4/*mmm* ($K_xFe_2Se_2$) material forms initially which then decomposes into the *I*4/*mmm*2 phase as more potassium is intercalated resulting the production of iron this is then followed by further decomposition of the *I*4/*mmm*2 phase into the amorphous material with the production of more iron. Therefore the amorphous phase is likely to be $KFeSe_2$ and the production of this material is coupled with a decrease in the shielding fraction of the material, a reduction of 5.1 %, when compared to the material obtained after reaction for 24 hours. This leads to the conclusion that short reaction times are best for obtaining superconducting materials.

6.2.5. Potassium iron selenide future work

The subsolidus reaction between K and Fe_ySe_2 produces superconducting materials with SFs of 19 % and T_cs of 33 K which inhibits the accuracy to which the composition of the superconducting phase can be known. Even when using multiple cooling protocols across a large compositional range the superconducting *I*4/*mmm* material has not been isolated in fractions over 18 %. The attempts to target the $K_{0.5}Fe_2Se_2$ composition which is thought to be superconducting using high temperatures results in non-superconducting material. This is due the inability to access the cooling pathways that enable the production of the superconducting minority phase which can be linked to the high temperature phase diagram where the superconducting material is only observed to form from high temperature phase assemblies consisting of *I*4/*mmm* and Fe. Therefore it is unlikely that the isolation of high phase fraction

of phase pure superconducting *I*4/*mmm* phase can be done using high temperature methods.

Considering the success of room temperature routes in synthesising superconducting $Li_xFe_2Se_2$ based materials it seems that pursuing the low temperature route described here is worthwhile. The methods of producing $K_xFe_2Se_2$ superconducting material at low temperatures use ammonia and pyridine. The ammonia protocols are particularly successful producing T_cs of 40 K and SFs of ~50 % but also contain ammonia within the sample, this means that linking the superconducting phase from these materials to those of the high temperature methods is not possible. The literature methods utilising pyridine are successful at producing superconducting $K_xFe_2Se_2$ material but its T_c is 40 K and its PXRD pattern is so complicated that identification of the superconducting phase is impossible. The literature methods use potassium metal and target the composition of $K_1Fe_2Se_2$ making them far more aggressive than the methods described in this work. A more gentle approach involving the exfoliation of the FeSe layers using sonication in a more appropriate solvent (such as amines but there are plenty of ether based solvents that could perform this role) beforehand would allow a more even intercalation of the FeSe starting material. This would give conditions that would promote the formation of single phase material where the exfoliated material would have a large surface area to react with the reducing agents inhibiting the decomposition of the product.

7. Appendix A

7.1. ICP Machine details

The machine set up is comprised of cross flow nebuliser, cyclonic spray chamber and peristaltic pump. The required elements were selected for their intensity and lack of interferences before being calibrated with certified standards, matrix matched and within a previously established concentration range via a 3 point calibration curve. Each peak was then maximised with a background correction applied before final recalculation. Instrument parameters from optimisation were; plasma power at 1380 W; nebulising flow of 0.9 L min^{-1}; coolant flow of 11.0 L min^{-1} and auxiliary flow of 0.8 L min^{-1}. Line selection for each element was K 766.491 nm, Fe 259.941 nm and Se 196.090 nm. Typical root-mean-squared standard deviation values were between 1-1.5 % indicating a stable plasma with consistent sample injection and aspiration.

8. Appendix B

8.1. Synchrotron X-ray patterns

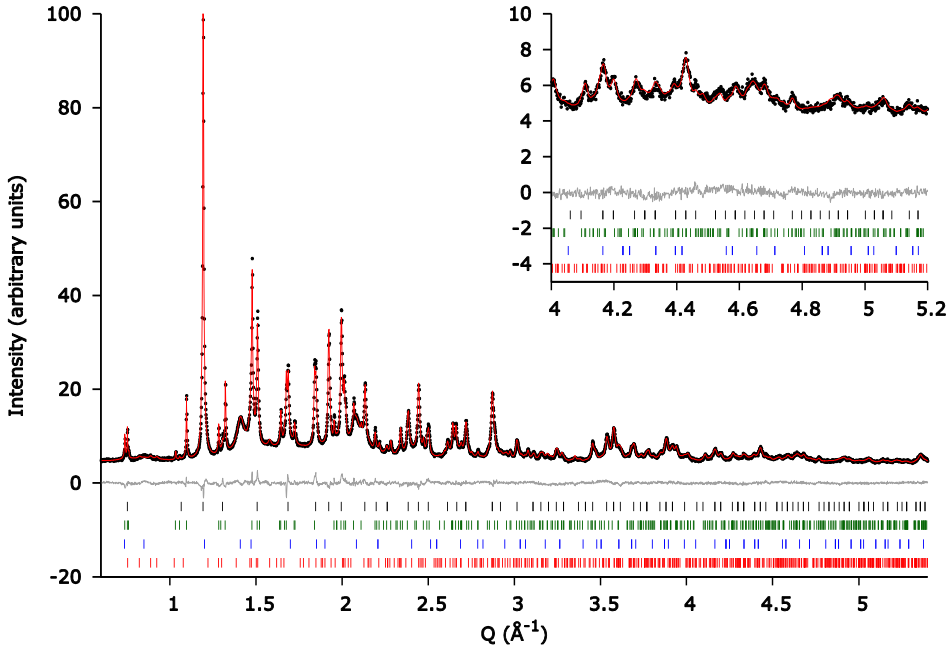

Figure 8.1 Rietveld plots for the material that was given the designation AM36_2 and synthesized with the nominal composition $Cs_{3.0}C_{60}$ where the structural models were refined against synchrotron powder X-ray data. Observed (black dots) and calculated (red line) data of the room temperature synchrotron powder X-ray diffraction pattern. The tics represent Bragg reflection positions of the "A15" (black), BCO (green), FCC (blue) andCs_1C_{60} (red) phases. The wavelength was λ = 0.81932 Å.

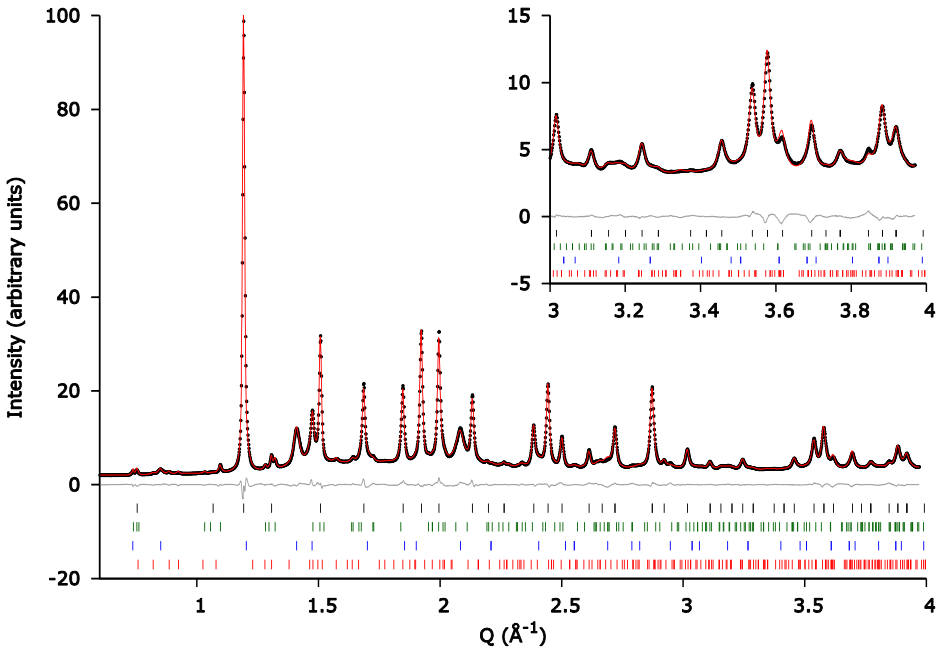

Figure 8.2 Rietveld plots for the material that was given the designation AM36_3 and synthesized with the nominal composition $Cs_{3.0}C_{60}$ where the structural models were refined against synchrotron powder X-ray data. Observed (black dots) and calculated (red line) data of the room temperature synchrotron powder X-ray diffraction pattern. The tics represent Bragg reflection positions of the "A15" (black), BCO (green), FCC (blue) andCs_1C_{60} (red) phases. The wavelength was λ = 0.81932 Å.

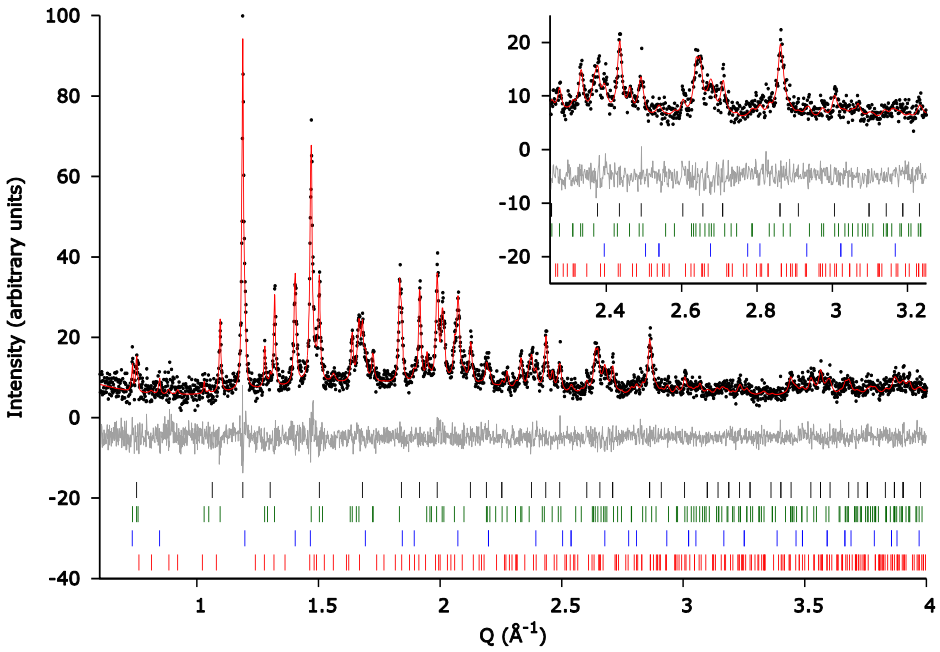

Figure 8.3 Rietveld plots for the material that was given the designation AM40_1 and synthesized with the nominal composition $Cs_{3.0}C_{60}$ where the structural models were refined against synchrotron powder X-ray data. This pattern was recorded at the temperature of 180 °C controlled by the hot air blower of I11 as a part of a variable temperature experiment. Observed (black dots) and calculated (red line) data of the room temperature synchrotron powder X-ray diffraction pattern. The tics represent Bragg reflection positions of the "A15" (black), BCO (green), FCC (blue) andCs_1C_{60} (red) phases. The wavelength was λ = 0.81932 Å.

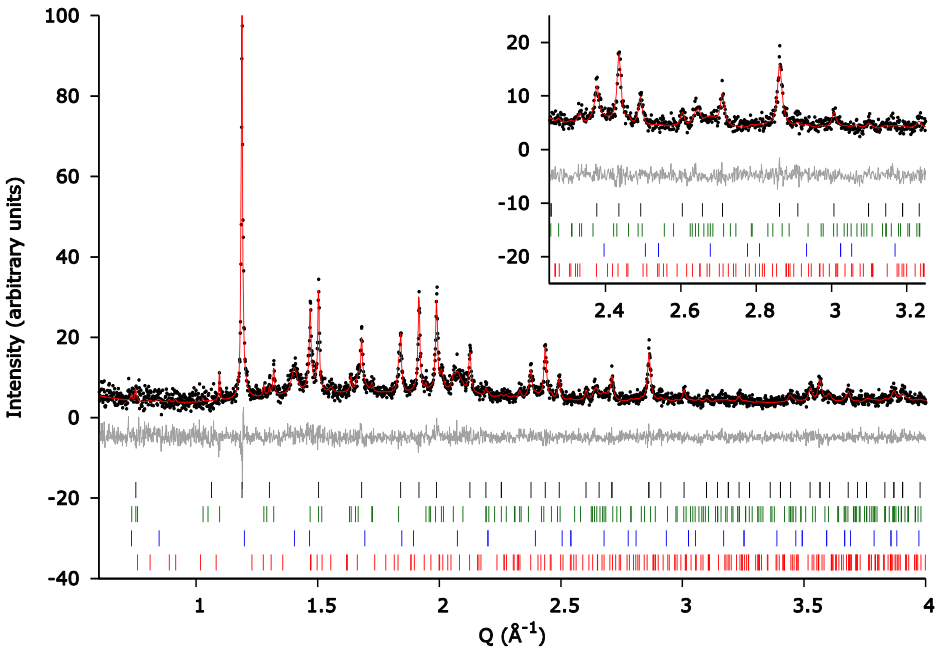

Figure 8.4 Rietveld plots for the material that was given the designation AM36_1 and synthesized with the nominal composition $Cs_{3.0}C_{60}$ where the structural models were refined against synchrotron powder X-ray data. This pattern was recorded at the temperature of 180 °C controlled by the hot air blower of I11 as a part of a variable temperature experiment. Observed (black dots) and calculated (red line) data of the room temperature synchrotron powder X-ray diffraction pattern. The tics represent Bragg reflection positions of the "A15" (black), BCO (green), FCC (blue) andCs_1C_{60} (red) phases. The wavelength was λ = 0.81932 Å.